

11-12-2021

Selected Tropical Cyclone Satellite Analyses with an Emphasis on 37 GHz Color Composite Imagery

Margaret Kieper
mkiep001@fiu.edu

Follow this and additional works at: <https://digitalcommons.fiu.edu/etd>



Part of the [Atmospheric Sciences Commons](#), and the [Meteorology Commons](#)

Recommended Citation

Kieper, Margaret, "Selected Tropical Cyclone Satellite Analyses with an Emphasis on 37 GHz Color Composite Imagery" (2021). *FIU Electronic Theses and Dissertations*. 4840.
<https://digitalcommons.fiu.edu/etd/4840>

This work is brought to you for free and open access by the University Graduate School at FIU Digital Commons. It has been accepted for inclusion in FIU Electronic Theses and Dissertations by an authorized administrator of FIU Digital Commons. For more information, please contact dcc@fiu.edu.

FLORIDA INTERNATIONAL UNIVERSITY

Miami, Florida

SELECTED TROPICAL CYCLONE SATELLITE ANALYSES WITH AN EMPHASIS
ON 37 GHZ COLOR COMPOSITE IMAGERY

A dissertation submitted in partial fulfillment of

the requirements for the degree of

DOCTOR OF PHILOSOPHY

in

GEOSCIENCES

by

Margaret Elizabeth Kieper

2021

To: Dean Michael R. Heithaus
College of Arts, Sciences and Education

This dissertation, written by Margaret Elizabeth Kieper, and entitled Selected Tropical Cyclone Satellite Analyses with an Emphasis on 37 GHz Color Composite Imagery, having been approved in respect to style and intellectual content, is referred to you for judgment.

We have read this dissertation and recommend that it be approved.

Christopher Landsea

Ping Zhu

Robert Burgman

Shu-Ching Chen

Hugh Willoughby, Major Professor

Date of Defense: November 12, 2021

The dissertation of Margaret Elizabeth Kieper is approved.

Dean Michael R. Heithaus
College of Arts, Sciences and Education

Andrés G. Gil
Vice President for Research and Economic Development
and Dean of the University Graduate School

Florida International University, 2021

© Copyright 2021 by Margaret Elizabeth Kieper

All rights reserved.

DEDICATION

I dedicate this work to my dear husband John L. Beven II and our conversations about tropical cyclones that occur most days, and for sharing my endless enthusiasm on this topic.

ACKNOWLEDGMENTS

The author is grateful for the longstanding support and advice given by the tropical cyclone community, especially the forecast community, and their interest in and willingness in accepting my rapid intensification forecast methodology when I had no formal training in the field. The author is especially grateful to Jeff Masters of Weather Underground for his encouragement and mentoring over many years, and for making me realize that I had something valuable to offer in the field. The author thanks FIU for the Presidential Fellowship that was offered at the onset of my tenure as a graduate student at FIU. The author would like to thank her major professor Hugh Willoughby for sharing his extensive knowledge of tropical cyclones and his aircraft reconnaissance experience, and Chris Landsea, Ping Zhu, Robert Burgman, and Shu-Ching Chen for serving on my committee, and Gail Excell and Assefa Melesse for their support. The author is especially indebted to Chris Landsea and John Beven for the opportunity to participate in the 1969 Hurricane Camille reanalysis, which was a joy to participate in, and which ultimately provided a sense of closure to mysteries of that hurricane. The author thanks NRLMRY and FNMOC whose extensive archive of passive microwave imagery made this dissertation possible, and particularly the support of Jeff Hawkins. The author thanks James Franklin and John Knaff for their early support of the rapid intensification forecast methodology and for encouraging me to attend the AMS 28th Hurricanes and Tropical Meteorology Conference in 2008 to present the rapid intensification forecast material.

ABSTRACT OF THE DISSERTATION
SELECTED TROPICAL CYCLONE SATELLITE ANALYSES WITH AN EMPHASIS
ON 37 GHZ COLOR COMPOSITE IMAGERY

by

Margaret Elizabeth Kieper

Florida International University, 2021

Miami, Florida

Professor Hugh Willoughby, Major Professor

This research expanded the understanding of the 37 GHz color composite imagery of tropical cyclones (using the Naval Research Lab Monterey image archive), by improved identification of precipitation types uniquely observed on this imagery, aided by creation of a conceptual model. This model distinguished between stratiform and convective rain, and identified the cyan color on this imagery as being warm rain from shallow and moderate convection, or "SAM." Patterns of SAM on this imagery uniquely identify tropical cyclone features: an early indicator of the onset of rapid intensification and early eyewall replacement cycles, both previously unobserved. These are identified by early eye development of a symmetric shallow convective ring now understood to be a "SAM ring." A forecast methodology created for the RI indicator was introduced globally to Regional Specialized Meteorological Centers. It has been suggested that this contributed to some improvement in NHC intensity forecasts in the past decade.

The 37color imagery also depicts precipitation patterns of sheared tropical cyclones, subtropical cyclones, monsoon trough development and intense tropical cyclones, and is used to develop a supplement to the Dvorak current intensity technique.

The need for a passive microwave repository based on the tropical cyclone life cycle is identified.

The Hurricane Camille reanalysis is presented, with additional material including an explanation for the unusual sea state contributing to the original HURDAT landfall intensity.

TABLE OF CONTENTS

CHAPTER	PAGE
1. INTRODUCTION	1
1.1 PMW Image Dataset	2
1.2.1 The Need for a Tropical Cyclone Life-Cycle PMW Repository	7
2. INTRODUCTION TO TROPICAL CYCLONE 37COLOR IMAGERY	13
2.1 Examples and Characteristics of the 37color Imagery	18
3. TROPICAL CYCLONE RAPID INTENSIFICATION INDICATOR AND FORECAST METHODOLOGY USING THE DEVELOPING EYE CYAN RING PATTERN.....	24
3.1 Importance of Forecasting Rapid Intensification for Severe Tropical Cyclones.....	38
3.2 Images of Convective Rings of Tropical Cyclones that Rapidly Intensified.....	42
3.3 Use of the 37color Ring as an Indicator of the Onset of RI at the NHC	51
4. EARLY EYEWALL REPLACEMENT CYCLES WITH THE ONSET OF THE DEVELOPING EYE CYAN RING PATTERN: A CASE STUDY	67
4.1 Methodology	67
4.2 Known Cases of "Early" ERCs.....	70
4.2.1 1997 Hurricane Danny	71
4.2.2 1991 Hurricane Bob	74
4.3 Passive Microwave Case Study of Four Similar "Early" ERCs	74
4.3.1 Case Study One: 2019 ATL Hurricane Lorenzo.....	78
4.3.1.1 Lorenzo Developing Eye	79
4.3.1.2 Lorenzo SEF Development and ERC Completion	82
4.3.2 Case Study Two: 2004 ATL Hurricane Karl	90
4.3.2.1 Karl Developing Eye.....	90
4.3.2.2 Karl SEF Development and ERC Completion.....	92
4.3.3 Case Study Three: 2006 EPAC Hurricane Daniel	101
4.3.3.1 Daniel Developing Eye	101
4.3.3.2 Daniel SEF Development and ERC Completion.....	105
4.3.4 Case Study Four: 2007 WPAC Yutu	113
4.4 Similarities and Conclusions.....	115
5. A DEEPER EXAMINATION OF THE 37COLOR IMAGERY	122
5.1 A Conceptual Model of the 37color Imagery	127
5.2 TRMM Precipitation Radar Case Studies Compared with 37color Imagery	129
5.3 WSR-88D Radar Cross Section Case Studies Compared with 37color Imagery	140

5.4	Highlighting Differences in Stratiform Precipitation and SAM on the TRMM Radar Cross Sections	145
5.5	Distribution of 37color Tb and Associated 2A23 Convective Rain Estimates.....	147
5.6	Stratiform Signal Masks the Convective Signal in the 2A23 Product.....	151
5.7	Conclusions Regarding Shallow and Moderate Convection in TC	157
6.	A 37COLOR TC PRECIPITATIVE INTENSITY ESTIMATE (PIE) UTILIZING THE 37COLOR IMAGERY	160
7.	ADDITIONAL CHARACTERISTICS OF TROPICAL CYCLONES OBSERVED ON 37COLOR IMAGERY: INTENSE, SHEARED, SUBTROPICAL, AND MONSOON DEVELOPMENT	169
7.1	37color Images of Intense Tropical Cyclones	169
7.2	Sheared Tropical Cyclones Observed on the 37color Imagery	174
7.3	Subtropical Cyclones Observed on the 37color Imagery	178
7.4	Monsoon Trough Development Observed on the 37color Imagery	182
8.	THE 1969 HURRICANE CAMILLE REANALYSIS	185
8.1	Background on the Observed Intensity by Reconnaissance and Related Forecast Intensity.....	206
8.2	The Historical Record of Hurricanes Making Landfall on the Northern Gulf Coast	208
8.3	Significance of an Eyewall Replacement Cycle for Camille.....	208
8.4	Available Satellite and Radar Imagery for Camille.....	210
8.4.1	Comparison of Camille and Wilma Eyewall Replacement Cycle	211
8.4.2	Cloud Motion Analysis of Camille	215
8.4.3	Comparison of Camille Radar Imagery and Wilma 37color Imagery	219
8.4.4	Radar Imagery for Hurricane Camille	222
8.5	The Last Reconnaissance Flight Into Camille	228
8.6	The Mystery of the Sea State Described in Camille Associated with Extreme Wind Speeds	234
8.7	Research Materials on Hurricane Camille	238
8.8	Key Data Relevant to Landfall Parameters.....	239
9.	CONCLUSIONS.....	251
	REFERENCES	256
	VITA.....	262

LIST OF TABLES

TABLE	PAGE
3.1 37color convective rings for selected rapid intensification cases 2008-2019.....	48-50
4.1 2007 WPAC Yutu Best Track.....	115
5.1 Color Combinations for the 37color Imagery and Interpretation	128
7.1 Intense TCs by basin and intensity at the time of the associated 37color overpass.....	171
7.2 Shear values for the Atlantic basin TC in the accompanying imagery	175
7.3 37color overpasses for subtropical cyclones for 2018 in the Atlantic basin and notes on their origins and evolution.....	181

LIST OF FIGURES

FIGURE	PAGE
1.1 Organization of the NRLMRY TC "tcdat" archive	5
1.2 Comparison of 37color PMW imagery for Hurricane Wilma	6
1.3 Hierarchy of directories in NRLMRY tcdat repository	9
1.4 An annotated life cycle temporal series of 37color images for 2017 Irma	10
1.5 NHC forecast advisory noting lack of PMW imagery for 2021 Hurricane Larry	11
1.6 NHC forecast advisory noting lack of PMW imagery for 2021 TS Sam	11
1.7 NHC forecast advisory noting lack of PMW imagery for 2021 Hurricane Sam	12
2.1 2015 Hurricane Patricia near peak intensity	14
2.2 2003 Cyclone Inigo near peak intensity.....	15
2.3 The central dense overcast for 2017 Hurricane Katia.....	17
2.4 Comparison of various stages of the life cycle of convection	18
2.5 2004 Tropical Storm Ivan at 55 kt	19
2.6 2005 Hurricane Wilma at 75 kt.....	20
2.7 2019 Subtropical Melissa at 50 kt.....	20
2.8 2019 Tropical Melissa at 45 kt.....	21
2.9 Category 4 2004 Ivan before landfall	22
2.10 2008 Hurricane Ike at 85 kt	22
2.11 2005 Hurricane Epsilon at 65 kt	23
3.1 2005 Wilma RI Event from Kieper and Jiang (2012).....	24
3.2 Page 1 of Kieper and Jiang (2012).....	25

3.3	Page 2 of Kieper and Jiang (2012).....	26
3.4	Page 3 of Kieper and Jiang (2012).....	27
3.5	Page 4 of Kieper and Jiang (2012).....	28
3.6	Page 5 of Kieper and Jiang (2012).....	29
3.7	Page 6 of Kieper and Jiang (2012).....	30
3.8	Page 7 of Kieper and Jiang (2012).....	31
3.9	2005 Wilma RI ring and precipitative structure before and after RI	34
3.10	2015 Patricia RI ring and precipitative structure before and after RI.....	35
3.11	Satellite Imagery for four developing Atlantic TC	36
3.12	RI ring for the same four developing Atlantic TC	37
3.13	Willis Island BOM Weather Station and last radar image from 2011 Yasi.....	39
3.14	NWS WSR-88D radar destroyed by 2017 Hurricane Maria	39
3.15	NWS WSR-88D radar destroyed by 2020 Hurricane Laura.....	40
3.16	NWS WSR-88D radar with protective radome	40
3.17	Storm surge damage from tropical cyclones.....	41
3.18	Convective Rings indicating a period of RI 2003-2019	43
3.19	Convective Rings indicating a period of RI 2003-2019	44
3.20	Convective Rings indicating a period of RI 2003-2019	45
3.21	Rapid intensification of 2004 WPAC Typhoon Dianmu	46
3.22	Rapid intensification of 2019 ATL Hurricane Dorian.....	46
3.23	Six WPAC convective rings marking the onset of RI from the 2004 WPAC typhoon season.....	47
3.24	Three SHEM convective rings that marked the onset of RI	47

3.25	TCR cover page for 2019 Jerry showing the RI ring (Brown 2019)	52
3.26	2016 Gaston RI rings from Tropical Cyclone Report (Brown 2017)	53
3.27	Identification of the RI ring in an NHC Tropical Cyclone Discussion.....	54
3.28	Identification of the RI ring in an NHC Tropical Cyclone Discussion.....	55
3.29	Identification of the RI ring in an NHC Tropical Cyclone Discussion.....	56
3.30	Identification of the RI ring in an NHC Tropical Cyclone Discussion.....	57
3.31	Identification of the RI ring in an NHC Tropical Cyclone Discussion.....	58
3.32	Identification of the RI ring in an NHC Tropical Cyclone Discussion.....	59
3.33	Identification of the RI ring in an NHC Tropical Cyclone Discussion.....	60
3.34	Identification of the RI ring in an NHC Tropical Cyclone Discussion.....	61
3.35	Identification of the RI ring in an NHC Tropical Cyclone Discussion.....	62
3.36	Identification of the RI ring in an NHC Tropical Cyclone Discussion.....	63
3.37	Identification of the RI ring in an NHC Tropical Cyclone Discussion.....	64
3.38	Identification of the RI ring in an NHC Tropical Cyclone Discussion.....	65
3.39	Improvement in NHC OFCL errors (from DeMaria et al. 2021)	66
4.1	Three classic ERCs for 2004 Hurricane Frances over a four-day period	69
4.2	2004 Hurricane Frances same as Figure 3.1 but in the corresponding 85h imagery .	70
4.3	Two SSMI F-13 passes of 1997 Hurricane Danny	71
4.4	Radar imagery from NWSFO Mobile, AL radar loop of 1997 Hurricane Danny	72
4.5	Three images of Hurricane Danny from NWSFO Slidell, LA (from Murillo et al. 2011)	73
4.6	1991 Hurricane Bob multiple wind maxima / eyewalls (Hugh Willoughby, personal communication).....	75
4.7	Radar imagery of 1991 Hurricane Bob.....	75

4.8	Tracks of 2004 Karl and 2019 Lorenzo during the early ERCs	76
4.9	Track of 2006 Hurricane Daniel during the early ERC	77
4.10	Best track intensities for 2004 Karl, 2006 Daniel, and 2019 Lorenzo with the period of the early ERC highlighted.	78
4.11	Developing eye in Lorenzo	80
4.12	Lorenzo's eye	82
4.13	Stationary Band Complex from Willoughby, Marks, and Feinberg 1984	83
4.14	Lorenzo's early eyewall replacement cycle.....	84
4.15	EIR-BD and VIS imagery during the time double eyewalls appeared as Lorenzo's ERC was completing	88
4.16	Developing eye of 2004 Hurricane Karl	91
4.17	First IR images of 2004 Karl's pinhole eye.....	92
4.18	2004 Karl precipitative banding surrounding the small eye	93
4.19	SEF development on PMW imagery for 2004 Karl.....	94
4.20	SEF and completing ERC comparing PMW and EIR-BD imagery for 2004 Karl .	96
4.21	The complete early ERC development of 2004 Karl on the 37color.....	100
4.22	Eye development of 2006 Hurricane Daniel.....	102
4.23	2008 Cyclone Jokwe in the Mozambique Channel comparing 85h and 150h imagery	104
4.24	Development of 2006 Daniel's secondary eyewall from the head of the principal band.....	106
4.25	Close-up of the extremely small eye for 2006 Daniel	107
4.26	Appearance of double eyewalls in Hurricane Daniel on IR and VIS imagery	108
4.27	Inner eyewall of 2006 Daniel briefly becomes prominent on VIS imagery	110

4.28	PMW and IR structure of 2006 Daniel when completion of ERC was noted on NHC discussion	111
4.29	The early ERC of 2006 Daniel.....	112
4.30	The early ERC of 2007 Super Typhoon Yutu, with early SEF prior to mature inner eye.....	114
4.31	Comparison of SEF in the four tropical cyclones in the case study of early ERCs	118
4.32	Continued comparison of the four cases during the last stage of the completing ERC.....	119
4.33	Additional examples of early ERCs with the secondary eyewall forming from the head of the principal band	120
4.34	Formation of a secondary eyewall in a stationary principal band	121
5.1	Typical schematic of a mature tropical cyclone	126
5.2	Schematic of evolution of tropical cyclogenesis and early development	126
5.3	Schematic of a conceptual model of the 37color imagery	128
5.4	TRMM PR cross section of 2005 Hurricane Katrina.....	131
5.5	TRMM PR cross section of 2005 Hurricane Katrina.....	132
5.6	TRMM PR cross section of 2005 Hurricane Katrina.....	133
5.7	TRMM PR cross section of 2008 Tropical Storm Paloma	134
5.8	TRMM PR cross section of 2008 Hurricane Ike	136
5.9	TRMM PR cross section of 2008 Hurricane Julia.....	137
5.10	TRMM PR cross section of 2008 Tropical Storm Hillary	139
5.11	WSR-88D radar cross section of 2019 Hurricane Sally	142
5.12	WSR-88D radar cross section of 2008 Tropical Storm Fay	143
5.13	WSR-88D radar cross section of 2019 Hurricane Dorian	144

5.14	WSR-88D radar cross section of miniature supercell of 2019 Hurricane Dorian	144
5.15	Stratiform rain areas from previous cross sections	145
5.16	Two examples of bright cyan SAM rain with different radar reflectivities, and an example of heavy stratiform rain	146
5.17	Pixels of 37color imagery graphed by their respective 37V and 37H brightness temperatures	149
5.18	Distribution of pixels that the TRMM PR 2A23 algorithm recognizes as convective	150
5.19	2005 Katrina deep convective eyewall labeled as stratiform by the 2A23	153
5.20	2004 Danielle RI ring labeled primarily stratiform by the 2A23	154
5.21	Four RI rings labeled primarily stratiform by the 2A23	155
5.22	Convective and stratiform CFADs from Hense and Houze (2011)	157
6.1	The four main Dvorak technique cloud patterns	161
6.2	Dvorak intensity estimation technique cloud patterns using satellite imagery	162
6.3	PIE intensity estimates for the range of tropical storm intensities	164
6.4	PIE pattern for low to moderate shear 30-35 kt intensity	165
6.5	PIE pattern for low to moderate shear 30-35 kt intensity	165
6.6	PIE pattern for low to moderate shear 35-45 kt intensity	166
6.7	PIE pattern for low to moderate shear 45-60 kt intensity	166
6.8	PIE pattern for low to moderate shear 50-60 kt intensity	166
6.9	PIE pattern for moderate to strong shear 30-35 kt intensity	167
6.10	PIE pattern for moderate to strong shear 40 kt intensity	167
6.11	PIE pattern for moderate to strong shear 45-50 kt intensity	167
6.12	PIE pattern for moderate to strong shear 55-65 kt intensity	168

6.13	PIE pattern for moderate to strong shear 50-55 kt intensity	168
6.14	PIE pattern for moderate to strong shear 50-65 kt intensity	168
7.1	37color images of intense TC with very small eyes	172
7.2	37color images of intense TC with small eyes	173
7.3	37color images of intense TC with eye diameters of about 20 n mi.....	174
7.4	2005 Dennis and 2005 Wilma under moderate shear of 10 kt.....	175
7.5	2014 Odile and 2019 Humberto under moderate shear of 15 kt.....	176
7.6	2005 Katrina and 2014 Rafael under moderate shear of 15-20 kt	176
7.6	2006 Alberto and 2006 Ernesto under strong shear.....	177
7.8	Two images of 2008 Omar under strong shear of, respectively, 20 kt and 25 kt	177
7.9	Six STC from 2018 Atlantic basin.....	179
7.10	Corresponding AMSU vertical cross section temperature anomalies for the six STC in Figure 3.57.....	180
7.11	Subtropical Cyclone ATL 2019 Melissa.....	182
7.12	Monsoon development of 2015 WPAC Typhoon Goni from TD to 80 kt	183
7.13	Monsoon development of 2005 ATL Wilma from TD to 70 kt	184
8.1	Page 1 of A Reanalysis of Hurricane Camille	186
8.2	Page 2 of A Reanalysis of Hurricane Camille	187
8.3	Page 3 of A Reanalysis of Hurricane Camille	188
8.4	Page 4 of A Reanalysis of Hurricane Camille	189
8.5	Page 5 of A Reanalysis of Hurricane Camille	190
8.6	Page 6 of A Reanalysis of Hurricane Camille	191
8.7	Page 7 of A Reanalysis of Hurricane Camille	192

8.8	Page 8 of A Reanalysis of Hurricane Camille	193
8.9	Page 9 of A Reanalysis of Hurricane Camille	194
8.10	Page 10 of A Reanalysis of Hurricane Camille	195
8.11	Page 11 of A Reanalysis of Hurricane Camille	196
8.12	Page 12 of A Reanalysis of Hurricane Camille	197
8.13	Page 13 of A Reanalysis of Hurricane Camille	198
8.14	Page 14 of A Reanalysis of Hurricane Camille	199
8.15	Page 15 of A Reanalysis of Hurricane Camille	200
8.16	Page 16 of A Reanalysis of Hurricane Camille	201
8.17	Page 17 of A Reanalysis of Hurricane Camille	202
8.18	Page 18 of A Reanalysis of Hurricane Camille	203
8.19	Camille radar fix indicating a double eyewall	210
8.20	All of the available satellite imagery remaining today for 1969 Hurricane Camille.....	211
8.21	Comparison of satellite imagery from hurricanes 1969 Camille and 2005 Wilma at two similar stages of development.....	213
8.22	Analysis of low level winds for Hurricane Camille showing significant inflow velocities over 25 kt.....	217
8.23	Analysis of upper level winds for Hurricane Camille showing significant outflow velocities in the 40-50 kt range with two main outflow channels.....	218
8.24	Upper level wind analysis for Hurricane Wilma showing a significant outflow channel to the northeast aided by strong westerlies.....	219
8.25	Comparison of 37color imagery of Wilma with radar image of Camille	220
8.26	Comparison of 37color imagery of 2005 Vince with corresponding radar image	221
8.27	Comparison of 37color imagery of 2003 Claudette with corresponding radar image.....	221

8.28 Comparison of 37color imagery of 2005 Katrina with corresponding radar image.....	222
8.29 Radar image of Hurricane Camille from NAS Fleet Weather Facility showing a double eyewall	223
8.30 One of the original radar images retrieved from the NCEI archive.....	226
8.31 The template overlay for the radar images with scaled map and radar rings	227
8.32 The radar image from Figure 8.29 with the overlay	228
8.33 Camille 901 mb drop later found to be in error	230
8.34 Photographs used for estimating surface wind speeds.....	231
8.35 Flight summary from the last reconnaissance flight into Camille	233
8.36 Sea state under eyewall of 2015 EPAC Hurricane Patricia	235
8.37 Sea state under eyewall of 1989 ATL Hurricane Hugo	236
8.38 Sea state under eyewall of 1988 ATL Hurricane Gilbert	237
8.39 Letter to NHC Deputy Director regards Camille's steep pressure gradient	240
8.40 Nash Roberts notes on Camille's steep pressure gradient.....	241
8.41 Photo of the Breath home early 1900s	245
8.42 Photo of the Breath home three days after landfall of Hurricane Camille.....	246
8.43 Forest damage from Camille overlaid with the track and RMW	249
8.44 Map of locations of key pressure readings, significant wind observations, and length of time in the eye.....	250

CHAPTER 1. Introduction

Satellite imagery and in particular the 37 color composite imagery (37color) in this work is of great importance in analyzing the structure and evolution of tropical cyclones (TC).

The 37color imagery was originally conceived to incorporate polarization correction temperature (PCT) to visually distinguish the radiometrically cold ocean surface from cold convection. This 37 GHz product when observed with higher-resolution sensors uniquely identifies rain because this band sees lower into the troposphere than the 85 GHz band. As a result, the 37color shows warm precipitation features in tropical cyclones not seen on other passive microwave imagery, as well as an ice signature, providing a more complete picture of the overall precipitative structure (Chapter 2).

A ring of cyan surrounding the warm center of a TC on the 37color image, associated with the developing eye, was found to be important in two previously undocumented processes. This has led to discoveries about eye and eyewall development in TC for rapid intensification (Kieper and Jiang, 2012) and eyewall replacement cycles (ERCs), presented in Chapters 3 and 4.

It will be shown that the cyan in the 37color corresponds to convective rain (Chapter 5).

This convective rain is generated from shallow and moderate convection, hereafter identified as "SAM." This is validated by use of a conceptual model and radar cross-sections of TC precipitation. The role of SAM in TC development has been under-examined.

A method for estimating intensity of tropical storms from precipitative patterns in the 37color is introduced (Chapter 6). Tropical cyclone forecasters have long had success

with estimating the intensity of TC from their visible and infrared imagery cloud patterns using the Dvorak technique (Dvorak, 1984; Velden et al. 2006). This work examines a microwave precipitation pattern-based analog to the Dvorak technique that addresses the period before eye formation.

In addition, other TC characteristics observed on the 37color imagery from precipitative structures are shown, including vertical shear, subtropical storms, intense TC, and monsoon trough development (Chapter 7).

Thus, the 37color imagery changes and expands our understanding of TC processes.

The reanalysis of 1969 Hurricane Camille (Kieper et al. 2015) is presented (Chapter 8). Camille's landfall intensity had long been uncertain due to lack of accurate wind measurements in the core. Whether Camille was a Category 5 at landfall was in question. Camille was a likely candidate for an eyewall replacement given its intensity while over the Gulf of Mexico. The reanalysis of Camille employed knowledge of TCs that was not known in 1969 (e.g. ERCs). Techniques of interpreting modern satellite images were applied to images of Camille to determine that an ERC occurred.

1.1 PMW Image Dataset

Real-time passive microwave (PMW) imagery has been provided by NRLMRY TC (Naval Research Lab Monterey) and FNMOC TC (Fleet Numerical Meteorology and Oceanography Center) webpages for over 20 years, beginning in 1997 with SSMI (Special Sensor Microwave Imager) imagery. In addition NRLMRY maintains an archived online repository. Infrared and visible satellite imagery were added and then TRMM (Tropical Rainfall Measuring Mission) TMI (TRMM Microwave Imager) images

beginning in 1999. Additional PMW imagery from SSMIS (Special Sensor Microwave Imager/Sounder), WindSat and AMSR-E (Advanced Microwave Scanning Radiometer for Earth Observing System) were added in subsequent years, and second generation AMSR-2 and GPM (Global Precipitation Measurement mission) GMI (GPM Microwave Imager) as well. The importance of this imagery was noted in (Hawkins et al 2001), "Visible and infrared (vis/IR) data provide the bulk of TC information, but upper-level cloud obscurations inherently limit this important dataset during a storm's life cycle. Passive microwave digital data and imagery can provide key storm structural details and offset many of the vis/IR spectral problems. The ability to view storm rainbands, eyewalls, impacts of shear, and exposed low-level circulations, whether it is day or night, makes passive microwave data a significant tool for the satellite analyst." NRLMRY introduced the 85 color composite imagery (85color) in 1998 and the 37color imagery the following year. At that time only the SSMI and TMI sensors were available to forecasters.

These studies of the 37color imagery utilize the online NRLMRY TC archive, "tcdat," which contains a repository of PMW imagery supplemented with additional geostationary satellite products (visible, infrared, water vapor), organized by year, basin, and tropical cyclone (Figure 1.1). This repository of imagery from 1997 to present day contains tens of thousands of PMW images. All PMW imagery in this dissertation is credited to NRLMRY.

Although the frequencies of the various sensors are slightly different, by convention the terms "37" and "85" are used in the repository for these bands. Thus 89 GHz and 91 GHz

images are still referred to as "85" and 36 GHz is referred to as "37," and this convention will be used here.

These PMW images are reviewed by tropical cyclone forecasters around the world in real time as a forecast aid, and are extremely valuable for their ability to see below the cirrus shield and display implied TC structure from hydrometeor patterns. The focus here is on visual interpretation of these images, with emphasis on the 37 GHz color composite imagery, abbreviated as 37color.

For the 37color imagery, the higher-resolution sensors – TMI (replaced by GMI), AMSRE (replaced by AMSR-2), and WindSat (no longer in service) – are more useful than the SSMI and SSMIS images, which are at a lower resolution, as shown for 2005 Hurricane Wilma (Figure 1.2). Note in particular that the lower-resolution 37color SSMI and SSMIS images cannot resolve Wilma's small inner eye unambiguously. Primarily these studies of the 37color images will utilize higher-resolution images, and occasionally use an 85color image when a higher-resolution 37color image is not available. Because the 85 GHz had higher resolution, it was the recommended channel by NRLMRY (and in COMET online classes) for assessing tropical cyclones, and the 37color channel was recommended for providing a center fix as it sees lower into the atmosphere. The importance of warm precipitative patterns in the 37color imagery was not recognized.

In addition these case studies utilize products available from the TRMM TCPF online database and also generated from the TRMM data set, including precipitation radar (PR) products and cross-sections, to examine the radar reflectivity patterns associated with the "cyan" color areas and to confirm that these areas coincide with SAM precipitation.

The image displays a 4x2 grid of screenshots from a web browser, showing directory listings from a website. The browser's address bar consistently shows 'reimry.navy.mil'.

Top Row:

- Left Screenshot:** 'Index of /'. The table lists the 'Parent Directory' and several files including 'NorthAmerica/', 'STDIN.ei612593', 'amsub_training/', 'license.txt', 'mint/', 'netCDF/', 'sectors/', 'ssmi_training/', 'tc90/', 'tc91/', and 'tc92/'.
- Right Screenshot:** 'Index of /tc05'. The table lists the 'Parent Directory', 'ATL/', 'CPAC/', 'EPAC/', 'IO/', 'SHEP/', and 'WPAC/'.

Second Row:

- Left Screenshot:** 'Index of /tc05/ATL'. The table lists the 'Parent Directory' and files including '01L.ARLENE/', '02L.BRET/', '03L.CINDY/', '04L.DENNIS/', '05L.EMILY/', '06L.FRANKLIN/', '07L.GERT/', '08L.HARVEY/', '09L.IRENE/', and '10L.HONANNE/'.
- Right Screenshot:** 'Index of /tc05/ATL/12L.KATRINA'. The table lists the 'Parent Directory' and files including 'amers/', 'amsub/', 'atcf/', 'icf/', 'ssmi/', 'tc_wmsia/', 'tmi/', 'vapor/', 'vis/', and 'windat/'.

Third Row:

- Left Screenshot:** 'Index of /tc05/ATL/12L.KATRINA/amsre'. The table lists the 'Parent Directory' and files including '26h/', '26v/', '89v/', '89w/', 'ciowd/', 'color/', 'color36/', 'composite/', 'gsocir/', 'gsocir2/', 'gsocir3/', 'pct/', 'rain/', and 'ssat/'.
- Right Screenshot:** 'Index of /tc05/ATL/12L.KATRINA/amsre/color36'. The table lists the 'Parent Directory' and a large number of files with names like '20050823_0713.equal.x.coloc16...', '20050823_1609.equal.x.coloc16...', etc., up to '20050830_0717.equal.x.coloc16...'.

5

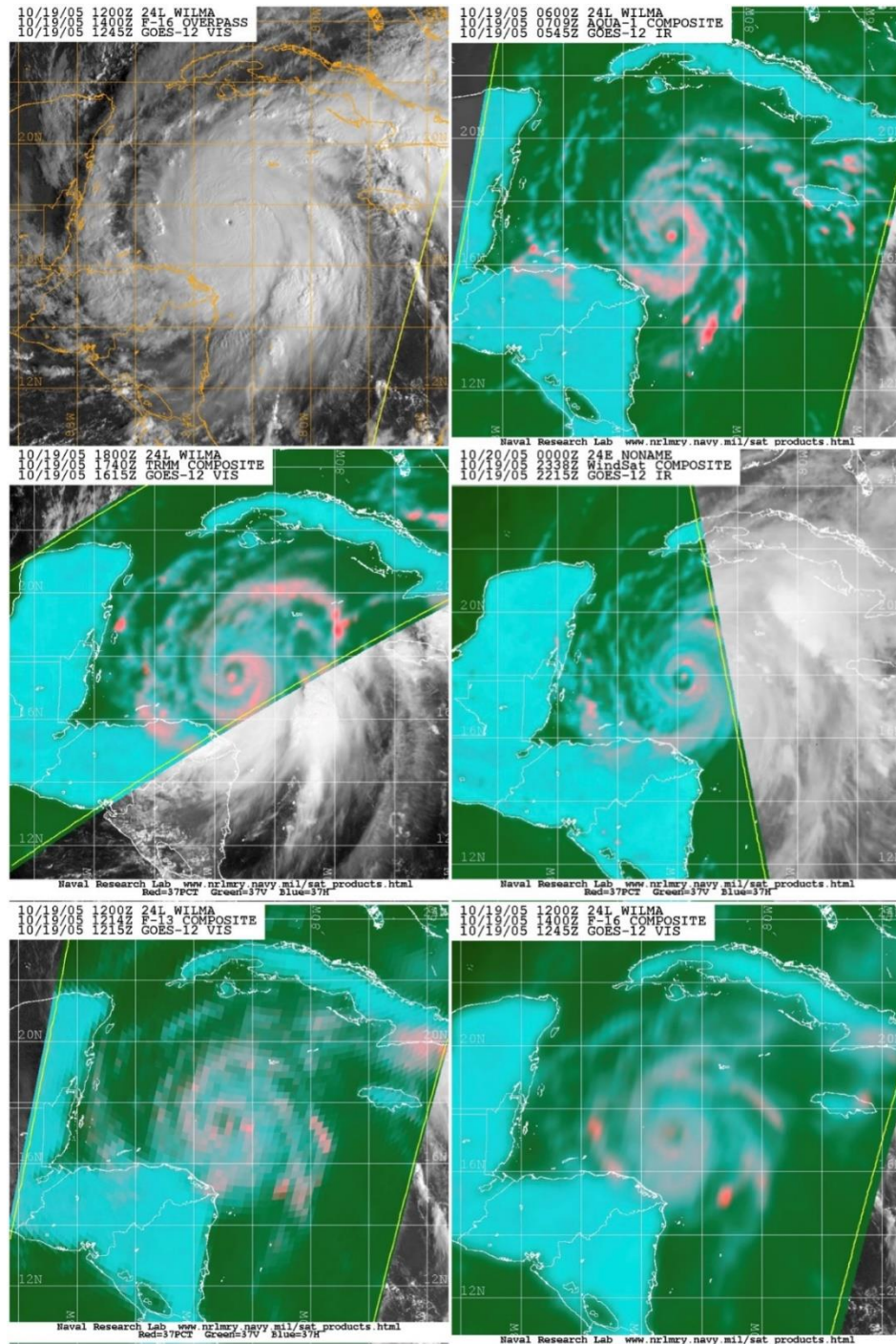


Figure 1.2 Comparison of 37color PMW imagery for Hurricane Wilma. These are at various times on the 19th of October 2005. A visible satellite image provided in the upper left corner for reference, followed by higher-resolution images from AMSR, TMI, and WindSat, with lower-resolution SSMI and SSMIS on the bottom row. The reduced resolution of these two sensors is clear by comparison.

1.2.1 The Need for a Tropical Cyclone Life-Cycle PMW Repository

In the NRLMRY TC archive, the "tcdat," geostationary imagery (visible, infrared, water vapor) for each tropical cyclone is stored in one folder, regardless of what sensor provides the image. Thus, if a tropical cyclone is in the Eastern Atlantic, imagery from GOES-East as well as Meteosat is available and is ordered temporally, providing a "life cycle" view of the TC from beginning to end. However this online repository is not a visual repository and each image must be selected in turn and the user must return to the directory to select and view the next image.

However for the PMW sensors, the images are separated by sensor. Therefore if one wants to look at all the PMW images for a TC each sensor's directory must be perused in turn, and it is not possible to even select all PMW images in temporal order (Figure 1.3).

This has led to an issue where it is not possible to view the progression of the TC structure on the PMW imagery. In order to view a particular type of PMW from the different sensors all together in temporal order, they would have to be downloaded from the archive. No one has done this (except the author). This is a hindrance in becoming familiar with the TC structure and in the progression of TC development that is offered by the PMW imagery.

An example has been annotated to highlight the benefits of a temporal view of 37color imagery for a long-lived "Cape Verde" hurricane, 2017 Irma, from genesis in the Eastern Atlantic to landfall in the Eastern Gulf of Mexico (Figure 1.4). Creating directories of such images that could be viewed by forecasters and researchers (such as on a cloud

server) by PMW image type, including all sensors, would be extremely useful, as PMW imagery shows underlying TC structure not apparent on geostationary satellite imagery.

Storage space on cloud servers is affordable and plentiful, and would also provide a more reliable storage medium than the NRLMRY TC servers, which in the past have lost data. It should be straightforward to move not only the PMW data but other supporting data in each TC directory to such a repository using web-based command language. The current data is already available to the public on the NRLMRY TC server as shown in Figure 1.3.

Supporting the International Workshop for Satellite Analysis of Tropical Cyclones (IWSATC) in 2016, a presentation of a life cycle repository covering several years of the WPAC TC was given to JTWC forecasters and was enthusiastically received, demonstrating the value of viewing the archive of PMW imagery as a visual life cycle.

Sadly in recent years PMW 37color imagery has become much less available. While GPM replaced TRMM, its orbit, not tropics-centric as TRMM was, results in much fewer passes over TC. WindSat is no longer operational. The bulk of higher-resolution 37color passes are now provided by the second generation AMSR. In addition the NRLMRY archive is no longer being maintained with the full complement of satellite imagery after 2020 and changes have been made to the provided images. Since FNMOC does not maintain a public repository images must be downloaded in real time to be viewed later. Tropical cyclone forecasters are aware of the dearth of PMW imagery. In 2021 comments were made a number of times about the lack of PMW imagery and consequently inability to observe TC structure (Figures 1.5 through 1.7).

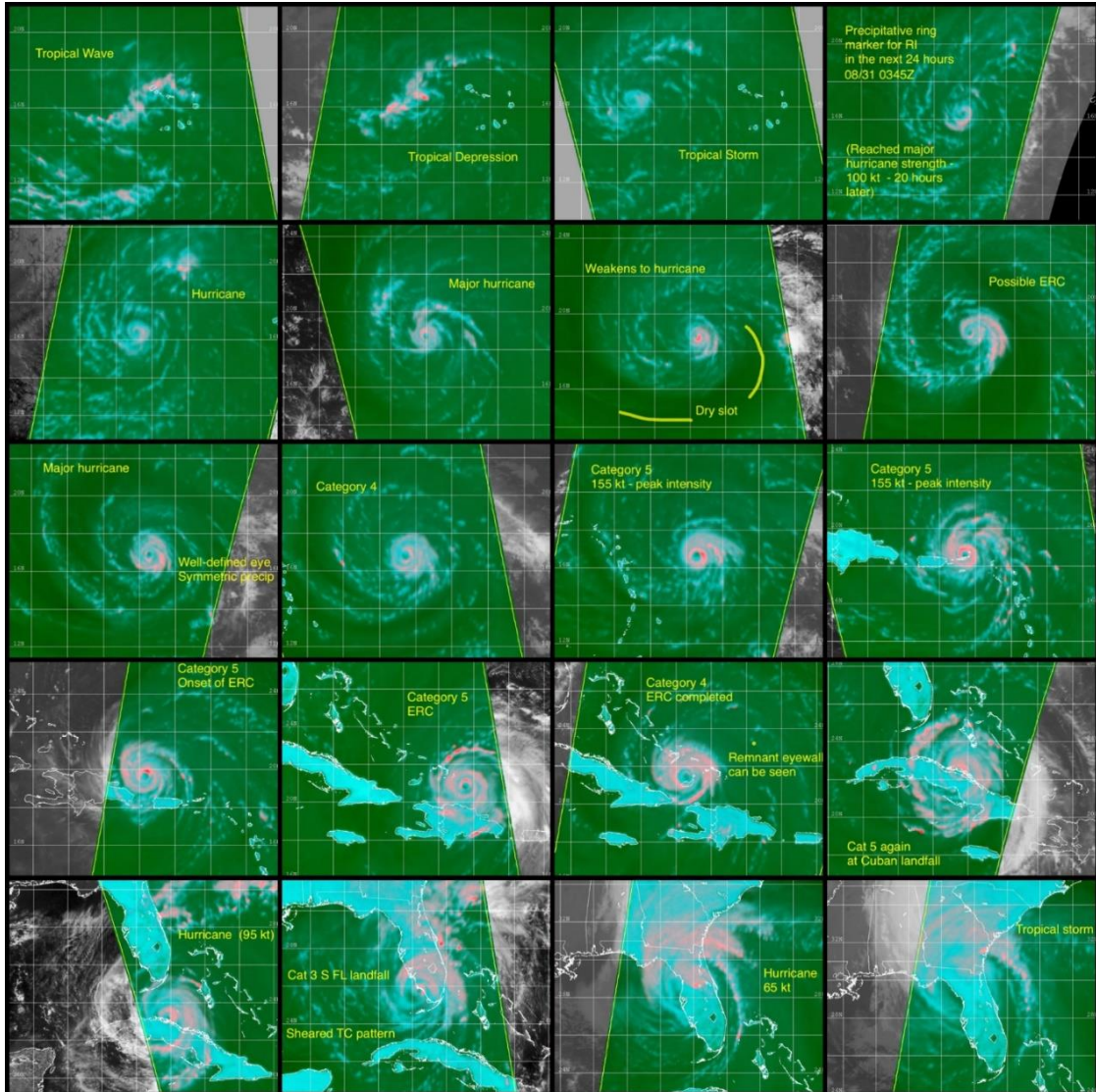


Figure 1.4 An annotated life cycle temporal series of 37color images for 2017 Irma. Images from AMSR-2, WindSat, and GMI imagers, showing the benefit of being able to view a "life cycle" of a TC in PMW imagery. Irma is shown from inception in the East Atlantic to landfall over Florida, a typical long-lived "Cape Verde" hurricane. The 37color image provides an important view of TC structure. Viewing the images together temporally provides a context for getting the maximum understanding from the imagery. Modern availability of cloud servers with large amounts of storage makes this a possibility.

Hurricane LARRY

ZCZC MIATCDAT2 ALL
TTAA00 KNHC DDHMM

Hurricane Larry Discussion Number 18
NWS National Hurricane Center Miami FL AL122021
1100 PM AST Sat Sep 04 2021

Larry has developed a large eye this evening that is 40-45 n mi in diameter, and the surrounding cloud tops have warmed somewhat. There have been no microwave passes over the hurricane for quite some time to assess its structure, but conventional satellite images suggest that Larry has taken on some annular characteristics (and the objective screening algorithm tagged it as marginally annular). Dvorak CI numbers and objective estimates are all between 100-102 kt, so Larry's initial intensity is lowered slightly to 105 kt.

Larry's motion remains west-northwestward (300 degrees) at 12 kt. The hurricane is expected to turn northwestward tonight or early Sunday around the southwestern periphery of a mid-level high

Figure 1.5 NHC forecast advisory discussion number 18 noting lack of PMW imagery for 2021 Hurricane Larry.

Tropical Storm SAM

ZCZC MIATCDAT3 ALL
TTAA00 KNHC DDHMM

Tropical Storm Sam Discussion Number 5
NWS National Hurricane Center Miami FL AL182021
500 PM AST Thu Sep 23 2021

Sam could be in the beginning stages of developing a small inner-core this afternoon as a central dense overcast is beginning to take shape. On geostationary visible satellite imagery, the storm has occasionally exhibited a clear area, though this feature has been tilted a bit southeast of the estimated low-level center position. In addition, overshooting convective cloud tops have been recirculating cyclonically around this feature, suggesting convective symmetrization that may help shield the low-level vortex from dry-air intrusion as seen earlier on the northwest side of Sam. Unfortunately, I have not received a high resolution microwave pass over Sam in 9-12 hours, so there remains some uncertainty on the structure underneath the cirrus canopy. The latest subjective Dvorak estimates from SAB and TAFB were 55-kt and 45-kt respectively. Taking a blend of these intensity estimates yields 50-kt for this advisory.

Figure 1.6 NHC forecast advisory discussion number 5 noting lack of PMW imagery for 2021 Tropical Storm Sam.

Hurricane Sam Forecast Discussion

[Home](#) [Public Adv](#) [Fcst Adv](#) [Discussion](#) [Wind Probs](#) [Graphics](#) [Archive](#)

000
WTNT43 KNHC 270848
TCDAT3

Hurricane Sam Discussion Number 19
NWS National Hurricane Center Miami FL AL182021
500 AM AST Mon Sep 27 2021

The satellite presentation of Sam deteriorated overnight, as GOES-16 infrared imagery showed periodic disruptions to Sam's inner core convection. The eye has not been readily apparent in conventional satellite imagery for much of the night, although very recent imagery suggests an eye could be re-emerging. Data from the reconnaissance aircraft last night indicated that an eyewall replacement cycle (ERC) was underway, and some dry mid-level air impinging on the western side of the circulation could also be negatively impacting Sam. No recent high-resolution microwave data is available, but an earlier scatterometer pass revealed that the tropical-storm-force wind radii had expanded just a bit in the eastern semicircle of the hurricane. The initial intensity is lowered to 115 kt for this advisory based on a blend of the objective and subjective Dvorak current intensity estimates. A NOAA hurricane hunter aircraft is scheduled to investigate Sam later this morning, which will provide crucial data to assess changes in Sam's structure and intensity.

Figure 1.7 NHC forecast advisory discussion number 19 noting lack of PMW imagery for 2021 Hurricane Sam.

CHAPTER 2. Introduction to Tropical Cyclone 37color Imagery

NRLMRY developed color composite imagery first for the 85 GHz band and then for the 37 GHz band (Hawkins et al. 2001, Lee et al. 2002), combining the vertical and horizontal polarizations and a polarization-corrected temperature (PCT). The low-emissivity ocean surface and cold convection can both have a low brightness temperature (T_b), and the PCT distinguishes between these and highlights the ice signature of cold convective tops, but cannot distinguish low-level clouds, water vapor and rain. The composite images can be created only by utilizing the differences between the horizontal and vertical polarization data when dual-polarized channels are available. The microwave imager T_b observed in the individual images for the 85H, 85V, 37H and 37V are of limited use because ice and ocean surface temperatures are similar and deep convection may not be clearly identified but can be distinguished with using the PCT (Figures 2.1 and 2.2). Thus 85color and 37color imagery was originally conceived primarily to incorporate polarization correction temperature (PCT) to visually distinguish the radiometrically cold ocean surface from cold convection.

The composites were created using red green blue (RGB) images by scaling the 37 GHz V in the green value, the 37 GHz H in the blue value, and the PCT in the red value, but in reverse tonality so that the colder the PCT temperature the higher the red value, in order to make the cold hydrometers stand out. PCT, or polarization corrected temperature, eliminates emissivity and only shows the scattering produced by ice hydrometers (ice, graupel, snow, etc.). This formula is developed empirically to take advantage of the fact that polarization temperatures for the ocean surface are slightly different for V and H,

while very similar for ice scattering, due to the random orientation of ice crystals in the upper troposphere (Spencer 1989). The formula that NRLMRY used for the 37 PCT is

$$\text{PCT}_{37} = 2.18(37V) - (1.18)37H \quad (\text{Grody 1993})$$

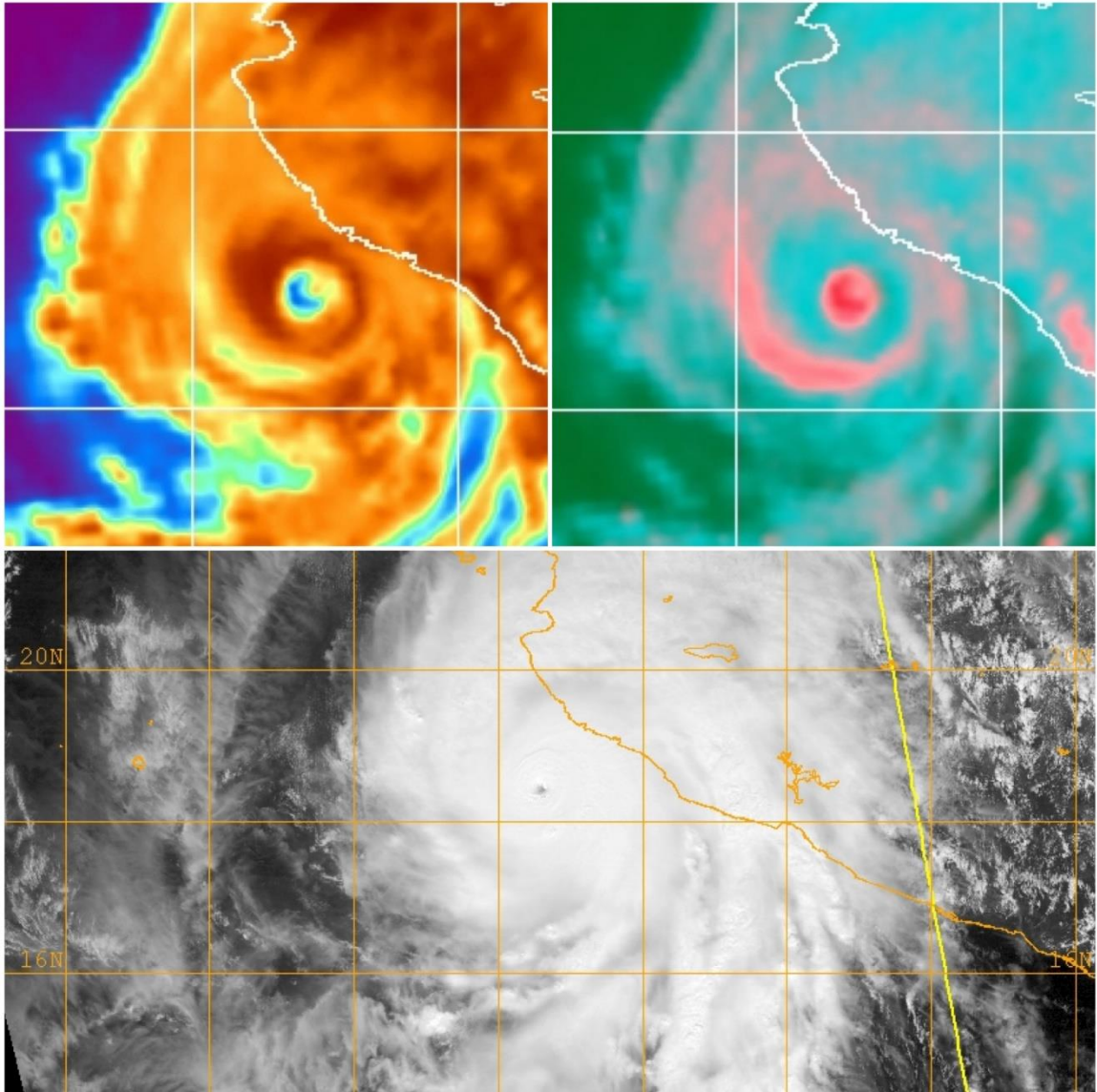


Figure 2.1 2015 Hurricane Patricia near peak intensity. Patricia intensified off the western coast of Mexico. On the left, the polarized image appears to show an eye in blue in the center, that appears to be the ocean surface. But the 37color image on the right shows that is actually a small strong eyewall that surrounds a pinhole eye. The visible geostationary image below shows this pinhole eye.

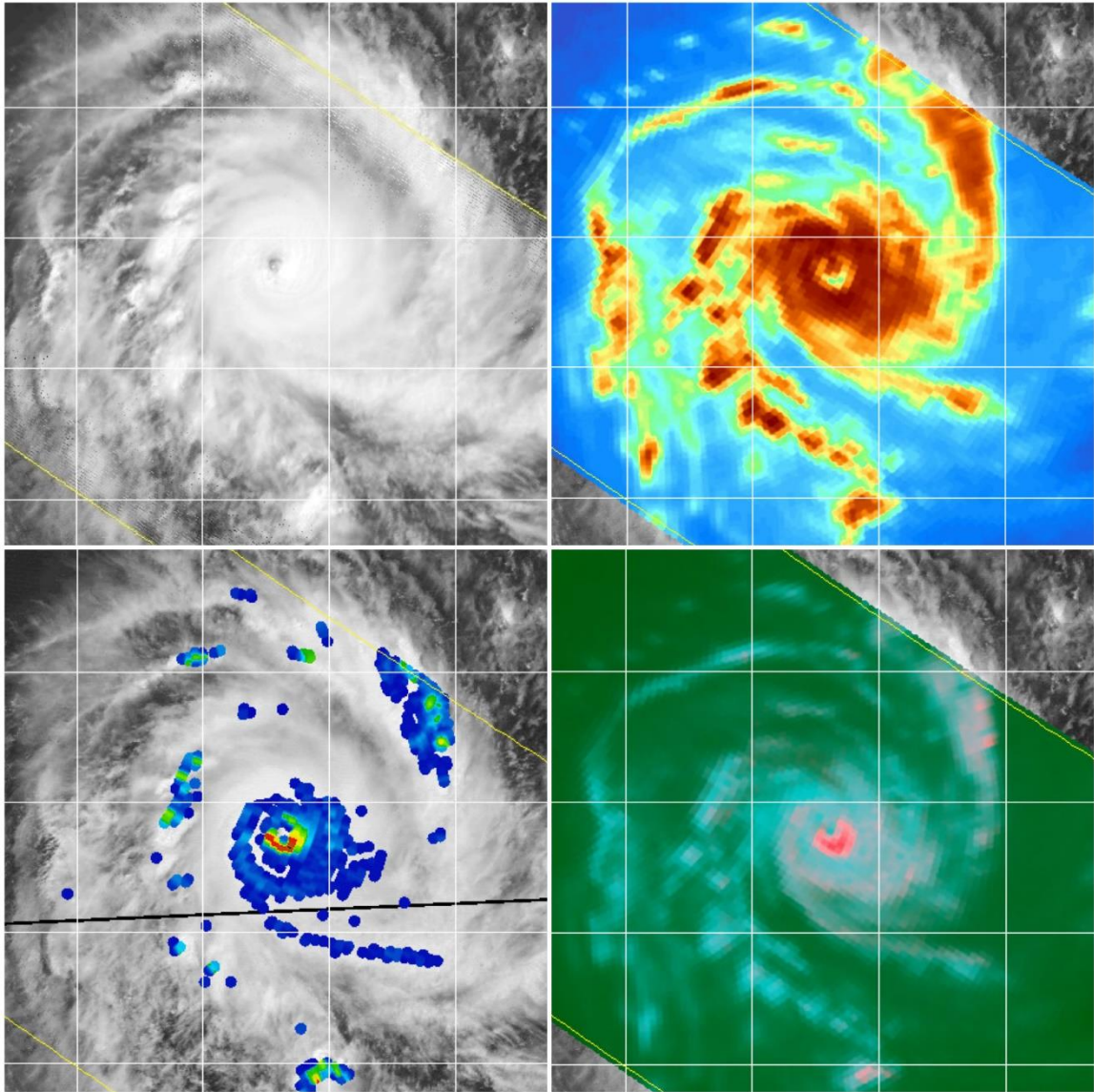


Figure 2.2 2003 Cyclone Inigo near peak intensity. Inigo was located off the northwestern coast of Australia, the 37PCT image on the lower left shows the ice coverage extends beyond the deep convection, in the blue color, but on the 37color image on the lower right it is a pale pink.

(Lee et al 2002). NRLMRY TC website originally had tutorials with examples for interpreting images of all the PMW products but they have been incorporated into COMET, and Lee et al. (2002) discussed the fundamentals of the imagery, but emphasized the usefulness of the 37color product mainly for providing center fix

locations due to its ability to see precipitation surrounding low-level circulation centers. As a result, "The sea surface in the color product appears green. Deep convection, including the portion of the eyewall mentioned above, appears pink. Low-level water clouds and rain appear cyan" (Lee et al 2002). Examples of 37color imagery that follow provide a more detailed interpretation of this more simplistic description to allow for some combinations of these colors, with guide to interpretation of each of them.

The frequencies chosen for PMW imagers have the advantage that they do not distinguish the smaller ice particles associated with cirrus outflow from the many deep convective cells in the TC, which creates the central dense overcast (CDO) that hides structural details of the TC when viewing geostationary visible, infrared, and water vapor imagery (Figure 2.3), but do observe the larger ice particles that form above the freezing level when moderate and deep convection glaciates. PMW imagery ice signatures do not always identify deep convection because "orphan anvils" may appear similar to deep convection (Figure 2.4) with a significant ice signature but without associated underlying surface reflectivity or significant precipitation signature. New convection does not have a prominent ice signature even though it has a high surface reflectivity and high precipitation rate (Figure 2.4).

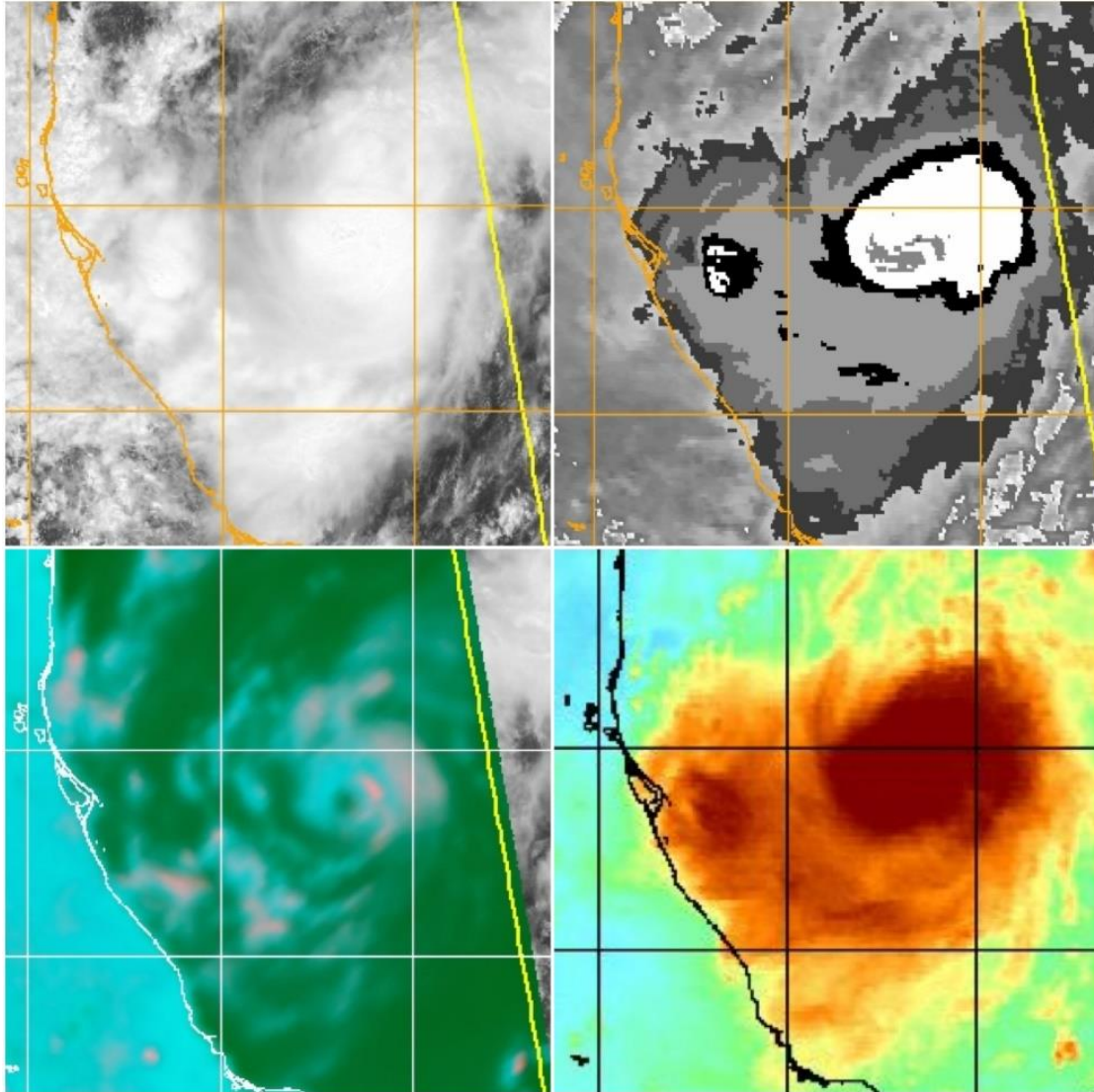


Figure 2.3 The central dense overcast or 2017 Hurricane Katia. These visible, infrared, and water vapor images hide the developing eye structure that is apparent on the 37color image on 1840Z 7 Sep. Shortly after this Katia intensified and an eye became apparent on geostationary imagery.

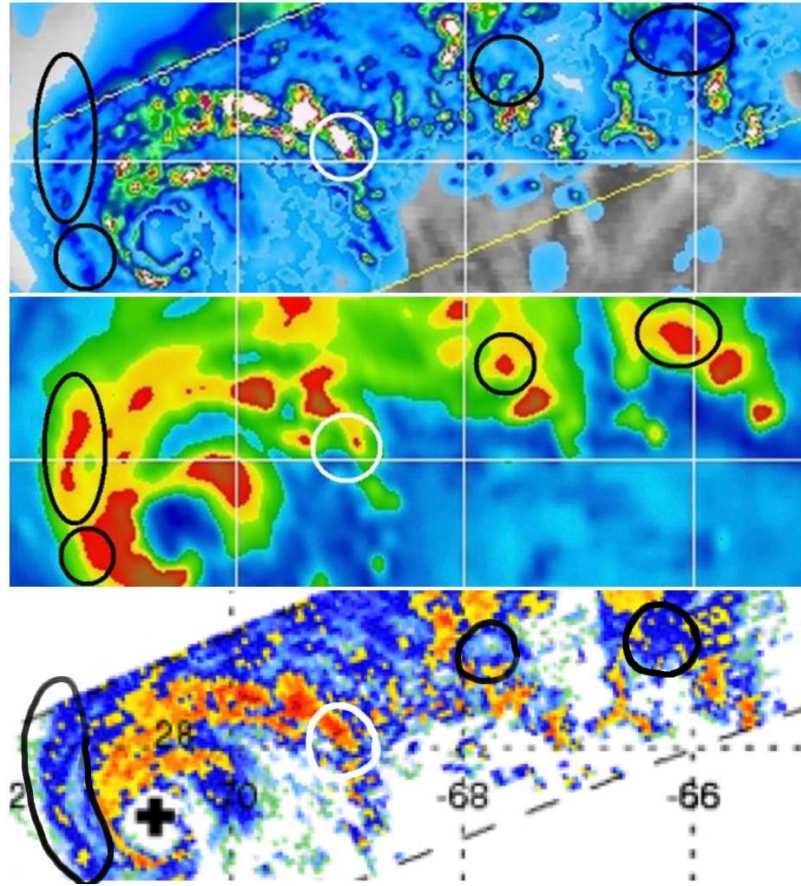


Figure 2.4 Comparison of various stages of the life cycle of convection. Products are the TRMM PR precipitation (top) and 85H (middle) products (NRLMRY TC) with the surface reflectivity of the TRMM PR (TCPF database, bottom). The area in the white circle is raining heavily and has a high surface reflectivity, indicating an area of moderate convection, but does not have a significant ice signature on the 85H like the other two areas to its left that are deep convective with a significant ice signature on the 85H. The four black circled areas could be interpreted as deep convection on the 85H, but no significant rain or surface reflectivity is associated with them, indicating they are orphan anvils. Thus, the ice signature of the 85H does not always correlate with deep convection. View of 2004 Hurricane Jeanne on 0118Z 21 Sep.

2.1 Examples and Characteristics of the 37color Imagery

Seven examples of 37color imagery (Figures 2.5 – 2.11) highlighting a variety of different TC types, selected during daylight hours, are shown next to the corresponding visible satellite imagery, all from the Atlantic basin: two developing TCs, 2004 Ivan and 2005 Wilma; a short-lived subtropical storm that subsequently became tropical, 2019

Melissa; two mature TC with double eyewalls undergoing eyewall replacement cycles (ERCs), 2004 Ivan and 2008 Ike; and a late-season long-lived TC at higher latitudes impacted by mid-latitude northwesterly shear, 2005 Epsilon. The precipitative areas on the 37color are seen to correspond to the TC structure on the visible imagery. Detailed descriptions of the characteristics of the 37color imagery for each TC are provided in the captions. Combinations of the three color categories are identified and will be described in detail in Chapter 5.

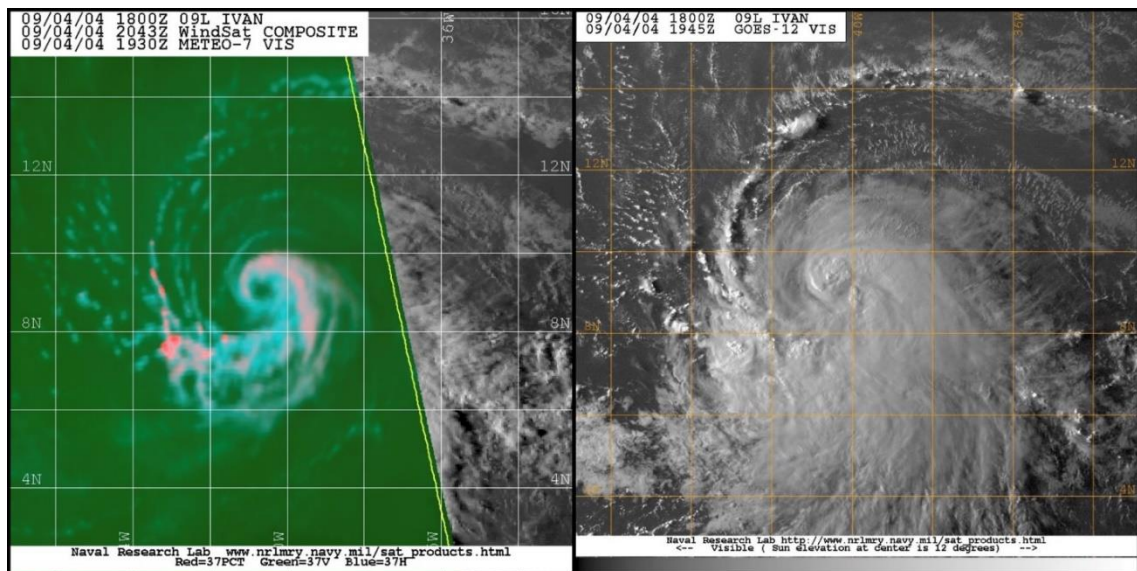


Figure 2.5 2004 Tropical Storm Ivan at 55 kt. Seen with a developing eyewall and secondary circulation embedded in a principal band. Trailing lines of convection extend from the tail of the band and wrapped around the outer edge of the circulation. The nascent eye can be clearly seen on the 37color but is obscured by a small CDO on the VIS. The eye development is advanced and a symmetric ring of bright cyan surrounds the center (marker for rapid intensification, Chapter 2). The principal band is clearly identified in cyan. Pink along the outer edge of the cyan indicates development of the secondary circulation. Cirrus emanating from the principal band to the ENE is thin and is not apparent on the 37color, nor is the CDO and additional cirrus outflow to the south. The shallow convective cells in cyan and faded cyan that make up the trailing thin bands in the tail, and the deeper convective cells marked by bright pink and intense pink ice signatures, are also clearly seen on the visible image where there is no cirrus overcast.

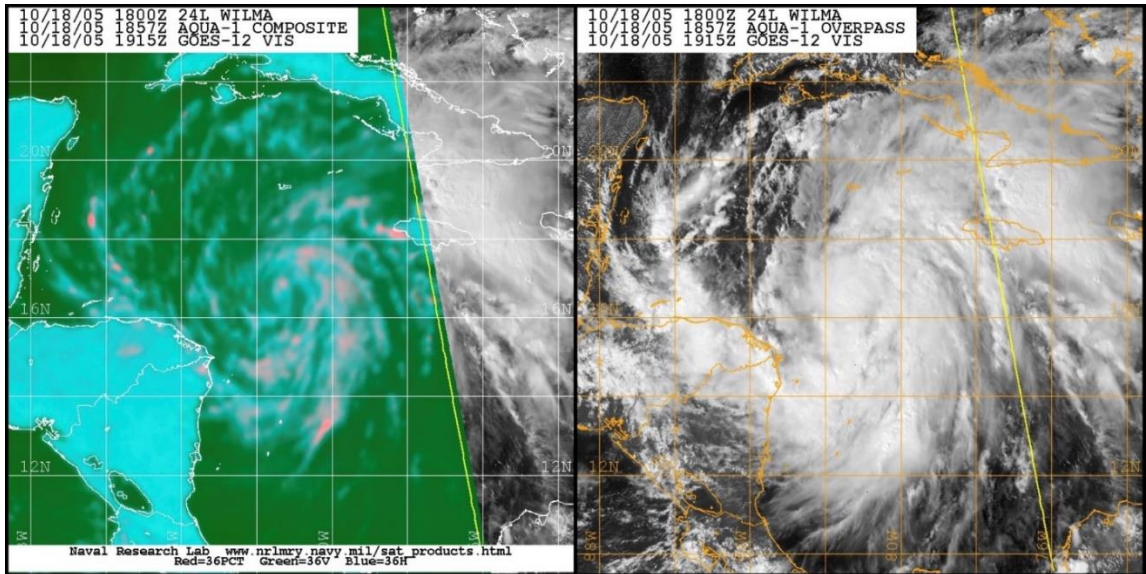


Figure 2.6 (above) 2005 Hurricane Wilma at 75 kt. Here just prior to explosive deepening, developing in a monsoon environment replete with a great deal of convection due to the low level convergence and upper level divergence associated with the monsoon trough. Again only a small CDO exists over the center and it and a large amount of cirrus outflow along the northern edge and wrapping almost completely around are transparent to the PMW imager. This allows a view of a very small developing eye and a massive loosely organized principal band consisting of numerous convective bands and individual groups of convective cells. Lines of precipitation in cyan to the northwest can be seen to correspond to several arc clouds in the VIS image, indicating drier air in that location. Deep convective cells are spotted throughout the principal band in bright pink and a few in intense pink. Because CDO coverage is limited many of the convective cells and bands that are producing a precipitative signal on the 37color can be identified on the VIS image.

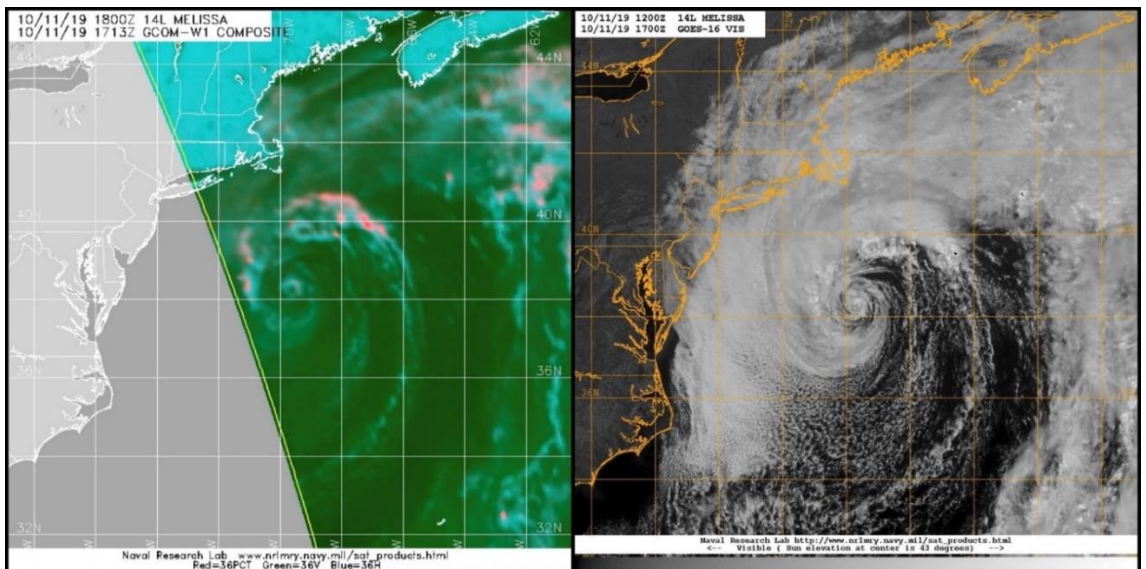


Figure 2.7 (bottom left) 2019 Subtropical Melissa at 50 kt. Melissa has evolved from a deep-layer extratropical low to a subtropical storm. On the 37color, even though a very small symmetric center almost completely surrounded by precipitation has formed, most of the convection is further out from the center, and there is a larger percentage of ice compared to the amount of precipitation, including some "faded pink over green" ice signature showing the typical larger amount of ice associated lower freezing level and colder air above associated with the larger extratropical low environment. There is typically less convection in subtropical systems because the environment is not as favorable for convective development. On the VIS image the cold air can be seen moving offshore from the west and the cold air clouds (marine layer) and cloud-free area wrapping around to the east of the center. The cloudy area to the east appears to have some cirrus coverage on the VIS, but some "weak cyan over green" areas indicating light rain. Also seen in this area along the right edge of the 37color are some thin bands of bright cyan relating to some convective banding that can be seen on the VIS image as well. The drier air moving offshore shows up well on the 37color as curved areas of darker green, and as cloud-free on VIS.

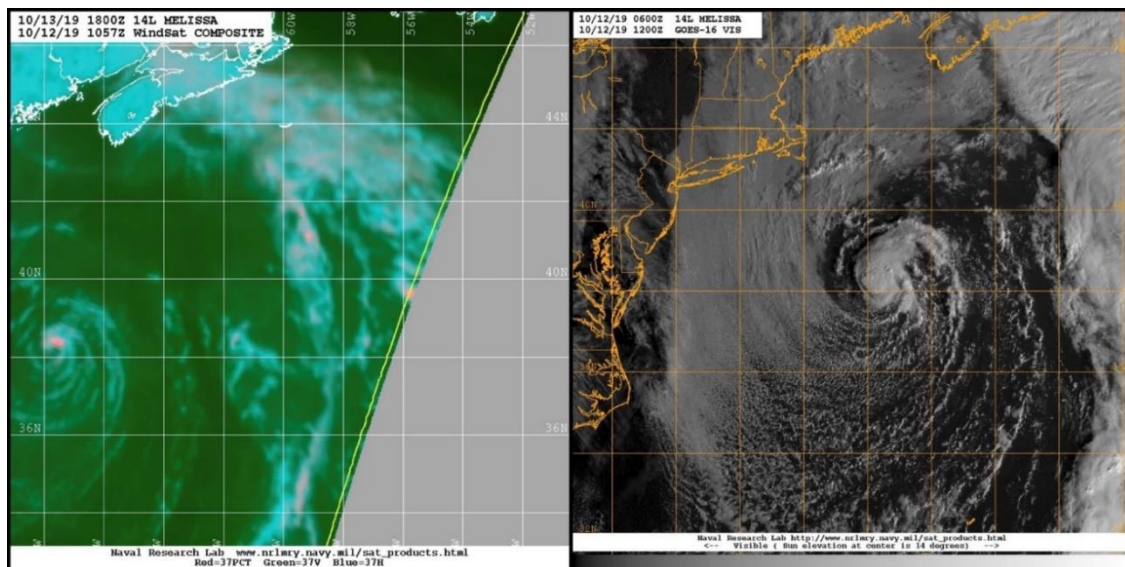


Figure 2.8 (above) 2019 Tropical Melissa at 45 kt. Melissa has become tropical while still embedded in the same deep layer extratropical low. There is much more cyan surrounding the small center taking the shape of a typical principal band, in miniature, and deep convection can be seen in bright pink on the 37color just north of the small clear center. The principal band is surrounded by additional bands in bright cyan, and some faded cyan showing lighter-raining bands for a short distance out from the principal band suggesting a hybrid environment where the original non-raining cold air clouds near the now-tropical environment have become weak rain bands. To the north on the 37color a broad area of rain associated with the deep layer low also has a diffuse weak ice signature that covers both raining areas (bright pink over cyan) and non-raining areas (faded pink over green).

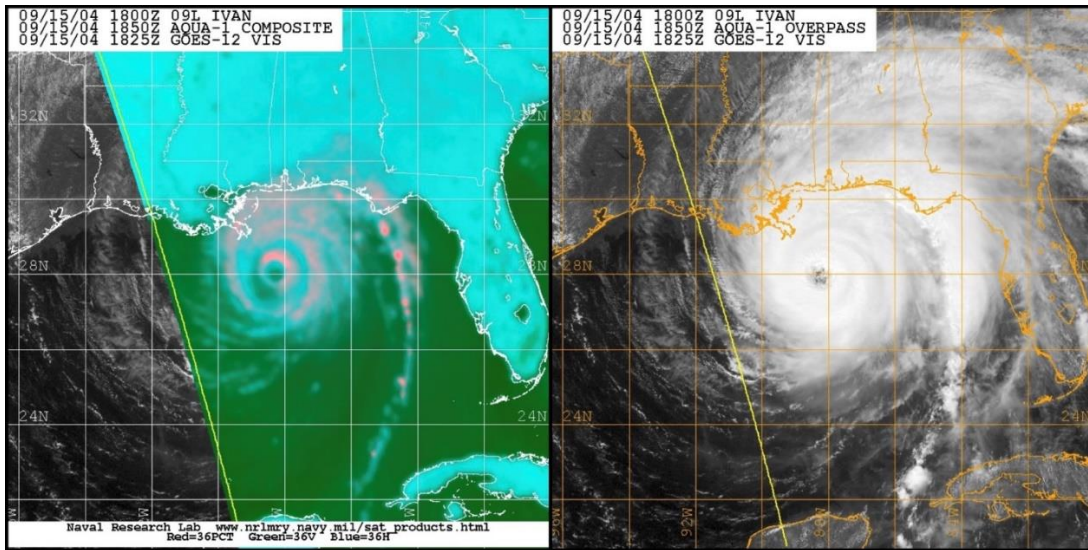


Figure 2.9 (above) Category 4 Ivan before landfall. Seen along the northern Gulf Coast at 115 kt, Ivan has largely-symmetric concentric eyewalls on the 37color but the strong inner eyewall is dominant on the VIS image and regular mesovortices are evident in the eye. On both eyewalls on the 37color the eyewall tilt is evident by a ring of bright cyan with bright pink along the outer edge. The pink of the inner eyewall is brighter, indicating that this eyewall is still the dominant eyewall. Ivan would be unable to complete the ERC before landfall. The bright cyan ring edged with bright pink is the typical presentation of mature eyewalls on the 37color (see Chapter 3). The principal band consisting of one thin tail of convective cells is seen along the eastern edge of the GOM into the Yucatan Channel, indicating warm moist low-level inflow was still being provided from the northwest Caribbean. Over water the cirrus seen on the VIS is again not obscuring the convective structure on the 37color. Note that since land is cyan, only the pink ice signature can be seen there.

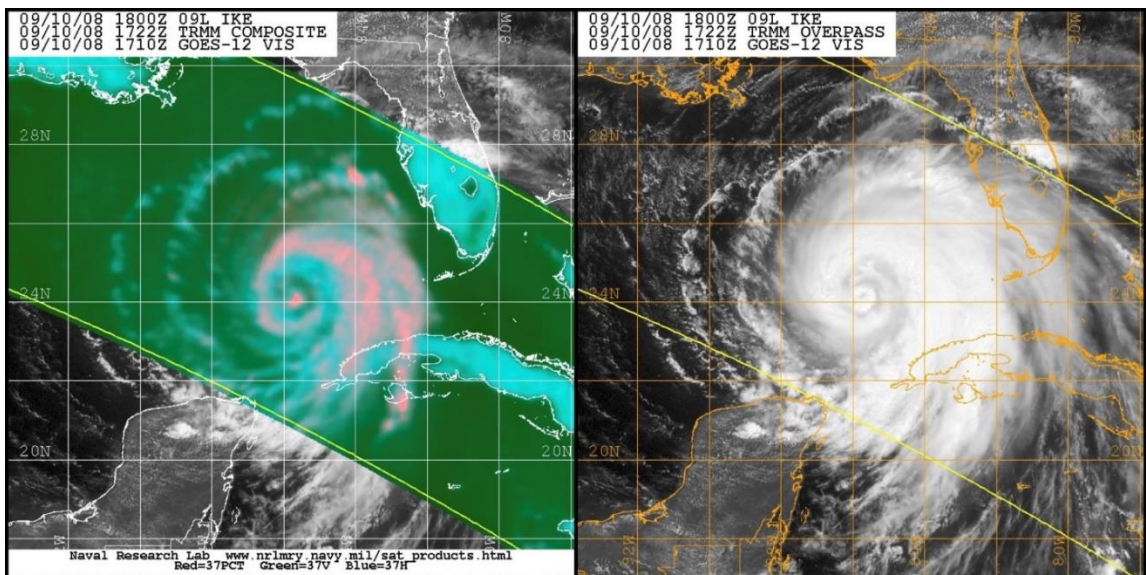


Figure 2.10 (bottom left) 2008 Hurricane Ike at 85 kt. Ike is traversing the eastern GOM with a concentric eyewall structure. Ike completed the eyewall replacement and strengthen slightly to 95 kt before making landfall along the northern Texas coast, decimating the Bolivar Peninsula. On the VIS image, the cirrus on the east over S FL and the Florida Straights is not seen on the 37color image. Both eyewalls are distinct on both the 37color and VIS images. The northeastern outer eyewall in bright pink corresponds to a well-defined area of convective tops on the VIS, but the lower area of precipitation under the deep convection, seen as a thick band of cyan on the 37color due to the tilt of the eyewall, does not appear on the VIS image, which instead seems to show a thin layer of cloud, but is obscuring the eyewall in this location. Frequently the appearance of the cloud layers on VIS can be deceiving and appear different than what is understood by the precipitative structure on the 37color. To the west, several arc clouds can be seen on both images due to dry air, but the lack of darker green suggests there is not a very significant amount of dry air that could impact the TC. There still exists a principal band structure wrapping around to the east and south of the center, with areas of bright hard ascending cloud tops on VIS corresponding to areas of bright pink on the 37color. The multiple banding at the tail of the principal band seen on both images indicates a rich inflow of moist warm low-level air and the primarily cyan color of this area shows this consists of shallow and moderate convection.

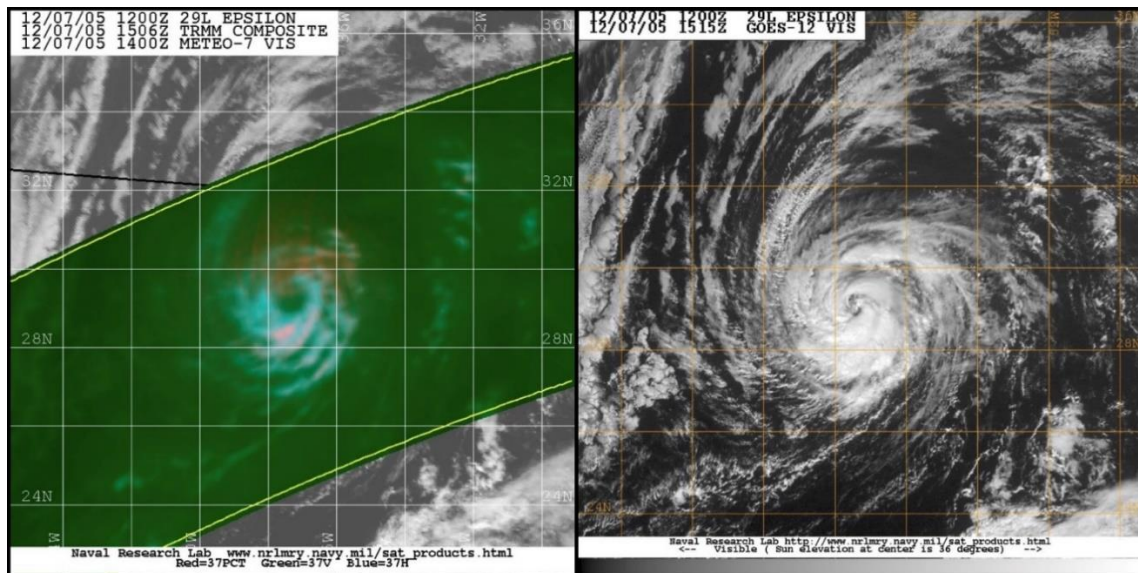


Figure 2.11 (above) 2005 Hurricane Epsilon at 65 kt. At the onset of weakening, at this time strong upper-level northwesterly flow associated with a mid-latitude trough just evident in the upper left of the imagery has begun to affect this small TC, shearing away the deep convection along the northern half of the system. This is evident on the VIS image by looking closely but is very apparent on the 37color, where convection is only seen along the bottom two-thirds of the eyewall and to the south, and where faded pink over green is seen, indicating that only anvil debris remains from the convection. Very few of the low-level clouds surrounding the TC are raining and the darker green indicates dry air surrounding the TC.

CHAPTER 3. Tropical Cyclone Rapid Intensification Indicator and Forecast Methodology Using the Developing Eye Cyan Ring Pattern

Please read (Figures 3.2 through 3.8 or hyperlink) [Predicting tropical cyclone rapid intensification using the 37 GHz ring pattern identified from passive microwave measurements](#) (Kieper and Jiang 2012) which formally presented a method for rapid intensification in the peer-reviewed literature that had been in use since the principal author introduced it to the tropical cyclone operational and research community four years earlier in 2008.

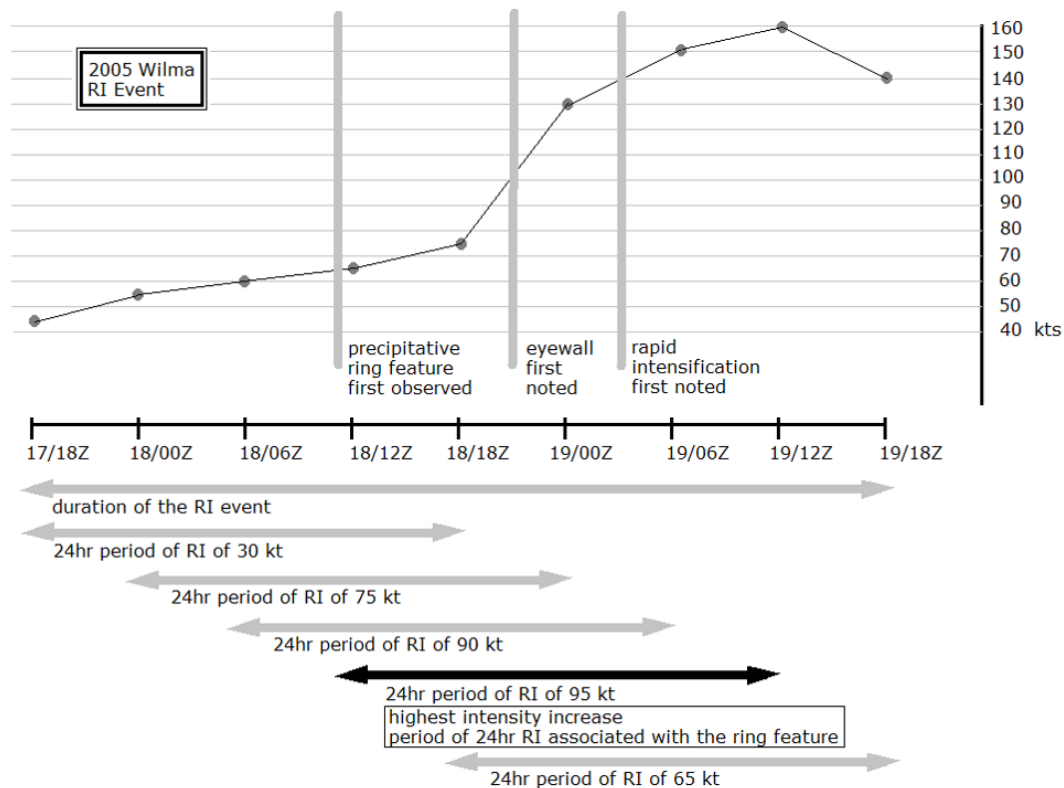


Figure 3.1 2005 Wilma RI Event from Kieper and Jiang (2012). Showing the individual periods of RI, and the 24 hour period associated with the developing eye, a ring of cyan convection on the 37 color, which was also the period of largest 24 hr intensity increase. NHC forecast advisory discussions first noted that Wilma had been going through a period of RI when it was 140 kt, but the ring was observed much earlier, when the intensity was 65 kt.

Predicting tropical cyclone rapid intensification using the 37 GHz ring pattern identified from passive microwave measurements

Margaret E. Kieper¹ and Haiyan Jiang¹

Received 26 April 2012; revised 28 May 2012; accepted 29 May 2012; published 6 July 2012.

[1] A distinctive satellite-derived precipitative ring pattern around the tropical cyclone (TC) center is found to be related to rapid intensification (RI). The ring pattern appears on the Naval Research Laboratory (NRL) 37 GHz passive microwave composite color product as a cyan color ring. The probability of RI is evaluated for cases with this ring pattern by reviewing images of the NRL product for 84 TCs during 2003–2007 in the Atlantic basin using 6-hourly National Hurricane Center (NHC) best track data. It is found that when combining the ring criterion with the Statistical Hurricane Prediction Scheme (SHIPS) RI Index (RII), the probability of RI almost doubled, indicating that both the ring and SHIPS RII contain independent information for RI prediction. A subjective technique for predicting RI is proposed using both the 37 GHz ring and the SHIPS RII. Both the probability of detection (POD) and the false alarm ratio (FAR) for the combined ring+SHIPS RII are lower than those for SHIPS RII alone (POD, 24% versus 77%, and FAR, 26% versus 66%) when treating every 6-hr synoptic time as a separate case. Since the method was initially developed for RI event-based forecasts, statistics based on 2003–2007 Atlantic RI events, which consist of a contiguous period where any 24-hour subset shows at least a 30 kt intensity increase, are also generated. The method captures 21 out of these 28 events and produces 2 false alarms, producing a POD of 75% and a FAR of 9%. **Citation:** Kieper, M. E., and H. Jiang (2012), Predicting tropical cyclone rapid intensification using the 37 GHz ring pattern identified from passive microwave measurements, *Geophys. Res. Lett.*, 39, L13804, doi:10.1029/2012GL052115.

1. Introduction

[2] Although tropical cyclone (TC) track forecasts have been improved substantially during the past 20 years, little gain in accuracy of forecasting TC intensity, especially rapid intensification (RI), over the same period has been achieved [Rappaport *et al.*, 2009]. The physical processes associated with RI, which is usually defined as 24-h intensity increase ≥ 30 kt [Kaplan and DeMaria, 2003], remain unsolved. Favorable large-scale environmental conditions that are near-universally agreed to be necessary for TC intensification include: warm sea surface temperature (SST), high low- to mid-level moisture, and low vertical wind shear [Merrill, 1988]. Kaplan *et al.* [2010] showed that a RI prediction index based on only environmental parameters is skillful

in the Atlantic and Northern East Pacific basins, while Hendricks *et al.* [2010] indicated that RI might be controlled by storm internal dynamics providing a favorable pre-existing environmental condition.

[3] The hot tower hypothesis [Malkus *et al.*, 1961; Simpson *et al.*, 1998] assumes that the latent heating release by those intense convective overshooting towers is crucial to TC intensification. Convective asymmetries [Braun *et al.*, 2006] and vortical hot towers [Montgomery *et al.*, 2006; Molinari and Vollaro, 2010] have also been indicated to be related to TC RIs. However, it has been indicated that the increase of the probability of RI for TCs with hot towers in the inner core is not substantial relative to the climatological mean [Jiang, 2012]. On the other hand, an alternative hypothesis to the hot tower hypothesis was developed in the early 1980s. It has been shown that symmetric heating was a major factor in most TC intensification through both theoretical [Shapiro and Willoughby, 1982; Nolan and Grasso, 2003] and observational studies [Willoughby *et al.*, 1982; Willoughby, 1990]. Recently, Nguyen *et al.* [2011] advance the idea that TC may vacillate between symmetric and asymmetric intensification through a modeling case study of Hurricane Katrina (2005). However, it is not clear whether the symmetric or asymmetric process leads the intensification.

[4] Satellite observations are often the only available means for estimating TC intensity. Unlike infrared sensors, passive microwave channels allow penetration into precipitating clouds, therefore providing information about precipitation and ice particles instead of just the cloud tops. This study uses the 37 GHz frequency measurements, which detect both emission from liquid hydrometeors and scattering of upwelling radiation by cloud ice [Weng and Grody, 1994]. The findings documented here represent the first time that the 37 GHz ring pattern in the inner core is identified as a specific and unique feature that is associated with TC RI, and in such cases immediately precedes eyewall development.

2. Data and Methods

[5] To examine TC precipitation morphology during periods of RI, a set of images is collected of all TC satellite overpasses during 2003–2007 in the North Atlantic basin from the 37 GHz color composite product provided by the Navy Research Laboratory (NRL) TC satellite web page (<http://www.nrlmry.navy.mil/TC.html>) [Hawkins *et al.*, 2001; Hawkins and Velden, 2011]. The 37 GHz is used here for its capacity of detecting low-level circulation centers, which are sometime unseen at 85 GHz [Lee *et al.*, 2002; Turk *et al.*, 2006]. In order to better display the 37 GHz observations including its sensitivity for both low-level clouds and deep convection, the 37 GHz color composite (hereafter 37color) product was developed at NRL for real-time TC image

¹Department of Earth and Environment, Florida International University, Miami, Florida, USA.

Corresponding author: H. Jiang, Department of Earth and Environment, Florida International University, 11200 SW 8th St., PC-342B, Miami, FL 33199, USA. (haiyan.jiang@fiu.edu)

©2012. American Geophysical Union. All Rights Reserved.

Table 1. List of Three RI Events of Hurricane Emily (2005)

	Time (mmddhh)	Initial Intensity (kt)	Intensity Increase During the Next 24-h
Event #1	071306	45	30
	071312	50	35
	071318	55	45
	071400	70	40
	071406	75	40
Event #2	071412	85	30
	071518	95	40
	071600	110	30
Event #2	071900	75	35
	071906	80	30

distribution [Lee *et al.*, 2002]. It is constructed by using 37 GHz vertically polarized (V37) and horizontally polarized (H37) brightness temperatures, and polarization correction temperature (PCT37 [Cecil *et al.*, 2002]). The ocean surface appears cold in V37 and H37, similar to ice-scattering in deep convection which also appears cold in both V37 and H37. To correct this ambiguity, the PCT37 is defined by $PCT37 = 2.18 \times 37V - 1.18 \times H37$. The resulting PCT37 is cold for ice-scattering and warm for the ocean surface. The 37color product implements a red/green/blue color composite from PCT37, H37 and V37 so that qualitatively the ocean surface in the color product appears dark green, deep convection appears pink, and low-level water clouds and warm rain appear cyan. The quantitative information is sacrificed. The 37color product is generated for all TC overpasses from the Tropical Rainfall Measuring Mission (TRMM) Microwave Imager (TMI), Advanced Microwave Scanning Radiometer for EOS (AMSR-E), WindSat, Special Sensor Microwave Imager (SSM/I), and Special Sensor Microwave Imager/Sounder (SSMIS) when these data are available.

[6] After examining many 37color images of the entire life cycle of TCs, we hypothesize that the first appearance of a well-defined cyan color ring pattern in the inner core immediately surrounding the warm center is associated with RI. The purpose of this study is to test this hypothesis. Using the 37color images collected for 84 named TCs during 2003–2007 hurricane seasons in the North Atlantic basin, the ring pattern is searched for within each satellite overpass that captures the TC inner core. The following criteria are used to define a ring pattern: 1) It immediately surrounds the warm center of the developing TC; 2) It is symmetric (round) and should be at least 90% closed (not a partial ring); 3) The minimum thickness between the inner and outer edges of the ring should be at least one-fourth of the diameter of the outer edges; 4) The ring should consist of mostly solid bright cyan and not a faded cyan; 5) Part of the ring could be pink (intense convection overlaying cyan ring).

[7] The best track data from the National Hurricane Center (NHC) are used to determine RI cases from the 84 TCs. RI cases are defined as those cases with 24-hour maximum wind speed intensity increase equal to or greater than 30 kt [Kaplan and DeMaria, 2003]. From the best track data, a 24-hour period beginning at each synoptic time (i.e., 0000, 0600, 1200 and 1800 UTC) is considered the starting point of one potential RI case. Therefore consecutive RI cases each overlap by 18 hours. To be included in the study, the inner core of the TC must be over water for the period of RI. The initial intensity must be less than or equal to 100 kt. The 84 TCs contributed a total of 1735 cases (i.e., 24-h periods

with initial time at the 6 hourly synoptic times). When environmental conditions are favorable for RI, in many instances the favorable environment exists for a day or so, so that when a TC starts to rapidly intensify, the intensification continues for at least 24 hours and can last as long as 48–60 hours. Here we define this period of RI as one *RI event*. Using the definition of RI as an increase of 30 kt or higher in 24 hours, with best track data for every 6-hour synoptic time, each RI event can be defined as a cluster of *continuous and overlapping* 24-hr RI cases. RI events in the study contained up to 6 overlapping RI cases, and each TC could have more than one RI event. For example, as shown in Table 1, Hurricane Emily (2005) experienced three RI events. The first RI event has 6 overlapping RI cases. The second and third events, both of which consist of two overlapping RI cases, began after the storm subsequently weakened. In this study, a ring pattern is searched from all the available 37color images with observation times within $t - 5$ h and $t + 1$ h (t is the initial time of each 6-h case). According to discussions with NHC forecasters, up to one hour delay of the microwave data is acceptable to be used in their forecasts. Since our hypothesis is that only the first ring occurrence during each RI event can be used as a predictor, here only the first ring during each TC intensifying period is counted and recorded. The Statistical Hurricane Intensity Prediction Scheme (SHIPS) RI index (RII) [Kaplan *et al.*, 2010] is used to evaluate the environmental factors for each best track case. The SHIPS RII probability values for a 30 kt intensity increase during 24 h (hereafter RII_30 kt) are obtained from the post-time dependent run of the most recent version of SHIPS RII algorithm for 1995–2010 storms. These values are matched with the 6-hourly best track data. One caveat is that there are 762 out of 1735 total cases with no SHIPS RII available due to either extra-tropical condition or low initial storm intensity. In the remaining 973 cases, there are 195 cases with no 37 GHz satellite data available. Therefore, the final total number of qualified cases used in this study is 778. There are 71 actual RI cases out of these 778 cases and these 71 RI cases are from 28 RI events. The total number of RI cases during 2003–2007 Atlantic hurricane seasons is 104 (including 7 overland RI cases) from 31 RI events.

3. Results and Discussion

[8] Identifying ring patterns in the 37color images mainly relies on higher resolution sensors including TMI, AMSR-E, and WindSat, although lower resolution sensors including SSM/I and SSMIS can be used for storms with very large eyes. Figure 1 shows an example of the ring feature, an NRL 37color image from a WindSat overpass at 11:05 UTC October 18, 2005 associated with a record-setting RI event for Hurricane Wilma (2005). The first ring pattern during each TC intensifying period occurred in 45 out of the 778 cases (Table 2). In the 45 possible RI cases with a ring, there are 23 cases that actually went through RI. There are 19 out of these 23 cases in which a ring pattern appeared during $t - 5$ h and $t + 1$ h period, but four other cases had a ring pattern more than one hour after the starting time of the 24-h RI period. In real-time NHC forecasts, these 4 RI cases will be missed if using the ring pattern as a predictor.

[9] The ring pattern also appeared at the beginning of 22 intensifying cases that did not go through RI (Table 2). There were no differences in the appearance of the ring

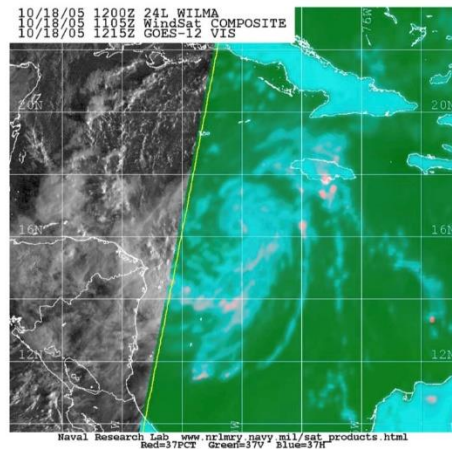


Figure 1. An example of a precipitative ring in Hurricane Wilma (2005)'s NRL 37color image from a WindSat overpass at 11:05 UTC October 18, 2005. The ring pattern occurred about one hour before an RI case with a 24-h intensity increase of 95 kts. Courtesy of the Naval Research Laboratory (NRL) TC satellite web page (<http://www.nrlmry.navy.mil/TC.html>). (Note that if you are reading a printed copy of the figure, the cyan color might not be as clear as in the electronic copy viewed from a computer screen).

pattern between cases that went through RI and those that did not. It is likely that all TCs at this point had reached a similar stage in their core development, but the environmental factors are different for these RI and non-RI cases. The SHIPS RII probability for a 30 kt increase in 24-h (RII_30 kt [Kaplan *et al.*, 2010]) is examined. The RII-30 kt values are probabilities scaled from 0 to 100%, with the higher values indicating higher probabilities of RI due to favorable environmental conditions. It is found that the average SHIPS RII-30 kt is much higher for RI cases (27.5%) than non-RI cases (4.5%). If an arbitrary threshold of RII-30 kt is selected to be $\geq 5\%$ for a favorable environment, 21 out of 23 RI cases satisfies this threshold and all but 2 non-RI cases do not meet this threshold. The 20 non-RI cases with a ring and SHIPS RII-30 kt $< 5\%$ are correct rejections, but the 2 non-RI cases with a ring and SHIPS RII-30 kt $\geq 5\%$ are false alarms. In the 23 RI cases, there are 17 correct forecast (hit) cases (with ring during $t - 5$ h and $t + 1$ h and SHIPS_RII $\geq 5\%$), 4 microwave late cases (with ring during $t + 1$ h and $t + 7$ h and SHIPS_RII $\geq 5\%$), and 2 misses (with ring during $t - 5$ h and $t + 1$ h and SHIPS_RII $< 5\%$, see Table 2). Therefore the SHIPS RII can be used as a discriminator for RI and non RI cases, even though both cases have a ring feature.

[10] Based on the result shown in Table 2, the probability of RI if using the 37 GHz ring as the sole criterion (the ring RI index) is 38% (17/45, Table 3). This represents a factor of 5.4 increases from the climatological mean during the same 5-yr period. Jiang [2012] indicated that the probability of RI for TCs with hot towers in the inner-core is 9.6%, which is only about a factor of 1.5 increases from the climatological

mean (6.3%) using TRMM precipitation radar observed TCs during 1998–2008. Although Jiang's [2012] results are for global TCs, the substantial difference with this study demonstrates that the ring pattern might be a better inner-core process related indicator for the RI prediction.

[11] The SHIPS RII probability threshold used to forecast RI is about 20% for the Atlantic basin [Kaplan *et al.*, 2010]. Here we use this threshold to evaluate the probability of RI for the SHIPS RII. There are 163 cases with RII_30 kt $\geq 20\%$, in which there are 55 actual RI cases. Therefore, the probability of RI is 34% (55/163, Table 3), which is slightly lower than the probability of RI for the ring RI index (38%). This indicates that environmental conditions and inner-core properties might weight almost equally in terms of determining RI, although other inner-core processes need to be taken into account as well besides the ring pattern.

[12] Since a favorable environment condition is necessary for RI, it is optimal to add the SHIPS RII criterion to the ring RI index (RII). Here it is decided to use RII_30 kt $\geq 5\%$ as the additional criterion besides the ring. We call this combined RI index Ring+SHIPS RII. As shown in Table 3, there are 23 (out of 778) cases that satisfy the ring and RII_30 kt $\geq 5\%$ criteria, in which there are 17 actual RI cases. This produces a probability of RI of 74% (17/23), which is about a factor 2 higher than the probability of either the ring or SHIPS RII alone. This indicates that the 37 GHz ring RII and SHIPS RII are independent predictors. This indicates that RI is dependent on favorable conditions and a certain level of internal core structure to a similar extent, and that symmetric warm rain (indicated by the cyan color ring on the 37 GHz product) is an important element in this core structure.

[13] The probability of detection (POD) and false alarm ratio (FAR) for 2003–2007 storms are also shown in Table 3. The POD is the percentage of RI cases that are correctly identified. The FAR is the number of times that RI is forecasted but does not occur divided by the total number of times RI is forecast. The FAR is equal to one minus the probability of RI. The PODs for the ring only, SHIPS RII only, and ring+SHIPS RII are 24% (17/71), 77% (55/71), and 24% (17/71), respectively. The POD for the combined RII is a factor of 3 lower than that for the SHIPS RII. The FARs for the ring only, SHIPS RII only, and ring+SHIPS RII are 62%, 66%, and 26%. The FAR for the combined RII is a factor of 2.5 lower than that for the SHIPS RII. This shows that the ring+SHIPS RII has a great potential to reduce the false alarm rate, but the detection rate is somewhat sacrificed when treating every 6-h synoptic time as one case.

[14] As mentioned above, RI usually happens as an event, noted in the best track data as a cluster of continuous and overlapping 24-h RI cases. Hurricane forecasters often prefer to characterize RI as an event. The ring+SHIPS RI forecast scheme was initially designed as an event-based forecast method. From this point of view, a separate statistic is done to evaluate the method based on RI events using the 2003–2007 Atlantic hurricane seasons. As listed in Table 4, there are a total of 28 RI events associated with 24 TCs: 21 hits and 7 misses. The ring+SHIPS RII forecast method captures 21 out of these 28 events, producing a POD of 75% (21/28). Two events are missed due to a low SHIPS RII value, and five events are missed due to a lack of a ring feature. After taking the two false alarm cases in Table 2 into account, the FAR is 9% (2/23), which corresponds to a 91% probability of RI. This extremely high performance comes with three

Table 2. List of RI (23) and Non-RI (22) Cases Having the First 37 GHz Ring Pattern Occurring During the Intensification Stages of TCs in the 2003–2007 Atlantic Hurricane Seasons^a

Number	Storm	Best Track Starting Time and Intensity (kt)	Best Track Ending Time	Time of Microwave Overpass With Ring Pattern	Intensity Change in 24 h (kt)	RII_30 kt (%)
<i>RI Cases With a Ring Between $t - 5$ h and $t + 1$ h (t is the RI Initial Time) and SHIPS_RII_30 kt $\geq 5\%$ (17 Hits)</i>						
1	2003 Fabian	08/30 06Z, 70 kt	08/31 06Z	08/30 0217Z TRMM	40	22
2	2003 Isabel	09/07 12Z, 65 kt	09/08 12Z	09/07 0906Z SSM/I	45	39
3	2004 Alex	08/02 18Z, 50 kt	08/03 18Z	08/02 1312Z SSM/I	35	20
4	2004 Danielle	08/14 18Z, 55 kt	08/15 18Z	08/14 1527Z TRMM	30	33
5	2004 Frances	08/26 12Z, 55 kt	08/27 12Z	08/26 1049Z TRMM	35	47
6	2004 Ivan	09/05 00Z, 60 kt	09/06 00Z	09/04 2043Z WindSat	55	23
7	2004 Jeanne (2)	09/19 18Z, 45 kt	09/20 18Z	09/19 1824Z AMSR-E	30	16
8	2005 Dennis (1)	07/07 12Z, 90 kt	07/08 12Z	07/07 0542Z TRMM	40	32
9	2005 Emily (1)	07/14 12Z, 85 kt	07/15 12Z	07/14 1037Z WindSat	30	30
10	2005 Emily (3)	07/19 00Z, 75 kt	07/20 00Z	07/18 2359Z WindSat	35	22
11	2005 Katrina	08/27 06Z, 95 kt	08/28 06Z	08/27 1942Z AMSR-E	50	23
12	2005 Rita	09/20 18Z, 85 kt	09/21 18Z	09/20 1500Z TRMM	60	31
13	2005 Wilma	10/18 06Z, 60 kt	10/19 06Z	10/18 1105Z WindSat	85	50
14	2006 Helene	09/17 00Z, 70 kt	09/18 00Z	09/16 2026Z WindSat	30	23
15	2007 Dean (1)	08/15 12Z, 50 kt	08/16 12Z	08/15 1105Z SSM/I	30	16
16	2007 Dean (2)	08/17 12Z, 90 kt	08/18 12Z	08/17 1220Z SSMIS	55	46
17	2007 Felix	09/02 00Z, 65 kt	09/03 00Z	09/01 2148Z WindSat	85	36
<i>RI Cases With a Ring After $t + 1$ h (t is the RI Initial Time) and SHIPS_RII_30 kt $\geq 5\%$ (4 Late Cases)</i>						
1	2004 Karl	09/17 18Z, 55 kt	09/18 18Z	09/17 2317Z TRMM	40	43
2	2004 Lisa	09/20 06Z, 30 kt	09/21 06Z	09/20 0818Z WindSat	30	16
3	2006 Florence	09/09 18Z, 50 kt	09/10 18Z	09/09 2001Z TRMM	30	31
4	2006 Gordon	09/13 06Z, 70 kt	09/14 06Z	09/13 1005Z WindSat	35	21
<i>RI Cases With a Ring Between $t - 5$ h and $t + 1$ h (t is the RI Initial Time) and SHIPS_RII_30 kt $< 5\%$ (2 Misses)</i>						
1	2005 Dennis (2)	07/09 12Z, 80 kt	07/10 12Z	07/09 1202Z WindSat	40	3
2	2005 Emily (2)	07/15 18Z, 95 kt	07/16 18Z	07/15 1801Z AMSR-E	40	3
<i>Non-RI Cases With a Ring and SHIPS_RII_30 kt $< 5\%$ (20 Correct Rejections)</i>						
1	2003 Ana	04/22 00Z, 50 kt	04/23 00Z	04/21 2338Z TMI	-10	3
2	2003 Danny	07/18 06Z, 55 kt	07/19 06Z	07/18 0558Z TRMM	10	3
3	2003 Juan	09/26 18Z, 70 kt	09/27 18Z	09/26 1639Z TRMM	20	3
4	2003 Kate	10/01 18Z, 65 kt	10/02 18Z	10/01 1659Z TRMM	15	3
5	2004 Alex (2)	08/04 06Z, 80 kt	08/05 06Z	08/04 0316Z TRMM	25	3
6	2004 Lisa (1)	09/21 06Z, 60 kt	09/22 06Z	09/21 0401Z AMSR-E	-10	3
7	2004 Lisa (2)	10/02 00Z, 60 kt	10/03 00Z	10/01 2008Z TRMM	-10	3
8	2005 Irene (1)	08/12 00Z, 45 kt	08/13 00Z	08/11 2201Z WindSat	15	3
9	2005 Irene (2)	08/15 12Z, 75 kt	08/16 12Z	08/15 0720Z TRMM	10	3
10	2005 Nate	09/07 18Z, 70 kt	09/08 18Z	09/07 1540Z TRMM	5	3
11	2005 Ophelia(1)	09/10 18Z, 70 kt	09/11 18Z	09/10 1428Z TRMM	-5	3
12	2005 Ophelia(2)	09/12 18Z, 60 kt	09/13 18Z	09/12 1730Z TRMM	0	3
13	2005 Vince	10/09 00Z, 45 kt	10/10 00Z	10/08 2133Z TRMM	15	3
14	2005 Epsilon(1)	12/03 00Z, 65 kt	12/04 00Z	12/02 1942Z TRMM	0	3
15	2005 Epsilon(2)	12/04 00Z, 65 kt	12/05 00Z	12/03 1847Z TRMM	5	3
16	2005 Delta	11/24 00Z, 55 kt	11/24 00Z	11/23 2131Z TRMM	5	3
17	2005 Zeta	12/30 12Z, 45 kt	12/31 12Z	12/30 0807Z WindSat	5	3
18	2006 Debby	08/23 06Z, 40 kt	08/24 06Z	08/23 0125Z TRMM	5	3
19	2006 Gordon(2)	09/17 18Z, 70 kt	09/18 18Z	09/17 1736Z TRMM	15	3
20	2006 Isaac	09/28 12Z, 40 kt	09/29 12Z	09/28 1040Z TRMM	5	3
<i>Non-RI Cases With a Ring and SHIPS_RII_30 kt $\geq 5\%$ (2 False Alarms)</i>						
1	2004 Ivan (2)	09/07 06Z, 95 kt	09/08 06Z	09/07 0528Z AMSR-E	25	16
2	2005 Maria	09/05 00Z, 75 kt	09/06 00Z	09/04 2007Z TRMM	25	23

Table 3. Probability of RI for 2003–2007 Atlantic TCs Using the Ring, SHIPS RII, and Ring+SHIPS RII Criteria for the 30-kt RI Threshold

	Climatological Mean	Ring	SHIPS RII $\geq 20\%$	Ring+SHIPS RII $\geq 5\%$
# of total forecasts	778	45	163	23
# of correct forecasted cases	71	17	55	17
Probability of RI	9%	38%	34%	74%
POD	100%	24%	77%	24%
FAR ($=1 - \text{Probability of RI}$)	91%	62%	66%	26%

Table 4. List of All Best Track RI Events (28) During 2003–2007 Hurricane Seasons in the Atlantic Basin^a

Number	Storm	Best Track RI Starting Time and Intensity (kt)	Total RI Event Duration	Number of RI Cases in the RI Event	Hours From the RI Starting Time to Ring Time (h)	Hours From Ring Time to the RI Ending Time (h)	Total Intensity Increase During the RI Event (kts)	24-h Intensity Increase Associated With the Ring (kts)	Highest 24-h Intensity Increase During the RI Event (kts)
<i>21 RI Events With Ring and SHIPS_RII_30 kt > 5% (RI Was Indicated and RI Occurred)</i>									
1	2003 Fabian	08/29 12Z, 50	42	4	14.5	27.5	60	40	45
2	2003 Isabel	09/07 06Z, 60	42	4	3	39	55	45	45
3	2004 Alex	08/02 06Z, 40	36	3	7	29	45	35	35
4	2004 Danielle	08/14 00Z, 35	42	4	15.5	26.5	50	30	35
5	2004 Frances	08/25 18Z, 35	54	6	17	37	65	35	35
6	2004 Ivan	09/05 00Z, 60	42	4	9	31	60	55	55
7	2004 Jeanne	09/19 18Z, 45	24	1	0.5	23.5	30	30	30
8	2004 Karl	09/17 00Z, 40	42	4	23.5	18.5	55	40	40
9	2004 Lisa	09/20 06Z, 30	24	1	2.5	21.5	30	30	30
10	2005 Dennis (1)	07/06 06Z, 50	54	6	23.5	30.5	75	30	50
11	2005 Emily (1)	07/13 06Z, 45	54	6	28.5	25.5	70	30	45
12	2005 Emily (3)	07/19 00Z, 75	30	2	0	30	35	35	35
13	2005 Katrina	08/27 06Z, 95	42	4	13.5	28.5	95	40	50
14	2005 Rita	09/20 00Z, 60	54	6	15	34	60	60	60
15	2005 Wilma	10/17 18Z, 45	48	5	17	30	105	95	95
16	2006 Florence	09/09 18Z, 30	24	1	2	22	30	30	30
17	2006 Gordon	09/12 12Z, 30	42	4	22	20	35	35	35
18	2006 Helene	09/17 00Z, 70	30	2	-3.5	26.5	35	30	30
19	2007 Dean (1)	08/15 12Z, 50	24	1	-3	21	30	30	30
20	2007 Dean (2)	08/16 18Z, 80	42	4	18.5	23.5	65	55	65
21	2007 Felix	08/31 18Z, 30	60	7	22	38	105	85	85
<i>2 RI Events With Ring and SHIPS_RII_30 kt < 5% (RI Not Indicated by Low SHIPS RII, but RI Occurred)</i>									
22	2005 Dennis (2)	07/09 06Z, 75	30	2	6	24	55	40	50
23	2005 Emily (2)	07/15 18Z, 95	30	2	0	30	45	40	40
	Mean		40	3.6	11	29	53	42	46
<i>5 RI Events Without Ring (RI Not Indicated by Lack of Ring Feature, but RI Occurred)</i>									
24	2005 Cindy	07/04 18Z, 30	30	2	N/A	N/A	35	N/A	35
25	2005 Stan	10/03 06Z, 35	24	1	N/A	N/A	30	N/A	30
26	2005 Beta	10/29 06Z, 70	30	2	N/A	N/A	40	N/A	30
27	2007 Karen	09/25 12Z, 35	30	2	N/A	N/A	30	N/A	30
28	2007 Lorenzo	09/26 12Z, 30	30	2	N/A	N/A	40	N/A	40

^aThe best track RI starting time and intensity, total RI event duration, hours from the RI starting time to the RI ring time, hours from the ring time to the RI ending time, total intensity increase during the RI event, 24-h intensity increase associated with the ring, and the highest 24-h intensity increase during the RI event are indicated.

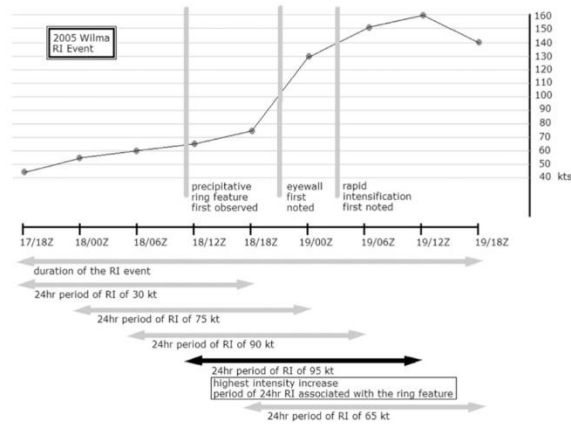


Figure 2. Time series of the 6 hourly best track maximum wind speed (in kts) of Hurricane Wilma (2005) during its 48-h RI event between 18Z October 17 and 18Z October 19. The times of the first ring feature seen in the 37color product, eyewall first noted by NHC in the advisory package, and RI first noted by NHC in the advisory package are indicated as vertical lines. Five overlapping 24-h periods of RI are indicated as arrows at the bottom of the figure. The ring was observed over 24 hours prior to the observation that the hurricane was going through an RI event.

compromises. First, the method usually does not detect the onset of the RI event, instead identifying one 24-hour period in the middle of the RI event. As seen in the fourth column of Table 4 (hours from the RI starting time to ring time), only 3 of the 21 captured RI events show that the ring appeared on or before the RI starting time. On average, the total RI event duration is 40 hours for the 23 RI events with rings. The ring appears 11 hours after the onset of RI on average. Second, due to microwave latency, lack of timely microwave passes over the center of the TC, lack of a higher-resolution pass over a TC with a small center, or a delayed onset of the ring feature associated with a moderately sheared environment, there are some late cases in which the period from the ring time to the RI ending time is less than 24 hours. There are 8 out of the 23 ring cases with hours from the ring time to the RI ending time less than 24 hours. Third, the method forecasts once for each RI event. As seen in the third column of Table 4, the number of overlapping RI cases (note that each case is one 24-h period of RI starting at 6 hourly synoptic times) in each RI event is usually greater than one. On average, the number is 3.6. Therefore, the method will miss about 72% of RI cases if evaluating it based on RI cases instead of RI events. This is reflected in the POD of 24% in Table 3 based on RI cases.

[15] Advantages that makes a strong argument for using the ring+SHIPS RII forecast method can be seen in Figure 2, which shows an example of Hurricane Wilma (2005)'s RI event between 18Z October 17 and 18Z October 19. The 48-h RI event contains five overlapping 24-h RI cases. The SHIPS RII 30 kt gives greater than 20% values for all these five cases, so it would technically forecast five hits for this one 48-hour RI event. The ring+SHIPS RII forecasts once at 12Z October 18 based on the ring pattern seen by a WindSat overpass at 11:05 UTC October 18 (Figure 1). Therefore,

the ring+SHIPS RII misses 4 out of 5 RI cases. However, it catches the RI case with highest intensity increase (24 hour intensity increase of 95 kt) of the five overlapping RI cases. The ring feature occurs prior to significant intensity increases, when there is also no indication from the conventional satellite imagery that Wilma is about to begin a period of RI, during what appears to be a period of gradual intensification. The first ring occurs prior to eyewall development and well in advance of the first mention of a period of RI in the NHC forecast discussions. It is the only early clue to the period of RI that is about to begin, and the transition from a Category 1 hurricane to a Category 5 hurricane in the subsequent 24 hours. The ability of the ring feature to precisely pinpoint large intensity increases should prove advantageous for improving intensity forecast performance.

[16] Statistics on these intensity increases for the RI events of 2003–2007 are presented in the last three columns of Table 4. The average total intensity increase during the 23 RI events with ring features is 53 kt, and the ring+SHIPS RII captures 43 kt of that on average, which is 79% of the total intensity increase for the RI event. The average highest 24-h intensity increase is 46 kt, which is only 3 kt higher than that captured by the method. By comparing the 7th and 8th columns of Table 4, we can see that the 37 GHz ring is associated with the highest 24-h intensity increase for 16 out of 23 RI events with rings. For the remaining 7 RI events, timing or lack of good microwave passes over the center might be a factor for the miss.

4. Conclusions

[17] Using the NRL 37color product during 2003–2007 for 84 TCs in the Atlantic basin, it is found that the first appearance of a cyan color ring around the storm center is associated with the subsequent storm rapid intensification

when environmental conditions are favorable for development. A simple subjective technique for predicting RI in the next 24 hours is proposed using both the 37 GHz ring pattern and the SHIPS RII for TCs with intensity ≤ 100 kt that are currently over water and are anticipated to remain over water for the next 24 hours. For the 84 TCs used in this study, this ring+SHIPS RI forecast method produces a probability of RI of 74%, which is about a factor of two higher than that for either of the ring or SHIPS RII. This indicates that the 37 GHz ring RII and SHIPS RII are independent predictors. Both the POD and FAR for the combined ring+SHIPS RII are lower than those for SHIPS RII alone (POD, 24% versus 77%, and FAR, 26% versus 66%) when treating every 6-hr synoptic time as a separate case.

[18] Because the method was initially developed for RI event-based forecasts, a verification based on 2003–2007 Atlantic RI events is performed. The method captures 21 out of these 28 events, producing a POD of 75% and a FAR of only 9%. This extremely high performance comes with three compromises: 1) the method usually does not detect the onset of the RI event, instead identifying one 24-hour period in the middle of the RI event; 2) due to microwave latency, lack of timely microwave passes over the center of the TC, lack of a higher-resolution pass over a TC with a small center, or a delayed onset of the ring feature associated with a moderately sheared environment, there are some late cases in which the period from the ring time to the RI ending time is less than 24 hours; 3) the method forecasts once for each RI event, which means that typically half to three quarters of overlapping 24-h RI cases will be missed if evaluating RI based on 24-hour RI cases instead of RI events. Major advantages of using the 37 GHz ring pattern to forecast an RI event are: 1) NHC forecasters usually couch rapid intensification in terms of an RI event in the forecast discussion of the advisory package, even though quantitative intensity increases are forecast; 2) the ring precedes observations that an RI event is in progress by at least 24 hours, well before any significant intensity increases, and before the TC appears to be intensifying on conventional Infrared satellite imagery; 3) this forecast method is often found to be associated with the highest intensity increase of the overlapping RI cases associated with the RI event; 4) the ring feature is often a hallmark of intensification to major hurricane; and 5) the ability of the forecast method to pinpoint large intensity increases should benefit the performance of intensity forecasting, which has consistently lagged behind track forecast performance improvements. Future study will focus on automating the ring identifying procedure in order to transfer the forecast method from subjective to objective. Study is also underway to analyze what is in the cyan ring using the three-dimensional observations of the TRMM Precipitation Radar.

[19] **Acknowledgments.** The authors acknowledge the Naval Research Laboratory's (NRL) Marine Meteorology Division for maintaining the NRL TC satellite webpage. Huge thanks go to John Kaplan for providing SHIPS RII data. Thanks to Jack Beven, John Knaff, James Franklin, Frank Marks, John Molinari, Mike Montgomery, Ed Zipser, Dave Roberts, Eric Blake and Todd Kimberlain for suggestions, comments, support, and encouragement for this work. The authors also would like to give acknowledgments to John Kaplan and another anonymous reviewer, whose comments helped improve the manuscript substantially. Support for this study is provided by the NOAA Joint Hurricane Testbed (JHT) grant (NA11OAR4310193) and NASA Hurricane Science Research Program (HSRP) grant (NNX10AG34G). The first author received support from the Florida International University Presidential Fellowship, and the second author received support from NASA New Investigator Program (NIP) award (NNX10AG55G).

[20] The Editor thanks the two anonymous reviewers for assisting in the evaluation of this paper.

References

- Braun, S. A., M. T. Montgomery, and Z. Pu (2006), High-resolution simulation of Hurricane Bonnie (1998). Part I: The organization of eyewall vertical motion, *J. Atmos. Sci.*, **63**, 19–42, doi:10.1175/JAS3598.1.
- Cecil, D., E. J. Zipser, and S. W. Nesbitt (2002), Reflectivity, ice scattering, and lightning characteristics of hurricane eyewalls and rainbands. Part I: Quantitative description, *Mon. Weather Rev.*, **130**, 769–784, doi:10.1175/1520-0493(2002)130<0769:RISALC>2.0.CO;2.
- Hawkins, J. D., and C. Velden (2011), Supporting meteorological field experiment missions and post-mission analysis with satellite digital data and products, *Bull. Am. Meteorol. Soc.*, **92**, 1009–1022, doi:10.1175/2011BAMS3138.1.
- Hawkins, J. D., T. F. Lee, F. J. Turk, C. Sampson, J. Kent, and K. Richardson (2001), Real-time Internet distribution of satellite products for tropical cyclone reconnaissance, *Bull. Am. Meteorol. Soc.*, **82**, 567–578, doi:10.1175/1520-0477(2001)082<0567:RIDOSP>2.0.CO;2.
- Hendricks, E. A., M. S. Peng, B. Fu, and T. Li (2010), Quantifying environmental control on tropical cyclone intensity change, *Mon. Weather Rev.*, **138**, 3243–3271, doi:10.1175/2010MWR3185.1.
- Jiang, H. (2012), The relationship between tropical cyclone rapid intensification and the strength of its convective precipitation features, *Mon. Weather Rev.*, **140**, 1164–1176, doi:10.1175/MWR-D-11-00134.1.
- Kaplan, J., and M. DeMaria (2003), Large-scale characteristics of rapidly intensifying tropical cyclones in the North Atlantic basin, *Weather Forecast.*, **18**, 1093–1108, doi:10.1175/1520-0434(2003)018<1093:LCORIT>2.0.CO;2.
- Kaplan, J., M. DeMaria, and J. A. Knaff (2010), A revised tropical cyclone rapid intensification index for the Atlantic and eastern North Pacific basins, *Weather Forecast.*, **25**, 220–241, doi:10.1175/2009WAF2222280.1.
- Lee, T. F., F. J. Turk, J. Hawkins, and K. Richardson (2002), Interpretation of TRMM TMI images of tropical cyclones, *Earth Interact.*, **6**, 1–17, doi:10.1175/1087-3562(2002)006<0001:IOITIO>2.0.CO;2.
- Malkus, J. S., C. Ronne, and M. Chaffee (1961), Cloud patterns in Hurricane Daisy, 1958, *Tellus, Ser. A*, **13**, 8–30, doi:10.1111/j.2153-3490.1961.tb00062.x.
- Merrill, R. T. (1988), Environmental influences on hurricane intensification, *J. Atmos. Sci.*, **45**, 1678–1687, doi:10.1175/1520-0469(1988)045<1678:EIOHI>2.0.CO;2.
- Molinari, J., and D. Vollaro (2010), Rapid intensification of a sheared tropical storm, *Mon. Weather Rev.*, **138**, 3869–3885, doi:10.1175/2010MWR3378.1.
- Montgomery, M. T., M. E. Nicholls, T. A. Cram, and A. B. Saunders (2006), A vortical hot tower route to tropical cyclogenesis, *J. Atmos. Sci.*, **63**, 355–386, doi:10.1175/JAS3604.1.
- Nguyen, C. M., M. J. Reeder, N. E. Davidson, R. K. Smith, and M. T. Montgomery (2011), Inner-core vacillation cycles during the intensification of Hurricane Katrina, *Q. J. R. Meteorol. Soc.*, **137**, 829–844, doi:10.1002/qj.823.
- Nolan, D. S., and L. D. Grasso (2003), Nonhydrostatic, three-dimensional perturbations to balanced, hurricane-like vortices. Part II: Symmetric response and nonlinear simulations, *J. Atmos. Sci.*, **60**, 2717–2745, doi:10.1175/1520-0469(2003)060<2717:NTPTBH>2.0.CO;2.
- Rappaport, E. N., et al. (2009), Advances and challenges at the National Hurricane Center, *Weather Forecast.*, **24**, 395–419, doi:10.1175/2008WAF2222128.1.
- Shapiro, L. J., and H. E. Willoughby (1982), The response of balanced hurricanes to local sources of heat and momentum, *J. Atmos. Sci.*, **39**, 378–394, doi:10.1175/1520-0469(1982)039<0378:TROBHT>2.0.CO;2.
- Simpson, J., J. B. Halverson, B. S. Ferrier, W. A. Peterson, R. H. Simpson, R. Blakeslee, and S. L. Durden (1998), On the role of “hot towers” in tropical cyclone formation, *Meteorol. Atmos. Phys.*, **67**, 15–35, doi:10.1007/BF01277500.
- Turk, F. J., S. DiMichele, and J. D. Hawkins (2006), Observations of tropical cyclone structure from WindSat, *IEEE Trans. Geosci. Remote Sens.*, **44**(3), 645–655, doi:10.1109/TGRS.2006.869926.
- Weng, F., and N. C. Grody (1994), Retrieval of cloud liquid water using the special sensor microwave imager (SSM/I), *J. Geophys. Res.*, **99**(D12), 25,535–25,551.
- Willoughby, H. E. (1990), Temporal changes of the primary circulation in tropical cyclones, *J. Atmos. Sci.*, **47**, 242–264, doi:10.1175/1520-0469(1990)047<0242:TCOTPC>2.0.CO;2.
- Willoughby, H. E., J. A. Clos, and M. B. Shoreibah (1982), Concentric eyewalls, secondary wind maxima, and the development of the hurricane vortex, *J. Atmos. Sci.*, **39**, 395–411, doi:10.1175/1520-0469(1982)039<0395:CEWSWM>2.0.CO;2.

Kieper and Jiang (2012) covered the Atlantic basin hurricane seasons 2003-2007. It is updated here with RI cases from the Atlantic basin for the years 2008-2019 and with the addition of EPAC 2015 Hurricane Patricia. The original paper provided one example of the 37color imagery, 2005 Wilma, but a catalog of images of the RI cases from the original paper and the additional years are presented in section 3.2 using primarily the higher-resolution PMW sensors (AMSR/AMSR2, TMI/GMI, WindSat) with some lower-resolution (SSMIS) of images that were timed well and where the TC was large enough so that the ring structure was well-represented in the image. While the images are primarily from the Atlantic basin, this precipitative pattern has occurred in all basins globally and has been used as a forecast aid by RSMCs in other basins, including the JTWC in the West Pacific (WPAC) Australia's Bureau of Meteorology (BOM), Météo-France La Réunion and RSMC Nadi in Fiji in the Southern Hemisphere (SHEM). Improving forecasts of RI has been a major focus of research efforts. The cyan ring RI indicator has helped improve them globally. Because the repository of the other basins is not complete it is not presented here, but examples from other basins are provided. A complete cataloguing of TC in the NRLMRY tcdat archive with the ring on the 37color imagery that best track data documented subsequently went through RI would probably run into the hundreds.

The history of this forecast aid began in the winter of 2007-2008, when this author was creating an offline repository of the tcdat 37 GHz, 85 GHz, and 150 GHz PMW imagery, and made the discovery that a specific pattern in the 37color imagery, a ring of cyan around the clear center, preceded a period of RI with approximate maximum or close to maximum 24 hour increase during the entire RI event. An example showing the

relationship between an RI event, the timing of the ring pattern, and individual 24 hr intensity increases during the RI event is shown for 2005 Wilma in Figure 3.1, from Kieper and Jiang (2012), shown here at higher resolution. Forecasts and best track data occur four times daily during "synoptic" times which are coordinated with data collection and model runs from National Weather Service (NWS) and other modeling centers. A key factor in determining whether RI could occur was whether the environment would be favorable in the next 24 hours, and the Statistical Hurricane Intensity Prediction System (SHIPS) was used as a diagnostic tool for determining a favorable environment (suggested by James Franklin and John Knaff, personal communication 2008).

This pattern identified is a symmetric solid ring in the bright cyan color that was not thin or unbroken, and in many cases edged with the bright pink color, immediately surrounding the warm center of the TC. Following interpretation from Chapter 5 this is understood to be a combination of shallow and deep convection where the pink outer edge indicates that the secondary circulation is established around at least part of the center – in other words, a developing eye/nascent eyewall. The ring forms in the area of surface convergence surrounding the calm center. This usually marks the first symmetric arrangement of precipitation around the center. The symmetric latent heat generated by this ring of convection is a factor in TC intensification through both theoretical (Shapiro and Willoughby, 1982) and observational studies (Willoughby et al. 1982, Willoughby 1990). Possibly some of the dynamics of these "convective rings" also apply to the shallow convection and weaker TC intensity associated with the initial appearance of the 37color RI ring. This ring pattern may also be associated with consolidation of a ring of vorticity around the center (Fuquig Zhang, personal communication). The symmetric

ring appears to be an early stage in eye development, a process that stabilizes the vortex and increases the TC efficiency (Smith, 1981; Schubert and Hack, 1982), aiding the intensification rate. This may explain why this period of RI is often associated with the highest 24 hr intensity increase.

Many Atlantic TC had principal bands prior to the formation of the ring, but the formation of a ring can occur from a variety of earlier TC structures. Two examples of rapid intensification showing the RI ring and the precipitative structure after RI had occurred, both record-setting cases, are 2005 Wilma in the Atlantic basin (Figure 3.9) and 2015 Patricia in the East Pacific basin (Figure 3.10)

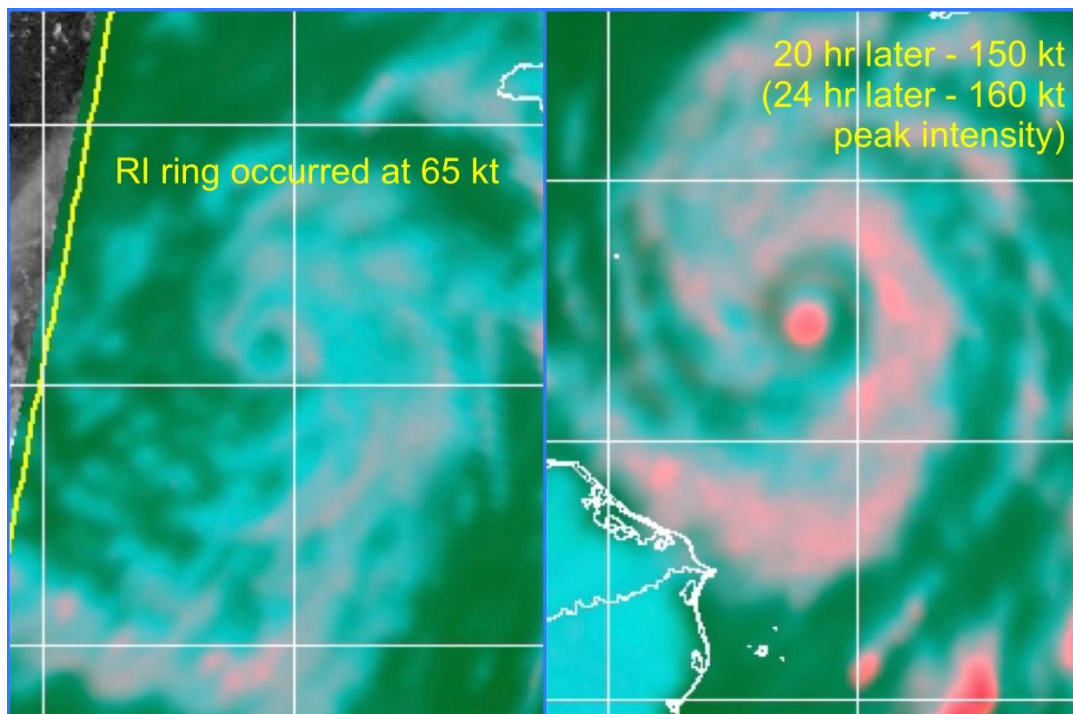


Figure 3.9 2005 Wilma ring and precipitative structure before and after RI.

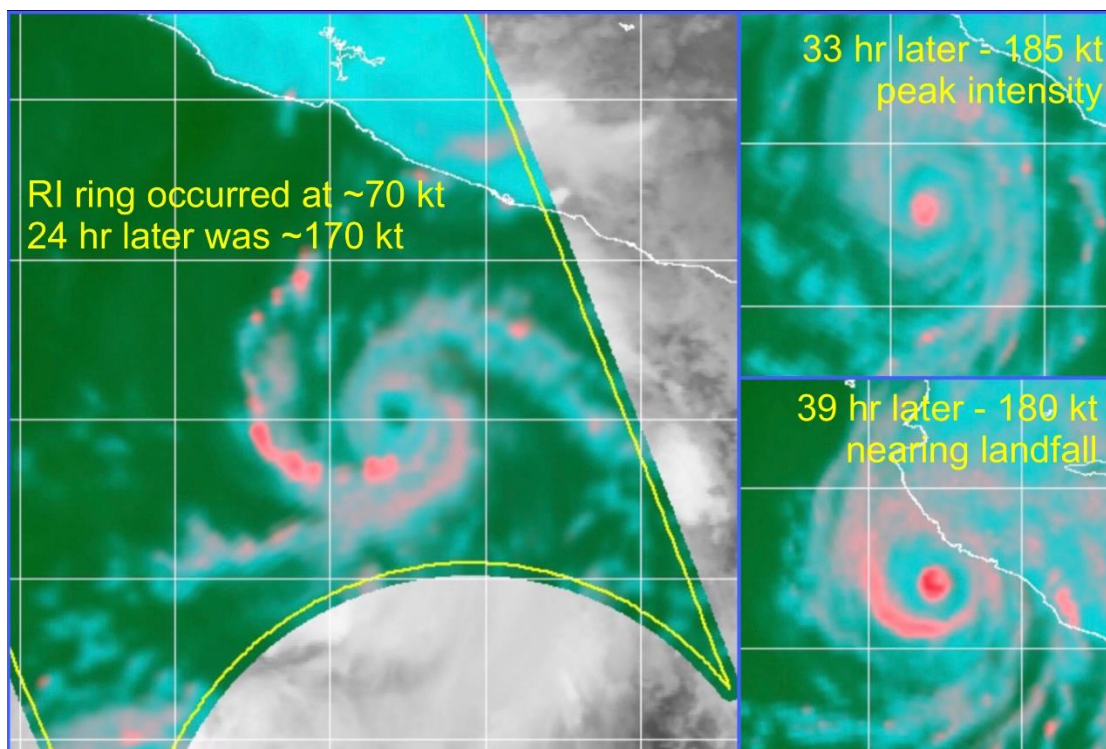


Figure 3.10 2015 Patricia, ring and precipitative structure before and after RI.

This ring is not seen on visible, infrared, 85H or 85color satellite imagery as observed for four TC in Figure 3.11, but is seen for the same four TC on the 37color imagery in Figure 3.12.

A poster on the RI forecast methodology using the 37color imagery for a set of Atlantic hurricanes from earlier years that went through RI was presented at the spring 2008 AMS 28th Conference on Hurricanes and Tropical Meteorology. To make this forecast methodology visible to the tropical cyclone community, in the summer of 2008 this author decided to use the tstorms listserve, available globally to tropical cyclone forecasters and researchers, to make real-time forecasts of RI for Atlantic TC. RI forecasts were made for Bertha, Dolly, Gustav (twice), Ike, Omar, and Paloma. All of the forecasts verified for RI within the next 24 hours. Coordinating with the National

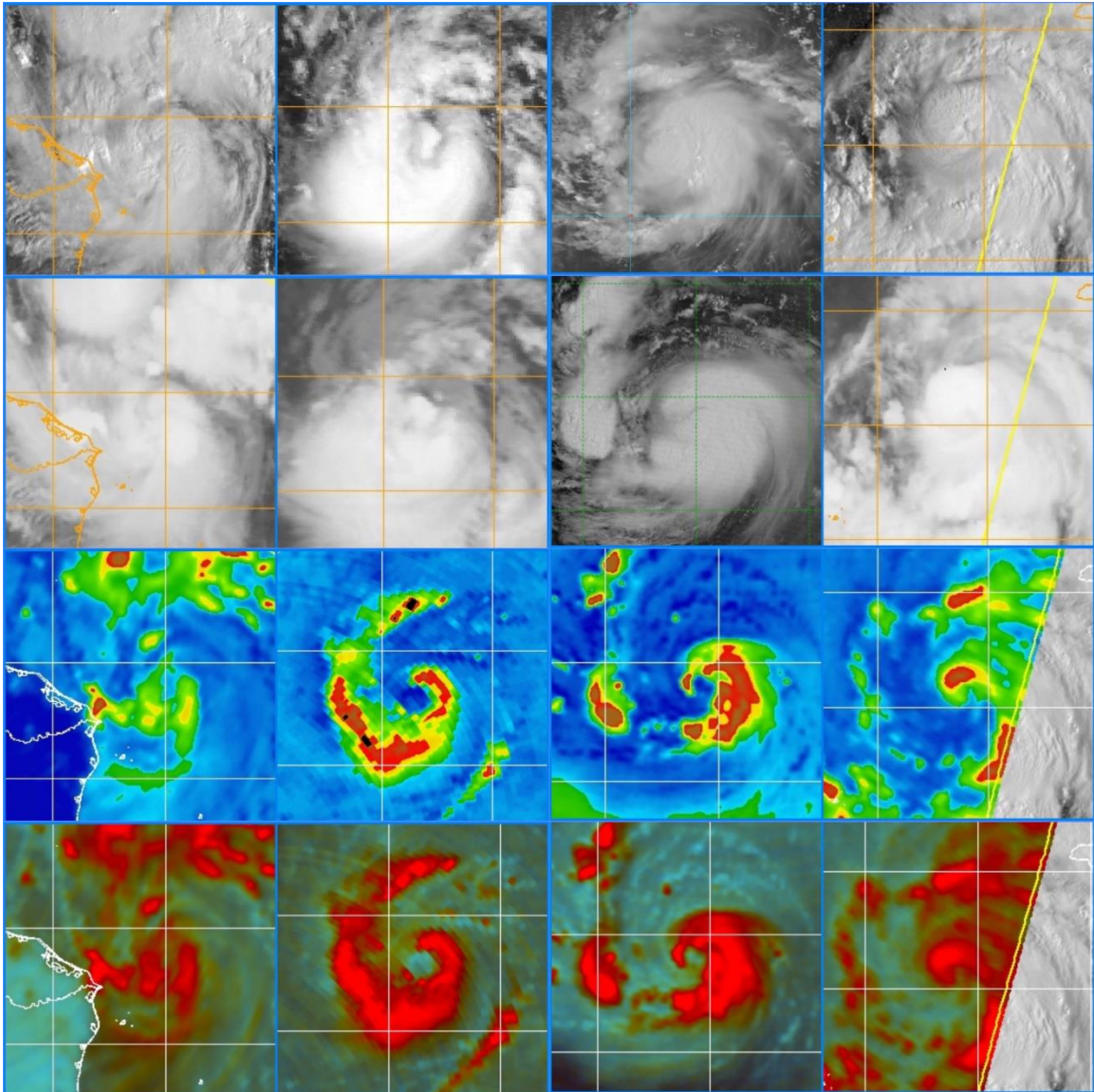


Figure 3.11 Satellite imagery for four developing Atlantic TC. Left to right) 2008 Paloma, 2004 Danielle, 2019 Jerry, and 2005 Wilma, seen on (top to bottom) visible, infrared, 85H, and 85color imagery. Note that the RI ring seen on the 37color (Figure 3.10) is not visible on any of these images. Also of note is that the IR image for Jerry is the NPP VIIRS Night-Visible image which uses the light of the moon to observe cloud imagery that is similar to visible imagery.

Hurricane Center (NHC) forecasters, a white paper describing the forecast methodology and two tests for forecasters to use to train and recognize the ring were provided. In 2009 working with NHC, RI forecasts were again tested in the ATL and EPAC basins. They were not as successful as in 2008 in that 100% accuracy was not achieved.

When a ring pattern was present in the 2003-2007 Atlantic dataset, in a favorable environment, RI occurred in 21 cases (hits) and in an unfavorable environment, in hindcast, RI did not occur in seven cases (two false alarms and five correct negatives), yielding a probability of detection (POD) of 75% and a false alarm ratio (FAR) of 9%.

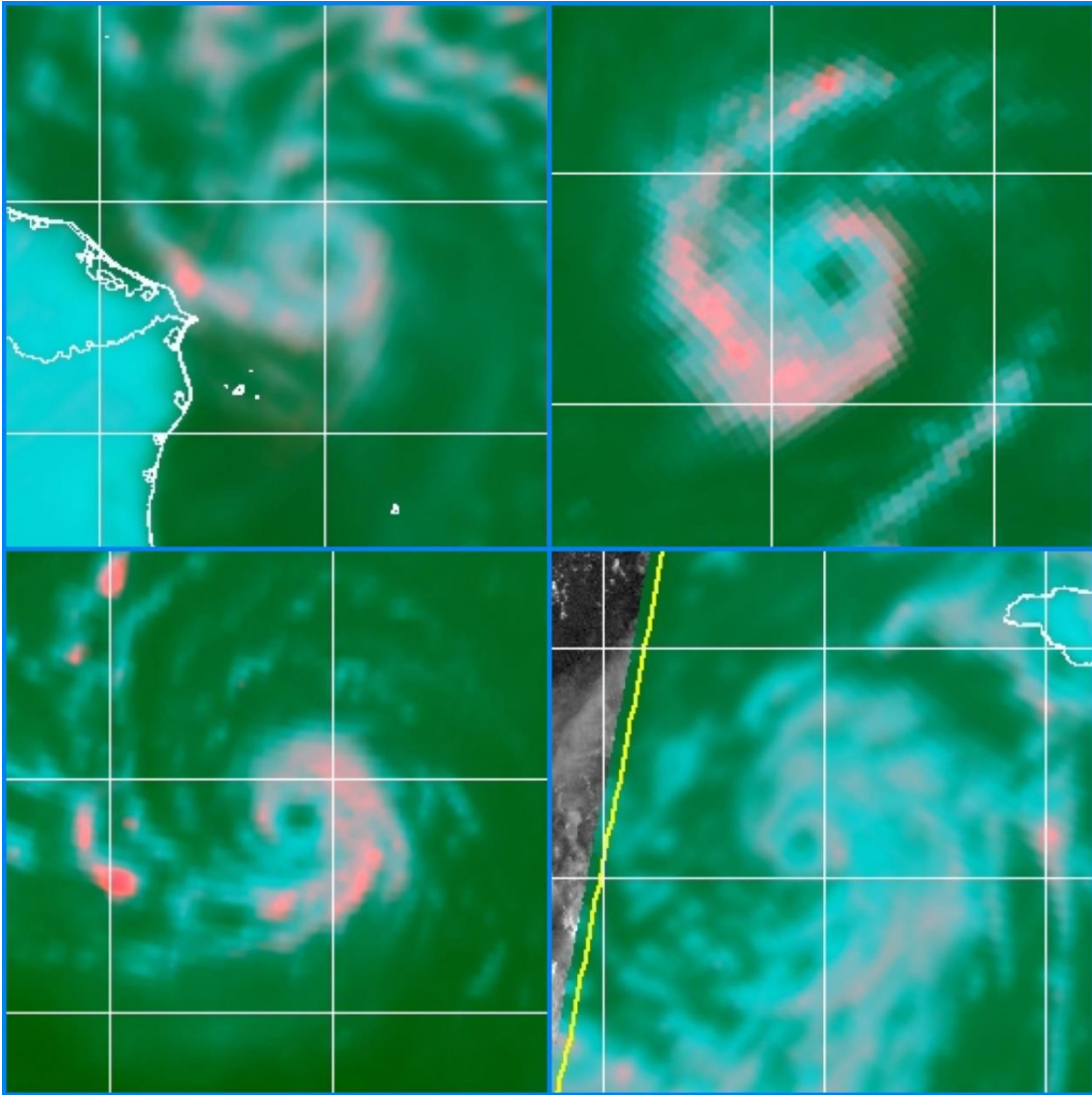


Figure 3.12 RI ring for the same four developing Atlantic TC. The ring is seen only on the 37color images, left-to-right and top-to-bottom, 2008 Paloma, 2004 Danielle, 2019 Jerry, and 2005 Wilma.

3.1 Importance of Forecasting Rapid Intensification for Severe Tropical Cyclones

Major hurricanes account for more than 80% of total damage caused by hurricanes in the continental U.S. (Weinkle et al. 2018). Rapid intensification is a challenge to tropical cyclone forecasting, for timely warnings and preparation prior to landfall. Kaplan and DeMaria 2003 determined, " 60% of all hurricanes, 83% of all major hurricanes, and all category 4 and 5 hurricanes underwent RI at least once during their lifetimes." Because of the severe damage and loss of life associated with intense TC, forecasting RI, especially prior to landfall, remains a critical requirement for TC forecasters, and the ring has been utilized to anticipate RI since introduced to the TC community 14 years ago.

As an example of use of this forecast aid, in February 2011 the BOM utilized an RI ring indicator for Severe Tropical Cyclone Yasi to increase their landfall forecast from Category 4 to Category 5 (note that the BOM scale for intensity is different from the one used in the US), and their forecast for Category 5 verified. Cyclone Yasi passed directly over Willis Island which contained a weather station and radar, completely destroying the radome, the radar inside, and damaged the power generator and other equipment, and removing the vegetation. The last radar image of Yasi from Willis Island, and a photo of the island and its weather station shown in Figure 3.13.

More recently, two U.S. weather radar were destroyed by major hurricanes. In 2017 Maria destroyed the NWS WSR-88D radar on Puerto Rico as a Category 4 (Figure 3.14) and 2020 Laura, also as a Category 4, similarly destroyed the NWS WSR-88D radar in Lake Charles (Figure 3.15). An undamaged WSR-88D, illustrating the protective radome, is shown in Figure 3.16.



Figure 3.13 Willis Island BOM Weather Station and the last radar image from 2011 Yasi. It destroyed the radar on 2 February 2011; the station was repaired and became operational again in December of that year.



Figure 3.14 NWS WSR-88D radar destroyed by 2017 Hurricane Maria. (Image credit NWS San Juan, Puerto Rico).



Figure 3.15 NWS WSR-88D radar destroyed by 2020 Hurricane Laura. The radar is located in Lake Charles, LA. (Image credit Brett Adair).



Figure 3.16 NSW WSR-88D radar with protective radome. This radar is located in Frederick, OK (Image credit: author, April 2017).

Severe TC can also cause extensive damage from surge, as well as extreme winds.

Figure 3.17 illustrates surge damage from four significant surge events at hurricane landfall: the Bolivar Peninsula, TX from 2008 Ike, Category 2 at landfall; Waveland and Bay St. Louis, MS, from 2005 Katrina, Category 3 at landfall; Holly Beach, LA, from 2005 Rita, Category 3 at landfall, and Mexico Beach, FL, from 2018 Hurricane Michael, Category 5 at landfall. Along these shorelines most buildings did not withstand the surge and vegetation was damaged.



Figure 3.17 Storm surge damage from tropical cyclones. Left to right, top to bottom: 2008 Hurricane Ike, 2005 Hurricane Katrina, 2005 Hurricane Rita, and 2018 Hurricane Michael (credits NOAA and USCG).

3.2 Images of Convective Rings of Tropical Cyclones that Rapidly Intensified

Images of the cyan rings, composed of shallow and moderate convection and considered to be a developing eye, from the Atlantic basin for the years 2003-2019 are shown in Figures 3.18–3.20 and the additional TC that exhibited the rings and went through RI for the period after Kieper and Jiang 2012, 2008-2019, are documented in Table 3-1. East Pacific 2015 Patricia is included as well. Images of two rapidly-intensifying TC, from the WPAC and ATL basins, are shown. These compare the structure when the ring occurred and the structure 24 hours later, after RI. 2004 WPAC Dianmu (Figure 3.21) intensified 80 kt in 24 hours after displaying the ring. 2019 ATL Dorian, (Figure 3.22) which intensified 30 kt in the 24 hr after the ring, went on to continue to intensify reaching an intensity of 160 kt at landfall in the Bahamas. In the two post-intensification images a very small intense eyewall is seen.

Examples of the ring from other basins are seen in Figures 3.23 and 3.24. First, six of the rings from the WPAC 2004 typhoon season are shown. Next are SHEMA images from Fiji in the SPAC, the SWIO near Madagascar, and the Indian Ocean off the NW coast of Australia. Note the banding in the SHEMA indicates the clockwise motion as opposed to the counterclockwise motion of TC in the NHEMA. The rings appear the same regardless of basin and can be used globally for forecasting RI.

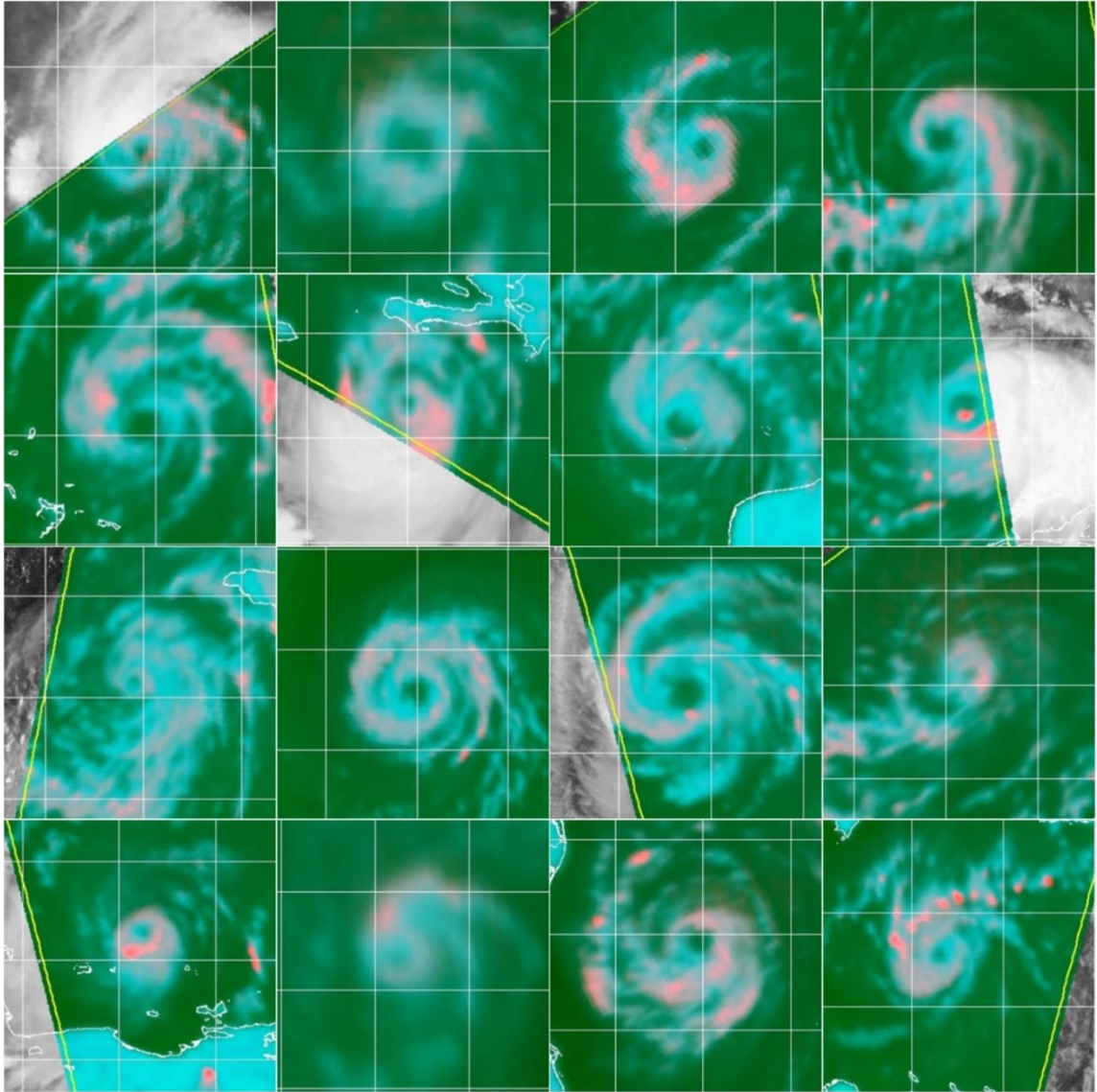


Figure 3.18 Convective rings indicating onset of a period of RI 2003-2019. Seen left to right, top to bottom: 2003 Fabian, 2003 Isabel, 2004 Danielle, 2004 Ivan, 2004 Jeanne, 2005 Dennis, 2005 Emily, 2005 Katrina, 2005 Wilma, 2006 Gordon, 2006 Helene, 2007 Dean, 2007 Felix, 2008 Bertha, 2008 Dolly, 2008 Gustav

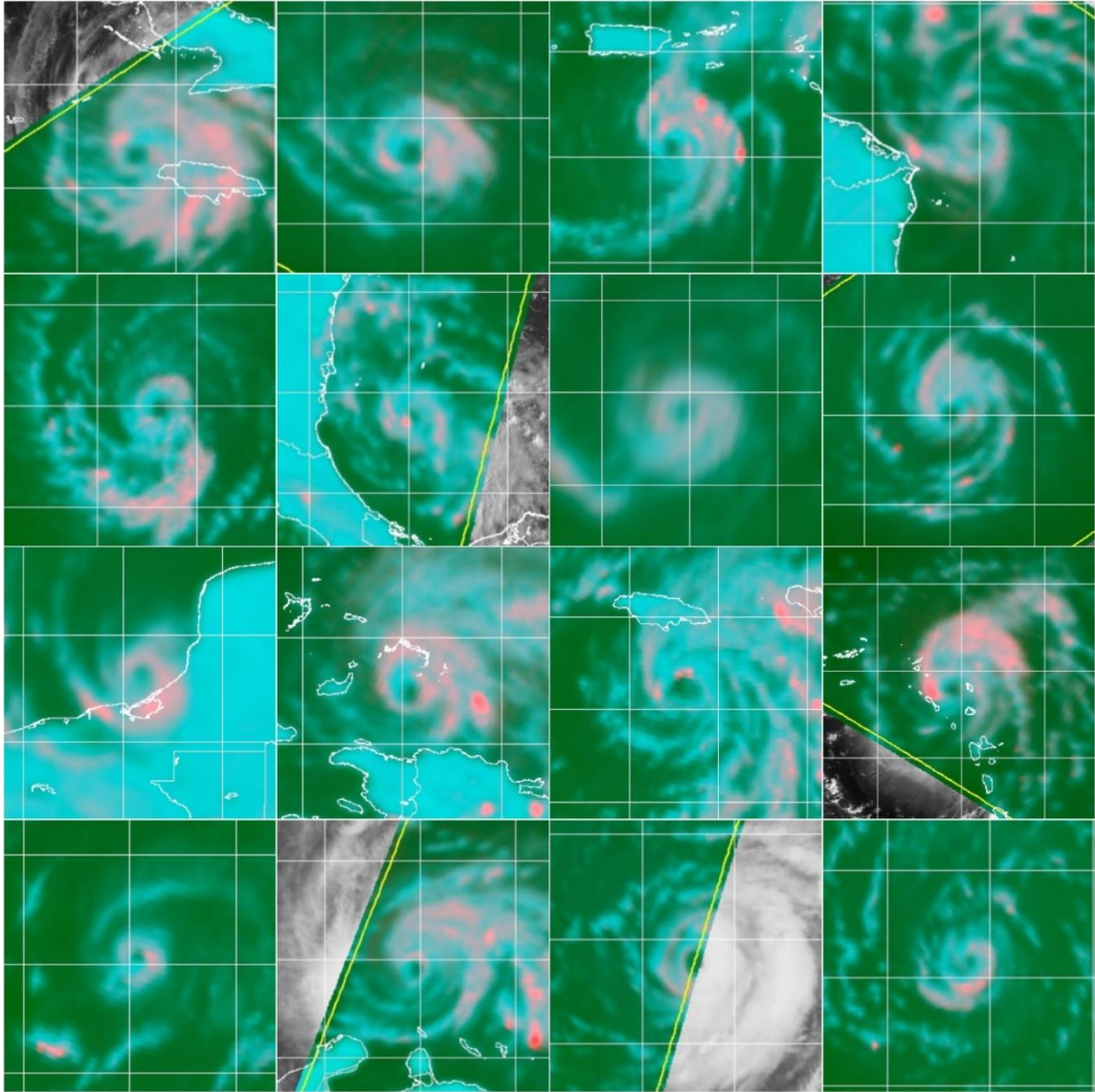


Figure 3.19 Convective rings indicating onset of a period of RI 2003-2019. Seen left to right, top to bottom: 2008 Gustav, 2008 Ike, 2008 Omar, 2008 Paloma, 2009 Fred, 2009 Ida, 2010 Igor, 2010 Julia, 2010 Karl, 2011 Irene, 2012 Sandy, 2014 Gonzalo, 2015 Danny, 2016 Matthew, 2016 Nicole, 2017 Irma

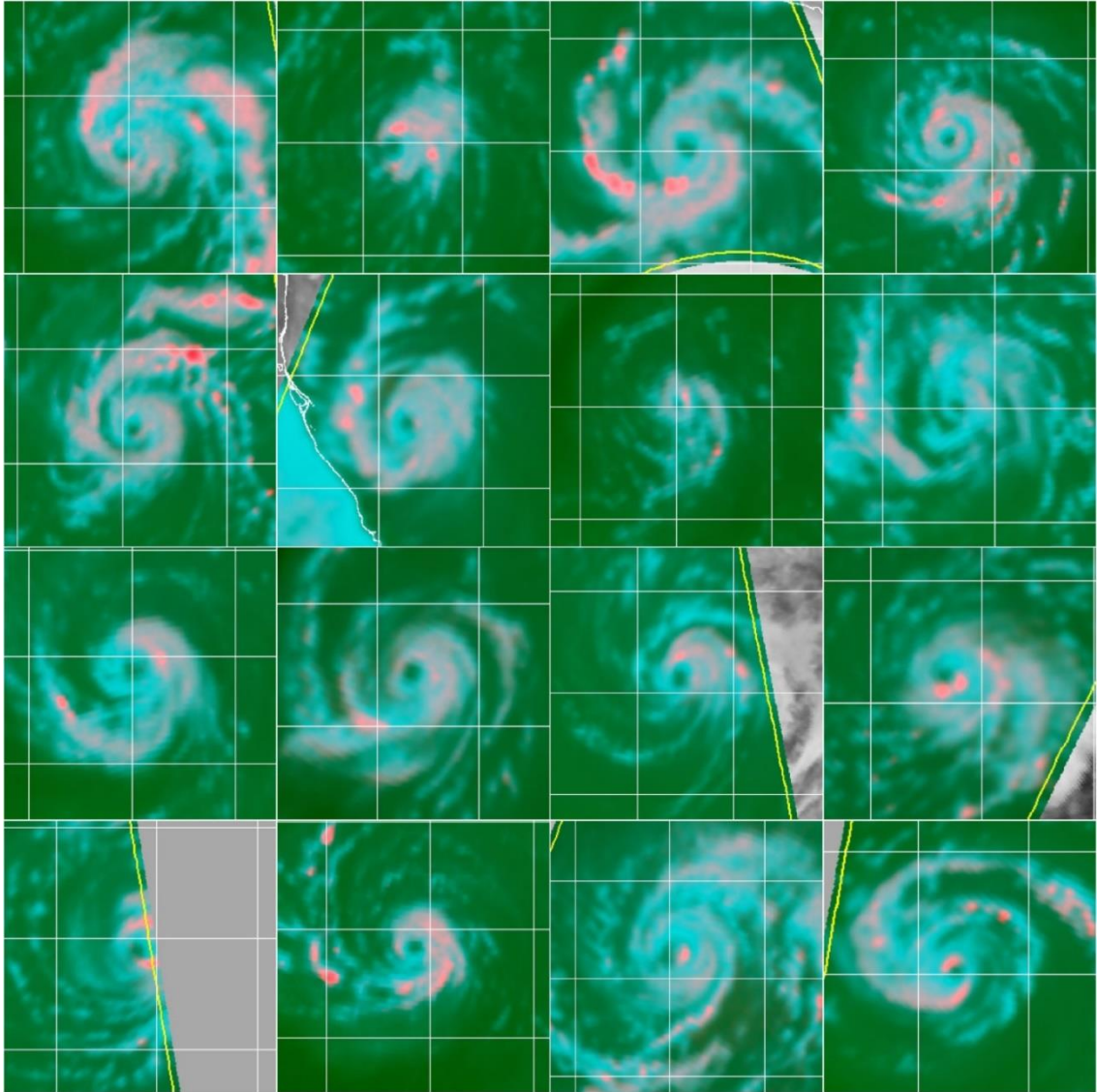


Figure 3.20 Convective rings indicating onset of a period of RI 2003-2019. Seen left to right, top to bottom: 2011 Ophelia, 2012 Michael, 2015 Patricia, 2016 Gaston, 2017 Harvey, 2017 Katia, 2017 Lee, 2017 Maria, 2017 Jose, 2018 Chris, 2018 Florence, 2018 Florence (2nd RI), 2018 Michael, 2019 Jerry, 2019 Lorenzo, 2019 Dorian

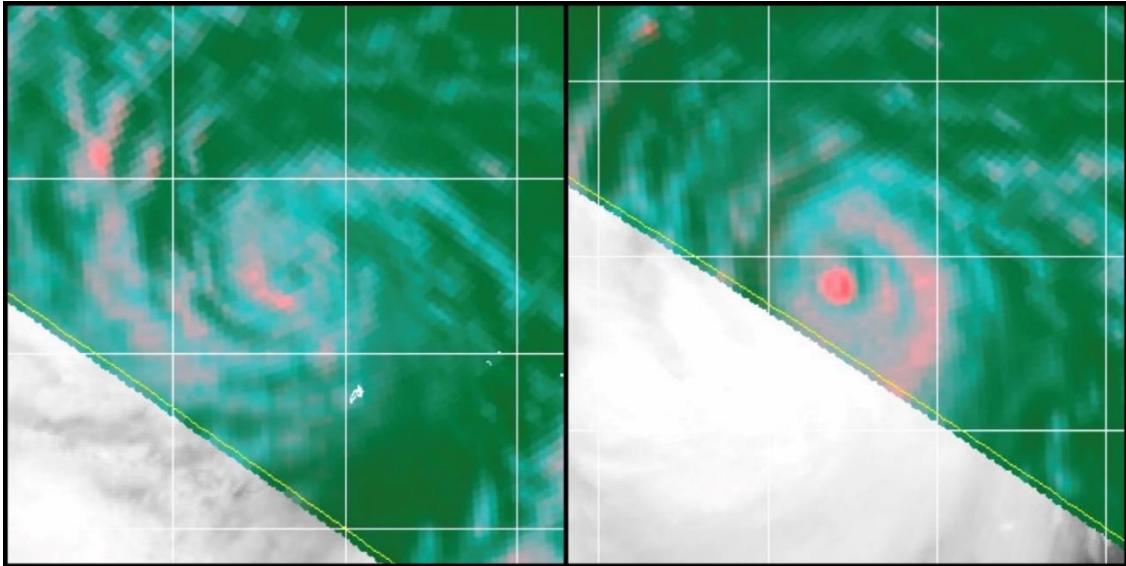


Figure 3.21 Rapid intensification of 2004 WPAC Dianmu. On the left the ring feature from a 2044Z 14 June TRMM pass when it was 65 kt, and on the right a 1948Z 15 June TRMM pass when it had rapidly intensified to 145 kt, gaining 80 kt in 24 hours.

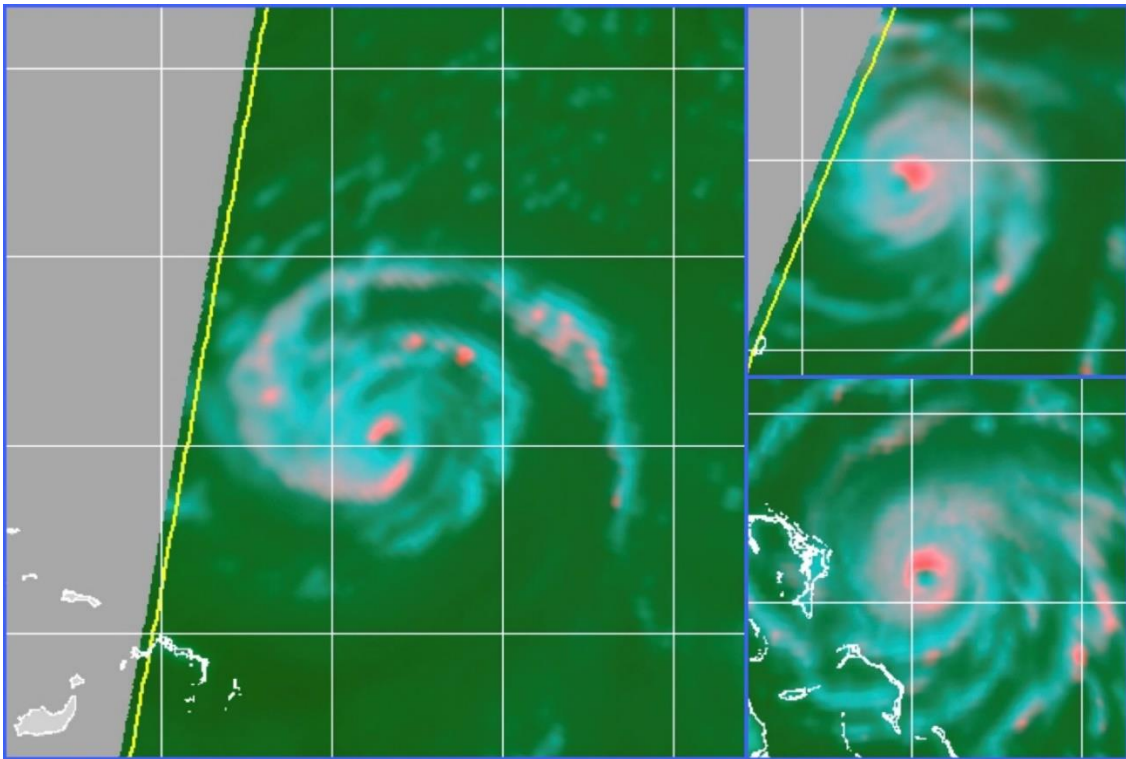


Figure 3.22 Rapid intensification of 2019 Hurricane Dorian. The ring feature (left, 1045Z 30 Aug WindSat pass at 95 kt), after RI (upper right, 1051Z 31 Aug TRMM pass at 125 kt, 30 kt in 24 hours) and 20 hours later (lower right, 0701Z 01 Sep AMSR-2 pass, continued intensification to 145 kt). It was at its maximum intensity of 160 kt when it made landfall over Great Abaco Island in the Bahamas, then on Grand Bahama at 155 kt, on 01/02 September.

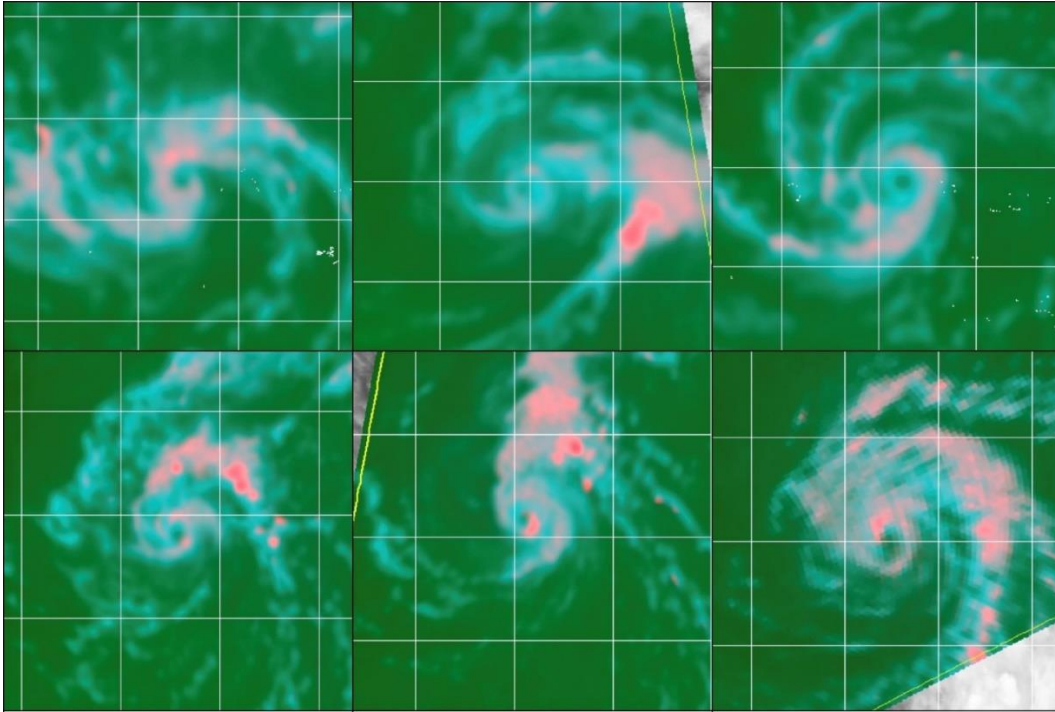


Figure 3.23 Six WPAC convective rings marking the onset of RI from the 2004 WPAC typhoon season. Seen left-to-right, top-to-bottom: a 0323Z 05 April AMSR-E pass of Sudal, 0226Z 05 August AMSR-E pass of Meranti, 0229Z 28 August AMSR-E pass of Songda, 0403Z 22 September AMSR-E pass of Meari, 1615Z 22 September pass of Meari, and 1524Z 25 July pass of Namtheun.

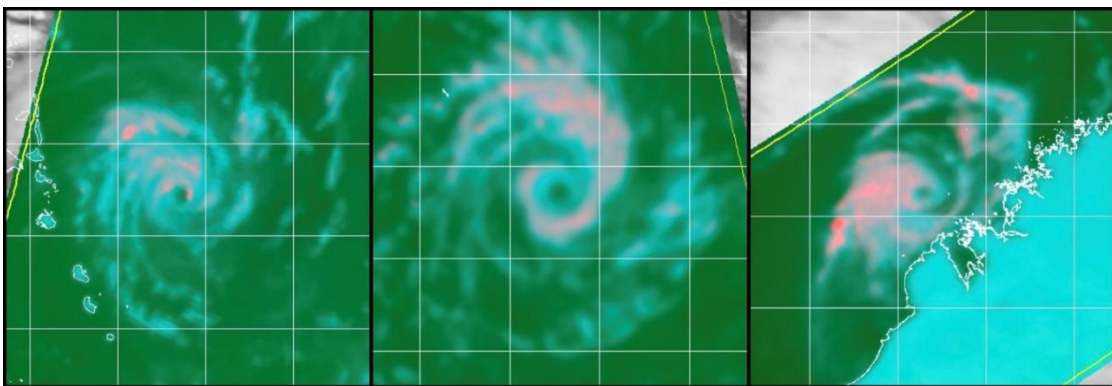


Figure 3.24 Three SHEM convective rings that marked the onset of RI. Left, an 1819Z 11 February WindSat pass of 2016 Winston at 55 kt. Winston intensified to 110 kt in 24 hr and damaged Fiji and Vanuatu. Center, an 0952Z 04 March AMSR-E pass of Cyclone Gafilo at 75 kt. Gafilo intensified to 125 kt in 24 hr and made landfall on Madagascar. Right, a 1536Z 27 March TRMM pass of Cyclone Glenda at 65 kt off the coast of Australia. Glenda intensified to 140 kt in 24 hr offshore before weakening and making landfall.

Year	Basin	Storm	Name	Sensor	Date	Time-Z	Notes
2008	ATL	02	Bertha	SSM/I SSMIS TRMM	2008/07/06 2008/07/06 2008/07/07	2159 2226 0031	55 to 100 kt incr 55 kt in 21 hr, from 07/0000Z to 07/2100Z
2008	ATL	02	Bertha	SSMIS TRMM	2008/07/09 2008/07/09	1214 1646	65 to 90 kt incr 25 kt in 12 hr, from 09/1200Z to 10/0000Z
2008	ATL	04	Dolly	TRMM	2008/07/22	1244	55 to 85 kt incr 30 kt in 24 hr, from 22/1200Z to 23/1200Z, 30 mb drop in 14 hr, 993 mb to 963 mb from 22/1200Z to 23/1400Z
2008	ATL	07	Gustav	WindSat SSM/I SSMIS	2008/08/25 2008/08/25 2008/08/25	1055 1122 1229	35 to 80 kt incr 45 kt in 24 hr, from 25/1200Z to 26/1200Z
2008	ATL	07	Gustav	WindSat TRMM	2008/08/29 2008/08/29	1124 1525	65 to 125 kt incr 60 kt in 24 hr, from 29/1800Z to 30/1800Z
2008	ATL	09	Ike	TRMM	2008/09/03	1905	75 to 125 kt incr 50 kt in 12 hr, from 03/1800Z to 04/0600Z
2008	ATL	15	Omar	AMSR-E WindSat	2008/10/15 2008/10/15	1742 2210	80 to 115 kt incr 35 kt in 12 hr, from 15/1800Z to 16/0600Z
2008	ATL	17	Paloma	WindSat TRMM	2008/11/06 2008/11/06	1116 1340	40 to 65 kt incr 25 kt in 12 hr, from 06/1200Z to 07/0000Z
2008	ATL	17	Paloma	TRMM AMSR-E SSMIS	2008/11/07 2008/11/07 2008/11/07	0432 0657 1109	65 to 110 kt incr 45 kt in 24 hr, from 07/0600Z to 08/0600Z, also 50 kt in 24 hr, from 07/1200Z to 08/1200Z
2009	ATL	07	Fred	AMSR-E WindSat	2009/09/08 2009/09/08	1514 1934	55 to 105 kt incr 50 kt in 24 hr, from 08/1200Z to 09/1200Z 45 kt in 18 hr, from 08/1800Z to 09/1200Z
2009	ATL	11	Ida	WindSat TRMM	2009/11/04 2009/11/04	1149 1202	35 to 70 kt incr 35 kt in 24 hr, from 04/1200Z to 05/1200Z
2010	ATL	11	Igor	TRMM AMSR-E WindSat	2010/09/12 2010/09/12 2010/09/12	0502 0503 0842	70 to 130 kt incr 60 kt in 24 hr, from 12/0600Z to 12/0600Z
2010	ATL	12	Julia	TRMM	2011/09/14	1807	70 to 120 kt incr 50 kt in 24 hr, from 14/1200Z to 15/1200Z
2010	ATL	13	Karl	AMSR-E	2011/09/16	0756	55 to 110 kt incr 55 kt in 24 hr, from 16/1200Z to 17/1200Z
2011	ATL	12	Katia	TRMM	2011/09/04	0852	90 to 120 kt incr 30 kt in 24 hr, from 05/0000Z to 06/0000Z
2011	ATL	16	Ophelia	AMSR-E	2011/09/29	1747	65 to 100 kt incr 35 kt in 24 hr, from 29/1800Z to 30/1800Z also 40 kt in 24 hr, from 55 kt on 29/1200Z to 95 kt on 30/1200Z,

Year	Basin	Storm	Name	Sensor	Date	Time-Z	Notes
							early ERC" on the 29 th while intensifying
2012	ATL	13	Michael	WindSat	2012/09/05	0900	50 to 100 kt incr 50 kt in 24 hr, from 05/1200Z to 06/1200Z
2012	ATL	18	Sandy	WindSat	2012/10/24	1116	60 to 100 kt incr 40 kt in 24 hr, from 24/0600Z to 25/0600Z
2014	ATL	08	Gonzalo	WindSat WindSat	2014/10/13 2014/10/14	2157 1028	80 to 115 kt incr 35 kt in 24 hr, from 14/0000Z to 15/0000Z
2015	ATL		Danny	AMSR-E	2015/08/20 2015/08/20	0425 0905	65 to 110 kt incr 45 kt in 24 hr, from 20/1200Z to 21/1200Z
2015	EPAC	20	Patricia	GPM	2015/10/22	0356	75 to 180 kt incr 105 kt in 24 hr, 22/0600Z to 23/0600Z
2016	ATL	07	Gaston	AMSR2	2016/08/28	1517	75 to 105 kt incr 30 kt in 24 hr, from 08/0000Z to 09/0000Z,
2016	ATL	14	Matthew	GMI	2016/09/30	0946	(90) 100 to 145 kt incr 45 kt in 12 hr, 55 kt in 15 hr, 75 kt from 30/0000Z to 01/0000Z, 70 to 145 w/partial eyewall from 29/2300Z to 30/0900Z
2016	ATL	15	Nicole	GMI SSMI	2016/10/12 2016/10/12	0632 0719	85 to 120 kt incr 35 kt in 24 hr, from 12/0600Z to 13/0600Z
2017	ATL	09	Harvey	AMSR2	2017/08/24	1828	80 to 115 kt incr 35 kt in 24 hr, from 25/0000Z to 26/0000Z
2017	ATL	11	Irma	AMSR2	2017/08/31	0349	55 to 100 kt incr 45 kt in 24 hr from 31/0000Z to 01/0000Z, had several subsequent ERC intensifications
2017	ATL	12	Jose	WindSat	2017/09/06	2105	70 to 105 kt incr 35 kt in 24 hr, from 07/0000Z to 01/0000Z, highest rate of intensification was 07/1200Z to 08/1200Z, 90 to 130 kt, 40 kt incr
2017	ATL	13	Katia	AMSR2 WindSat GMI AMSR2	2017/09/07 2017/09/08 2017/09/08 2017/09/08	1840 0012 0731 0752	70 to 90 kt incr 20 kt in 24 hr, proximity to land could have been a factor best ring did not appear until 08/0800Z
2017	ATL	14	Lee	WindSat	2017/09/23	2102	50 to 85 kt incr 35 kt in 24 hr, from 24/0000Z to 25/0000Z NHC 24/0000Z forecast noted cyan ring and forecast 20 kt incr in 24 hr.
2017	ATL	15	Maria	WindSat	2017/09/16	2123	45 to 75 kt incr 30 kt in 24 hr, from 17/0000Z to 18/0000Z

Year	Basin	Storm	Name	Sensor	Date	Time-Z	Notes
							even though eye opened during this time. *
2018	ATL	03	Chris	WindSat	2018/07/10	1155	65 to 90 kt incr 25 kt in 12 hr, from 10/12Z to 11/00Z, 65 to 90 kt
2018	ATL	06	Florence	AMSR2 WindSat	2018/09/04 2018/09/04	1420 2110	75 to 115 kt incr 40 kt in 24 hr, from 04/18Z to 05/18Z, 75 to 115 kt, followed by rapid weakening
2018	ATL	06	Florence	GMI WindSat	2018/09/09 2018/09/09	1811 2121	70 to 120 kt incr 50 kt in 24 hr, from 09/18Z to 10/18Z, 70 to 120 kt
2018	ATL	14	Michael	GMI AMSR2	2018/10/09 2018/10/09	1056 1930	90 to 125 kt incr 35 kt in 24 hr from 10/09 12Z to 10/10 12Z --- 100 to 140 kt incr 40 kt in 23.5 hr from 10/09 18Z to 10/10 1730Z (landfall) **
2019	ATL	05	Dorian	WindSat	2019/08/30	1045	95 to 125 kt incr 30 kt in 12 hr, from 30/12Z to 31/12Z
2019	ATL	10	Jerry	AMSR2	2019/09/19	0513Z	60 to 90 kt incr 30 kt in 18 hr, from 19/06Z to 20/00Z
2019	ATL	13	Lorenzo	GMI	2019/09/26	0051	85 to 110 kt incr 25 kt in 9 hr, from 26/00Z to 26/09Z, 85 to 110 kt

Table 3.1. 37color convective rings for selected rapid intensification cases 2008-2019.

** This was not Maria's most impressive intensification - a second period of intensification occurred immediately after: 75 kt to 145 kt - 75 kt from 18/0000Z to 19/0000Z. Recon showed eye diameter decreased significantly (by 20 n mi) during this subsequent intensification, even eye though open until 18/16Z, Maria gained 65 kt in 18 hr - from 80 kt at 18/06Z to 145 kt at 19/00Z. Recon: 17/2049Z – C28 OPEN S, 18/1116Z – C12 OPEN SW, 18/1159Z – C10 OPEN SW, 18/1443Z – C10 OPEN SW, 18/1635Z – C8 CLOSED, 18/2330Z – C8 CLOSED.*

*** First RI recon reported no eye at 10/09 1221Z and C32 OPEN W-SW at 10/09 1313Z, RI initiated when cyan ring was not closed. Second RI, almost-closed ring in PMW imagery, recon reported C20 OPEN SW S, RI initiated when cyan ring was not closed, but had estimated 90% azimuthal coverage*

3.3 Use of the 37color Ring as an Indicator of the Onset of RI at the NHC

When passive microwave imagery became widely available to tropical cyclone forecasters, when it was observed that a ring of ice around the developing center suggesting a developing eyewall of deep convection was present, but an eye was not apparent in geostationary satellite imagery (visible, infrared, and water vapor), forecasters would refer to this as a "microwave eye." This is because an eye must clear out enough to show an indication on geostationary imagery, whether it is a clear area over the warm center or even what is referred to as a "dimple" or "hint of an eye." Thus the matured eye is technically what can be referred to as an eye and it was necessary to preface the convective ring identified only on the PMW imagery (usually 85H imagery) as a "microwave" eye to distinguish it from what was considered an eye.

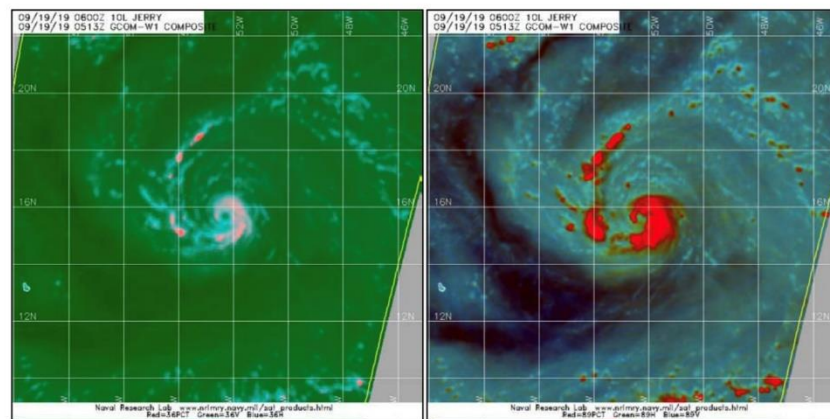
With the discovery of an indicator of RI as a similar ring but seen only on the 37color imagery, forecasters began observing this shallow convective pattern as well. Since there was no acronym that had been developed for this pattern, the appearance of the ring on microwave imagery was also referred to in Tropical Cyclone Reports (TCRs) and Tropical Cyclone Discussions (TCDs) also as a "microwave eye," as well as a variety of other names, including "convective ring," "mid-level microwave eye," "cyan ring around the eye," "ring of shallow to moderate convection surrounds the center," "low-level eye feature," "low-level eye-like feature," "well-defined inner core," "inner-core...in recent microwave imagery," "eye feature...at the mid-levels" "mid-level eye," "closed low-level ring of convection," "low-level ring," "eye that appeared in microwave imagery" and "a closed ring of shallow convection around the center."

Since 2009 NHC forecasters observe PMW for the formation of the ring when RI is likely, it is mentioned in the forecast discussions (here limited to the Atlantic basin), and the 2019 Tropical Cyclone Report for Hurricane Jerry (Brown, 2006) featured the

HURRICANE JERRY (AL102019)

17–24 September 2019

Daniel P. Brown
National Hurricane Center
11 December 2019



37-GHZ (LEFT) AND 89-GHZ (RIGHT) MICROWAVE IMAGES OF JERRY WHILE IT WAS RAPIDLY STRENGTHENING EAST OF THE LEEWARD ISLANDS ON 19 SEPTEMBER. IMAGES COURTESY OF THE U.S. NAVAL RESEARCH LABORATORY.

Jerry was a category 2 hurricane (on the Saffir-Simpson Hurricane Wind Scale) that developed over the tropical Atlantic Ocean east of the Lesser Antilles. Jerry passed

Figure 3.25 TCR cover page for 2019 Jerry showing the RI ring. (Brown 2019)

37color and 85color images of the ring as the cover image (Figure 3.25), noting "images of Jerry while it was rapidly strengthening."

Other Atlantic basin TCRs that mention the 37color RI ring are: Hurricane Lee 2017 (Blake, 2018), "A symmetric area of deep convection then formed over the center of Lee, and microwave data showed that a mid-level eye was present. Lee rapidly intensified...";

Hurricane Nicole 2016 (Kimberlain and Latto, 2017), "a microwave pass from around 1200 UTC that day showed a closed low-level ring of convection, typically a harbinger of rapid intensification. Indeed, Nicole rapidly strengthened into a major hurricane about 24h later."; Hurricane Gaston 2016 (Brown 2017), "Gaston's inner-core structure increased in organization early the next day with a low-level ring and mid-level eye feature noted in microwave imagery (Fig. 4)" (reproduced in Figure 3.26); Hurricane Danny 2015 (Stewart 2016), "...the cyclone rapidly intensified into a 110-kt major hurricane...The 45-kt rapid strengthening phase coincided with the development of a well-defined 5-10 n mi diameter eye that appeared in microwave satellite imagery...";

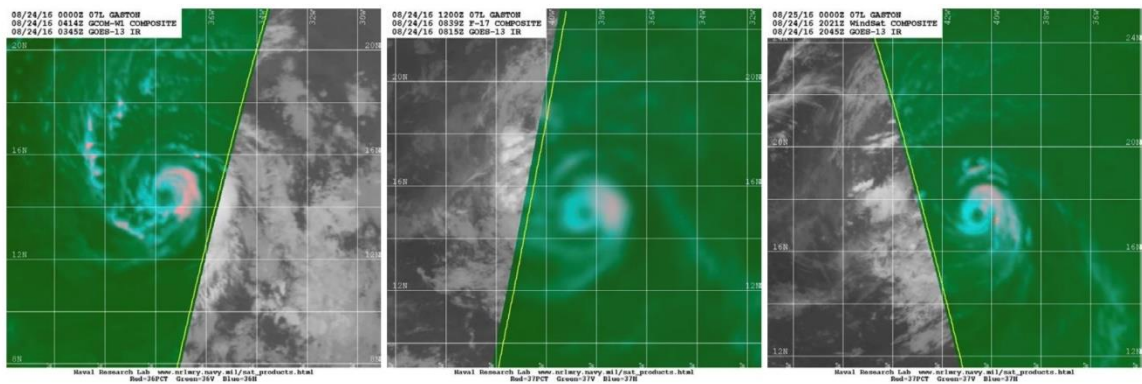


Figure 4. Series of 37-GHz color composite microwave satellite images of Gaston between 0414 UTC and 2021 UTC 24 August 2016. Note the presence of a well-defined low-level cloud ring. Gaston is estimated to have first reached hurricane strength during this time. Images courtesy of the Naval Research Laboratory.

Figure 3.26 2016 Gaston RI rings from Tropical Cyclone Report. (Brown 2017)

Hurricane Michael 2012 (Kimberlain and Zelinsky 2012), "...microwave data confirmed the existence of a closed ring of shallow convection around the center...a period of rapid intensification...began..."; and Hurricane Fred 2009 (Brennan 2009), "Subsequent microwave imagery confirmed the formation of an eye, and the hurricane intensified rapidly...The intensity of Fred increased 55 kt in the 24-hr period ending at this time, including a 35-kt increase in 12 h."

In addition, a series of images of the RI ring identified by NHC forecasters in the Tropical Forecast Discussions (TCDs) of the synoptic-time Tropical Cyclone Advisory packages for the Atlantic basin are shown in Figures 3.27 – 3.38.

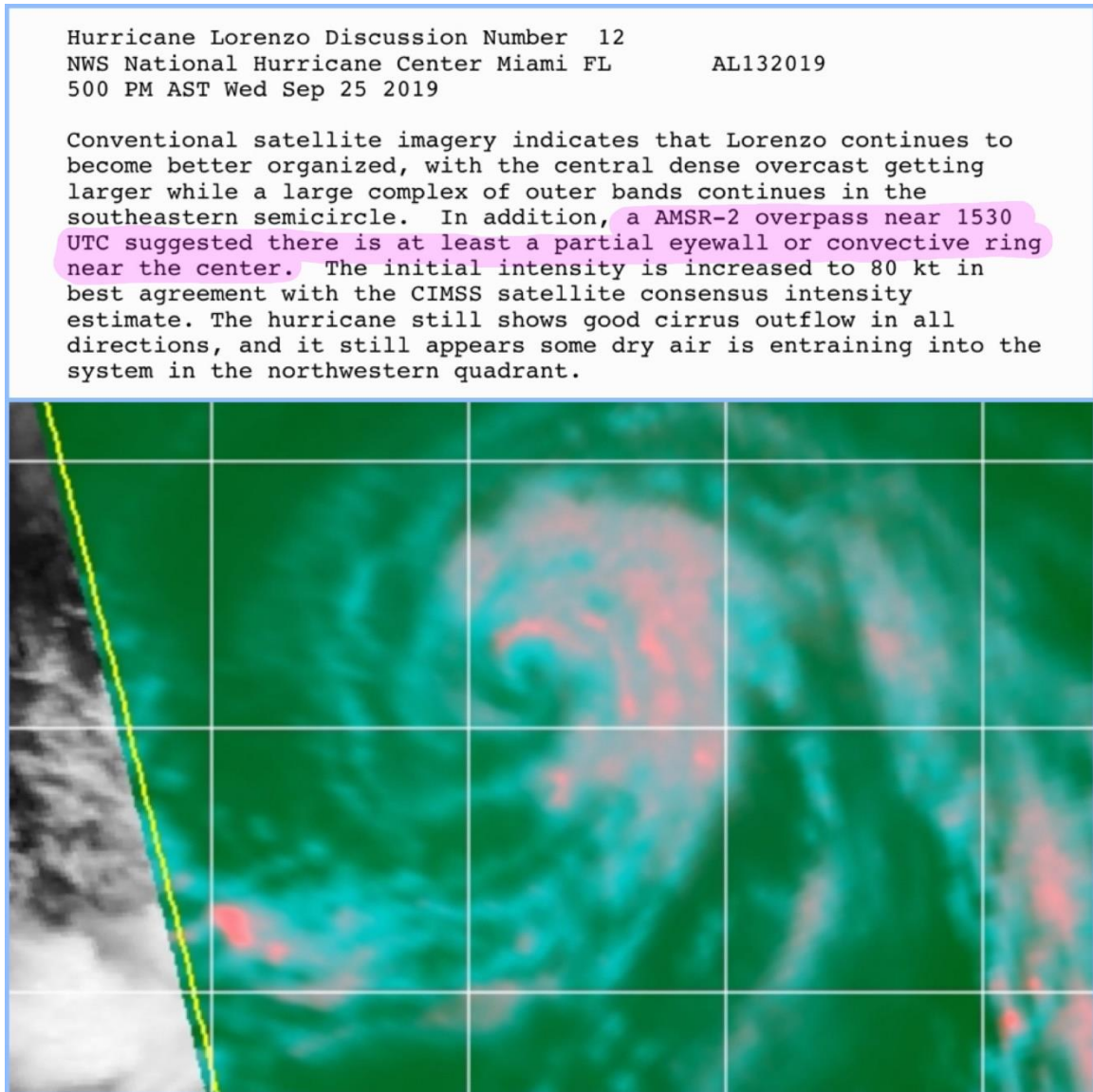


Figure 3.27 Identification of the RI ring in an NHC Tropical Cyclone Discussion (NHC archives).

Hurricane Lorenzo Discussion Number 14
NWS National Hurricane Center Miami FL
500 AM AST Thu Sep 26 2019

AL132019

Lorenzo's satellite appearance continues to steadily improve. The cyclone has a large central dense overcast, with outflow established in all quadrants. The hurricane has at times shown signs of a developing eye, however, it has been mostly obscured during the last few hours by expanding cloud tops associated with central (and likely eyewall) convection. Although the eye is not yet apparent in geostationary imagery, a 0618 UTC SSMIS overpass showed that Lorenzo has developed a well-defined mid-level eye. TAFB and SAB Dvorak classifications both support an intensity of 90 kt but objective estimates are lower. The intensity of Lorenzo is therefore held at 85 kt as a compromise of the higher subjective and lower objective assessments, but this could be a little conservative.

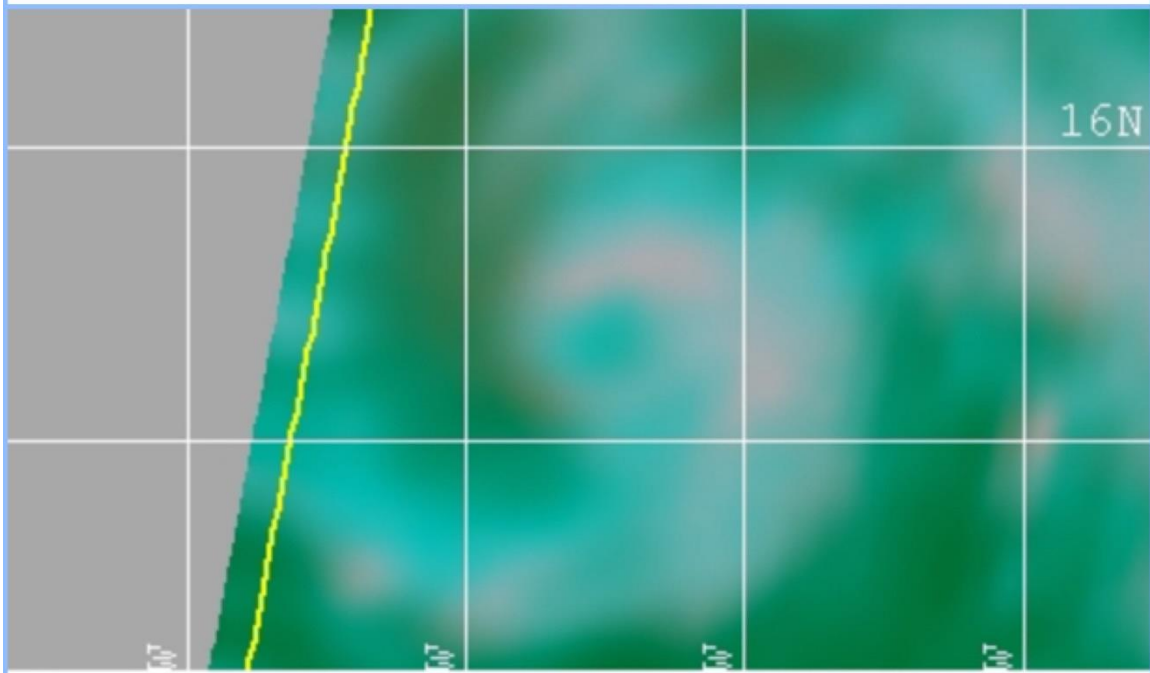


Figure 3.28 Identification of the RI ring in an NHC Tropical Cyclone Discussion (NHC archives).

Hurricane Florence Discussion Number 21
NWS National Hurricane Center Miami FL AL062018
1100 AM AST Tue Sep 04 2018

Florence's structure has gradually increased in organization, with SSMIS passes from a few hours ago revealing the development of a mid-level microwave eye. Dvorak estimates have responded in kind--TAFB is up to T4.0, SAB is at T4.5, and the objective ADT is in between at T4.4. Since there still appears to be moderate southwesterly shear inducing some tilt to the cyclone and disrupting the infrared satellite pattern, the initial intensity is raised conservatively to 65 kt, making Florence a hurricane.

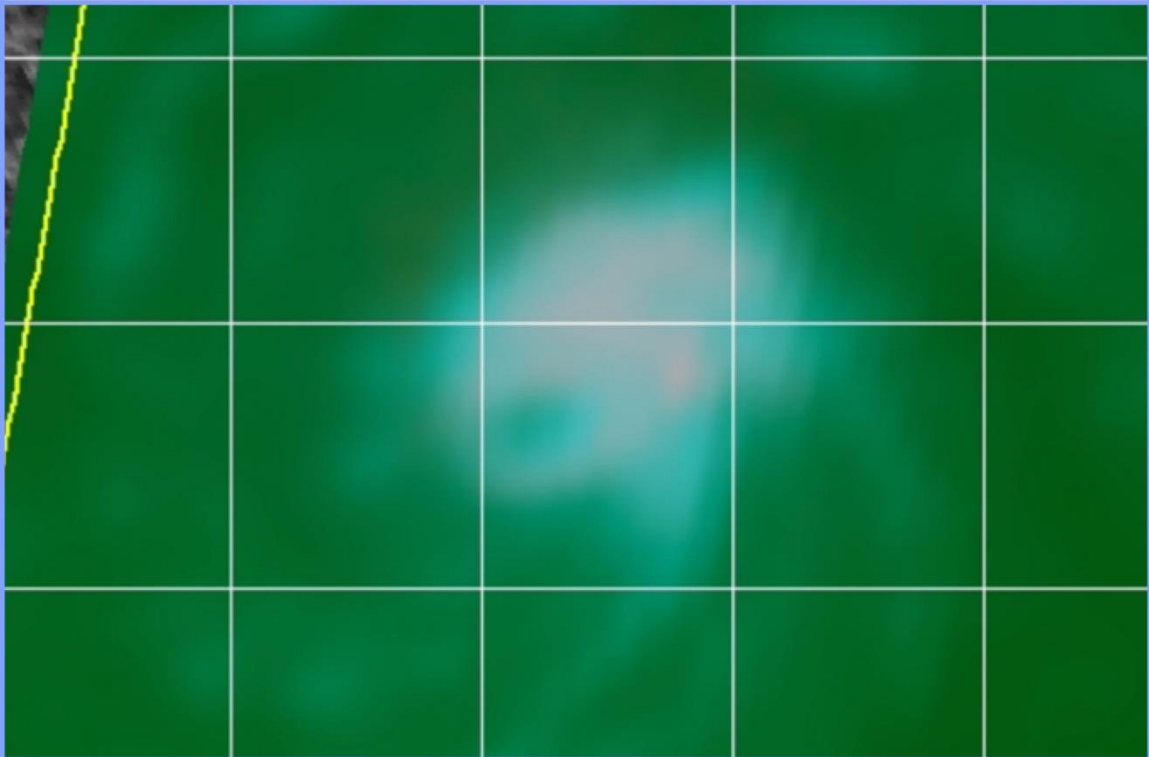


Figure 3.29 Identification of the RI ring in an NHC Tropical Cyclone Discussion (NHC archives).

HURRICANE PATRICIA DISCUSSION NUMBER 8
NWS NATIONAL HURRICANE CENTER MIAMI FL EP202015
400 AM CDT THU OCT 22 2015

The environment appears to be very conducive for strengthening for the next 24 hours or so, with some increase in south-southwesterly shear and some mid-tropospheric drying later on Friday. An earlier 37 GHz GPM image showed a cyan ring around the eye, which often presages rapid intensification. Given that, and the currently favorable atmospheric and oceanic conditions, rapid strengthening (30 kt over 24 h) is forecast through tonight followed by a slower pace of intensification up to landfall. This is in good agreement with the latest DSHIPS prediction.

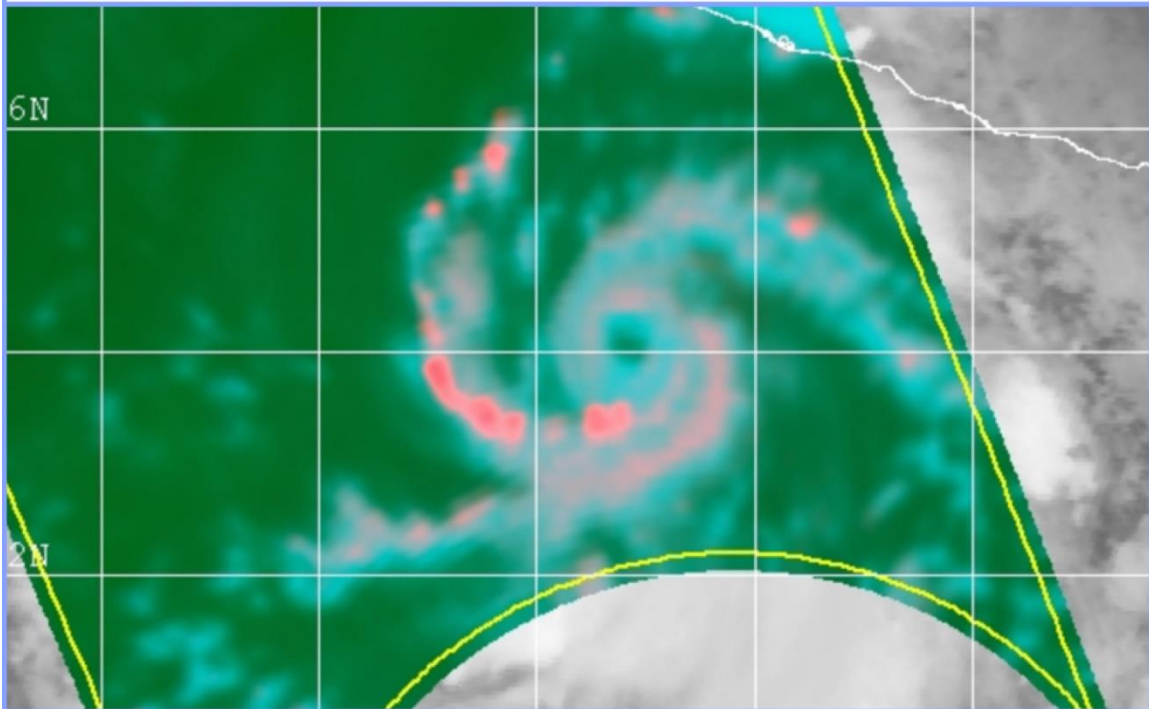


Figure 3.30 Identification of the RI ring in an NHC Tropical Cyclone Discussion (NHC archives).

Tropical Storm Lee Discussion Number 23
NWS National Hurricane Center Miami FL
1100 PM AST Sat Sep 23 2017

AL142017

A WindSat overpass from 2102 UTC indicated that Lee has developed a coherent inner-core. In fact, the 37 GHz RGB composite from the WindSat overpass indicated that a ring of shallow to moderate convection surrounds the center of Lee, often a signature of a rapidly intensifying cyclone. The NHC intensity forecast has therefore been significantly increased for the first 48 hours of the forecast, but falls short of explicitly forecasting rapid intensification. Beyond that time, most of the intensity guidance is higher than before, and shows Lee maintaining hurricane

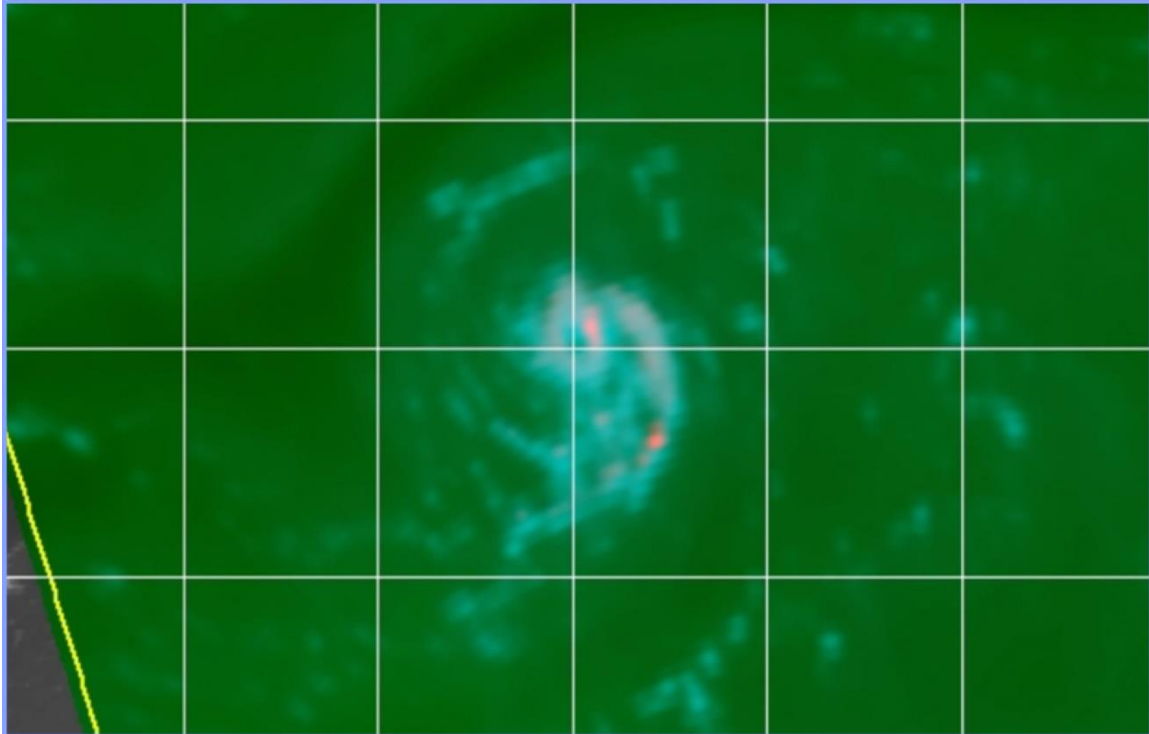


Figure 3.31 Identification of the RI ring in an NHC Tropical Cyclone Discussion (NHC archives).

Tropical Storm Irma Discussion Number 3
NWS National Hurricane Center Miami FL AL112017
1100 PM AST Wed Aug 30 2017

Irma continues to become better organized, with the development of a small CDO feature and increased banding near the center. An earlier high-resolution Windsat microwave overpass showed that Irma has a tight inner core and a low-level eye-like feature was present. A Dvorak classification of T3.5 from TAFB is the basis for the initial intensity of 55 kt. Irma is expected to steadily strengthen during the next couple of days while it moves through a low-shear and moist environment, and remains over warm sea surface temperatures. After that time, slightly cooler SSTs and lower mid-level moisture may temper the intensification process.

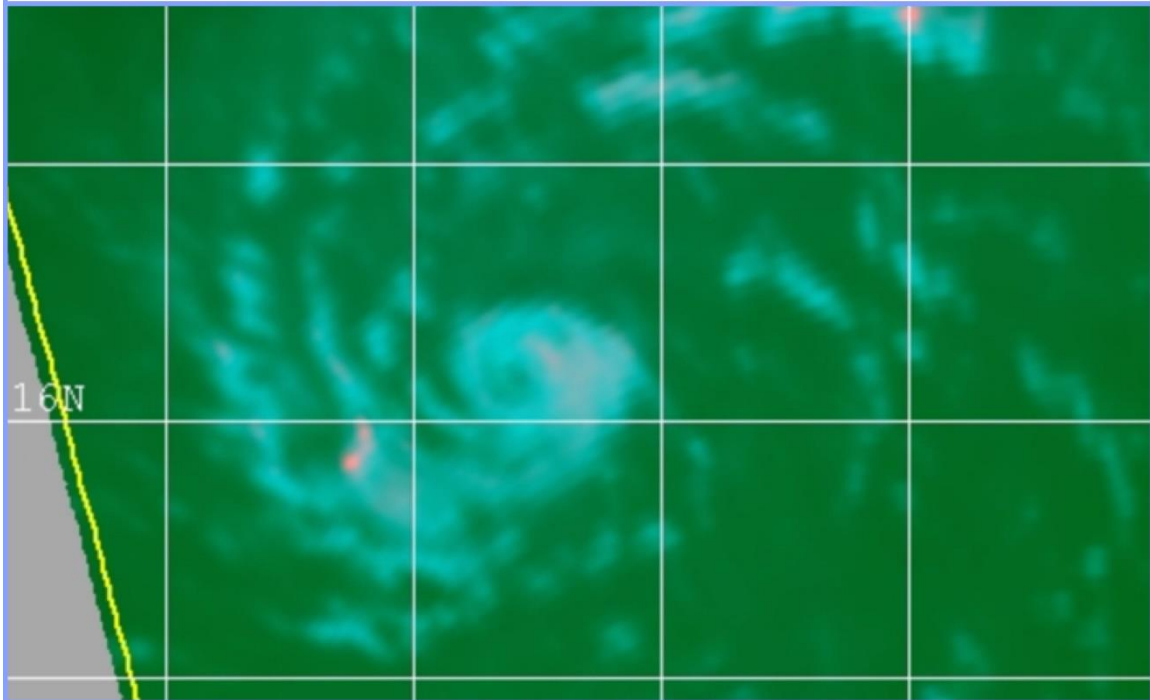


Figure 3.32 Identification of the RI ring in an NHC Tropical Cyclone Discussion (NHC archives).

TROPICAL STORM DANNY DISCUSSION NUMBER 7
NWS NATIONAL HURRICANE CENTER MIAMI FL AL042015
1100 PM AST WED AUG 19 2015

Earlier Windsat data shows that Danny has a well-defined inner core, and this, combined with a light-vertical wind shear environment, should allow strengthening for the next three days or so. However, experimental Saharan Air Layer (SAL) Meteosat imagery continues to show abundant dry air not far from the storm in the northern semicircle. Entrainment of this air is expected to limit intensification, and this is reflected by a downward trend in the intensity guidance. After 72 hours, the cyclone is expected to encounter even drier air and southwesterly shear, which should cause weakening. The new intensity forecast is identical to the previous forecast through 48 hours and then shows slightly lower intensities

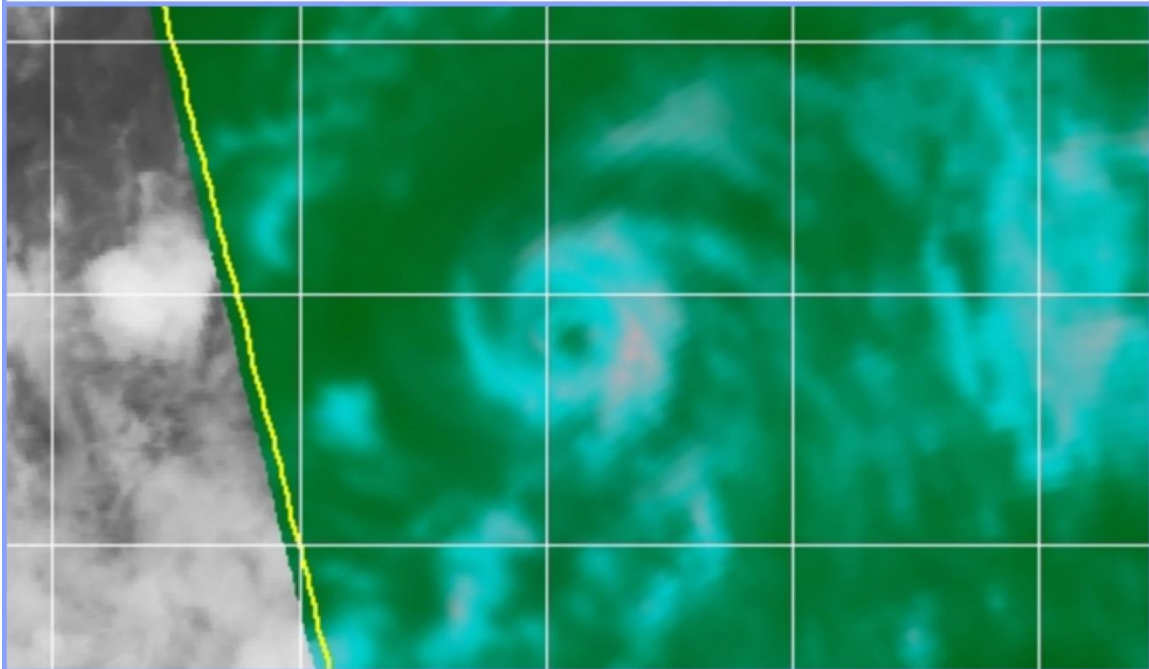


Figure 3.33 Identification of the RI ring in an NHC Tropical Cyclone Discussion (NHC archives).

TROPICAL STORM DANNY DISCUSSION NUMBER 8
NWS NATIONAL HURRICANE CENTER MIAMI FL AL042015
500 AM AST THU AUG 20 2015

The cloud pattern resembles a tropical cyclone much more than 12 hours ago. An irregular Central Dense Overcast(CDO) has formed, and the center continues to be remarkably well depicted in microwave images. In fact, it has a much better structure than earlier. The outflow remains fair. Dvorak numbers suggest that the winds are still 45 kt. Danny has the opportunity to strengthen a little during the next 2 to 3 days while embedded within very light shear. Models in general, however, no longer intensify the cyclone as much as they did in earlier runs and, in fact, the GFS and ECMWF weaken Danny to a tropical wave in the eastern Caribbean Sea. The NHC forecast calls for some intensification for the next 3 days, and calls for slight weakening as Danny encounters high shear and dry air in the eastern

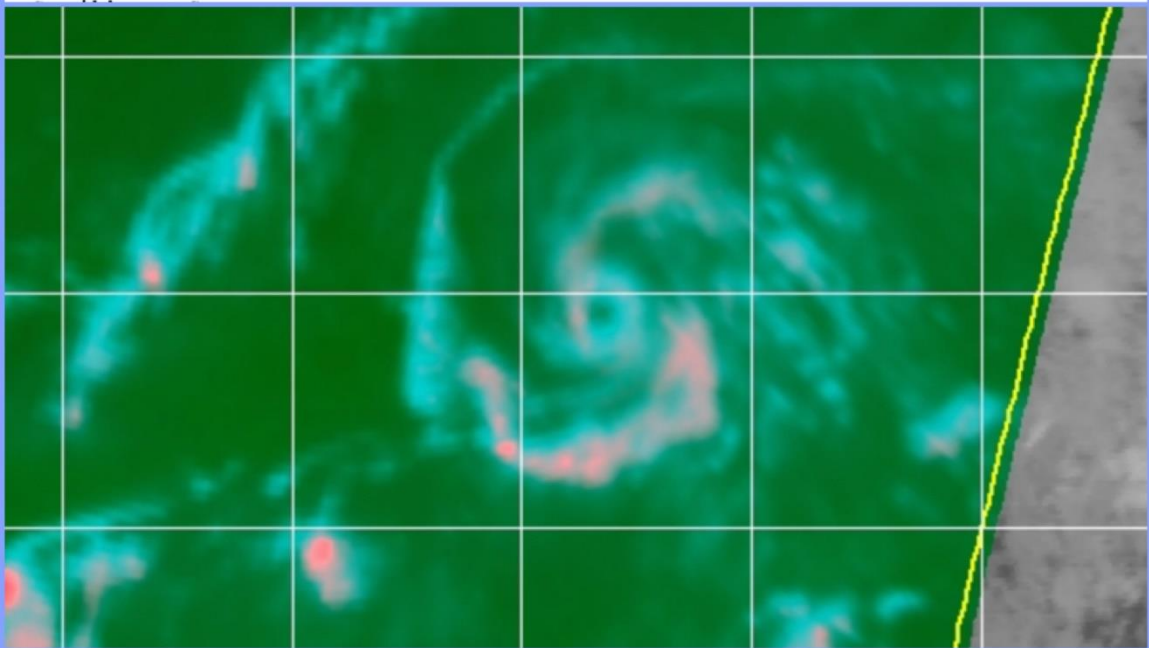


Figure 3.34 Identification of the RI ring in an NHC Tropical Cyclone Discussion (NHC archives).

HURRICANE GONZALO DISCUSSION NUMBER 7
NWS NATIONAL HURRICANE CENTER MIAMI FL
1100 PM AST MON OCT 13 2014

AL082014

Gonzalo appears to be poised to intensify, perhaps rapidly, in the next day or so. The inner-core features are quite distinct in recent microwave imagery and a warm spot has recently developed in infrared imagery with a more symmetric cloud pattern. Given these trends and the overall favorable environment, the intensity forecast has been adjusted upward and is close to the the SHIPS model on the high end of the intensity guidance through the first 48 hours, showing Gonzalo becoming a major hurricane in about 36 hours. As Gonzalo gains latitude later in the period, southwesterly shear ahead of a mid-latitude trough and cooler SSTs should result in gradual weakening.

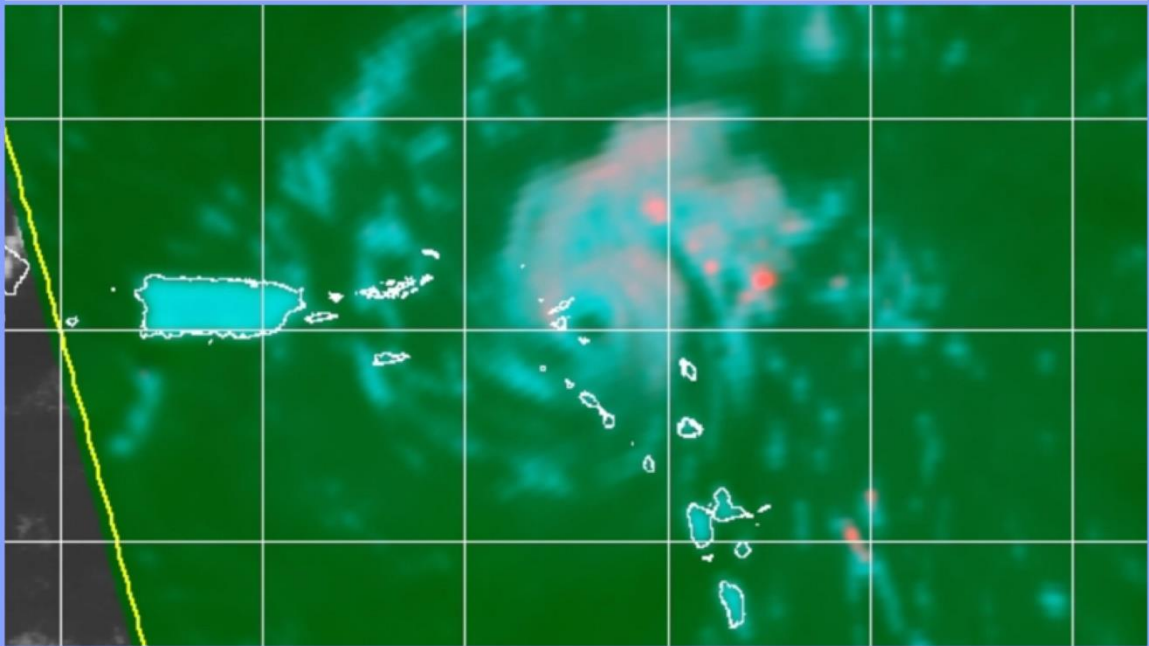


Figure 3.35 Identification of the RI ring in an NHC Tropical Cyclone Discussion (NHC archives).

HURRICANE OPHELIA DISCUSSION NUMBER 29
NWS NATIONAL HURRICANE CENTER MIAMI FL
500 PM AST THU SEP 29 2011

AL162011

SATELLITE IMAGES AND MICROWAVE DATA INDICATE THAT THE CLOUD PATTERN HAS CONTINUED TO ACQUIRE ORGANIZATION. THERE IS A CYCLONICALLY CURVED CONVECTIVE BAND WRAPPING AROUND THE CENTER AND THE UPPER-LEVEL OUTFLOW HAS EXPANDED IN ALL QUADRANTS. THERE HAS BEEN AN EYE FEATURE INTERMITTENTLY APPEARING ON VISIBLE IMAGES...BUT THERE IS DEFINITELY A DISTINCT ONE AT THE MID-LEVELS ON EARLIER MICROWAVE DATA. T-NUMBERS FROM TAFB AND SAB HAVE INCREASED TO 4.0 ON THE DVORAK SCALE AND ON THIS BASIS...OPHELIA HAS BEEN UPGRADED TO HURRICANE STATUS...THE FOURTH OF THE 2011 SEASON.

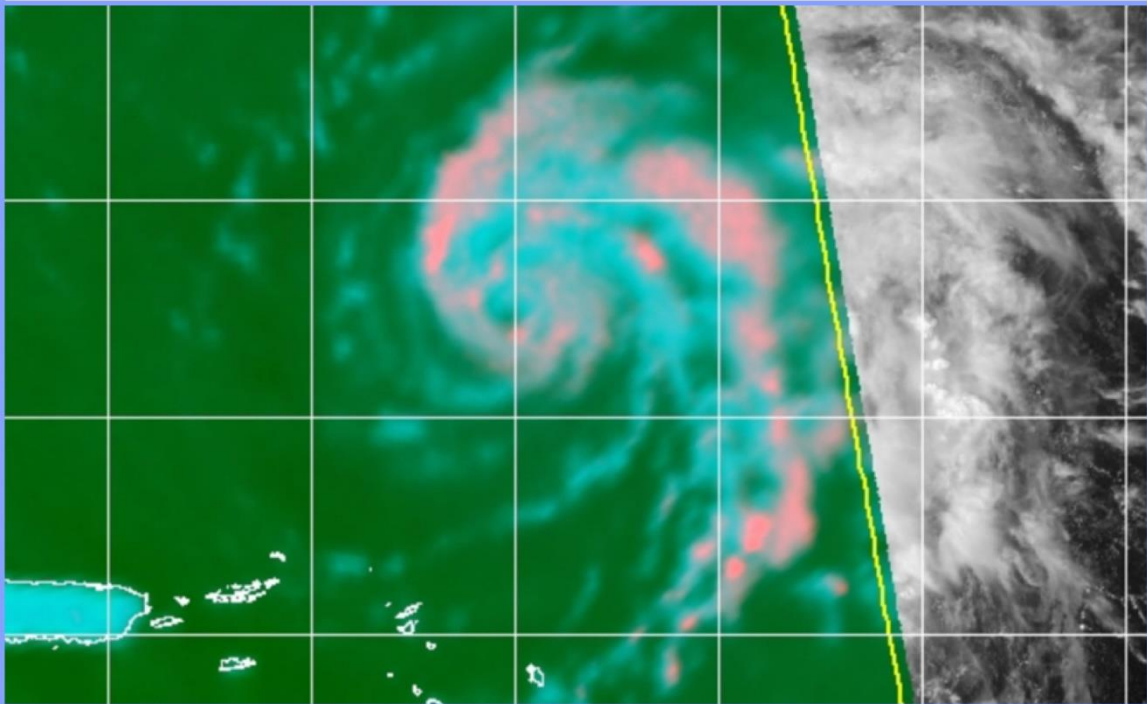


Figure 3.36 Identification of the RI ring in an NHC Tropical Cyclone Discussion (NHC archives).

TTAA00 KNHC DDHHMM
HURRICANE IGOR DISCUSSION NUMBER 15
NWS TPC/NATIONAL HURRICANE CENTER MIAMI FL AL112010
1100 PM AST SAT SEP 11 2010

THE CLOUD PATTERN ASSOCIATED WITH IGOR HAS INCREASED IN ORGANIZATION DURING THE PAST SEVERAL HOURS. A TIGHTLY-COILED BAND...WITH CLOUD TOP TEMPERATURES TO -85°C ...WRAPS AROUND THE EASTERN SEMICIRCLE INTO A DEVELOPING CENTRAL DENSE OVERCAST. AN EYE FEATURE HAS ALSO BEEN BRIEFLY INTERMITTENT IN CONVENTIONAL SATELLITE IMAGERY...AND A NUMBER OF MICROWAVE PASSES SEVERAL HOURS AGO REVEALED A DISTINCT CONVECTIVE RING SURROUNDING THE CENTER. SUBJECTIVE DVORAK T-NUMBERS AT 0000 UTC WERE A CONSENSUS 4.0 FROM BOTH SATELLITE AGENCIES...AND 3-HOURLY AVERAGED ADT VALUES FROM UW-CIMSS ARE 4.3. THE INITIAL

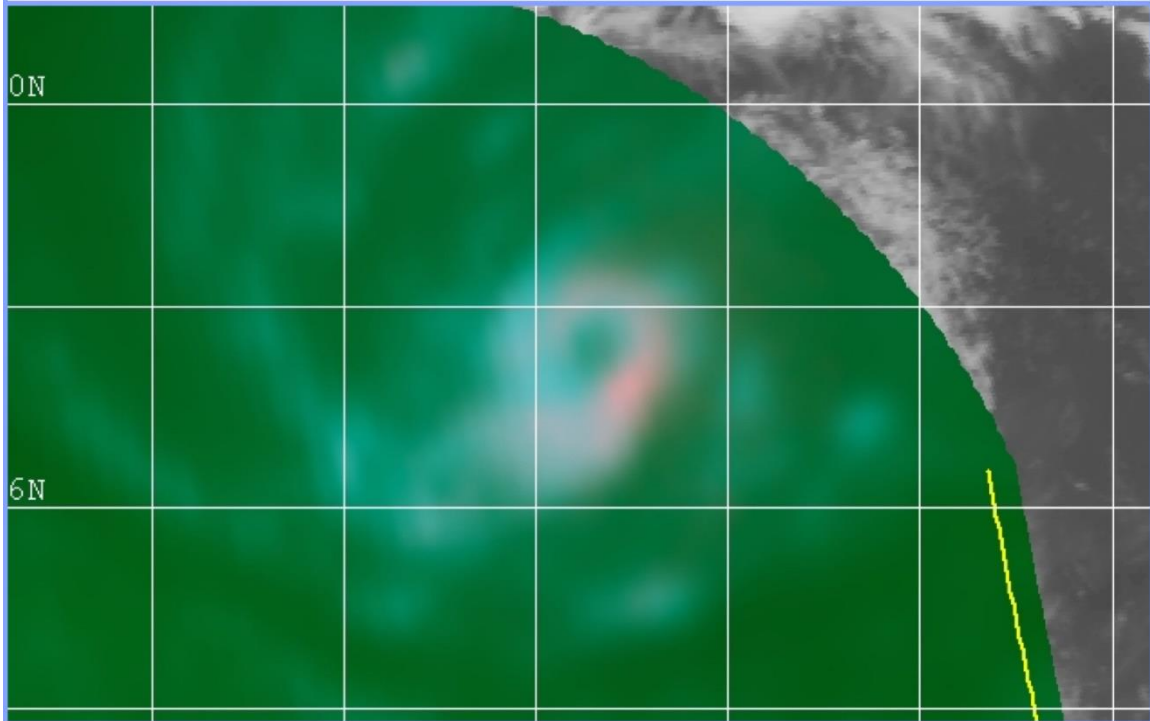


Figure 3.37 Identification of the RI ring in an NHC Tropical Cyclone Discussion (NHC archives).

TTAA00 KNHC DDHHMM
TROPICAL STORM FRED DISCUSSION NUMBER 5
NWS TPC/NATIONAL HURRICANE CENTER MIAMI FL AL072009
500 PM AST TUE SEP 08 2009

HIGH-RESOLUTION METEOSAT VISIBLE IMAGERY SHOW THAT FRED REMAINS A WELL-ORGANIZED TROPICAL CYCLONE WITH PROMINENT BANDING AND EXPANDING OUTFLOW IN ALL QUADRANTS. THE BIGGEST CHANGE DURING THE PAST SEVERAL HOURS IS THAT A CENTRAL DENSE OVERCAST FEATURE HAS FORMED NEAR THE CENTER. A 1514Z AMSR-E MICROWAVE PASS ALSO SHOWS THE BEGINNING STAGES OF AN EYEWALL. ALTHOUGH DVORAK INTENSITY ESTIMATES ARE UNCHANGED...THE IMPROVED STRUCTURE ON MICROWAVE IMAGES SUGGESTS SOME STRENGTHENING HAS OCCURRED AND THE INITIAL INTENSITY IS RAISED TO 60 KT.

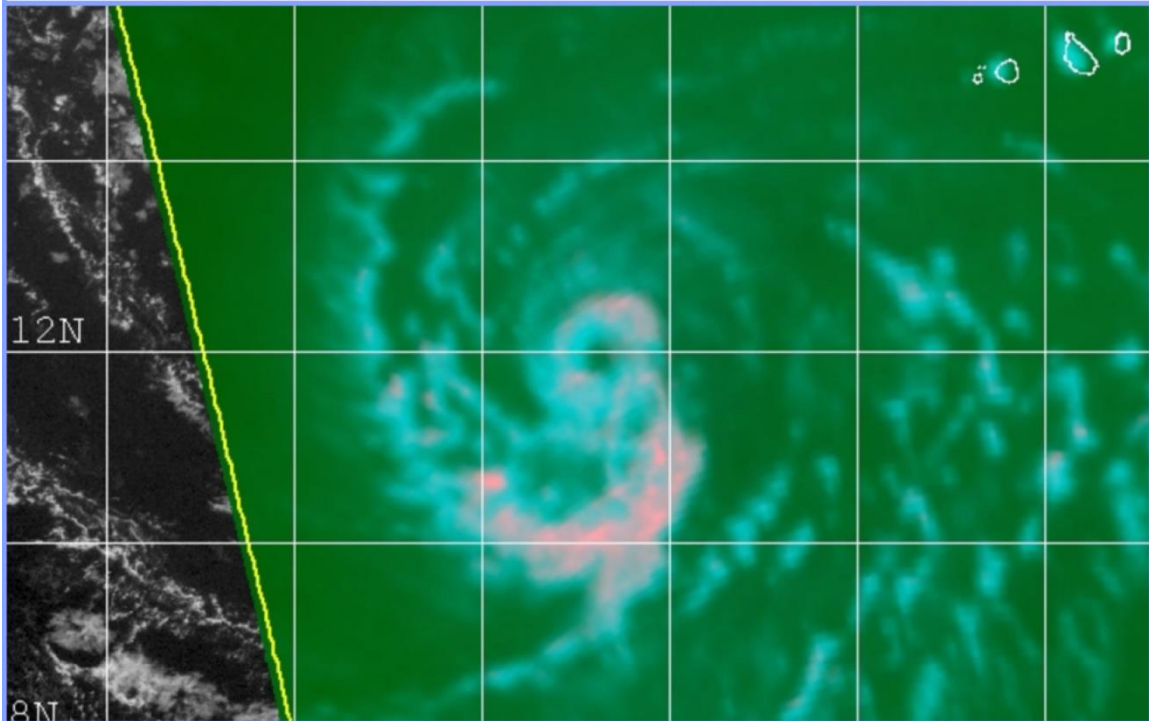


Figure 3.38 Identification of the RI ring in an NHC Tropical Cyclone Discussion (NHC archives).

Retired NHC forecaster James Franklin attributed use of the ring indicating onset of a period of RI to a subtle improvement in the NHC OFCL (official forecast) errors for the sample of cases when RI was either observed or forecast (Figure 3.39) for the period beginning around 2010-2011 through 2016, and that after 2016 improvement in forecast errors was related to improvements in the numerical guidance (personal communication).

However since a number of the references to the ring as an RI indicator came after 2016, perhaps there is a continuing improvement, albeit subtle, in the forecast errors. However simply because the RI ring indicator is noted in the TCDs, and a TC subsequently went through RI, this does not mean that RI was explicitly forecast in advance, as there are many factors to consider in the intensity forecast. In the TCRs however it would be noted as a hindcast.

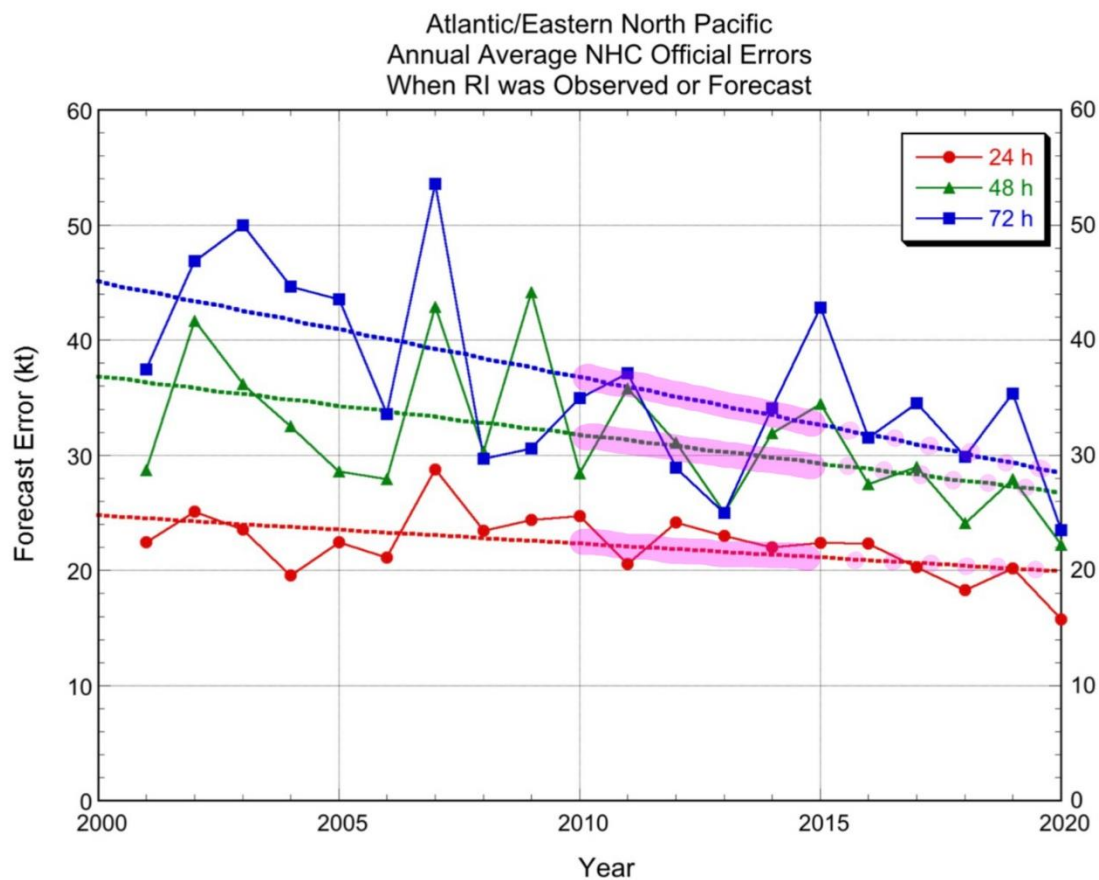


Figure 3.39 Improvement in NHC OFCL errors (from DeMaria et al. 2021, Figure 15). For cases when RI was observed or forecast, the time period from 2010 to 2015 is highlighted where use of the ring was believed to have had an impact. Because of the number of times the RI ring is mentioned in TCDs and TCRs since 2016, it can be suggested that it has had a continuing small impact since that time (dot highlighting).

CHAPTER 4. Early Eyewall Replacement Cycles With the Onset of the Developing Cyan Eye Ring Pattern: A Case Study

We examine four cases where eyewall replacement cycles (ERCs) that had characteristics very different from classical ERCs. They are: 2019 ATL Lorenzo, 2004 ATL Karl, 2006 EPAC Daniel, and 2007 WPAC Yutu. These ERCs all began at minimal hurricane intensity, had similar precipitation patterns, and were in similar stages of early development. Moderate convection appears to have played a strong role in the development of the ERCs. The development of the primary and secondary eyewalls appeared to overlap in time. These ERCs seemingly defied the conventional wisdom but produced the same end result, a completed ERC.

4.1 Methodology

The methodology used here focuses on extensive examination of passive microwave (PWM) satellite imagery with to reveal details of tropical cyclone (TC) structures. It is recommended that the reader view the figures side-by-side with the text. In addition to passive microwave (PMW) imagery, we use geostationary visible and infrared (IR) imagery, generated and archived in a publicly-available repository by Naval Research Lab Monterey (NRLMRY - Lee et al 1999, Hawkins et al. 2001, Lee et al. 2002). Particular emphasis is placed on 37 GHz color composite imagery (37color) and on lower-resolution SSMI and SSMIS, 85 GHz color composite imagery (85color). Since they were outside the range of aircraft reconnaissance, the hurricanes in this study were observed only through satellite imagery. When the suite of PMW imagery became available online through NRLMRY TC webpage, ERCs, which were not visible under the

cirrus canopy, were easily identified on PMW. They were primarily observed on the 85 GHz channel, and were found to be commonplace (Hawkins et al. 2006, Kossin and Sitkowski, 2009). We also utilize the National Hurricane Center (NHC) forecast advisory packages, Tropical Cyclone Reports and best track data from the NHC archives, for three cases that were forecast by NHC (RSMC Miami), to determine whether an ERC was detected in real-time forecasts or in post-analysis. The JTWC best track was reviewed for 2007 WPAC Yutu.

Eyewall replacement cycles (ERCs) involve development of a second ring of convection outside a pre-existing eyewall. Over time, the inner eye weakens while the secondary eyewall becomes dominant, and the inner eye eventually dissipates, with contraction of the outer eyewall (Willoughby et al. 1982, Shapiro and Willoughby, 1982). This cycle is associated with a slight weakening while the ERC completes (Sitkowski et al. 2011). ERCs are defined as associated only with "strong, axisymmetric tropical cyclones" (Willoughby et al. 1982). They were not normally observed in weak tropical cyclones, were associated with axisymmetric convective rings and excluded spiral bands, and developed from convective rings with persistent convection (Willoughby et al. 1982). The development of the secondary eyewall, called secondary eyewall formation (SEF), has been extensively studied (Kossin and Sitkowski, 2009, Zhang et al. 2017, Wang and Tan, 2020). Most published studies of eyewall replacements focus on mature strong tropical cyclones. These can be referred to here as "classic" ERCs.

Atlantic basin 2004 Frances is shown in Figure 4.1, 37color imagery, and Figure 4.2, 85h imagery. It went through three consecutive classic eyewall replacements over a four-day

period from 08/28 0449Z through 09/01 0602Z. Concentric axisymmetric eyewalls formed in each case. At the onset Frances was a major hurricane, starting at 100 kt intensity, and a partially cleared eye was apparent on IR. During this period Frances peaked at 125 kt after the second ERC in the image had completed, and at 120 kt intensity at the last image when the third ERC was in progress, so only slight weakening was associated with the ERCs.

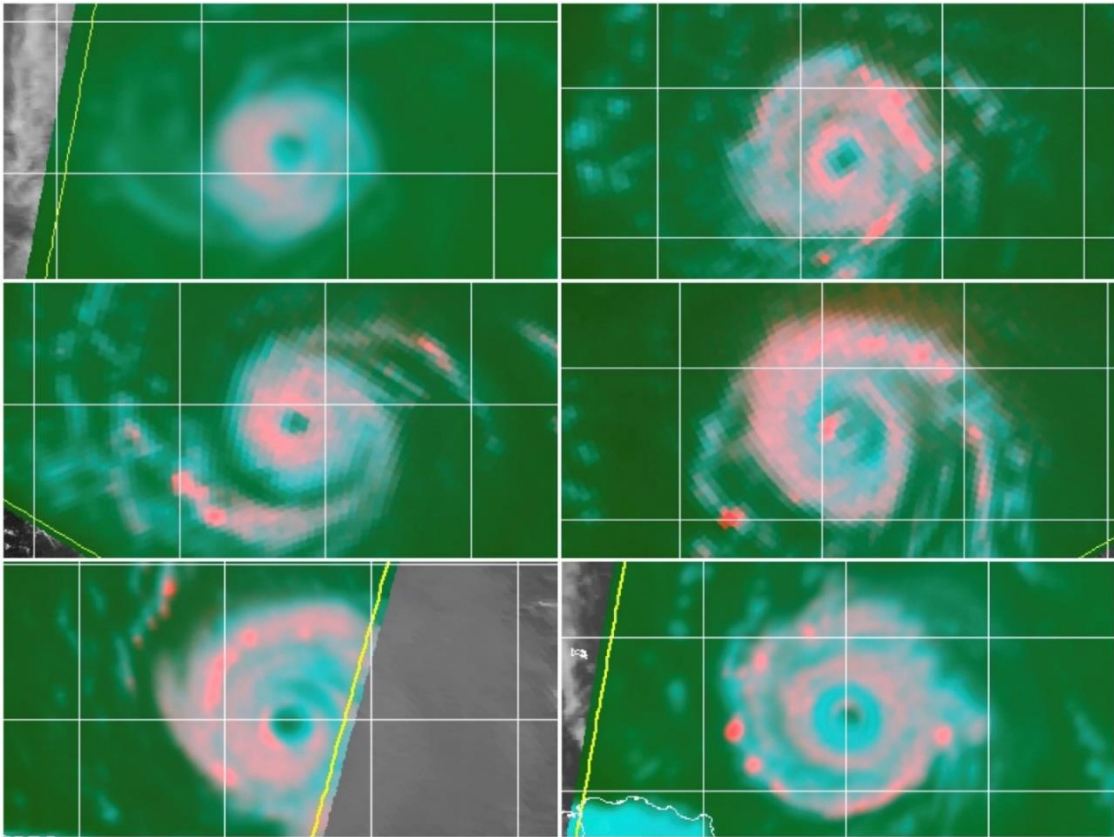


Figure 4.1 Three classic ERCs for 2004 Hurricane Francis over a four-day period. Between 08/28 0449Z through 09/01 0602Z, starting at 100 kt and ending at 120 kt, with the beginning of each ERC on the left and the resulting double eyewall of each ERC on the right. A 15 kt decrease in intensity was associated with the second ERC, which also took longer to complete.

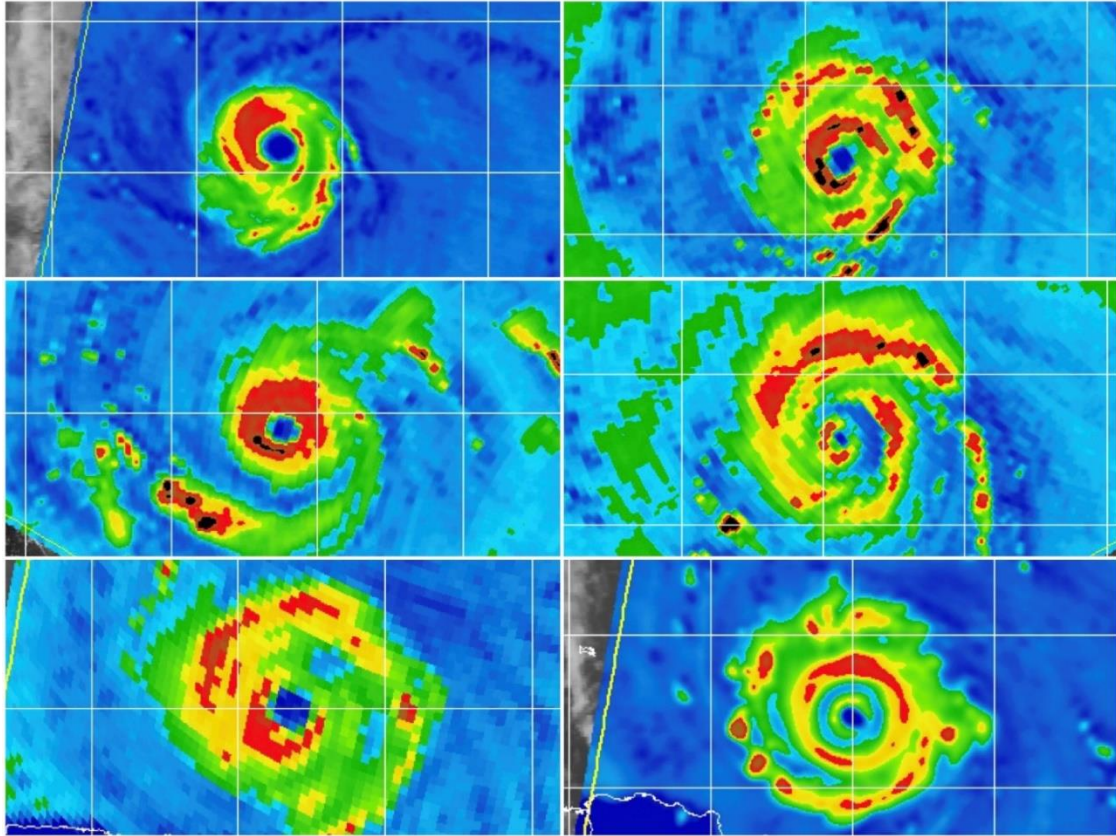


Figure 4.2 2004 Hurricane Frances, same as Figure 4.1, but in the corresponding 85h imagery.

4.2 Known Cases of "Early" ERCs

There are no documented cases of early ERCs that resemble the four in this case study. However, there are two documented cases of ERCs that occurred at minimal hurricane strength: 1991 ATL Hurricane Bob (Mayfield, 1992) and 1997 ATL Hurricane Danny (Pasch 1997). Both of these appear to have much in common with "classic" ERCs rather than with the four hurricanes in this case study. Both showed a classic precipitation pattern of multiple bands surrounding a mature eye during the ERC, rather than a developing tropical storm associated with a stationary band complex (SBC). Both were near land and were observable by land-based radar. The primary anomaly in these two

cases is the occurrence of ERCs at minimal hurricane intensity. There was no significant difference in precipitation structure from the expected axisymmetric convective rings.

4.2.1 1997 Hurricane Danny

Danny was a compact hurricane with most of the convection confined to a small symmetric core. It did have a well-defined eye prior to the ERC. Despite proximity to land, Danny did form a double eyewall and completed an ERC. The double eyewall and

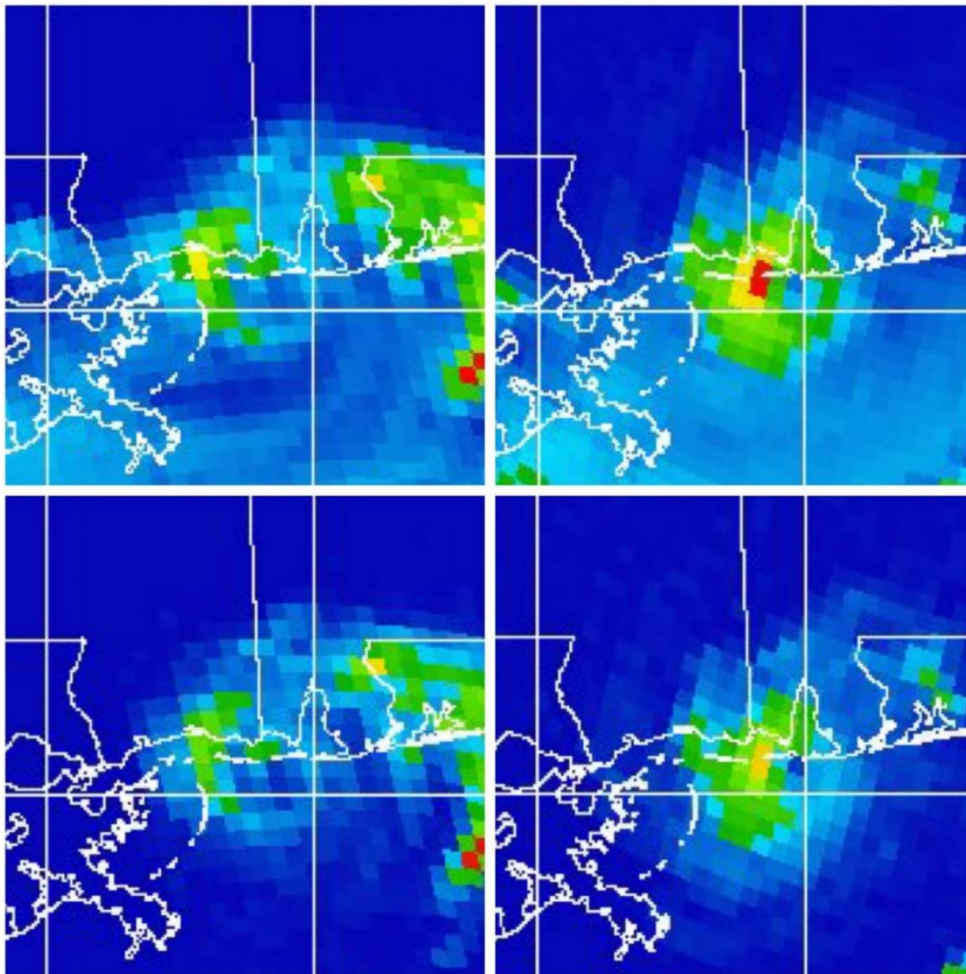


Figure 4.3 Two SSMI F-13 passes of 1997 Hurricane Danny. Images are from 18 July 2254Z and 19 July 1140Z, 85h imagery on the top and 85 PCT on the bottom, providing a low-resolution view of the prior structure with two partial concentric eyewalls on the left to the completed ERC and single eyewall on the right.

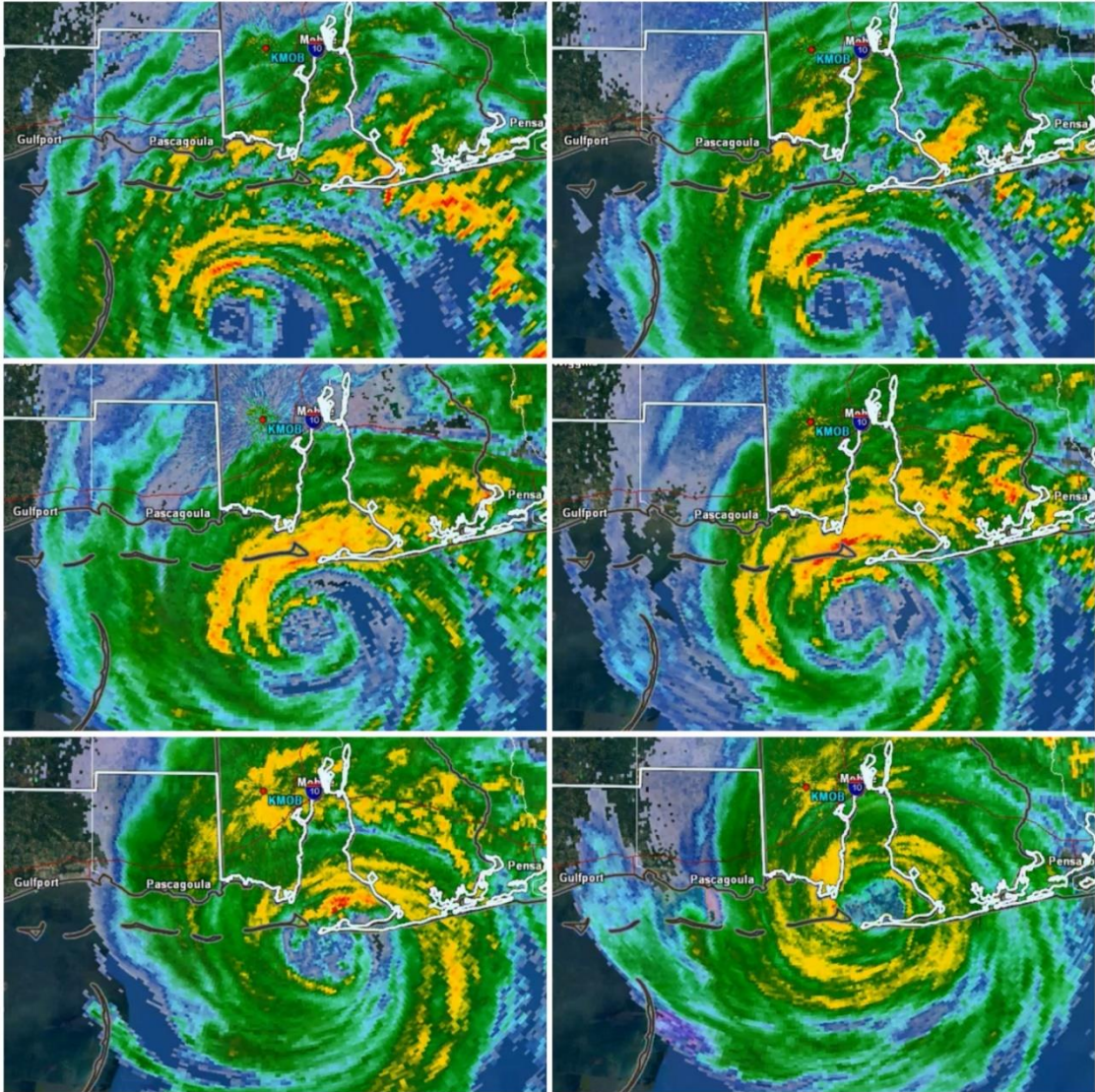


Figure 4.4 Radar imagery from NWSFO Mobile, AL radar loop of Hurricane Danny. From 19 July 1997, showing the evolution of the ERC, at 0003Z, 0208Z, 0440Z, 0554Z, 0759Z, and 1034Z, reading across and down. The double eyewall becomes apparent beginning in the third image and the ERC is complete by the last image.

the subsequent completed ERC with larger eye diameter was noted in an SSMI F-13 lower-resolution PMW imagery, Figure 4.3, and in ground-based weather radar, Figure 4.4 (NWSFO Mobile, 1997) and also in as well as aircraft reconnaissance observations over the Gulf of Mexico.

The radar was close to the core of the hurricane for some time, allowing almost continuous coverage of the evolution of the wind field (Blackwell 2000, Murillo et al. 2011). Having non-tropical origin in the Gulf of Mexico, Danny did not exhibit the stationary band complex (SBC) associated with ATL tropical cyclones (TC) that formed from Easterly waves and were subject to southwesterly shear over the West Atlantic and Caribbean. Danny also exhibited another trait in common with classic ERCs that the other hurricanes in this case study do not. There was a brief decrease in intensity upon completion of the ERC and before the secondary eyewall became dominant. As the inner eyewall dissipated the maximum wind decreased from 70 kt at 19/0000Z to 65 kt at 19/0600Z and then increased to 70 kt at 19/1200Z, but as 5 kt changes in the best track can be considered "in the noise" the only thing that can be confidently stated is that the intensity remained about steady on the 19th. Determining the mechanism of secondary eyewall formed, was not the focus of this research into Danny, and radar and PMW imagery of that period is archived. But three available images (Murillo et al. 2011) suggest that a dry slot may have contributed to the SEF (Figure 4.5).

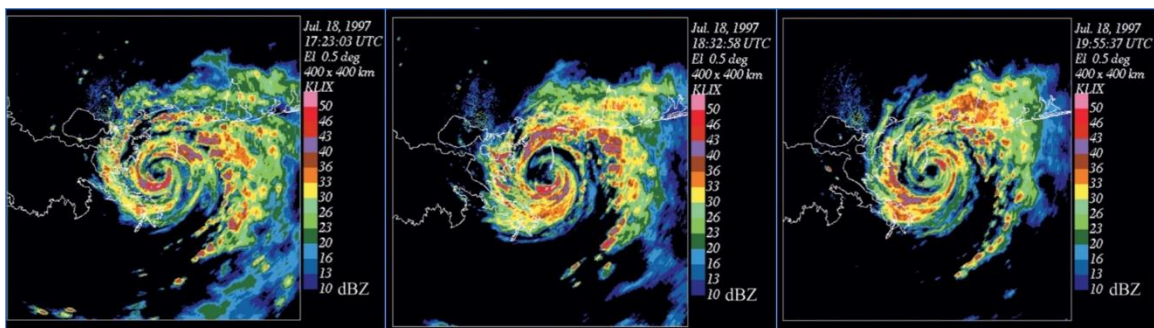


Figure 4.5 Three images of Hurricane Danny on 18 July 1997 from NWSFO Slidell, LA (from Murillo et al. 2011). At 1723Z, 1832Z, and 1955Z showing a pronounced dry slot wrapping into the circulation, and Danny's evolution from an open eyewall, then decay of the eyewall due to dry air intrusion, to reformation of the eyewall, but with a well-defined spiral convective band that is almost axisymmetric surrounding it and a moat between. The dry slot could have facilitated the SEF.

4.2.2 1991 Hurricane Bob

Hurricane Bob of 1991 had multiple cases of overlapping eyewall development and wind maxima, as revealed by aircraft reconnaissance flights over a two-day period between 17/1200Z and 19/1800Z August (Figure 4.6, Hugh Willoughby, personal communication). Bob's initial intensity during this period was 55 kt and steadily increased to 100 kt by 19/0600Z, and then decreased steadily as extratropical transition occurred (at 20/1800Z). Radar imagery from a brief period between about 19/000Z and 19/0400Z, when Bob's intensity was 95 kt, was also available (Figure 4.7). The NHC preliminary report noted that, "a well-defined eye appeared on satellite pictures late on 18 August...the eye became even more distinct as it passed 25 to 30 n mi east of Cape Hatteras early on the 19th" (Mayfield, 1992). This observation indicates that Bob had multiple wind maxima/partial eyewalls for a little over 24 hours before the eye became evident in geostationary satellite imagery and did not completely clear out until about 36 hours after the onset, at which time there were three distinct partial eyewalls, two at a radius of about 20 km and one at a radius of about 50-60 km (Figure 4.6).

4.3 Passive Microwave Case Study of Four Similar "Early" ERCs

Tracks of 2019 ATL Lorenzo, 2004 ATL Karl, 2006 EPAC Daniel, during early ERCs are shown in Figure 4.8 and Figure 4.9. A track map is not available for 2007 Yutu. Interestingly the tracks of Karl and Lorenzo during this time are very close to each other and both occurred in September. It will be shown that these four hurricanes all have the similar characteristics that are quite different from classic ERCs.

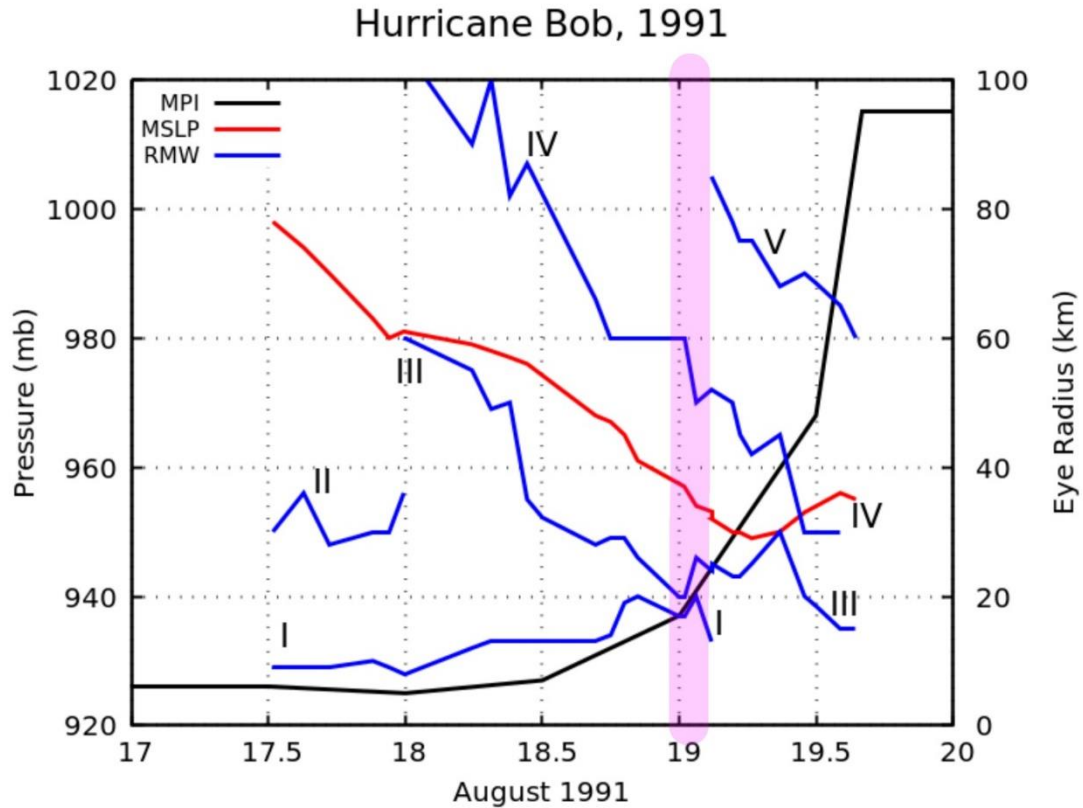


Figure 4.6 1991 Hurricane Bob multiple wind maxima / eyewalls (Hugh Willoughby, personal communication). Observed in from aircraft reconnaissance data from August 17/1200Z through 19/0600Z. Radar imagery from Cape Hatteras radar is shown in Figure 3.7 for the shaded region.

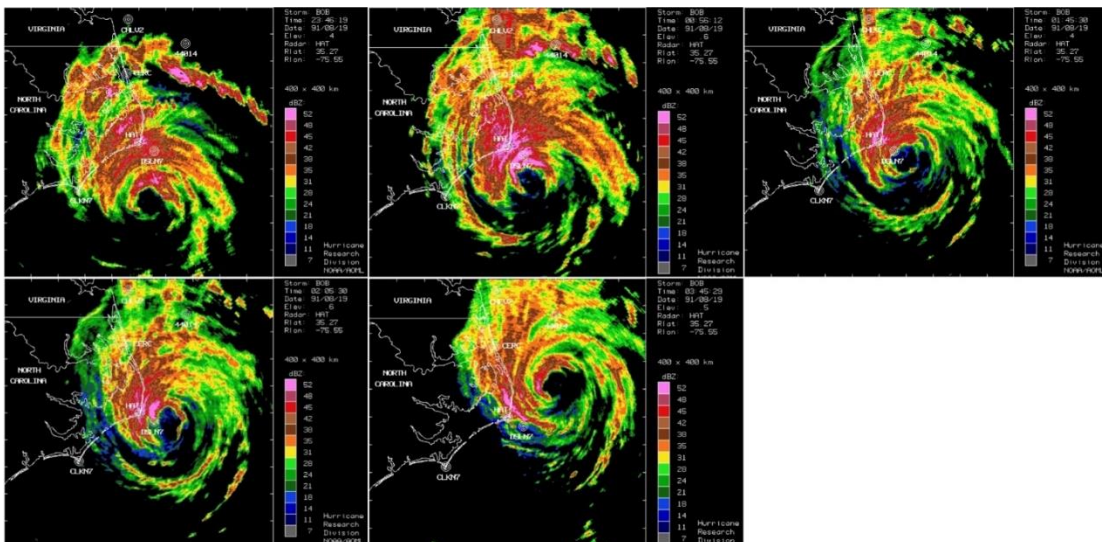


Figure 4.7 Radar imagery of 1991 Hurricane Bob. Shown on August 18 2346Z and August 19 0056Z, 0145Z, 0205Z, and 0345Z (HRD NOAA/AOML courtesy of Hugh Willoughby).

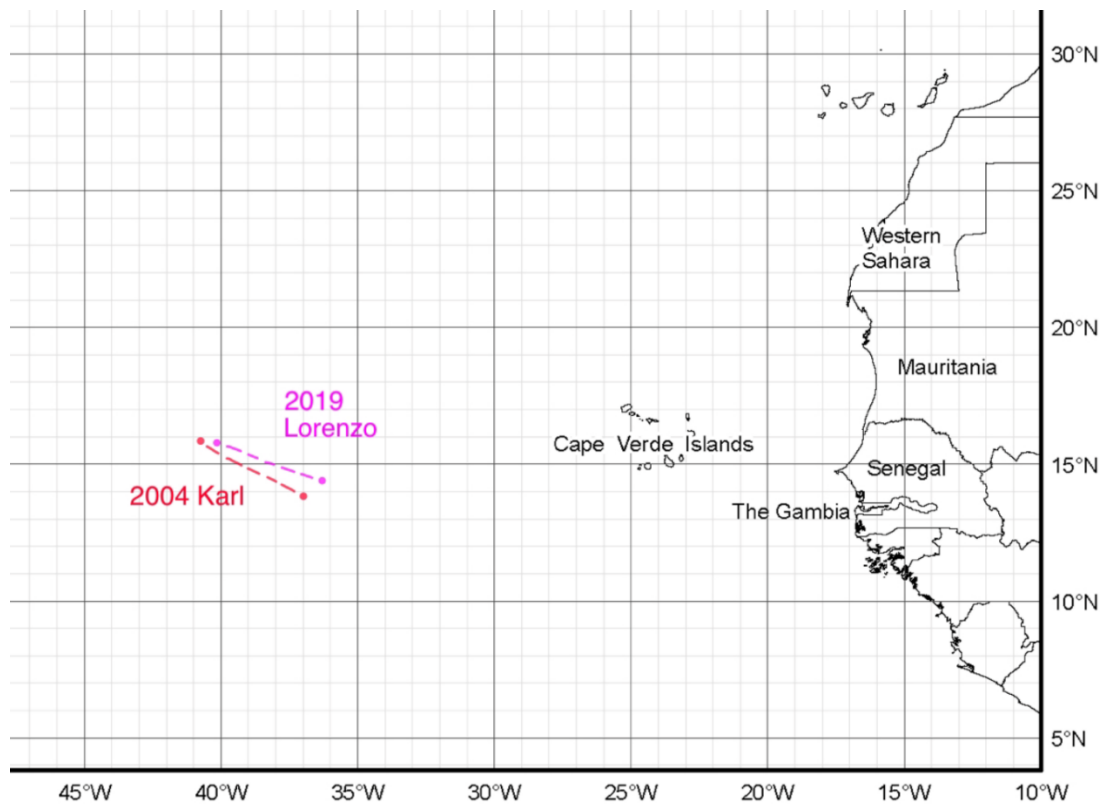


Figure 4.8 Tracks of 2004 Karl and 2019 Lorenzo during the early ERCs.

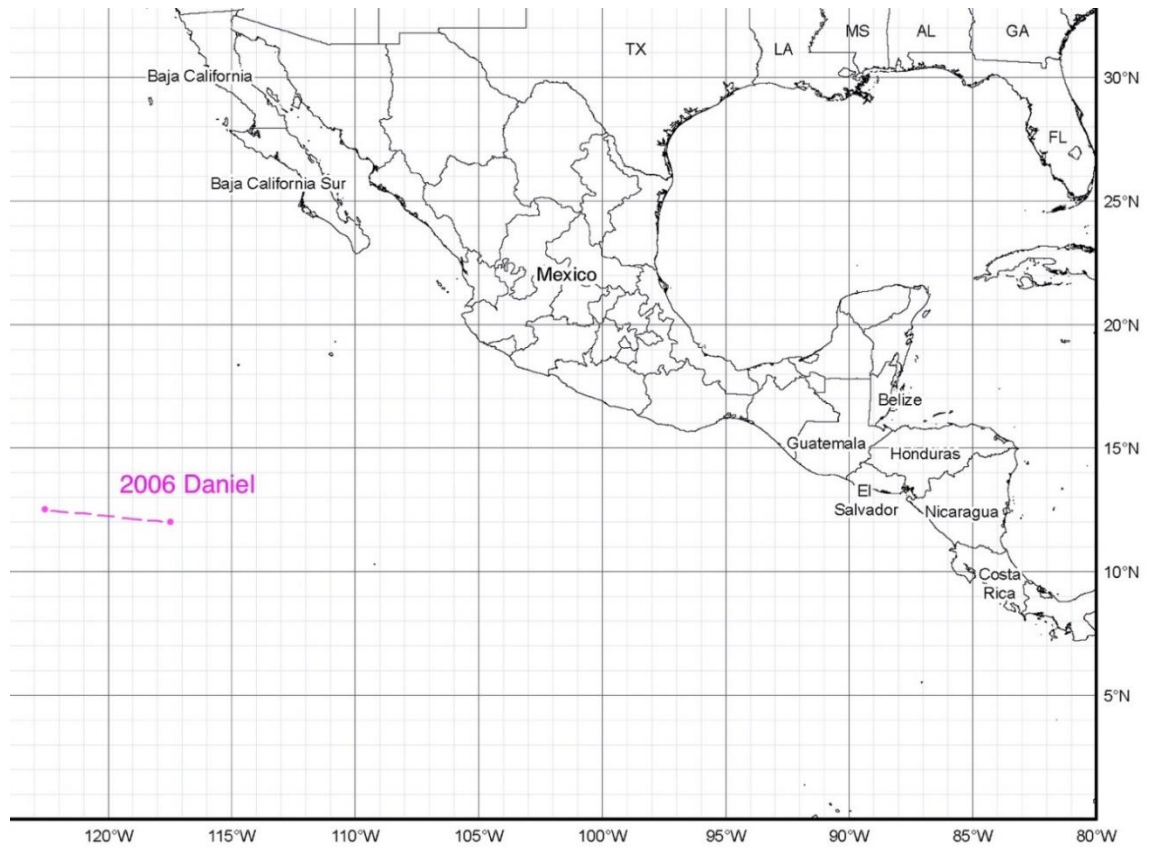


Figure 4.9 Track of 2006 Hurricane Daniel during the early ERC.

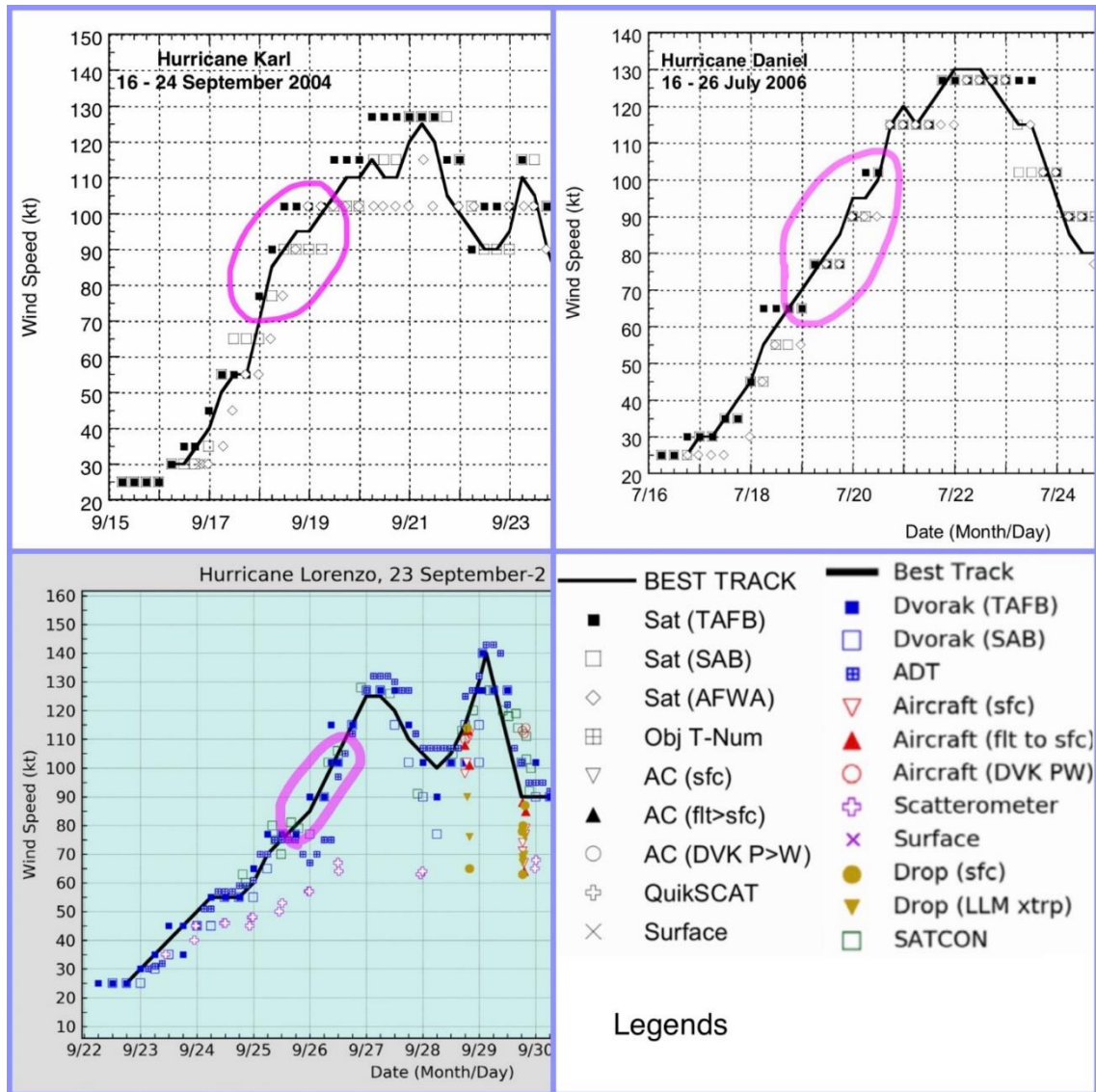


Figure 4.10 Best track intensities for 2004 Karl, 2006 Daniel, and 2019 Lorenzo with the period of the early ERC highlighted. From the respective NHC Tropical Cyclone Reports. In all the cases, the ERC occurred as part of an intensification phase, prior to the peak intensification, with no weakening associated with the ERC.

4.3.1 Case Study One: 2019 ATL Hurricane Lorenzo

During a period of rapid development from a tropical storm to a Category 4 hurricane, Lorenzo as described in the NHC Tropical Cyclone Report (Zelinsky, 2019), "...rapidly strengthened 70 kt over the next 48 h and reached an initial peak intensity of 125 kt."

Passive microwave (PMW) imagery suggested that Lorenzo developed a small eye seen only on passive microwave imagery, then went through an eyewall replacement cycle (ERC), before a classic mature eye had formed., It is suggested that the development of the mature eye was the result of the completing "early" ERC. The ERC was not observed until it had been completed but was then identified in the next advisory package.

The period of rapid intensification (RI) ran from 1800Z on the 24th of September with a current intensity of 55 kt, through 0000Z on the 27th of September, when intensity had increased to 125 kt.

While the duration of the ERC depends on how the start and end of the ERC are defined, in this case about 24-30 hours elapsed between the beginning of initial (inner) eye development until a cleared eye was apparent on geostationary satellite imagery.

Another 18 hours elapsed between the development of the SEF and when the ERC completed. A number of specifics on the core development were observed on the NHC forecast advisories, as detailed below.

4.3.1.1 Lorenzo Developing Eye

Four PMW passes, Figure 4.11, show a developing small eye. These three SSMIS and one SSMI pass span a time of 15 hours, from 24/1800Z through 25/0900Z, and an intensity increase from 55 kt to 70 kt. All four passes show west-northwesterly shear and possible dry air entrainment. The convection is primarily to the east of the center.

Convection is in the shape of the principal band as is often seen in moderately sheared

tropical cyclones. NHC advisories describe the shear as strongest on the 24th and decreasing during the period of these images, allowing the eye development. During this time, SHIPS identified moderate shear of 10 kt from westerly and northwesterly directions, from 24/1200Z through 25/0000Z, consistent with the satellite appearance. We can hypothesize that the shear did not lessen all at once but that bursts of shear occurred during this time, interrupting the development, because the partial eyewall

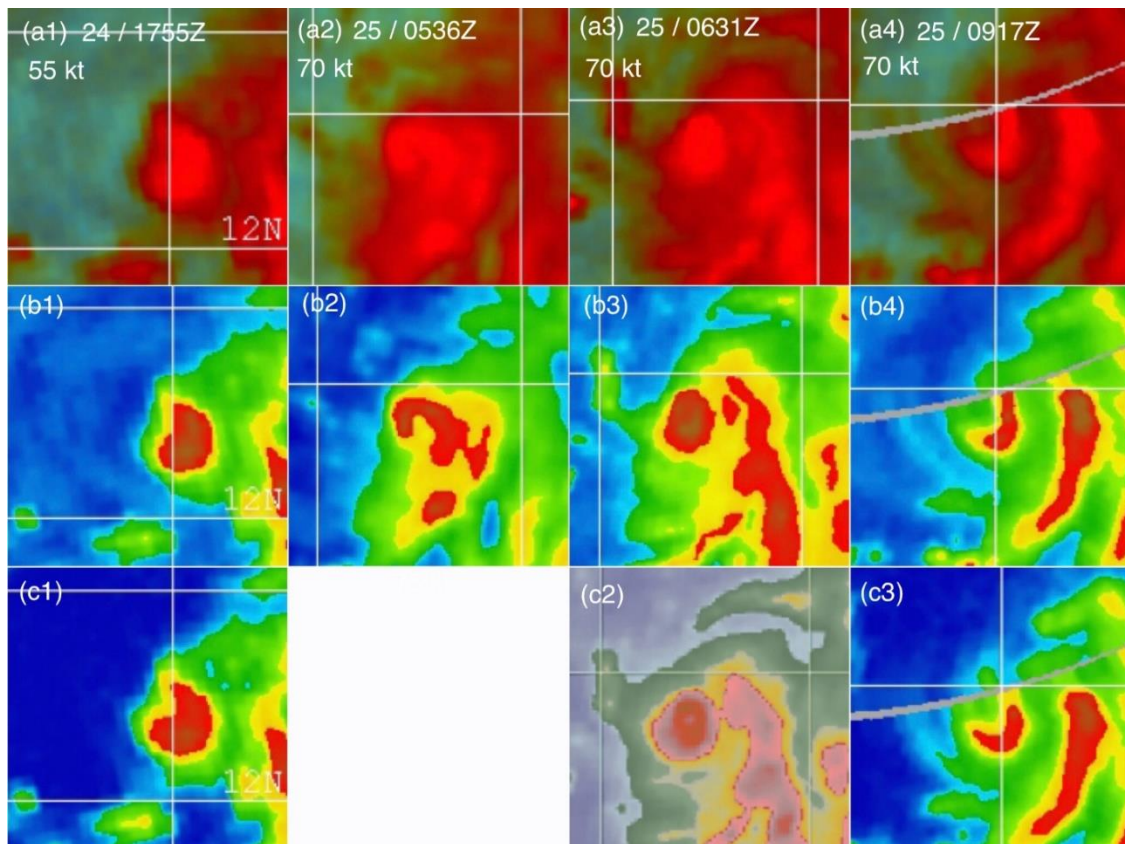


Figure 4.11 Developing eye in Lorenzo. SSMIS and SSMI passes over a 15-hour period show a developing banding eye. Columns identify passes at 24/1755Z, 25/0536Z, 25/0631Z, and 25/0971Z in September 2019. First row shows 85color imagery, second row, 85h imagery, and third row, 150 GHz imagery (SSMIS only). All images show curvature of a "banding eye" and the 25/0612Z pass shows an ice signature completely encircling the eye (150 GHz image is color enhanced so this feature stands out). EIR-BD images did not indicate an eye forming until the time of the last pass at 25/0917Z with a warm spot in the center of the CDO.

development did not progress much during this time and did not completely wrap around and become a closed eyewall. However, the intensity did increase from 55 kt to 70 kt during this time. The RAMMB TC AMSU area-averaged wind shears and layer means shows moderate northwesterly shear between 200-850 hPa at 24/0000Z peaking at 24/1800Z and dropping to 25/1800Z, and similarly between 500-850 hPa with primarily southerly shear.

The 25/0900Z forecast discussion states, "There have been no good microwave passes over the cyclone since yesterday, however, a partial SSMIS pass showed hints that a mid-level eye is forming." This was the earlier 24/1755Z F-16 SSMIS pass showing a deep convective partial eyewall, seen on (a1), (b1), and (c1). At the time of this advisory, 25/0900Z, Dvorak analyses supported increasing the intensity to 70 kt making Lorenzo a hurricane. It appears that two key PMW passes were unavailable for this and the subsequent 25/1500Z advisory, as the 25/1500Z forecast discussion specifically mentions only geostationary satellite imagery: "Conventional satellite imagery indicates that Lorenzo continues to become better organized..." These two missing passes, a 25/0536Z F-15 SSMI (a2) and (b2), and a 25/0631Z F-16 SSMIS (a3), (b3), and (c2), as well as a 25/0917Z F-17 (a4) (b4) and (c3), show an ice signature consistent with a deep convective partial eyewall, and in the 25/0631Z pass (b3) and (c2) either a complete eyewall or ice from deep convective anvils being advected around the center. This feature was not present in the fourth pass three hours later. At 25/0900Z both the MSG-4 and GOES-East EIR-BD detected the eye, but it was transient (see Figure 3.12), which may be why the 25/1500Z advisory only noted "better organized."

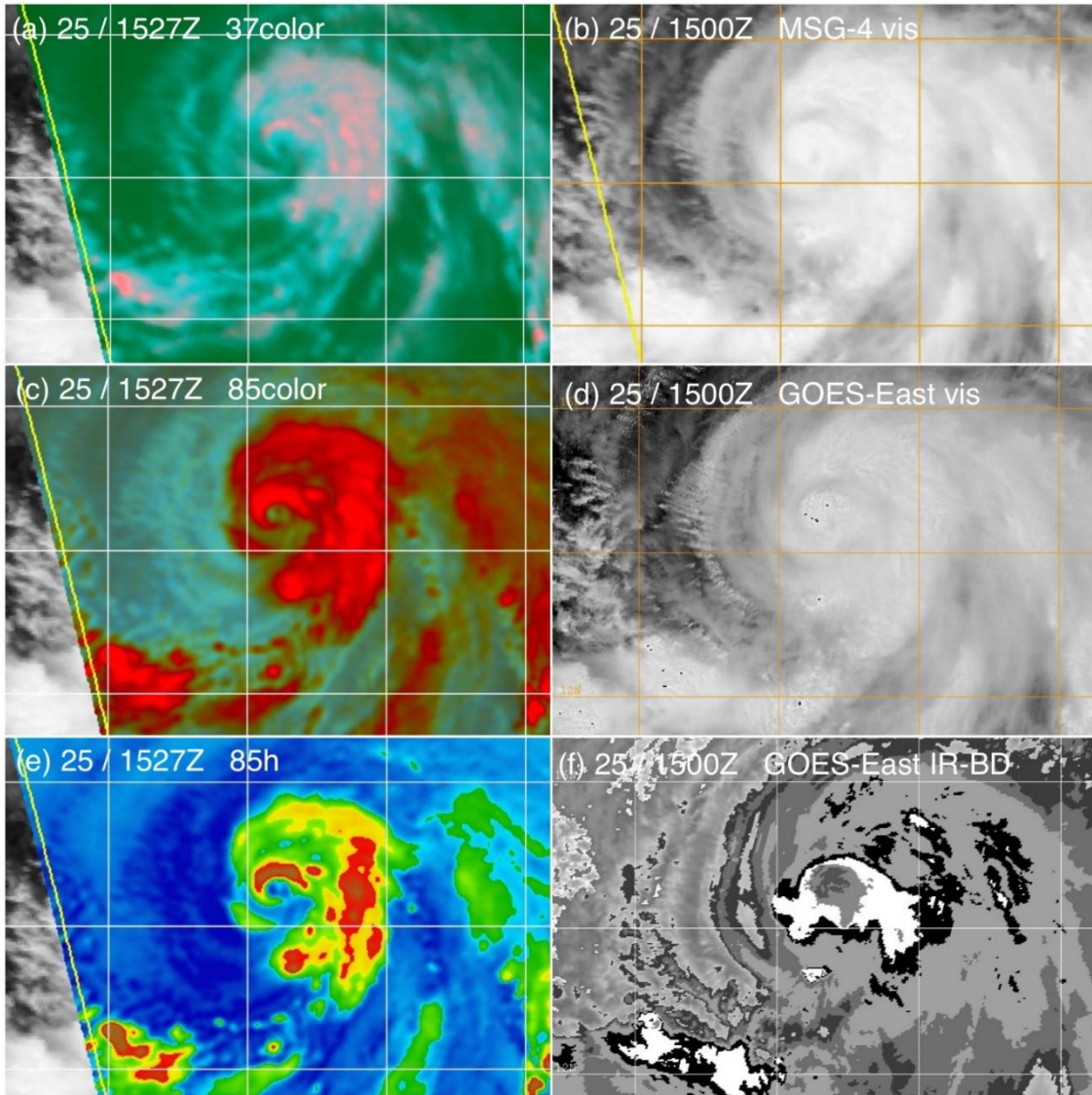


Figure 4.12 Lorenzo's Eye. By 25/1527Z Lorenzo formed an eye. It was only transiently visible on both the Goes-East (b) and MSG-4 (d) VIS at 1500Z, and not apparent on the EIR-BD (f). The eyewall was not closed but passive microwave (a) (c) and (e) showed it extended $> 50\%$ around the center. The 37color (a) shows that the secondary circulation is well established on the northern side with the eyewall showing tilted deep convection (curved band of aqua bordered with pink).

4.3.1.2 Lorenzo SEF Development and ERC Completion

The 25/2100Z NHC forecast advisory on 25 September, from a 25/1527Z AMSR2 overpass in Figure 4.12, noted a small "partial eyewall or convective ring" in the discussion. This is the only PMW higher-resolution pass that was available to utilize the

37color image (a). It shows a small well-defined partial eyewall. The location in relation to the principal band is consistent with the eyewall placement in the stationary band complex (Figure 4.13 – from Willoughby et al 1984).

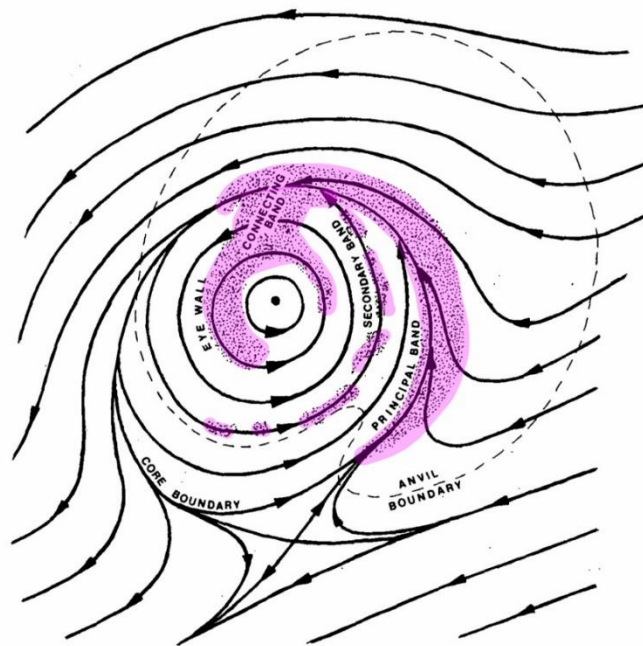


FIG. 18. Schematic representation of the stationary band complex, the entities that compose it and the flow in which it is embedded.

Figure 4.13 Stationary Band Complex from Willoughby, Marks, and Feinberg 1984.

The signature of ice banding along the northern portion of the eyewall indicates that the secondary circulation has developed there. This partial deep convective eyewall is also visible on both the 85color (c) and 85h (e). It shows an additional weak ice signature advected completely around the eye. While enhanced infrared (ERI-BD) from both MSG-4 and GOES-E, both at approximately the same viewing angle from nadir, show a CDO that covers both the core and the principal band (f), interestingly the GOES-E (d)

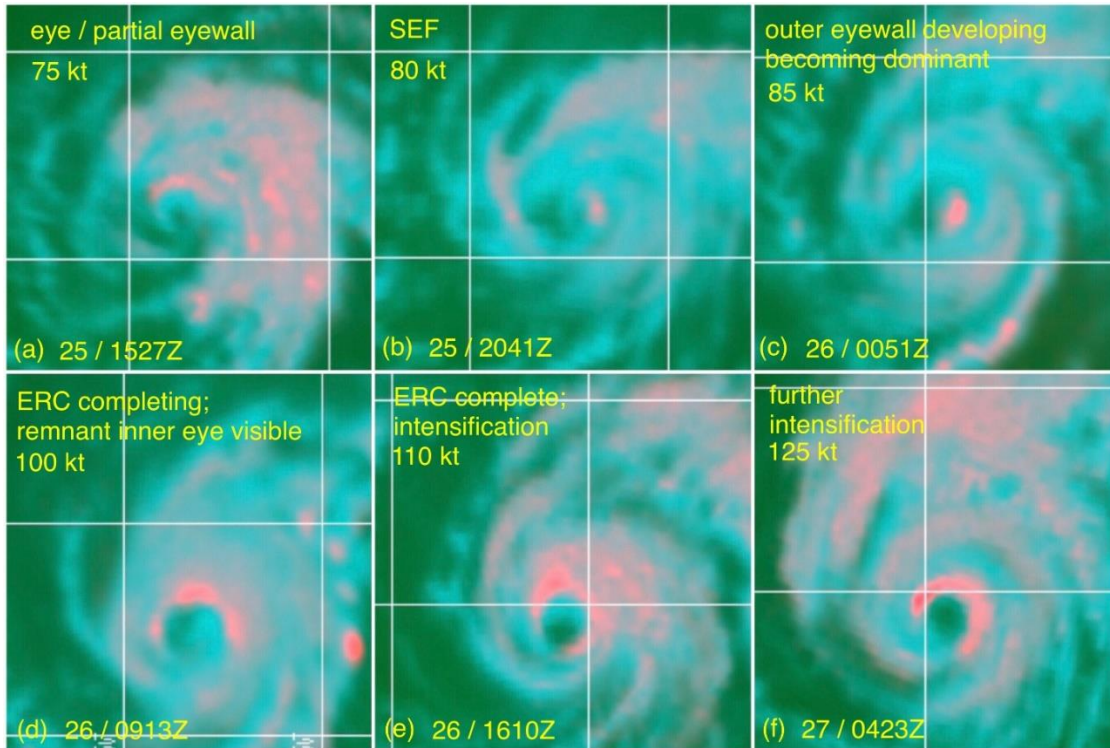


Figure 4.14 Lorenzo's early eyewall replacement cycle. These six 37color images show stages in the eyewall replacement cycle spanning a 37hour period, including before and after development. The timing of the actual ERC including t SEF (falling somewhere between (b) and (c) to completion shown in (e), is ~18 hours. In (a) an eyewall has formed within the principal band. About 5 hours later outer banding surrounds the developing eye indicating the onset of SEF (b) and then (c) it becomes symmetric, shows increased precipitation (band of bright cyan), and development of an outer secondary circulation (pink ice signature surrounding the band). During this time the inner eyewall fades except for a single strong convective burst (pink dot) but the small curvature of the eyewall appears faintly in the warm precipitation signature. Shortly after (c) the inner eye appears intermittently on EIR-BD imagery, and then the double eyewall clears and is apparent on both VIS and EIR-BD (next image). In (d) the secondary eyewall is now prominent with strong convection surrounding the northern half of the eyewall (bright pink) and the inner eye is still distinct but dissipating. By 26/0600Z 85h imagery (not shown) was showing a prominent outer eyewall with no deep convection in the inner eyewall. The ERC is completed by the time of the pass in (e) and further strengthening occurred following the ERC (f) with a more intense symmetric ice signature around the eye.

and MSG-4 (b) visible images from 25/1500Z show a small CDO with a faint "dimple" over the center, indicating the beginning of an eye. This signature was transient. It was

not visible on subsequent images, which also show the principal band separated from the CDO, possibly as a result of dry air wrapping around the core, or subsidence from the partial eyewall. This observation suggests a region functioning in effect like a moat between the core and the principal band, providing a convective band configuration that may have lent itself to SEF development.

The stages of the ERC development and completion as seen in the 37color composite are shown on Figure 4.14. The sampling characteristics of the 37 GHz microwave channel and this particular derived color composite imagery provide a unique perspective, It shows these developments more clearly than any other PMW imagery type, by displaying areas of warm precipitation. This first image (a) is same as in Figure 4.12, the formation of the eye and partial eyewall. Banding suggesting a developing secondary eyewall appeared by 25/2041 WindSat (b), and was characterized in the 26/0300Z forecast as "the inner-core of Lorenzo is trying to consolidate." This secondary eyewall-type banding is also observed on a 26/0051 GMI (c). The rain signature is stronger than before, signified by the brighter cyan in the secondary developing eyewall. Also notable is the symmetry and smoothed curvature of the band. This observation suggests the secondary eyewall is becoming more established. It is not yet deep convection because it does not show up on the 85h and 85color images from this pass. Concurrent with its formation, the well-defined partial inner eyewall became smaller and less prominent, but still easily distinguished on the imagery. However, this fact was not noted in the NHC forecast discussions, probably because secondary eyewall development is not expected to be observed at this stage. The 26/0300Z advisory also noted, " A small eye has been intermittently appearing in infrared satellite imagery over the past few hours..." At this

stage the PMW imagery shows the inner eye to have weakened, but vestiges of the inner eyewall, including a small dot of deep convection, still remained (c). CIRA RAMMB ocean heat content and forecast track product showed ocean heat content increased from 0-15 kJ/cm² to 15-35 kJ/cm², between 26/0000Z and 26/1200Z. Usually greater than 50 kJ/cm² is considered favorable for higher rates of intensification but in this case the increase may have been a factor in the intensification if sea surface temperatures (SSTs) were higher in this region. Lorenzo's speed was 13 kt at this time so it was not moving slowly.

The 26/0900Z advisory noted, " The hurricane has at times shown signs of a developing eye, however, it has been mostly obscured during the last few hours by expanding cloud tops associated with central (and likely eyewall) convection. Although the eye is not yet apparent in geostationary imagery, a 0618 UTC SSMIS overpass showed that Lorenzo has developed a well-defined mid-level eye." Unfortunately, this pass is missing from the NRLMRY TC archives, but a 26/0913 WindSat shows a well-defined, large, deep convective eye with the remnant smaller eyewall still visible (d). It suggests that the ERC is almost complete.

An hour later, a special 26/1000Z advisory was issued, stating, "Shortly after the issuance of the 0900Z advisory, Lorenzo's eye quickly and drastically became more apparent in conventional satellite imagery. The slightly ragged but clearing eye of the hurricane is surrounded by very cold cloud tops, and it has become clear that Lorenzo is rapidly intensifying." The 26/0900Z intensity of 85 kt was increased to 110 kt at 26/1000Z operationally. Because the eye had cleared, the Dvorak method resulted in a

classification of 115 kt at that time. In the best track the intensities for this period were adjusted for the period prior to the eye clearing, when the Dvorak estimates can fall behind actual intensity. A review of both B&W IR and EIR imagery not only show the clearing eye but also clearly show the double eyewall structure, especially between 26/0730Z and 26/0900Z, as seen in Figure 4.15.

The forecast advisory the next morning, 26/1500Z, noted, " A review of microwave satellite imagery from last night suggests that Lorenzo underwent an eyewall replacement cycle, with the outer eyewall becoming predominant around 06Z-09Z." As mentioned, Figure 4.15 shows the concentric eyewalls during this period. Shortly after the ERC completed it was noted in the NHC advisories, but not during the event.

A 26/1610Z AMSR-2 pass (e) shows the eye has cleared out and contracted so that there is no trace remaining of the inner eye. A 27/0423Z AMSR-2 pass (f) shows a brighter well-defined more extensive ice signature surrounding the eye as Lorenzo continued strengthening. After this ERC, Lorenzo continued to rapidly intensify to 125 kt by 27/0000Z. It completes a second ERC, and then intensified into a Category 5 hurricane during recurvature. The earlier 26/1500Z advisory also noted, "Around that time, the hurricane started to rapidly intensify..." And the best track does show a 30 kt intensity increase in 18 hours, from 95 kt to 125 kt, from 26/0600Z to 27/0000Z.

The structure, a developing eye adjacent to a principal band, and the intensity at the time of eye formation, 70 kt, are very different from the classic ERC that occurs only after a mature eye has developed, usually with associated major hurricane intensity, and with an outer eyewall forming from accumulating concentric banding around the inner eye.

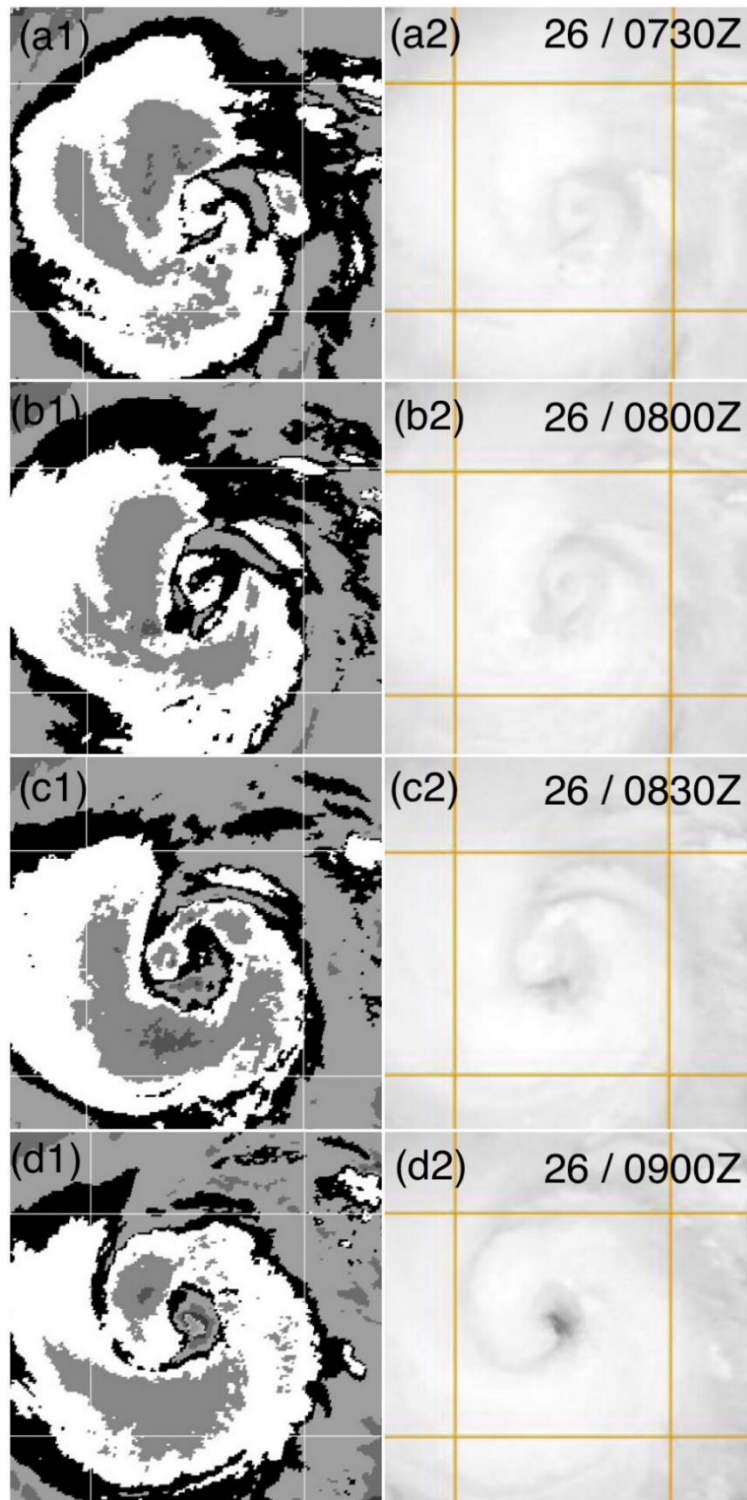


Figure 4.15 EIR-BD and VIS imagery during the time double eyewalls appeared as Lorenzo's ERC was completing. By the time of (d1) and (d2) the inner eye was no longer distinct and was dissipating. During this time PMW did not show deep convection in the inner eyewall. The coldest cloud tops are in the outer eyewall.

The classic ERC is associated with a small dip in intensity during the ERC when the secondary eyewall becomes dominant while the inner eyewall is decaying. Lorenzo's early ERC did not result in even a temporary reduction in intensity, but an increase of 15 kt in 12 hours (which is a significant intensity increase) between 25/1800Z, when the secondary eyewall can first be seen on PMW, and 26/0600Z. In considering the entire 48-hour period of RI mentioned in the TCR, the ERC had no negative impact on the intensification increase during the RI event.

In classic ERCs, often the process is hidden from view under the CDO, when the eye that was previously clear clouds over. PMW imagery, particularly the 85h (to 91h), has been used extensively to identify the onset of both the development of the secondary eyewall and the subsequent ERC. Lorenzo's early ERC was also not apparent on geostationary imagery except for an occasional warm center that came and went, but surprisingly a very well-defined double eyewall structure was visible on IR for several hours right at the end of the ERC. But, strikingly, the ERC was also not readily apparent on the 85h channel during the time the secondary eyewall was developing. The reason appears to be that the eyewalls were composed of a considerable amount of moderate convection, not deep convection, as they were developing. This makes the 37color imagery important as it is the only channel that can observe moderate convection with enough resolution to show its precipitative structure. It is also striking that deep convective eyewalls are not necessary for early ERC to occur, and it renders the 85 GHz channel less useful in observing their development.

4.3.2 Case Study Two: 2004 ATL Hurricane Karl

Unlike 2019 Hurricane Lorenzo, Hurricane Karl did form a distinct eye around 18/0600Z on September 2004. Its best track intensity was 70 kt, shortly before the onset of the ERC, but the SEF development began almost immediately after the eye was first observed, unlike classic ERCs. Like the other hurricanes in this study, the secondary eyewall formed as an extension of the head of the principal band, and the ERC did not cause even a small temporary reduction in intensity. As seen in Figure 4.8, the track of both hurricanes during the eye development and subsequent ERC were practically coincided, suggesting similar stages of development and similar synoptic environment.

4.3.2.1 Karl Developing Eye

A developing eye revealed by PMW was noted in the NHC forecast discussion of 18/0300Z: " A 17/2148Z SSMI OVERPASS SUGGESTS THAT KARL MAY POSSESS A VERY SMALL EYE...AND THIS WAS LATER SUPPORTED BY A 17/2317Z TRMM OVERPASS." In both images the position of the developing eye is seen in relation to the principal band matching the SBC structure (Figure 4.16). A partial eyewall is seen on the 85color and 85h imagery. Cold cloud tops appeared on EIR-BD coincident with the developing eye.

A pinhole eye became apparent on METEO-7 IR at 18/0500Z and on GOES-East after the eclipse at 18/0645Z (Figure 4.17). Subsequently, the NHC 18/0900 forecast discussion noted, " KARL HAS RAPIDLY INTENSIFIED OVER THE PAST 6 HOURS OR SO BASED ON THE APPEARANCE OF A SMALL BUT DISTINCT 10 NMI

DIAMETER EYE IN INFRARED SATELLITE IMAGERY." The best track shows a 30 kt increase of intensity in 12 hours, from 55 kt at 17/1800Z to 85 kt at 18/0600Z.

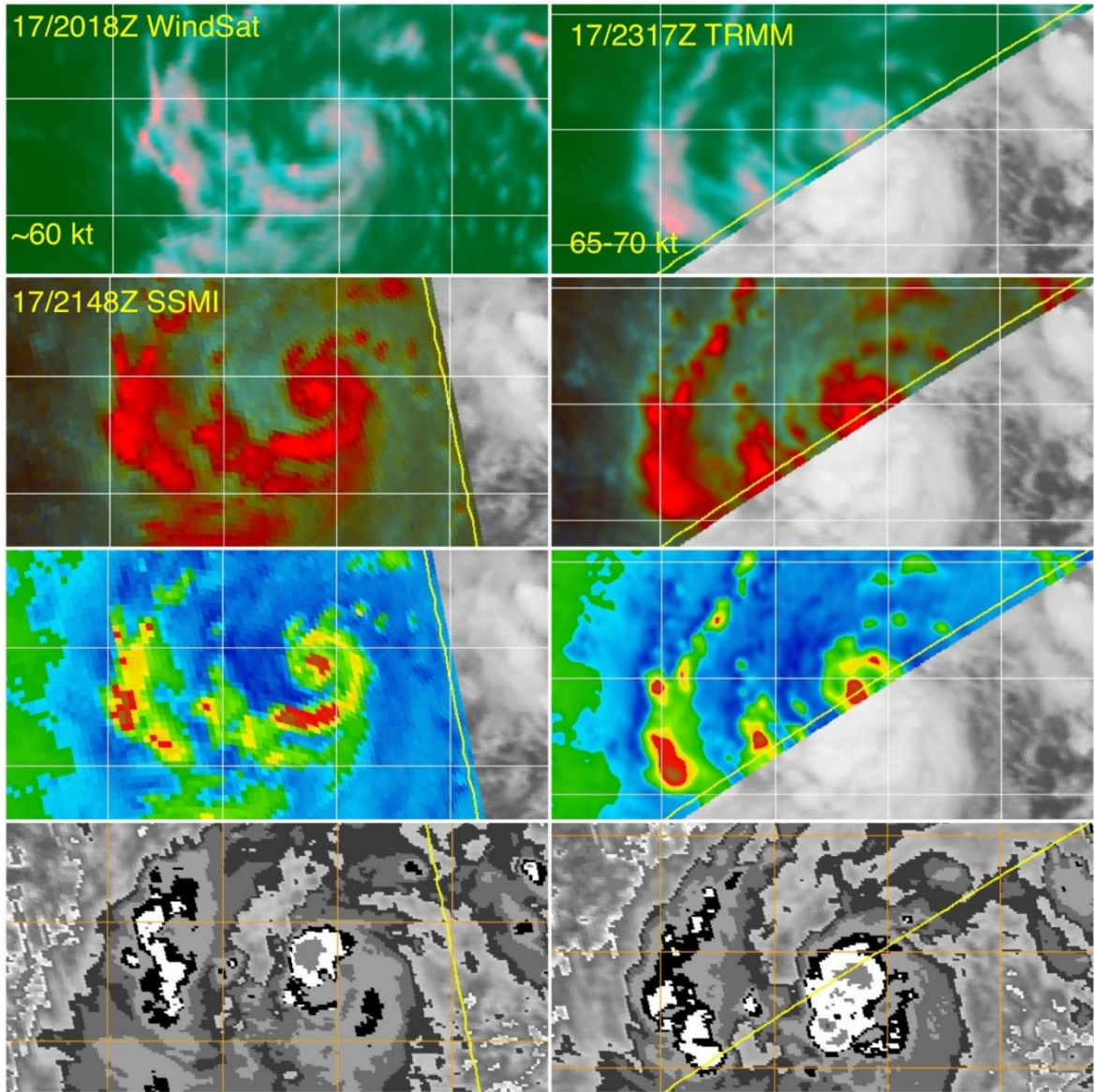


Figure 4.16 Developing eye of 2004 Hurricane Karl. The rows show 37color, 85color, 85h, and the corresponding EIR-BD imagery, respectively. The first column are pairs the 37color WindSat with nearly simultaneous SSMI imagery, and in the second column, a TRMM pass.

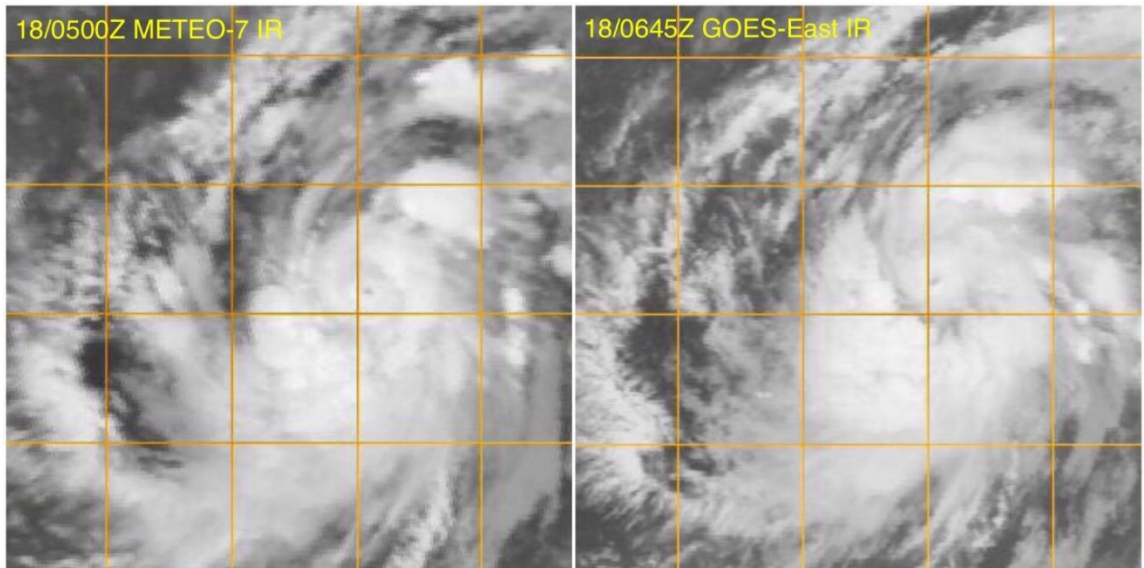


Figure 4.17 First IR images of 2004 Karl's pinhole eye. GOES image is later because of the satellite eclipse between about 0345Z and 0645Z daily. Images have been slightly contrast-enhanced to emphasize the small inner eye.

4.3.2.2 Karl SEF Development and ERC Completion

Almost immediately after the eye appeared at 18/0500Z on infrared imagery, bands of precipitation extending from the principal band and surrounding the eye were well-established on PMW 37color, on an 18/0730Z TRMM and on 18/0852Z WindSat (Figure 4.18). Note from the TRMM 85color image on the same pass states that these precipitative bands cannot be observed on this channel, but are only appeared on the 37color. This is another example of the value of the 37color imagery. It is the only imagery that can see mid-level precipitation patterns providing information on TC structure changes and aid intensity forecasts. Significantly, the first appearance of the pinhole eye on IR imagery occurred only two and a half hours before these passes (Figure 4.17), which already show these established rain bands encircling the new eye. This observation suggests that, as with 2019 Lorenzo, the development of the outer eye was already underway while the inner eye was being established, unlike classic ERCs.

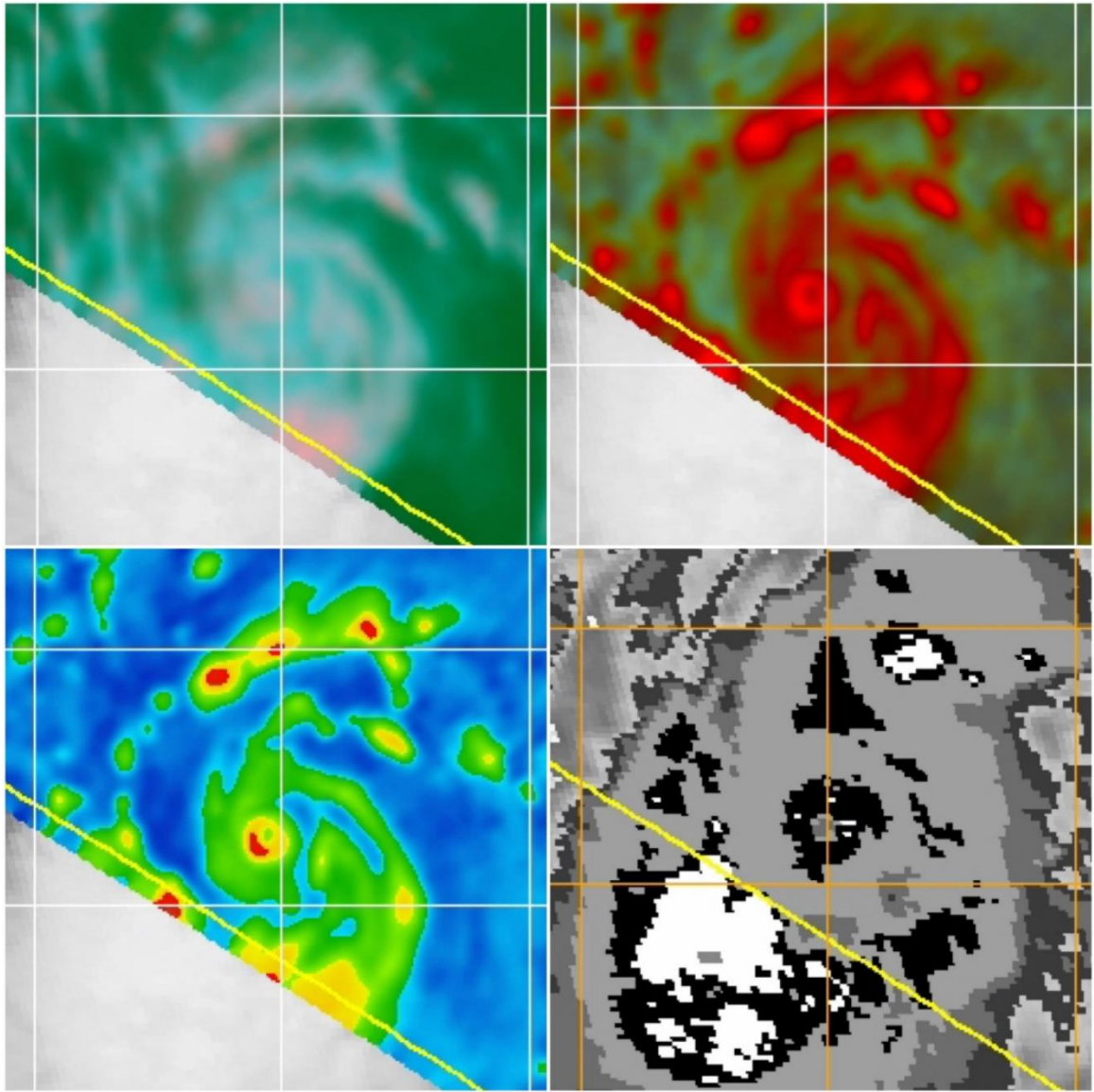


Figure 4.18 2004 Karl precipitative banding surrounding the small eye. An 18/0730Z TRMM shows precipitative banding from the head of the principal band surrounding the just-formed small eye. The pink ice signature encircling the small eye can be made out on the 37color image but is not prominent. For clarity, since the eye is difficult to see in the lower resolution of the 37 GHz channel, the 85color, 85h, and EIR_BD TRMM images are supplied. Significantly, the first appearance of the pinhole eye on IR imagery occurred only two and a half hours before these passes (Figure 3.17), which already shows established rain bands encircling the new eye: the developing SEF. This suggests that, as with 2019 Lorenzo, the development of the outer eye was already underway while the inner eye was being established.

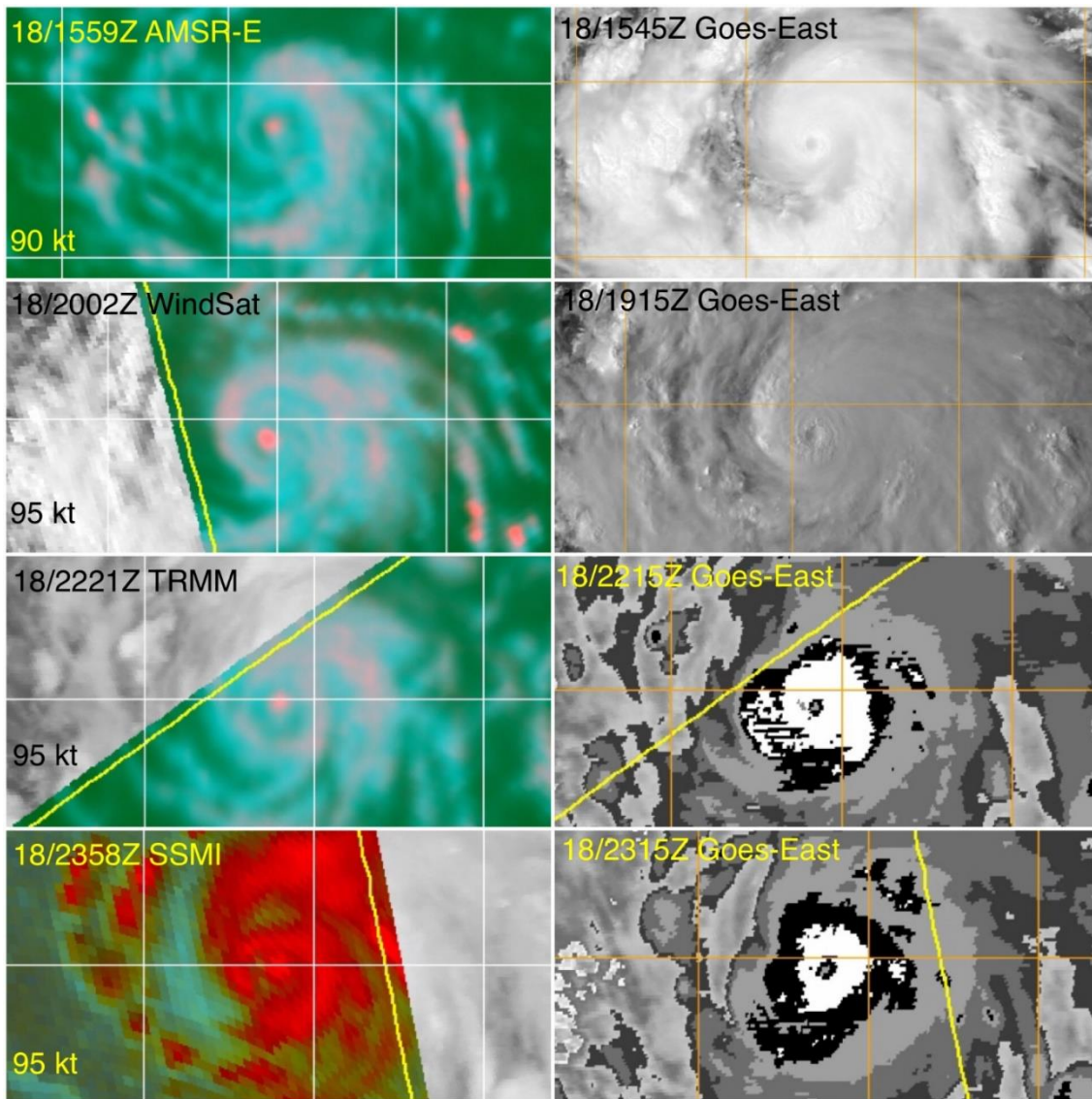


Figure 4.19 SEF development on PMW imagery for 2004 Karl. Seen over a period of eight hours, with corresponding geostationary imagery showing the inner eye but with no evidence of the developing secondary eyewall. As with “classic” ERCs, conventional satellite imagery does not show the convective banding under the cirrus overcast, while PMW imagery reveals it.

A well-defined concentric convective band and moat developing into the SEF were clearly observed on 18/1559Z AMSR-E, 18/2002Z WindSat / 18/2102Z F-13 SSMI, 18/2221Z TRMM, and 18/2358Z F-15 SSMI. During this period the inner eye remained

distinct on geostationary satellite imagery but with no hint of concentric eyewalls (Figure 4.19), as is typical during ERCs.

Examining the PMW passes during the time of the SEF and the ERC completion and corresponding EIR-BD imagery in more detail (Figure 4.20), and focusing on the different TC structure as depicted in the 37color and 85color/85h imagery, we see in the first column that the 37color clearly shows a symmetric, concentric convective band surrounding the inner eye. It consists of moderate convection (aqua color – warm precipitation – but little established ice signature indicating deeper convection except along the area embedded in the principal band) and also a well-established moat between the two. The 85color and 85h only see the deep convection associated with the inner eye and the principal band at this time. Again, these observations establish the value of the 37color imagery in showing important details of TC structure that cannot be observed with any other satellite imagery. Note that the 37color at this time appears to show the secondary convective banding as being essentially the head of the principal band, again not consistent with classic ERC development.

In the second column of Figure 4.20 we see on the 37color that the secondary eyewall has established deep convection all around as the ice signature is present throughout the entire ring. This is also clear on the 85color and 85h images, which, unlike the s image from six hours earlier, show a clear double eyewall structure, with the outer eyewall linked to the principal band structure. During the time of the first two passes, the EIR-BD shows a CDO with only the well-defined inner eyewall.

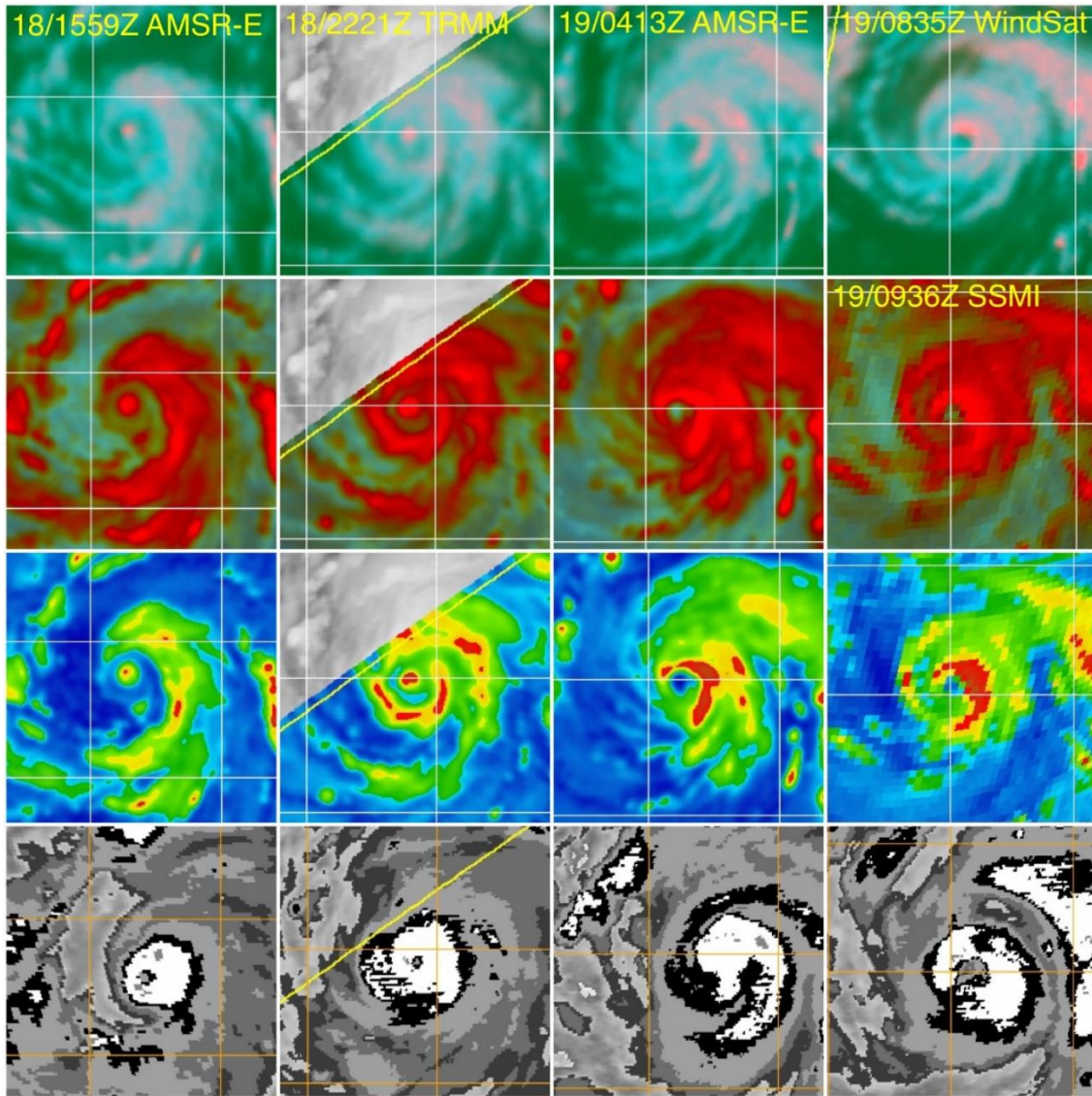


Figure 4.20 SEF and completing ERC comparing PMW and EIR-BD imagery for 2004 Karl. In the first column, an AMSR-E pass shows the developing secondary eyewall on 37color, but not on the 85color and 85h imagery, and the EIR-BD images only show the inner eye. However, in a TRMM pass six hours later, in the second column, both eyewalls are present on the 85color and 85h. In another AMSR-E pass about six hours later, the third column, the ERC is nearly complete but a remnant inner eye remains, apparent on the 37color, but the 85color and 85h show only the new larger eye. On EIR-BD, the eye is no longer present. In the fourth column, in WindSat and SSMI passes from 4-5 hours later, the new eye is established, no remnant eye is present on the 37color, and the larger eye is well-defined on EIR-BD.

In the third column of Figure 4.20 the ERC is completing, with the 37color showing the outer eyewall has contracted, and also showing a residual inner eye, notably moved from the center to a position where it is along the edge of the new larger outer eye, and showing a stronger ice signature associated with the outer eyewall. It also shows the principal band being reestablished further away from the core to the northeast of the center. These changes are also reflected on the 85color and 85h, but they do not show the remnant eyewall, which has no deep convection. At this time the EIR-BD signature had changed significantly with the small eye no longer visible and a CDO accompanied now by a new signature of colder cloud tops due to outer banding.

In the fourth column of Figure 4.20 the ERC had completed. The 37color showed an even stronger ice signature in the eyewall, and also showed another ERC is beginning with a developing outer deep convective band partially established around the eye. It also showed a stronger ice signature in the new principal band that was established northeast of the center, and the core convection was significantly symmetric even with some banding of moderate convection south and west of the center. On the 85color and 85h the appearance of a symmetric core of deep convection was even more strongly apparent. On the EIR-BD a new much larger eye with a symmetric CDO was well-established. The eye did not cloud over until just before the ERC completed. As with most ERCs, geostationary satellite images provide little information about ERCs until just before completion.

NHC forecast discussions from 18/1500Z and 18/2100Z noted " A SMALL WELL-DEFINED EYE" but did not make note of the concentric convective rings seen in the

PMW passes between around 18/1600Z and 18/2200Z, but the 19/0300Z did note the concentric eye in the SSMI pass around 19/0000Z forecast discussion:

"INFRARED SATELLITE IMAGERY HAS SHOWN THAT THE EYE DIAMETER HAS GOTTEN SMALLER DURING THE PAST SIX HOURS...SUGGESTING THAT THE STORM IS STRENGTHENING...WHICH THE INTENSITY ESTIMATES ABOVE CONFIRM. A 2357Z MICROWAVE SATELLITE IMAGE ALSO GAVE SUPPORTING EVIDENCE FOR THIS...SHOWING A DOUBLE EYEWALL WITH THE INNER EYE JUST ABOUT TO COLLAPSE AND DISAPPEAR. THE EYEWALL REPLACEMENT CYCLE SCENARIO REQUIRES THE WIND SPEED TO DECREASE AS THE OUTER EYE BECOMES DOMINANT AND REPLACES THE DISAPPEARING INNER ONE. THIS IS REFLECTED IN THE INTENSITY FORECAST AT THE 12 HOUR TIME FRAME."

In 2004 observing ERCs using PMW imagery was fairly new, hence the explanatory tone in the discussion. In this case Karl did not have a reduction in intensity due to the ERC, but the best track does show a brief period where intensification halted between 18/1800Z and 19/0000Z with 95 kt intensity at both best track points. Otherwise this early ERC was embedded in a longer period of intensification (Figure 4.10).

With the onset of frequent PMW passes over tropical cyclones, ERCs could be observed readily. The result was the conclusion that ERCs were much more common than previously thought. A nine-year study (Hawkins et al 2004, Hawkins et al 2006) of PMW imagery of TCs reaching 120 kt or greater in the life cycle found that in the Atlantic basin 70% had an occurrence of concentric eyewalls, and 50% in the East Pacific basin.

On the 19/0900Z the forecast discussion notes, "THE DISAPPEARANCE OF THE SMALL EYE PREVIOUSLY OBSERVED" and "INFRARED IMAGERY SUGGESTS

THAT AN OUTER EYEWALL MAY BE STARTING TO BECOME BETTER DEFINED." This would likely reflect imagery from a few hours prior to the release of the forecast advisory package, and probably refers to a larger CDO appearing on EIR-BD imagery. But we know from an analysis of the 19/0835Z WindSat and 19/0936Z SSMI in Figure 3.20 that at this time the ERC had completed because the inner eye had dissipated and a well-defined eyewall signature was evident on a contracting outer eyewall.

A large eye was apparent on a 19/0715 Goes-East EIR-BD, and a clearing larger eye on a 19/0915Z Goes-East VIS, and subsequently on a 19/0815 Goes-East EIR-BD, and 19/0945 Goes-East VIS, and finally with the eye completely cleared out on a 19/1215Z Goes-East VIS (images not shown). Subsequently the NHC 19/1500Z forecast discussion noted, "THE EYE IS WELL DEFINED ON SATELLITE IMAGERY," with an eye diameter of 15 nm noted on the forecast advisory. Karl underwent a later ERC, where the newly formed larger eye was contracting, as apparent on PMW imagery on a 19/2303Z TRMM (image not shown), and that second ERC completing only twelve hours after the eye completely cleared out from the first ERC.

The complete cycle of the development of the initial eye through to the completion of the ERC, on 37color imagery, is shown in Figure 4.21. Even though other satellite imagery, specifically 85 GHz channel and geostationary satellite imagery, supports the structural evolution, some characteristics can only be seen on the 37color. This is particularly true

of moderate convective structures. A comprehensive understanding of the TC

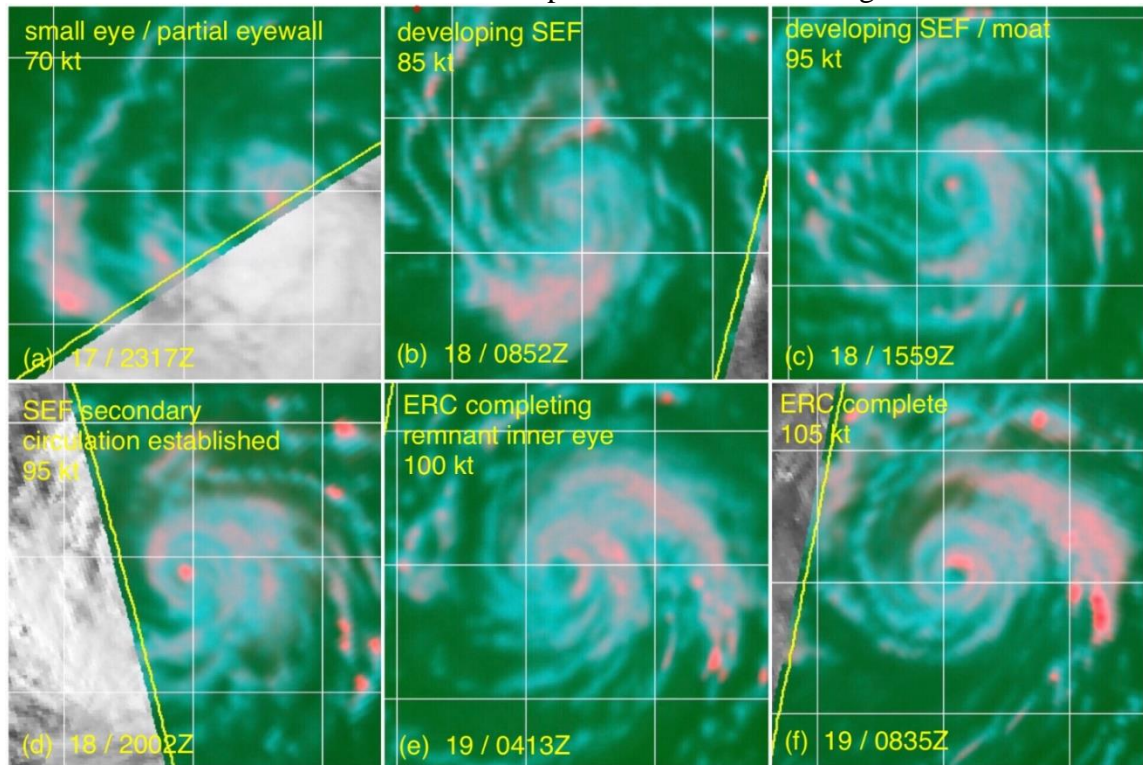


Figure 4.21 The complete early ERC development of 2004 Karl on the 37color. Beginning with a developing small eye (a), the newly-established eye surrounded with precipitative banding from the head of the principal band (b), development of concentric and symmetric convective banding and a moat around the small inner eye that appeared to be an evolution of the principal band (c), SEF development evidenced by the concentric ice signature around the outer convective band, indicating tilted convection and a strong secondary circulation exist (d), ERC completing with reduction in size of the secondary eyewall and a small remnant inner eyewall apparent (d), and the ERC completed with the inner eyewall dissipated and the secondary eyewall well-established (e). As the ERC completes, a new principal band establishes itself and moves outward from the core. Also in (f) a new secondary eyewall has already formed, as in a “classic” ERC development.

precipitative features on 37color imagery can provide an earlier and clearer understanding of evolution of the TC structure.

In conclusion even though the development of the SEF was well-observed on PMW beginning at 18/1600Z, it was not noted in the NHC forecasts until 19/0300Z. The

mention at 19/0900Z, when the ERC was completing, that an outer eyewall was becoming better defined on infrared imagery suggests that expectations of an ERC were tied to concentric eyewalls as observed in geostationary satellite imagery rather than in PMW imagery. As with Lorenzo, this "early" ERC only became apparent on geostationary satellite imagery as it was completing, and as in Karl's case, the only a suggestion of an outer eyewall is tied to expansion of the CDO on EIR-BD images.

4.3.3 Case Study Three: 2006 EPAC Hurricane Daniel

These early ERC cases are not common – with only four identified at this time in almost a twenty-year period of PMW imagery (and with much of the EPAC imagery not yet searched for this phenomenon), but 2006 Hurricane Daniel did demonstrate that the "early ERC" phenomenon was not limited to the Atlantic basin.

4.3.3.1 Daniel Developing Eye

The 18/2100Z forecast advisory upgraded Daniel to a minimal hurricane and the forecast discussion noted, "A BANDING TYPE EYE FEATURE APPEARS TO BE FORMING....SHOULD DANIEL GO ON AND FORM AN EYE LATER TODAY...THE CYCLONE COULD STRENGTHEN MORE RAPIDLY THAN SHOWN BY THE OFFICIAL FORECAST." During this forecast period an 18/1327Z WindSat and 18/1621Z SSMI showed that while Daniel's convection was rather sparse and dry air appeared to be wrapping into the center, a banding eye was forming as the top of a small principal band was curving around the center (Figure 4.22 first column). Forecasts had noted favorable environmental conditions of low shear, warm SSTs, and good outflow.

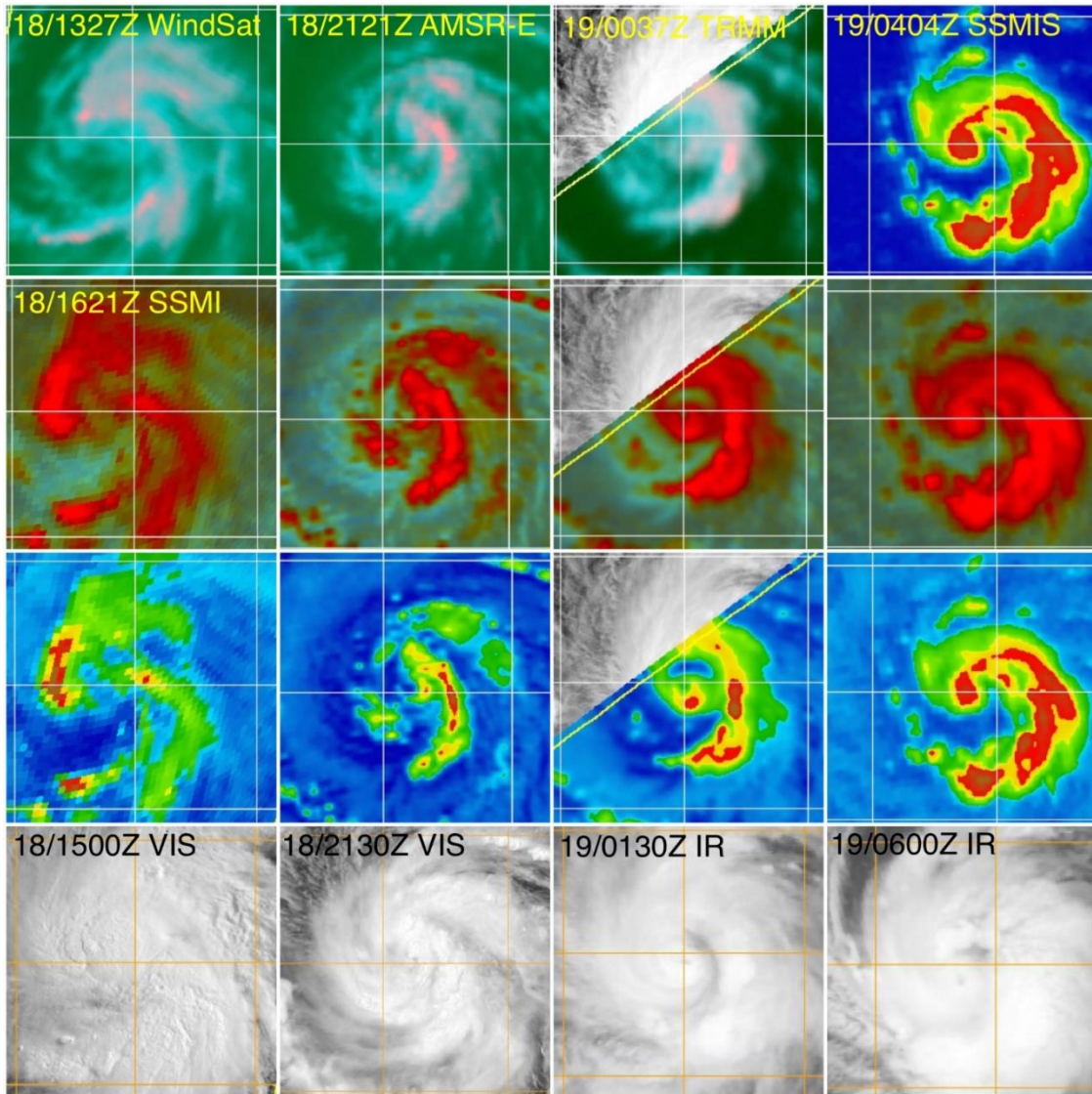


Figure 4.22 Eye development of 2006 Hurricane Daniel. Shown between 18/1300Z and 18/0600Z. The WindSat is shown in tandem with a concurrent SSMI, and visible or infrared imagery closest in time to the PMW passes are shown at the bottom. The top row is 37color imagery except for the SSMIS at 19/0404, which is too low resolution, and instead is used to show the SSMIS 150h. The second row is 85color imagery and the third, 85h. In the last column, note that while the eye is visible on the 18/0600Z IR (and could be made out on the 18/0500Z and 18/0530Z images but not quite as clearly), the eye is too small to be well-defined on the 85h and the 150h images at around 18/0400Z, suggesting that it was extremely small. In the TRMM pass in column three, the eyewall completely encircles the eye on the 37color and 85color but the strongest convection on the 85h shows an ice signature about $\frac{3}{4}$ of the way around the eye.

The 19/0300Z forecast discussion observed, "A SMALL EYE IS BECOMING MORE EVIDENT IN THE CENTRAL DENSE OVERCAST." An 18/2121Z AMSR-E showed a partial eyewall and partial secondary circulation had become established around a small center and A 19/0037Z TRMM suggested a small eyewall has formed with convective banding completely surrounding a tight center. An ice signature on the 85color wrapped completely around the center, indicating the maturing of the secondary circulation. A pinhole eye was seen at this time on 19/0130Z Goes-East IR (Figure 4.22 second and third columns).

And at 19/0900Z, "AN EARLIER SSMIS OVERPASS SUGGESTED THAT DANIEL WAS DEVELOPING A BANDING EYE FEATURE. ENHANCED INFRARED IMAGERY NOW DEPICTS A WARM SPOT...INDICATING POSSIBLE PIN HOLE EYE DEVELOPMENT WITHIN THE CORE CONVECTION." This was the 19/0404Z pass which showed an eye too small to resolve on both the 91h and 150h, which is rare. In spite of this difficulty, starting at 19/0500Z a pinhole eye was apparent on infrared imagery, suggesting that in spite of its small size it was a mature eye (Figure 4.22 last column). A good example of how the 150h channel resolved a small eye that was not observed in the 85h is shown in Figure 4.23, two sets of images spaced about 24 hours apart showing 2008 22S Jokwe transiting the Mozambique Channel from Madagascar to the African coast.

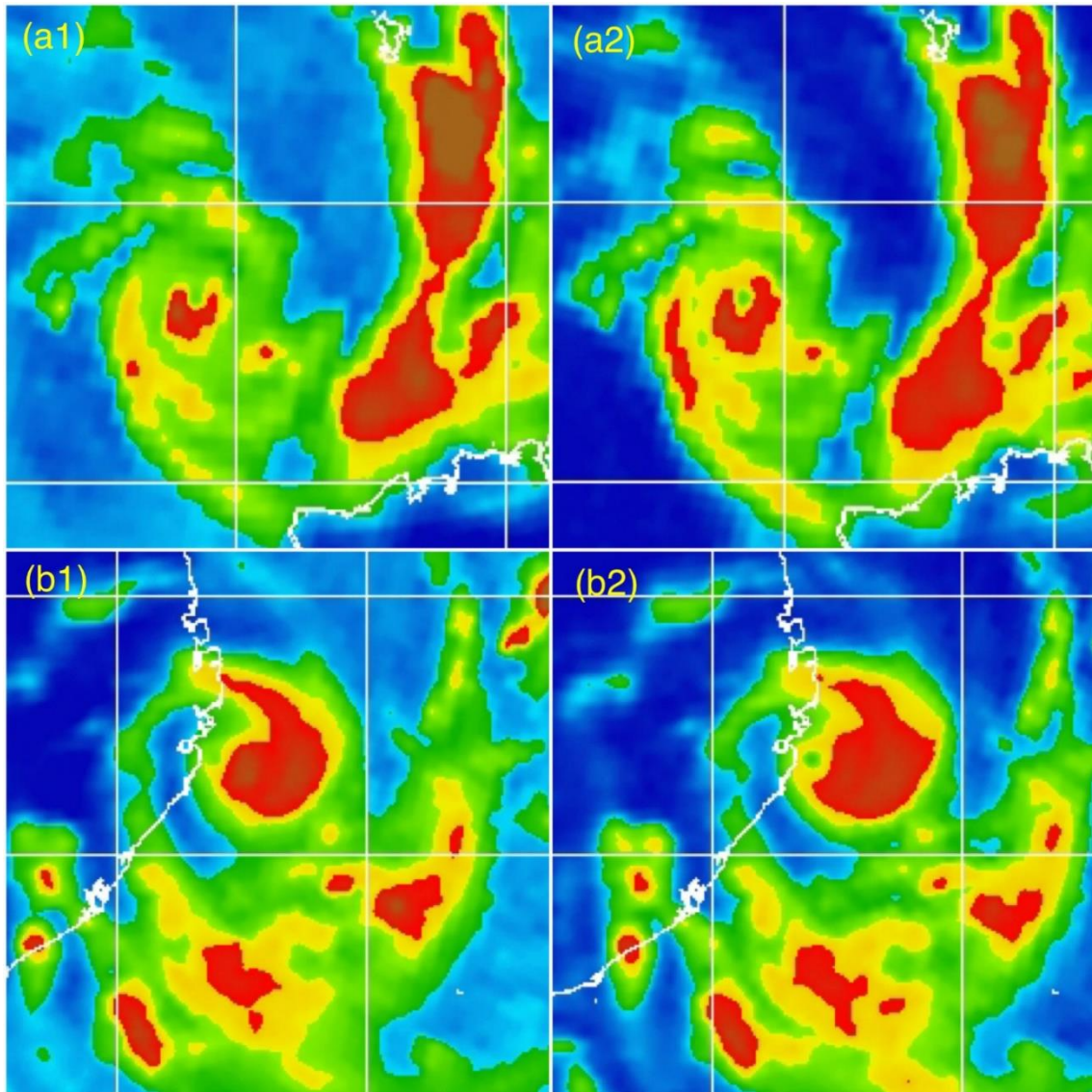


Figure 4.23 2008 Cyclone Jokwe in the Mozambique Channel comparing 85h and 150h imagery. Figures (a1) and (a2) are the same 07/0452Z SSMIS pass with (a1) the 85h image and (a2) the 150h. The lower two images are the same but for a day later at 08/0440Z SSMIS pass. In both images the small eye is not completely resolved in the 85h (left side) but is resolved on the 150h (right side). Usually the 150h can resolve small mature eyes, but not the smallest eyes. Note: this figure was brought to the attention of the tstorms listserve in 2008 by Philippe Caroff of Meteo France.

4.3.3.2 Daniel SEF Development and ERC Completion

At 19/1500Z, "A BANDING TYPE EYE HAS RECENTLY BECOME EVIDENT IN CONVENTIONAL SATELLITE IMAGERY...THE EYE FEATURE HAS BECOME BETTER DEFINED DURING THE PAST HOUR OR SO." As shown in Figure 4.24, a 19/0936Z AMSR-E showed an extremely small eye resolved only on the 85color and 89h, and the 37color also indicated a small eye with deep convection by a small strong ice signature at the center. Significantly it also showed that the head of the principal band had become a developing outer eyewall wrapping almost completely around the center. Another interpretation was that a partial outer band wrapped around about three-quarters of the way around with a moat between it and the eye on the 85h and 85color. A 19/1028 TRMM pass showed much the same, however after the passage of only an hour, the 37color showed the inner eyewall as not as intense, the outer eyewall had developed more extensive precipitation, and had contracted to a smaller diameter. This TRMM pass also was close enough to the center so that the PR radar captured both the inner and outer eyewalls. The 19/1330Z and 19/1400Z Goes-East infrared images showed concentric eyewalls, but this event may have occurred too late to be mentioned in the 19/1500Z advisory. Figure 4.25 is a close-up of the 19/0936Z AMSR-E 85color and 85h, showing the extremely small eyewall. At this time the infrared imagery mentioned in the forecast discussion showed a suggestion of development of an outer eyewall (Figure 4.26 first row) but it was not noted in the discussion because an ERC at this intensity was not anticipated (as was made clear in the subsequent discussion).

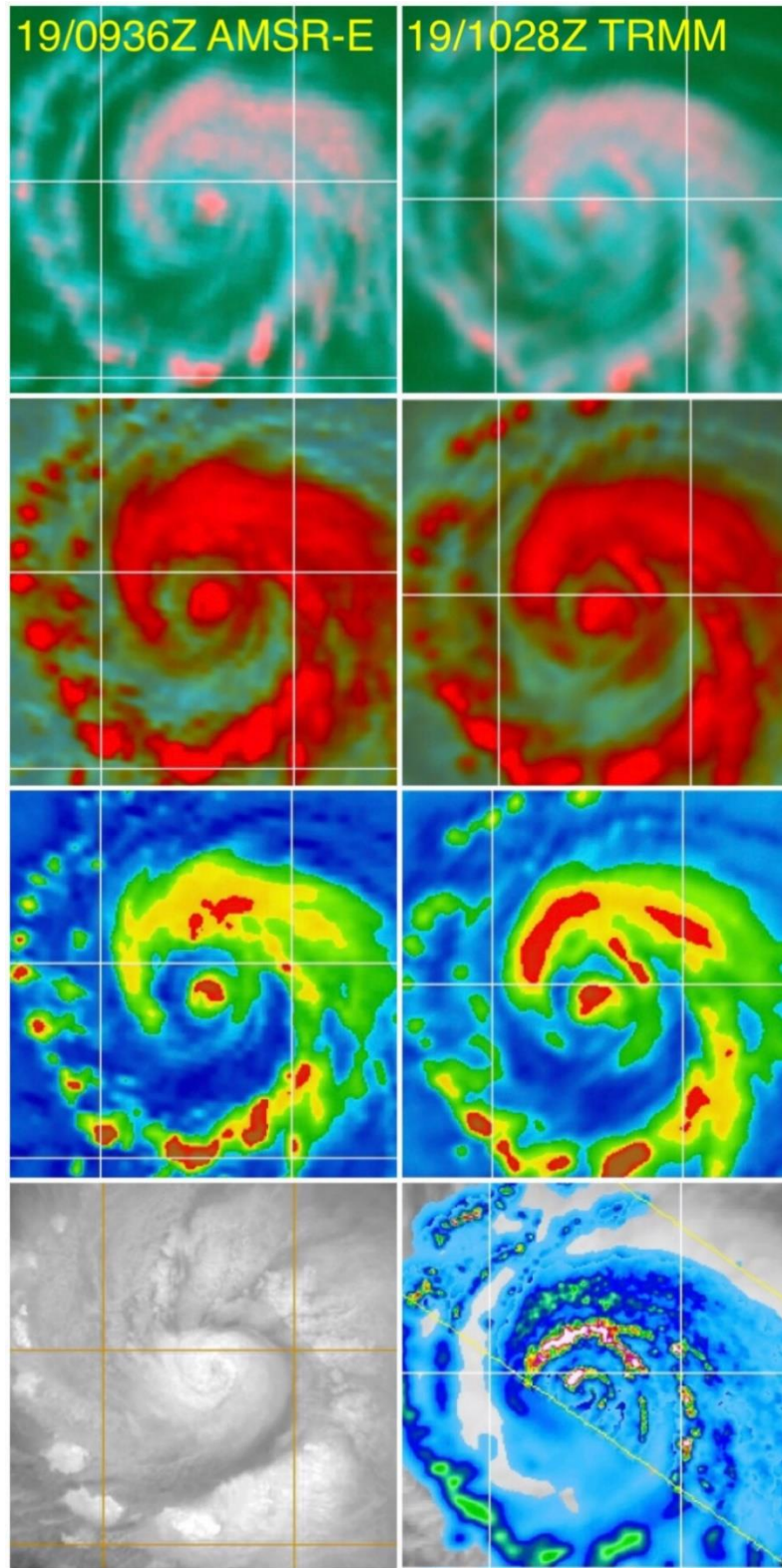


Figure 4.24 Development of 2006 Daniel's secondary eyewall from the head of the principal band.

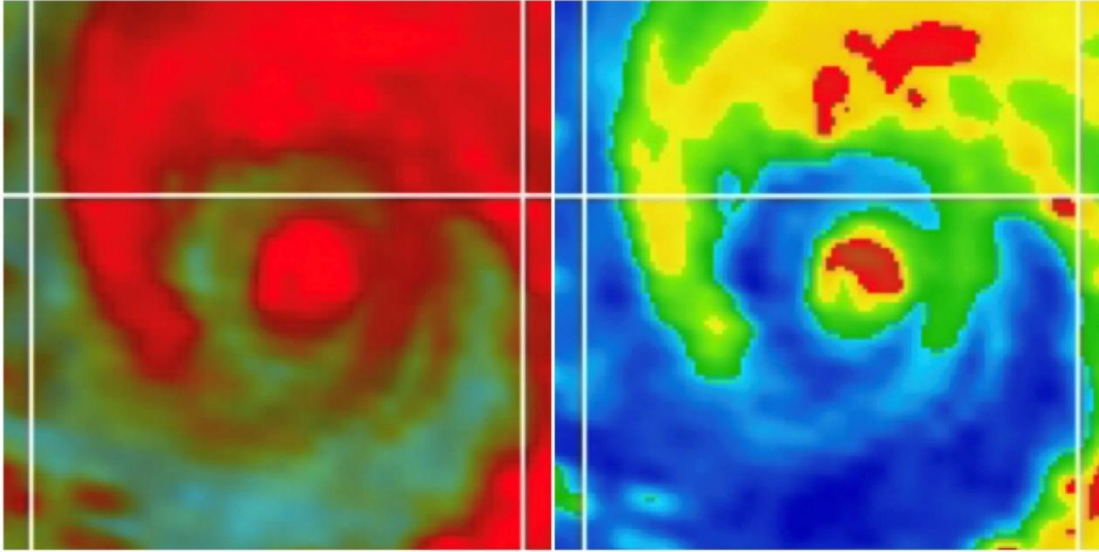


Figure 4.25 Close-up of the extremely small eye for 2006 Daniel. Seen on the 19/0936Z AMSR-E in the preceding figure.

The unusual nature of the early ERC was noted in the 19/2100Z forecast discussion, "VISIBLE SATELLITE IMAGERY REVEALS A VERY SMALL PINHOLE EYE SURROUNDED BY A MUCH LARGER CONCENTRIC EYEWALL. DESPITE THE APPEARANCE IN VISIBLE IMAGERY...DVORAK SATELLITE INTENSITY ESTIMATES REMAIN UNCHANGED AT 77 KT FROM ALL AGENCIES. RAW CIMSS ADT INTENSITY ESTIMATES SINCE 1800 UTC HAVE BEEN MUCH HIGHER...AROUND T5.5 OR ABOUT 100 KT. THE INITIAL INTENSITY WILL REMAIN AT 85 KT...A BLEND OF THE SUBJECTIVE AND OBJECTIVE ESTIMATES." It also added, "THE SMALLER INNER EYEWALL WILL LIKELY COLLAPSE WITH THE LARGER EYE CLEARING OUT AND BECOMING THE DOMINANT FEATURE. ONCE THIS OCCURS ADDITIONAL STRENGTHENING IS ANTICIPATED." The best track maintained 85 kt intensity for 19/1800Z. Beginning at 19/0730Z concentric symmetric eyewalls were apparent in visible imagery, with the

secondary eyewall becoming dominant by 19/1900Z, and the eye clearing out and the convection in the inner eyewall appearing weaker (Figure 4.26 second row).

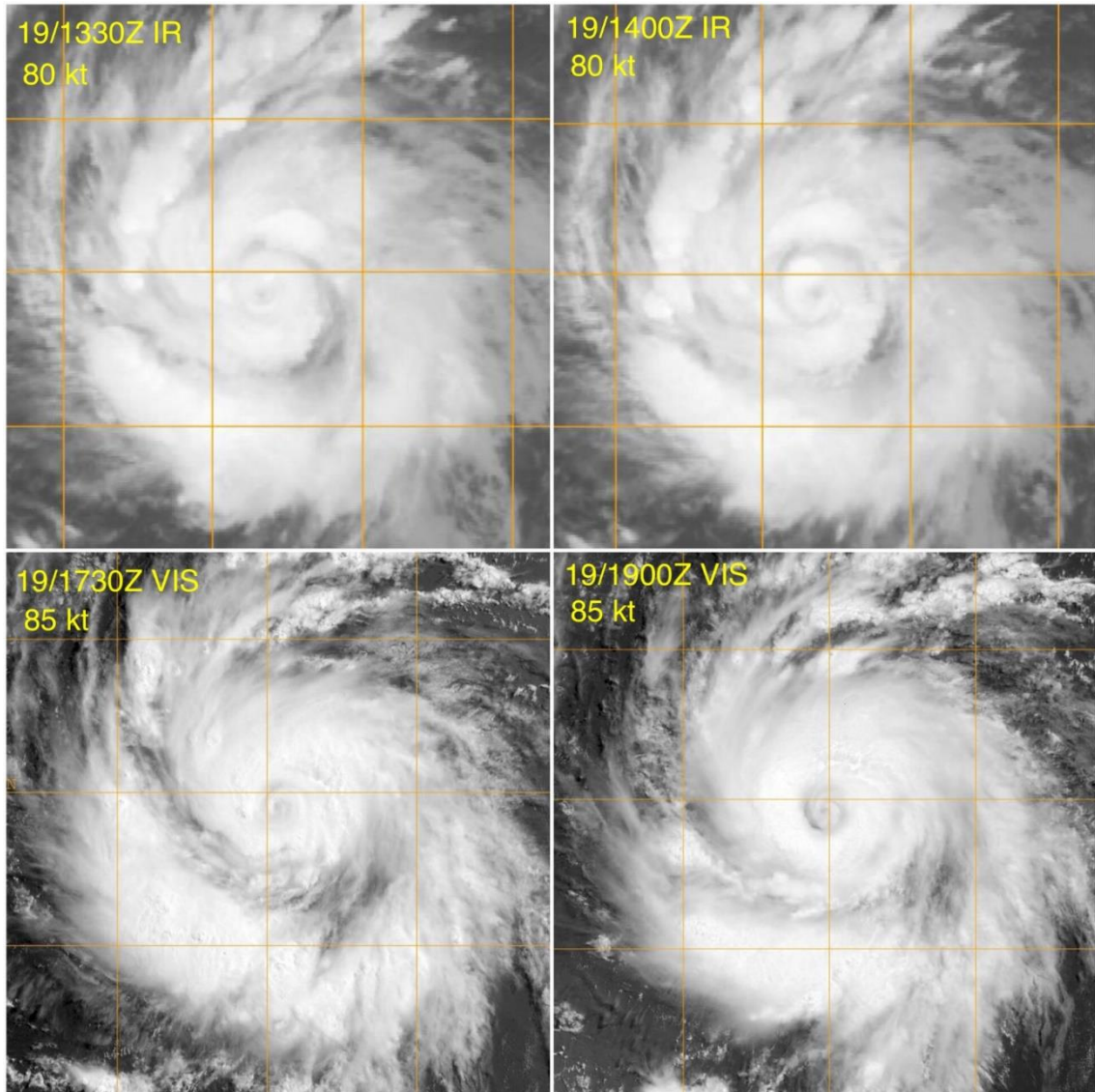


Figure 4.26 Appearance of double eyewalls in Hurricane Daniel on IR and VIS imagery.

The 20/0300Z forecast advisory increased the intensity by 10 kt, to 95 kt, while the forecast discussion noted the ongoing ERC, "THE LATEST SATELLITE AND MICROWAVE IMAGES SUGGEST THAT DANIEL HAS NOT FINISHED ITS

EYEWALL REPLACEMENT CYCLE. WHILE CONVECTION HAS BECOME STRONGER IN THE OUTER EYEWALL...THE INNER EYEWALL HAS ALSO BECOME BETTER-DEFINED DURING THE PAST FEW HOURS. Visible imagery from GOES-East between 20/0000Z and 20/0130Z show deep convection returning to the inner eyewall (Figure 4.27) – an unusual occurrence. These were the last available visible images of the day. The 95 kt 20/0300Z forecast current intensity was also maintained in the 20/0000Z best track.

A 20/0158Z WindSat (Figure 4.28 lower left) showed a well-defined outer eyewall with a remnant inner eye that nevertheless had a strong precipitative and ice signature along the northern edge. Only two hours later a 20/0352Z SSMIS pass showed an intense outer eyewall and no inner eyewall convection on the 85color and 89h (Figure 4.28 top row), indicating the ERC had completed. However, the remnant inner eyewall is still visible on a 20/0230Z Goes-West IR and there is a small curved area of cold cloud tops associated with it on the EIR-BD (image not shown). The 20/0900Z forecast advisory observed, "SHORT-WAVE VISIBLE AND INFRARED SATELLITE IMAGERY...AS WELL AS AN EXCELLENT SSMIS OVERPASS FROM AROUND 0400 UTC...INDICATE DANIEL'S EYEWALL REPLACEMENT CYCLE IS NOW COMPLETE." So, the PMW in this case was used to identify the completion of the ERC even though the eye took some time to completely clear out after this time on visible and IR.

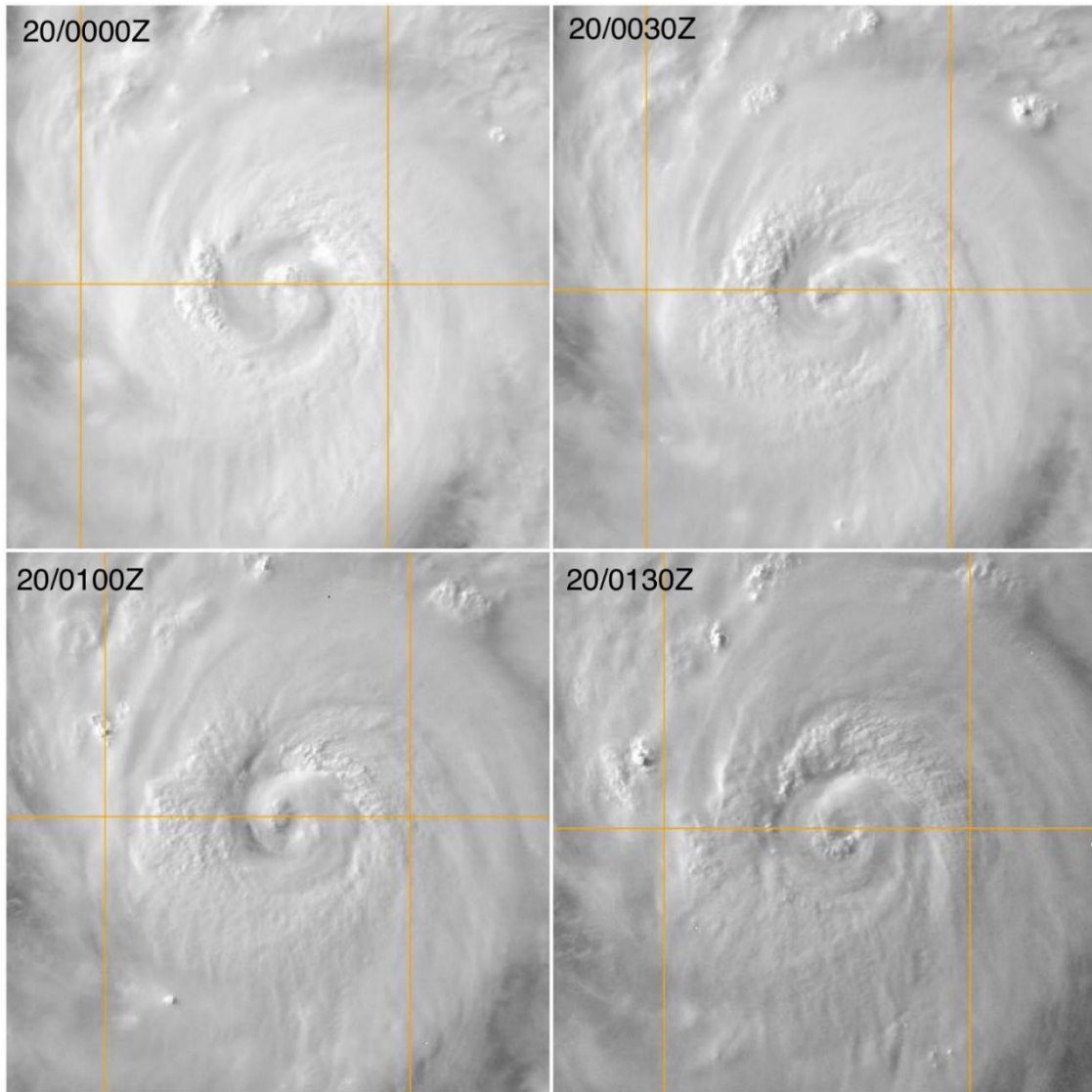


Figure 4.27 Inner eyewall of 2006 Daniel briefly becomes prominent on VIS imagery. Images are of Goes-West between 20/0000Z and 20/0130Z.

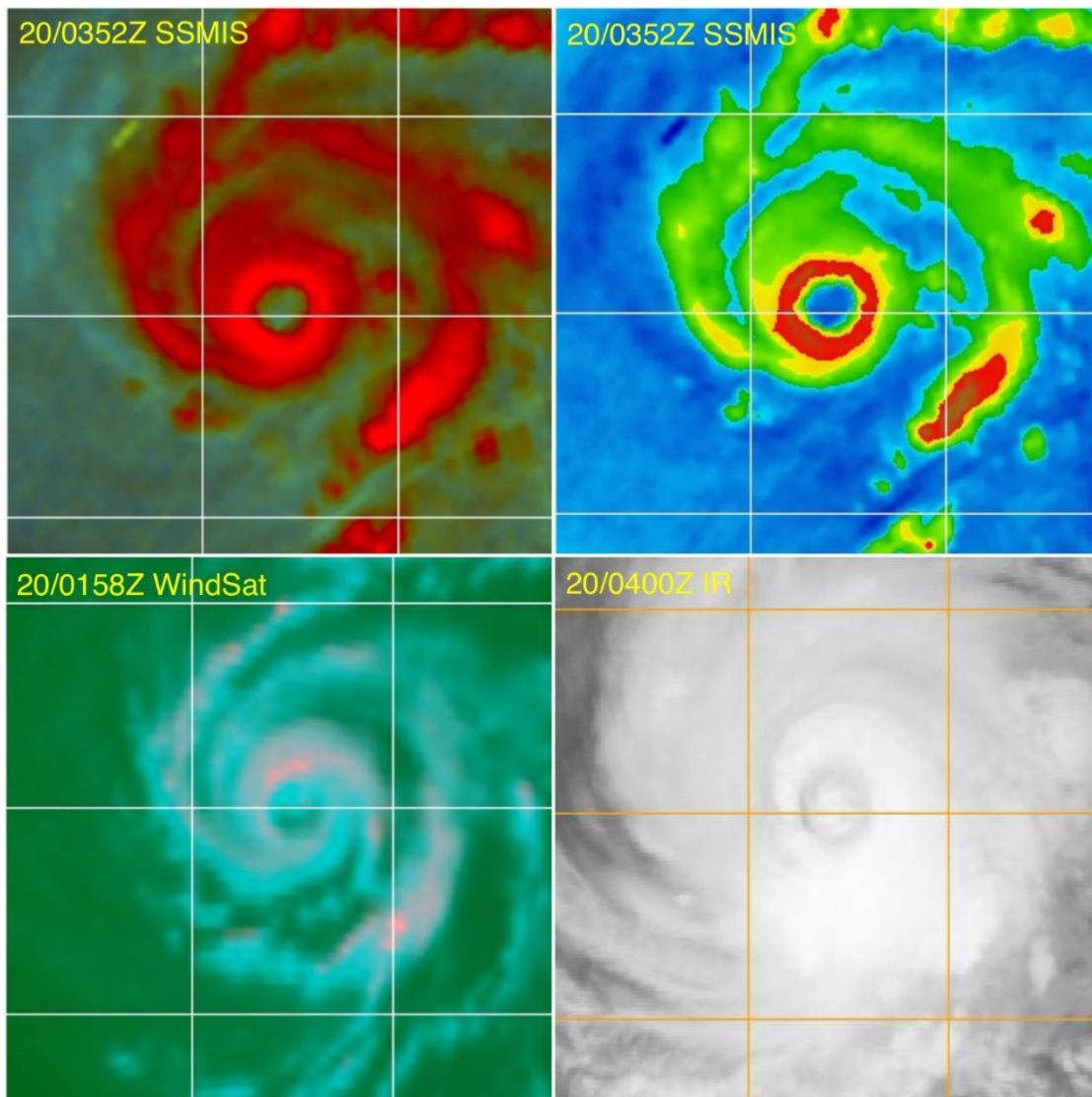


Figure 4.28 PMW and IR structure of 2006 Daniel when the completion of the ERC was noted on NHC discussion. Note that while the SSMIS 85color and 85h images show a strong ring of convection in the outer eyewall and no trace of convection in the inner eyewall, the concurrent IR image shows the outer eye is not yet completely cleared, and a 37color WindSat pass from two hours earlier showed a small remnant eye along the inner edge of the well-defined secondary eyewall. In this case a "microwave eye" is considered an eye even if it has not completely cleared out on conventional satellite imagery, because the remnant eye seen in the second row has no deep convection.

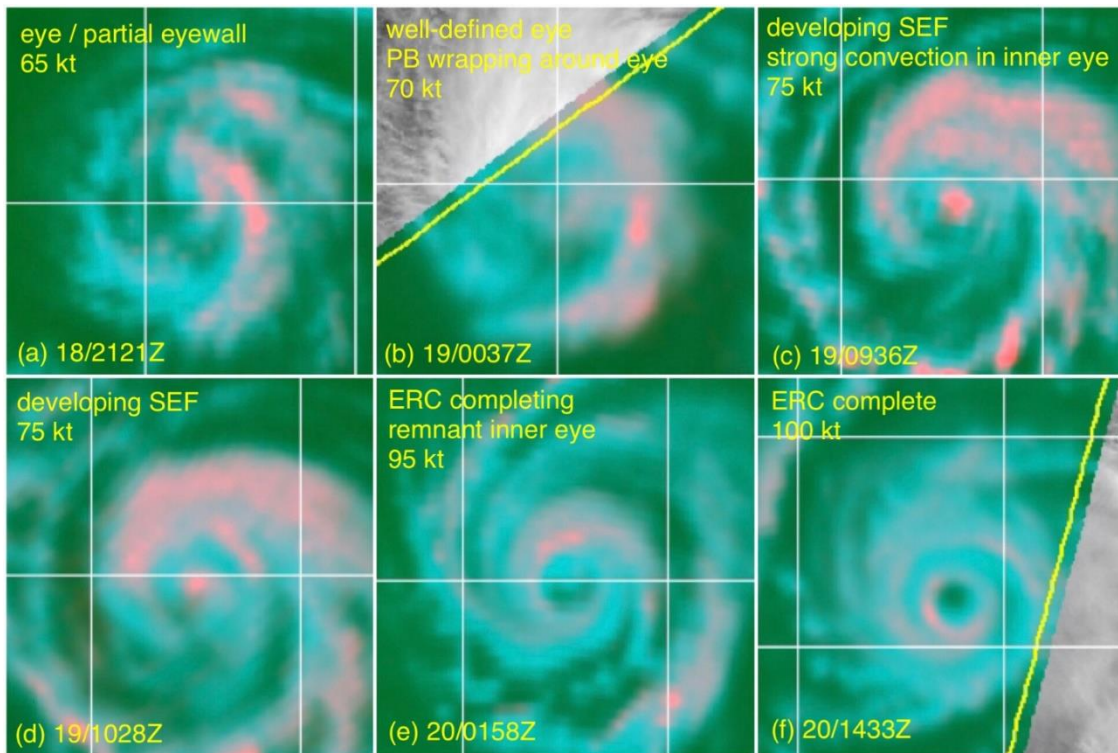


Figure 4.29 The early ERC of 2006 Daniel. Note that there was only an hour time difference between figures (c) and (d), then about a 15-hour time difference between (d) and (e). The ERC was determined to be completed at (e) but the eye did not clear out for another 12 hours, when a second ERC was about to occur.

The complete early ERC of 2006 Hurricane Daniel is shown in Figure 4.29. The developing eye and partial eyewall, and a small curved principal band surrounding it, occurred at 65 kt intensity (a). Only three hours later a well-defined small eye appeared in PMW imagery at 75 kt intensity (b) and also on IR. On two closely-timed PMW passes from 19/0936Z and 19/1028Z, (c) and (d), development of the SEF is observed with the band wrapping from the head of the principal band around a very small, distinct eye with a strong convective signature. The ice signature associated with the northern half of the secondary eyewall shows that the secondary circulation of this banding eye is well-established. There is no clear moat seen between the inner eye and developing outer

eyewall and the precipitative banding is profuse, but only three hours later, during a stretch when no PMW overpasses occurred, concentric eyewalls were apparent on IR. The first available PMW pass after this time shows the ERC completing (e) with a remnant inner eyewall attached to the inner edge of the by now well-defined and strong convective outer eyewall. The eye did not clear out completely until twelve hours later (f) when a second ERC appears to be developing.

The best track dropped the 20/0900Z intensity of 100 kt to 95 kt at 20/0600Z and the TCR (Beven, 2007) noted, "intensification was briefly halted" with the two best track points of 95 kt at 20/0000Z and 20/0600Z, but they were the only track points with no increase. The ERC was part of an intensifying event that began shortly after being designated as a depression and continued over a four day period to 21/0000Z with a peak of 120 kt.

4.3.4 Case Study Four: 2007 WPAC Yutu

2007 Super Typhoon Yutu developed quickly from a disturbance located southwest of Guam. With initial eye development, JTWC observed a "distinct eye *feature*" (Figure 4.30 (a)) referencing PMW imagery, shortly before upgrading to a typhoon, but an eye was not apparent on conventional satellite imagery until the ERC had completed. Its intensity increases were not well-anticipated in the forecasts. The ERC occurred over about a 36-hour period, from 18/1800Z through 20/0600Z, gaining 50 kt (Table 4.1). Like the other cases examined in this study, the SEF formed from extension of the head of the principal band, with the principal band itself wrapping to some extent around a small inner eye seen in (b) and (c). There was a steady intensity increase during the early

ERC, and Yutu reached super typhoon intensity of 130 kt right after completion of the ERC. As the ERC was completing the secondary eyewall contracted significantly (d) and (e). A second ERC began hours after the first one had completed (f) as intensification continued.

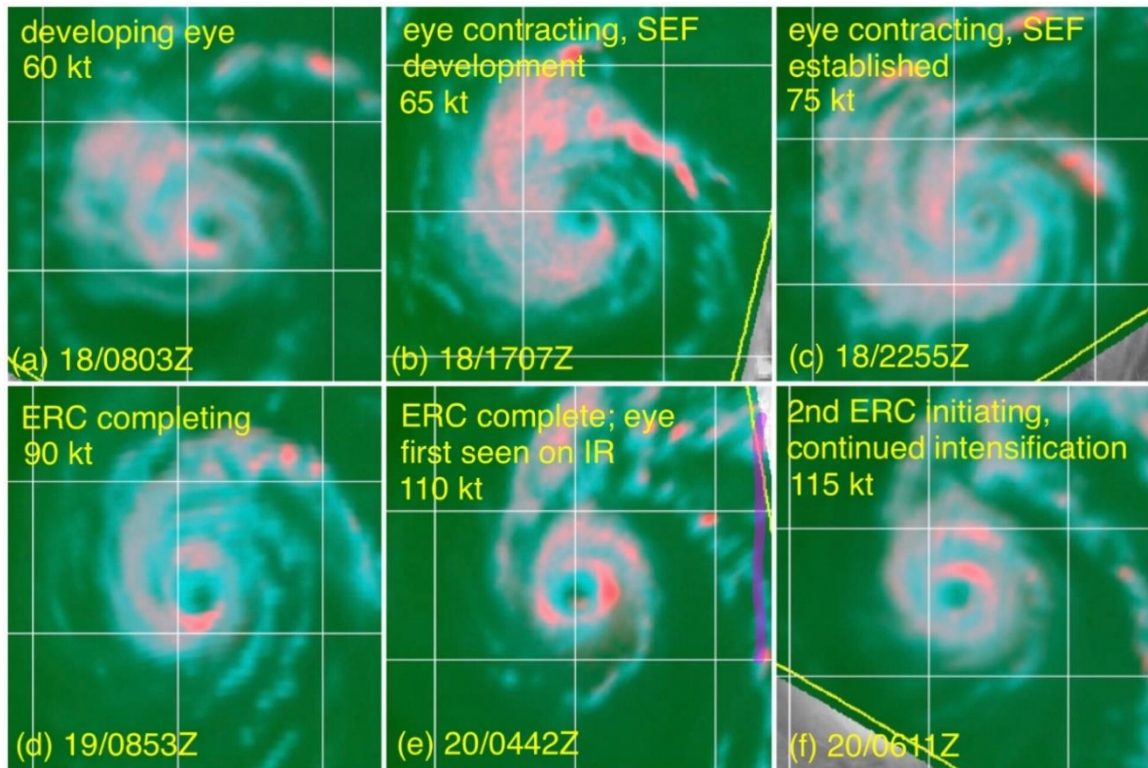


Figure 4.30 The early ERC of 2007 Super Typhoon Yutu, with early SEF prior to mature inner eye. The SEF forms from head of the principal band, which wraps around the inner eye, and, after completion of the ERC, an immediate development of another outer convective band leading to a second ERC and additional intensification.

WP	02	2007051700	85N	1410E	30	1000	TD
WP	02	2007051706	90N	1394E	35	997	TS
WP	02	2007051712	97N	1378E	45	991	TS
WP	02	2007051718	107N	1369E	45	991	TS
WP	02	2007051800	116N	1360E	55	984	TS
WP	02	2007051806	124N	1347E	60	980	TS
WP	02	2007051812	132N	1337E	65	976	TY
WP	02	2007051818	140N	1328E	65	976	TY
WP	02	2007051900	150N	1323E	75	967	TY
WP	02	2007051906	161N	1321E	85	958	TY
WP	02	2007051912	169N	1323E	95	952	TY
WP	02	2007051918	177N	1328E	105	938	TY
WP	02	2007052000	183N	1335E	105	944	TY
WP	02	2007052006	191N	1344E	115	937	TY
WP	02	2007052012	199N	1354E	130	926	ST
WP	02	2007052018	207N	1364E	130	926	ST

Table 4.1 2007 WPAC Yutu Best Track. This shows the portion of the best track during eye development and the early ERC (highlighted).

4.4 Similarities and Conclusions

Most important to this study of early ERCs, the 37color composite imagery is the only imagery that can observe key precipitative features of the tropical cyclone structure for this phenomenon, especially regarding observation of small details. Without this imagery, we would not have been able to observe these early ERC cases, as shown in comparisons with 85color and 85h imagery. These products were primarily useful in identifying extremely small diameter developing eyes in this case. Second, prior to suggestion of an eye on geostationary imagery, a small developing eye seen only in the 37color is key to understanding TC structure and anticipating structural and intensity changes in the short term (24-30 hours ahead) that are associated with the early ERC.

Since these events are a harbinger of a longer-term intensity increase, recognition of early ERCs through observation of 37color imagery would be a forecasting aid.

PMW passes are infrequent. The different stages of the ERC captured for these four cases do not line up perfectly in time, but enough imagery is available for a comparison (Figure 4.31 and Figure 4.32) showing that the cases are similar.

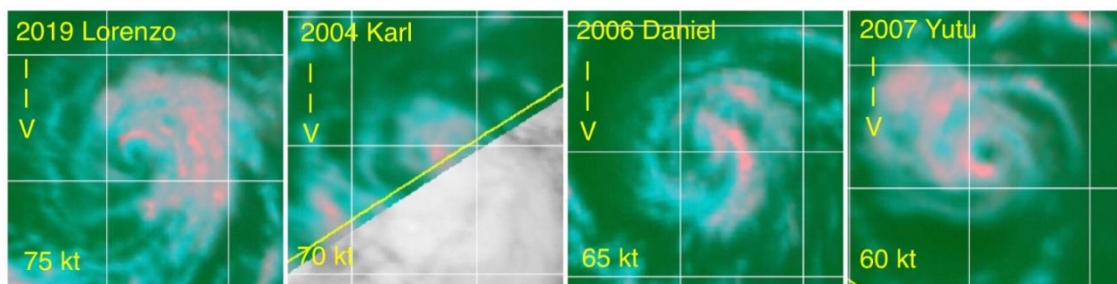
The key characteristics of early ERCs that differ from the “classic” ERC:

- **Early development** – The eye is not yet established or just becomes apparent, vs a mature eye of a strong hurricane, when the SEF begins.
- **Lower intensity** - The intensity is minimal hurricane strength as the eye is becoming established, vs. a major hurricane (100 kt), with the initial eye development between 60-75 kt, the onset of the SEF at 65-85 kt, ERC completing between 90-100 kt, and ERC completed between 100-110 kt.
- **Small eye size** – Rather than an easily-identified clear eye, the inner eye in these cases is small. In one example too small to even be resolved on 150 GHz imagery.
- **Stationary band complex** - The eye is part of a stationary band complex where the principal band is close to the center, even for disturbances that did not form from a tropical wave.
- **SEF generated from the principal band** - The head of the principal band generates the secondary eyewall, and the principal band itself to some extent wraps around the inner eye.

- **Part of a period of intensification** – These early ERCs are embedded in a longer period of intensification and unlike classic ERCs, do not result in a brief small lowering in intensity (Figure 4.10 and Table 4.1).
- **Low shear** – In all these cases there is only moderate or low shear, and other environmental conditions appear favorable for development or rapid development.
- **Best observed on 37 color composite imagery** - The developing eyewalls were initially composed primarily of moderate, not deep, convection, and consequently were at times not well observed on the 85 GHz channel but were well observed on the 37 GHz channel.

Given these characteristics, examining known cases of rapid intensification (RI) we can find similar cases where the secondary eyewall developed from the principal band at an early stage, including 2004 Frances (which subsequently went through six additional ERCs, for a total of seven ERCs), 2005 Katrina and 2005 Wilma (Figure 4.33).

Compare this to the characteristics of classic ERCs, as shown in the example of 2004 Frances in Figure 4.1 and Figure 4.2, where the eye was not small and is apparent on geostationary satellite imagery, the intensity was at the threshold of major hurricane intensity (100 kt), there was no stationary band complex and no principal band, the SEF is generated by axisymmetric concentric convective bands forming outside the inner eye, there is a slight lowering of intensity after the ERC, and the ERC is apparent on 85h imagery.



above - developing eye

below - SEF development

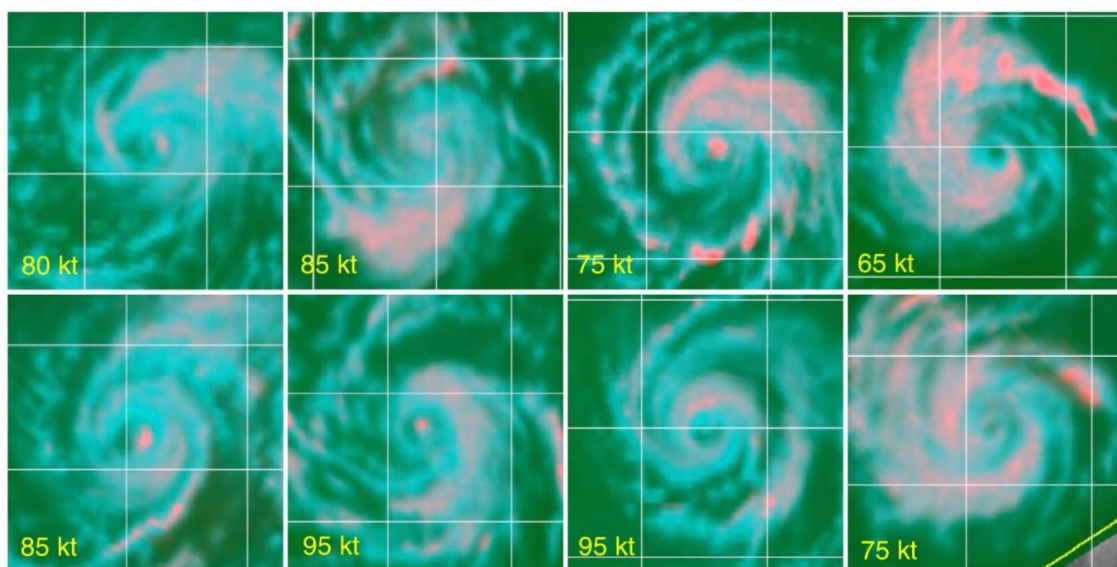


Figure 4.31 Comparison of SEF in the four tropical cyclones in the case study of early ERCs.

Top row - completing ERC
with visible remnant eyewall

Bottom row - ERC has completed

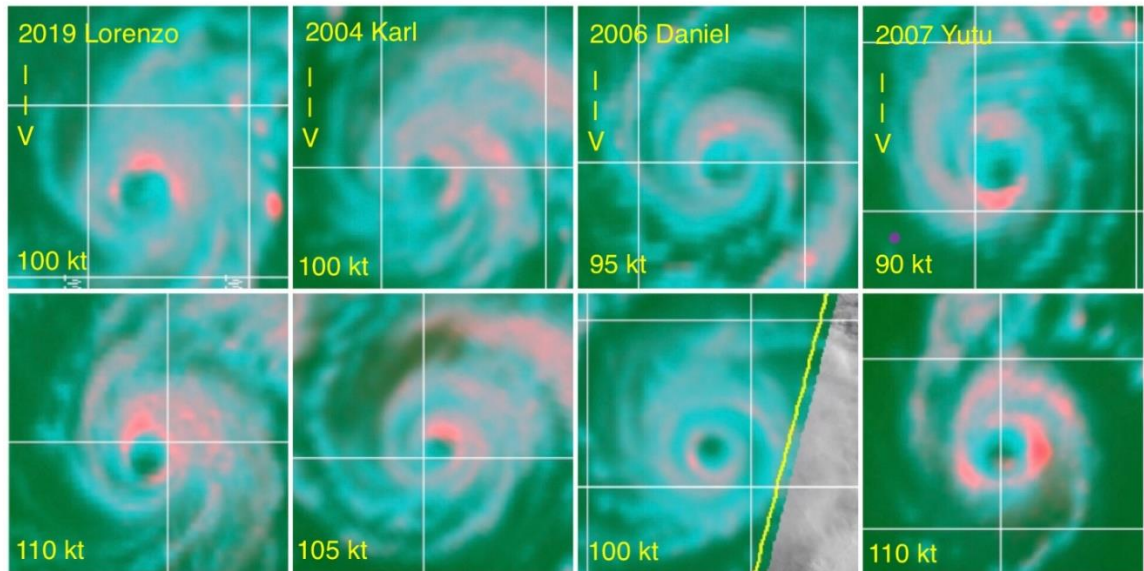


Figure 4.32 Continued comparison of the four cases, during the last stage of the completing ERC. Seen from a remnant inner eye visible inside the dominant secondary eyewall, to the fully completed ERC. It is only in the last stage of the ERC completion of early ERCs that the tropical cyclone reaches equivalent of major hurricane intensity. The eye sometimes is not apparent in visible or infrared satellite imagery until this time.

Thus, it is evident that early ERCs have a different genesis, develop structurally along a different path, and occur much earlier in the TC life cycle. The primary trigger for these events appears to be the tendency for the head of the principal band to generate banding around a very small developing eye. Why would this occur?

In all these examples the developing inner eye is small - sometimes extremely small. We can assume subsidence is generated outside of the developing eye in response to the core convection, and, at the same time, subsidence is being concentrated along the inside of the curved top of the principal band, eventually resulting in a convection-free area surrounding the small developing eye. In this case the normal pattern of SBC

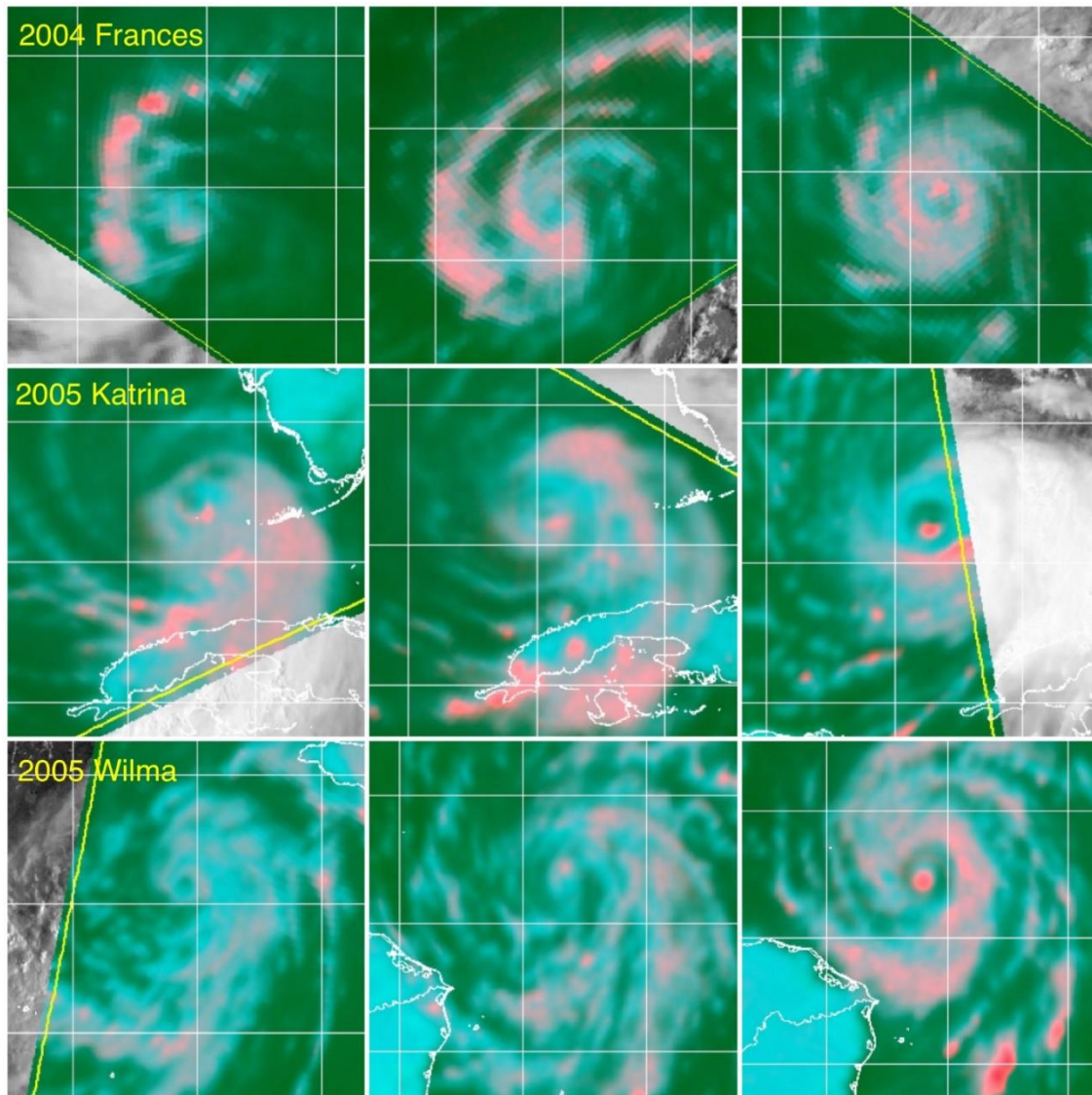


Figure 4.33 Additional examples of early ERCs with the secondary eyewall forming from the head of the principal band. Top row, 2004 Frances, middle row, 2005 Katrina, and bottom row, 2005 Wilma. The columns show the evolution from a developing eye, to SEF, to concentric eyewalls.

development is cut off, as the connecting band is eliminated, and the principal band can only extend convective banding around the developing eye. In some cases, the principal band first appears to a thick mass of convection surrounding the developing eye, but eventually does sort itself out and a moat area eventually appears on the 37color imagery

as the secondary eyewall becomes more established. The reason that the ERC development is early is that the same dynamics that would develop the eyewall are still in place and because of the existence of an inner developing eye, are focused instead on the nascent secondary eyewall (Figure 4.34), and perhaps related to the dynamics of an outer rain band SEF (Wang and Tan, 2020).

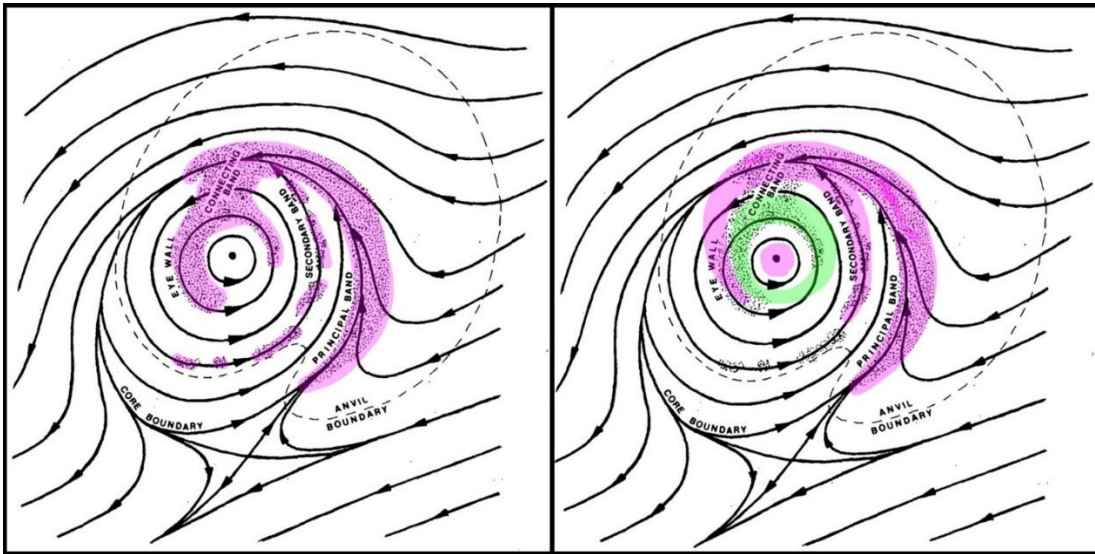


Figure 4.34 Formation of a secondary eyewall in a stationary principal band. On the left, the SBC leading to a developing eye. But when the eye has formed and is very small, the convective pattern of the SBC alters due to subsidence (green color) and leads to developing a secondary eyewall, even if the inner eye is still developing. As before, the Stationary Band Complex from Willoughby, Marks, and Feinberg (1984).

CHAPTER 5. A Deeper Examination of the 37color Imagery

Recall from Chapter 2 the interpretation of 37color was presented as an elementary view where three different colors defined three specific things: "The sea surface in the color product appears green. Deep convection, including the portion of the eyewall...appears pink. Low-level water clouds and rain appear cyan" (Lee et al 2002). In this approach, the sea surface is simply a dark green and gradations in lighter or darker green due to moisture distribution in the low levels that result in slight differences in T_b are not identified, but they are useful in observing dry air entrainment into TC, where there is usually abundant moisture in the low levels. The pink that is noted to identify deep convection is only the bright pink that appears on the image, often corresponding well to the ice signature on the 85H imagery, but the pale pink that is only subtly observed on the 37color is not considered. Low-level water clouds refers to the water droplets of clouds below the freezing level, many of which would be convective, and rain refers to warm precipitation.

But in order to understand the 37color imagery, and in particular the developing eyewall composed of the cyan color discussed in the previous chapters and important in indicating the onset of RI in favorable environments and in the small developing inner eye of early ERCs, it is important to understand the nature of the rain. It may seem obvious that this developing eyewall seen as a symmetric cyan ring is shallow convective rain, since this is an area of surface convergence and the TC is convectively-driven. Nevertheless it is important to establish that this is shallow convection, because this means that shallow convection is important in tropical cyclone development. Because

the original description of the cyan color was simply labeled as rain, this shallow convection has gone unrecognized and its significance has not been fully realized, especially due to the greater importance of deep convection in TC.

In the deep convective life cycle, convective cells begin as shallow cumulus (Cu), growing into towering cumulus (TCu, aka cumulus congestus), before glaciating into cumulonimbus (Cb) as deep convection. This is also the trimodal spectrum of clouds in the tropics associated with stable layers in the tropical atmosphere: the trade wind inversion around 2 km, 0°C around 5 km, and the tropopause around 15-16 km (Johnson et al. 1999). In Kodama et al. 2009, a climatology of warm rain in the tropics, it is noted that, "The majority of rainfall from congestus is warm rain because the tops of most congestus clouds are near the 0°C level and considered not to be frozen," so that rain from both Cu and TCu can be considered warm rain – convective rain. *This warm precipitation will be referred to in this dissertation as originating from "shallow and moderate convection," and as "SAM," and it will be established that the cyan warm precipitation on the 37color imagery is SAM.*

There is also a large amount of stratiform rain overall in a TC because of the growth of deep convection. The larger ice crystals – snow – are big enough that they do not become entrained into the cirrus outflow and instead slowly descend to eventually become stratiform rain. This snow associated with glaciated convection can produce bright bands (Smyth and Illingworth, 1998). The ice crystals may reside in a fairly thick layer of the troposphere above the freezing level. But the stratiform rain falls over a very large area, while the heavy and moderate rain falls over a much smaller fraction of the

area encompassed by the TC circulation, which also consists of nascent or mature eyewall convection and banding convection. Because of the slow rate of descent of the ice crystals and large area over which the ice crystals are carried by the secondary circulation, the resulting stratiform rain is for the most part light throughout the tropical cyclone, but extensive in coverage; heavy stratiform rain occurs just outside the eyewall and strong convective bands. Overall the melting and evaporative cooling primarily just below the melting level associated with the widespread areas of lighter stratiform rain has little impact on the dynamics of tropical cyclone. So, while widespread, stratiform rain is not a significant "player" in TC dynamics. The areas of rain seen in the cyan color of the 37color images correspond to SAM. The lack of very strong updrafts in deep convection in the TC limits the amount of graupel and hail production.

Deep convection has been the focus of studies of TC cloud structure (Simpson et al 1998, Houze 2010). Shallow and moderate convection is not represented in typical TC cloud structure schematics, either for mature or developing storms (Figures 5.1a and 5.1b).

The emphasis on deep convection is reinforced by the introduction of the Dvorak technique in the 1970s and expansion to use enhanced infrared imagery (Dvorak 1984) for tropical cyclone intensity estimation. It is based on cloud top temperatures and deep convective coverage. As Cb expand higher into the atmosphere the temperature of the cloud tops decreases, so that cloud top temperature can be a proxy for the intensity of the deep convection. Dvorak analysis is used globally for determination of tropical cyclone intensity over water due to the unavailability of aircraft reconnaissance in most basins and lack of "ground truth" over water.

Because of this long-term perspective, little emphasis has been placed on the importance of the warm precipitation that is only seen in the 37color as cyan. Prior to the availability of the 37color imagery for tropical cyclones on the NRLMRY TC and FNMOC TC webpages, satellite imagery that provided a view of the warm precipitation structure was not widely available. Over time fewer satellites with 37 GHz band were operational, so that this imagery has become less and less available to forecasters, but historical imagery is available in the NRLMRY TC "tcdat" archive. The lack of this available imagery has been noted by NHC forecasters in the forecast discussions for the 2021 Atlantic hurricane season.

Tropical cyclones are developed and maintained by convection, which requires continuous formation of convective cells over a large area, necessitating a large population of SAM. This also logically supports a hierarchy of distribution, with many more shallow convective cells than moderate convective cells, and more moderate convective cells than deep convective cells and banding convection, from the constant overturning of convective development and the short convective life cycle of individual cells. The environment in a TC is very favorable for convective development because of the abundant moisture and warming of the boundary layer by the ocean, and the convergent inflow into the TC. Shallow and moderate convection provides heating and over time moistens the atmosphere above – the tropical atmosphere is climatologically dry above the boundary layer (Dunion and Marron 2008), eroding the trade wind inversion cap and paving the way for deeper convection. In addition the nature of tropical convection is that it is gregarious (Mapes 1993) although in a TC on a smaller scale than MCS superclusters. *In summary there should be a great deal of SAM in a TC,*

both in the developing and mature stages. Case studies of a mature hurricane and developing TC in the Atlantic (ATL) and East Pacific (EPAC) basins will confirm the existence of SAM in all examined "cyan" areas of the 37color imagery. SAM is important because it is convection; it is just not deep convection.

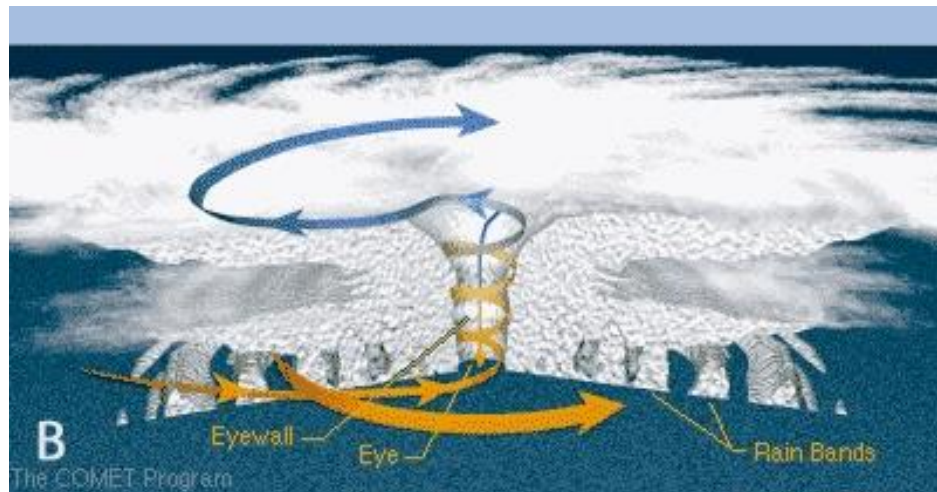


Figure 5.1 Typical schematic of a mature tropical cyclone. Note that even though rain bands are shown as decreasing in height with distance from the center in these typical schematics, in reality outer rainbands can reach heights equal to the eyewall. (from COMET training module).

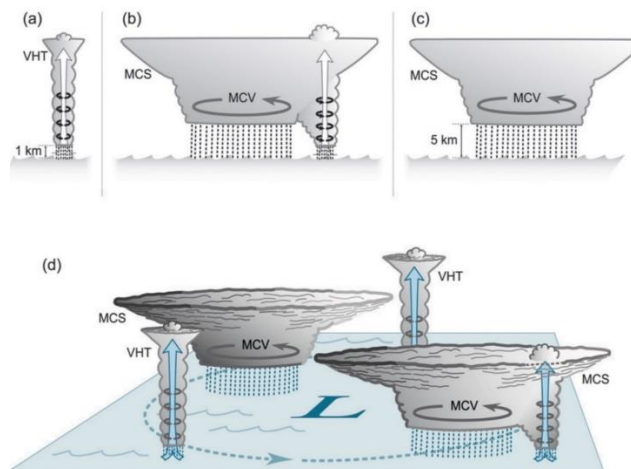


Figure 5.2 Schematic of evolution of tropical cyclogenesis and early development. This consists only of deep convective elements with no shallow or moderate convection playing a significant role in the development. (Houze, 2010)

5.1 A Conceptual Model of the 37color Imagery

There are three different levels in the atmosphere represented by the green, cyan, and pink colors: the ocean surface, the region of warm rain (near-surface up to the zero degree isotherm, 5-6 km), and the glaciated region (above the freezing level to cloud top, which can reach to the tropopause and sometimes "overshoot" the tropopause). Therefore there are varying combinations of the cyan (below freezing) and pink (freezing) that can appear over the green ocean surface, and each has a specific interpretation that can go beyond the original characterization of green/ocean, cyan/rain and pink/deep convection, an interpretation that follows logically based on empirical understanding of the TC convectively-driven environment.

To illustrate this, Figure 5.2 uses a conceptual model of a mature TC cross section radially outward from the eye, to identify the different combinations of the green, cyan, and pink in the 37color images and what each represents. This information is also listed in Table 5.1. Analysis of the following case studies of the 37color imagery will utilize this enhanced empirical interpretation of the 37color imagery.

Note that light stratiform precipitation is associated with a specific signature on the 37color but that an ice signature over moderate or heavy rain can be either SAM developing under ice, such that a bright band (BB) is not clearly indicated and there is a combination of stratiform and convective rain, or it can be the heavy stratiform rain that occurs just outside the eyewall and other heavy convective bands, where the highest concentration of ice particles fall out. The smaller ice particulates from the cirrus comprising the CDO should not produce a significant emissivity signature on this

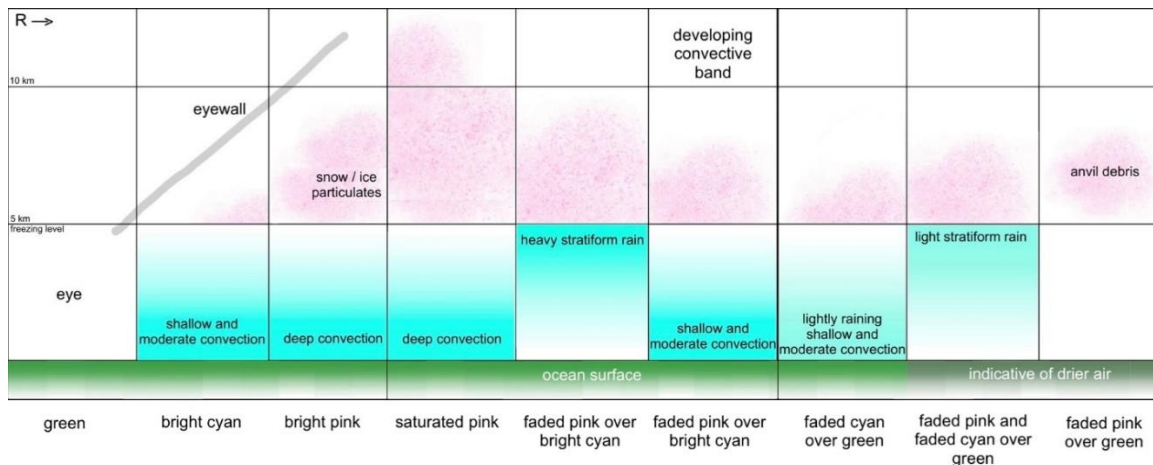


Figure 5.3 Schematic of a conceptual model of the 37color imagery. The three colors are identified as three layers, as seen in actual images in Figure 1.3, depicted as a TC cross section extending radially outward from the eye, containing a developing convective band and an area affected by dry air on the outer edge. This diagram illustrates the relationships between the ocean surface and the troposphere below and above the freezing level that comprise the 37color imagery, and what the different combinations of these colors on the imagery represent. The "bottom up" coloring of warm rain represents the collision coalescence process, and the "top down" coloring of stratiform rain represents ice accretion processes.

37color Color Characterizations	Interpretation for Tropical Cyclones
Green	Ocean surface
Darker Green	Drier air, usually seen in a curved swath in the environment around the TC
Bright Cyan	SAM convective precipitation (rain)
Bright Pink	Deep convective precipitation (ice over heavy rain)
Intense Pink	Deep convective precipitation with significant ice saturating the channel (usually deeper/taller Cb)
Faded Cyan over Green	SAM light convective precipitation
Faded Pink over Green	Ice with no rain underneath (anvil debris from convection)
Faded Pink and Faded Cyan over Green	CDO(Central Dense Overcast)/anvil with light stratiform rain
Faded Pink over Bright Cyan	Heavy stratiform rain, SAM underneath ice / deep convective precipitation

Table 5.1 Color Combinations for the 37color Imagery and Interpretation.

imagery, which is limited to a study of the core and surrounding area in a TC. Indeed, considering the widespread nature of lofted ice in the TC once the secondary circulation

has been established, if it were the light stratiform rain being observed by the cyan signature, then the entire ocean surface around the center would be completely covered in cyan in the 37color images, resembling a CDO. Ice particles in the tops of TC are primarily snow.

Because of the many transitional areas, these characterizations are necessarily broad and intended to represent a majority of the cases in each category rather than a hard and fast guideline. In summary, precipitative types can be understood by considering the different vertical layers represented by the green, cyan, and pink colors and what those combinations mean in the context of TC.

5.2 TRMM Precipitation Radar Case Studies Compared with 37color Imagery

In addition to interpreting 37color images, case studies of the 37color imagery also utilize TRMM Precipitation Radar (PR) vertical cross sections. Two types of case studies are examined: one of a mature strengthening hurricane, and a second case study of four developing TC also focusing on cyan areas, specifically the RI forecast indicator known previously as the "cyan ring" in the 37color images of the core area of four TC that subsequently went through RI (Kieper, AGU poster 2012).

The mature TC case study examines three cross sections through 2005 Hurricane Katrina on 28 August, in the middle of an intensification period that would result in a 25 kt increase in just six hours from 100 kt at 0000Z to 125 kt at 0600Z, peaking at 150 kt by 1800Z. Three cross sections through the TRMM PR swath are viewed (Figures 5.3-5.6). The PR swath in this case passed over the northeastern portion of the hurricane, with the bottom edge of the swath crossing through the center of the eye. The first cross section

examines the northern portion of the eye, NW eyewall and an area of bright cyan in the northwest of this mature intensifying hurricane. The second swath examines an area of cyan between two convective bands. The third area examines an outer convective band with an intense convective cell that was primarily bright pink on the 37color.

Each of the four TC in the second case study observe two cross sections through the "cyan ring" marker for the onset of RI (Figures 5.7-5.10). The interpretations of the 37color combinations presented in Table 5.1 are also utilized here and shown to be consistent with the TRMM PR radar reflectivity. In all of the radar cross-sections that corresponded to cyan areas on the 37color, SAM was indicated with the TRMM PR radar reflectivity showing higher reflectivities below 5 km and average precipitation echo tops averaging out to 8 km, indicating moderate convection. These areas also included echoes with near-surface reflectivity in the 30-35 dBz range that did not go above 3 to 4 km indicating shallow convection. Bright pink areas generally corresponded to stronger echoes in the 36 to 48 dBz range from near-surface up to 5km and areas of higher precipitation echo tops.

The cross sections of Tropical Storm Paloma, the storm that was examined at the earliest point in its development, at 40 kt intensity, had the least deep convection and consisted primarily of SAM with the highest precipitation echo tops associated with the principal band to the southwest. This is consistent with the idea that deep convection cannot take a foothold until SAM have made the tropospheric environment more favorable, and that earlier in the life cycle of the tropical cyclone there might be a predominance of SAM convection. But not all TC develop in the same manner.

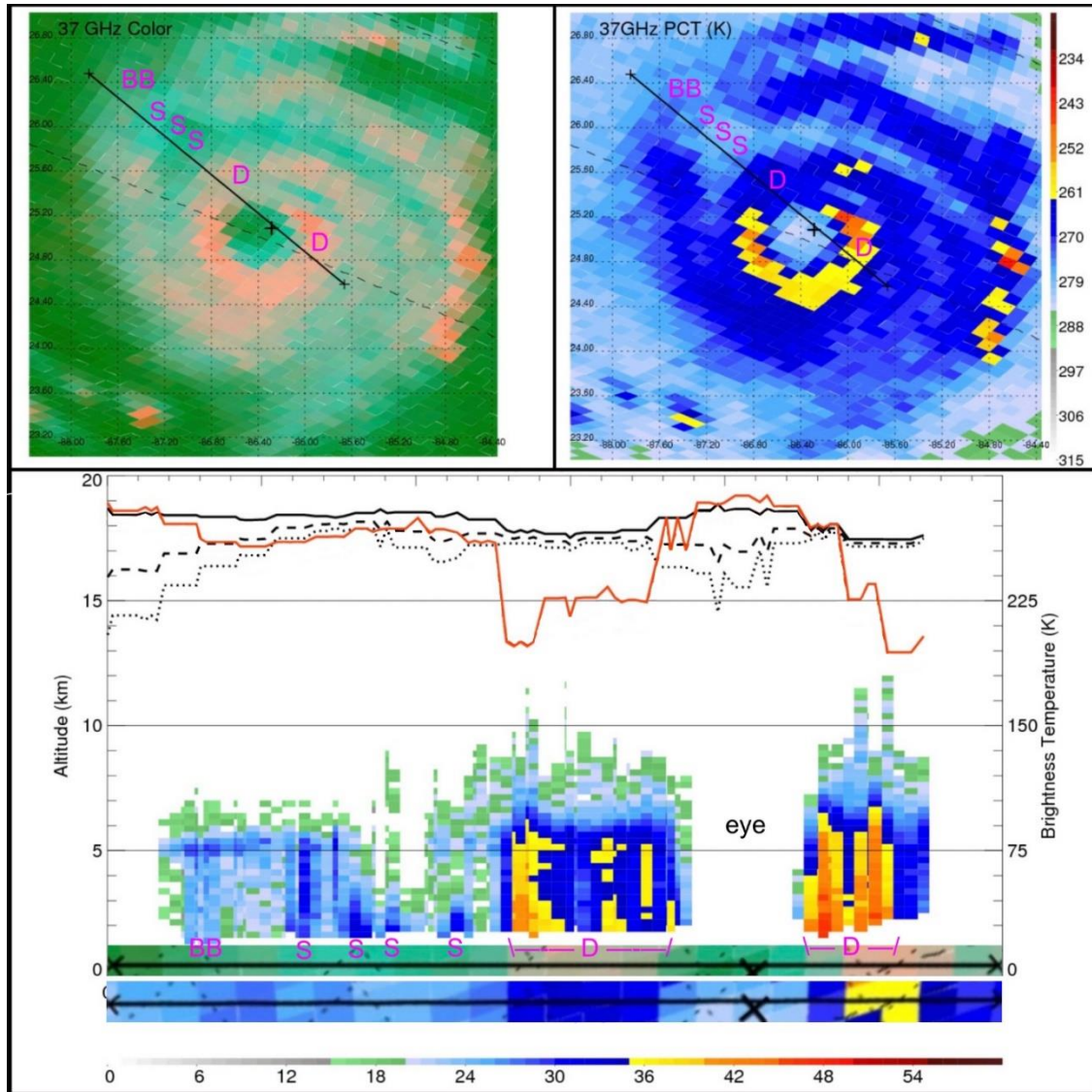


Figure 5.4 TRMM PR cross section of 2005 Hurricane Katrina. At 0324Z 28 August Katrina was a major hurricane and was strengthening. In this cross section, "S" stands for SAM and "D" stands for deep convection, and the corresponding areas of the 37color and 37PCT images are shown below the reflectivity cross section, making it easier to see the correspondence between reflectivity profiles and colors on the 37color image. In this NW to SE cross section a BB area corresponds to a weak pink / weak cyan area, followed by cyan corresponding to a number of SAM cells. Next an area of pink corresponds to deep convection outside the eye. Next to the clear eye the other eyewall consists of deep convection with the secondary circulation indicated by the slope of the precipitation echo tops. (Reflectivity scale on the left, Tb scale on the right; red solid line 85PCT values, black solid 37PCT, black dashed and dotted 37H and 37V).

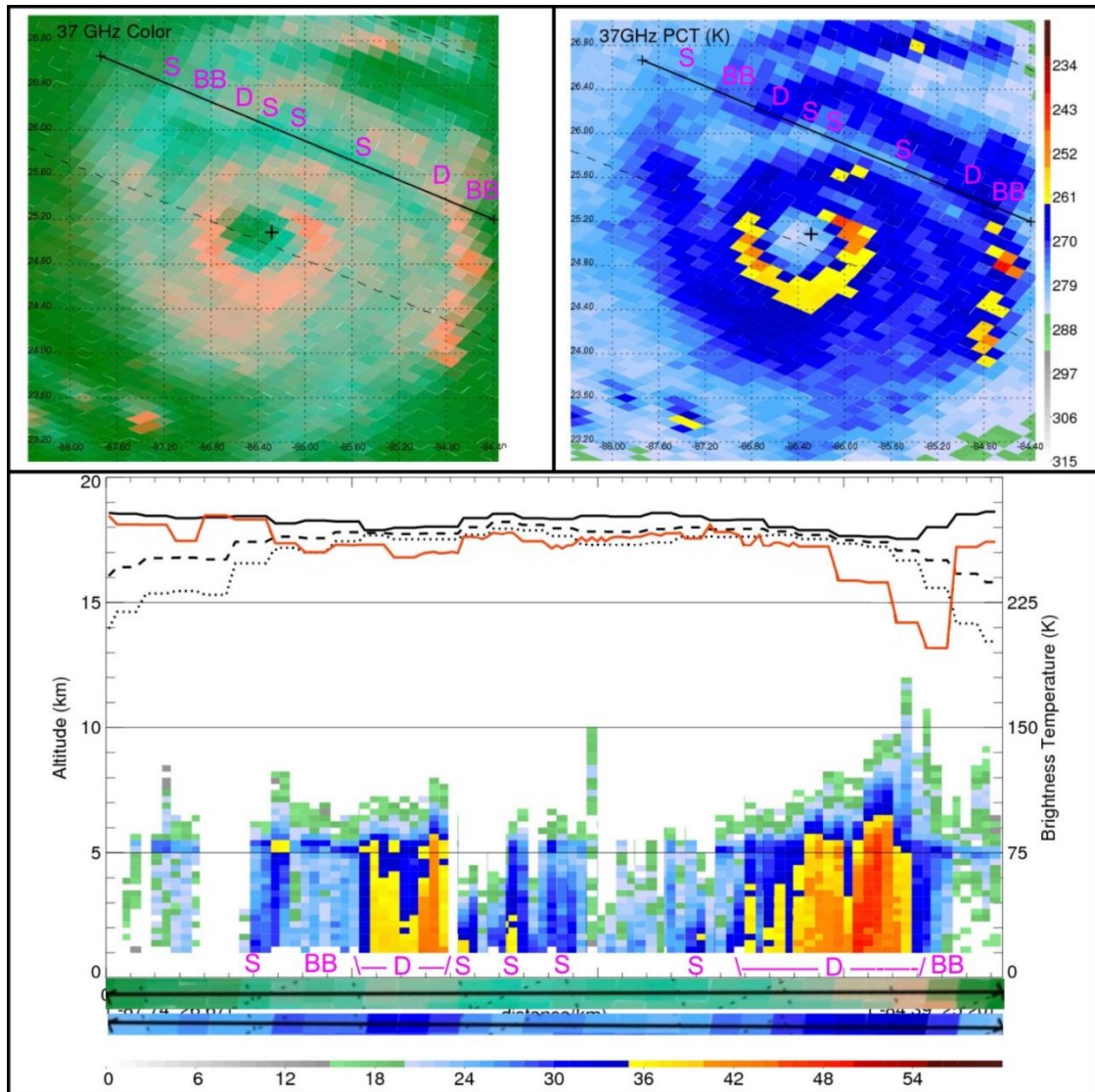


Figure 5.5 TRMM PR cross section of 2005 Hurricane Katrina. At 0324Z 28 August Katrina was a major hurricane and was strengthening. In this cross section, "S" stands for SAM and "D" stands for deep convection, and the corresponding areas of the 37color and 37PCT images are shown below the reflectivity cross section, making it easier to see the correspondence between reflectivity profiles and colors on the 37color image. This cross section captures an area between convective bands. A lightly raining area corresponds to weak cyan. A brighter cyan pixel aligns with a SAM cell, followed by a BB area corresponding to weak pink / weak cyan, and then heavy stratiform rain just outside the convection identified by weak pink / bright cyan. Then a developing deep convective area corresponds to weak pink over bright cyan. An area of SAM cells corresponds to the stretch of cyan between the convective bands. Then it crosses a vigorous deep convective band on the outer edge of the circulation, corresponding to bright pink, and a BB area, to faded pink / bright green just outside the band, indicating heavy stratiform rain, followed by weak pink / weak cyan indicating light stratiform rain.

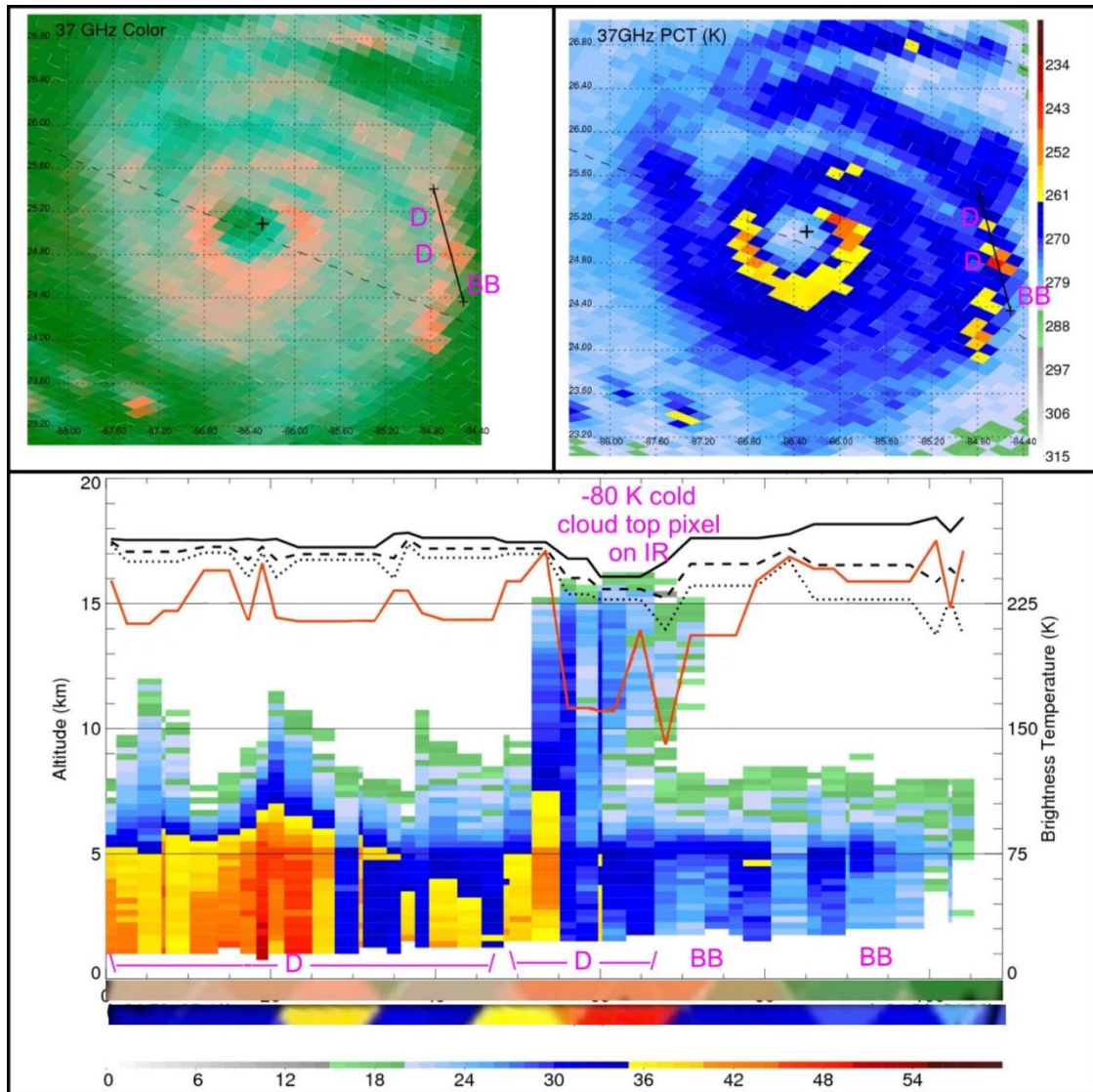


Figure 5.6 TRMM PR cross section of 2005 Hurricane Katrina. At 0324Z 28 August Katrina was a major hurricane and was strengthening. In this cross section, "S" stands for SAM and "D" stands for deep convection, and the corresponding areas of the 37color and 37PCT images are shown below the reflectivity cross section, making it easier to see the correspondence between reflectivity profiles and colors on the 37color image. This short cross section goes through a vigorous outer band that also had a very cold cloud top pixel on IR and also apparent on the 37PCT. The end of the pass tails into an area of stratiform rain behind the rain band corresponding to faded pink / faded cyan signature on the 37color. One pixel indicates heavier stratiform rain (yellow in the bright band area with higher reflectivity below). The cold pixel on the 37PCT corresponds to a precipitation echo top at 16 km and the entire deep convective area has high reflectivity cores.

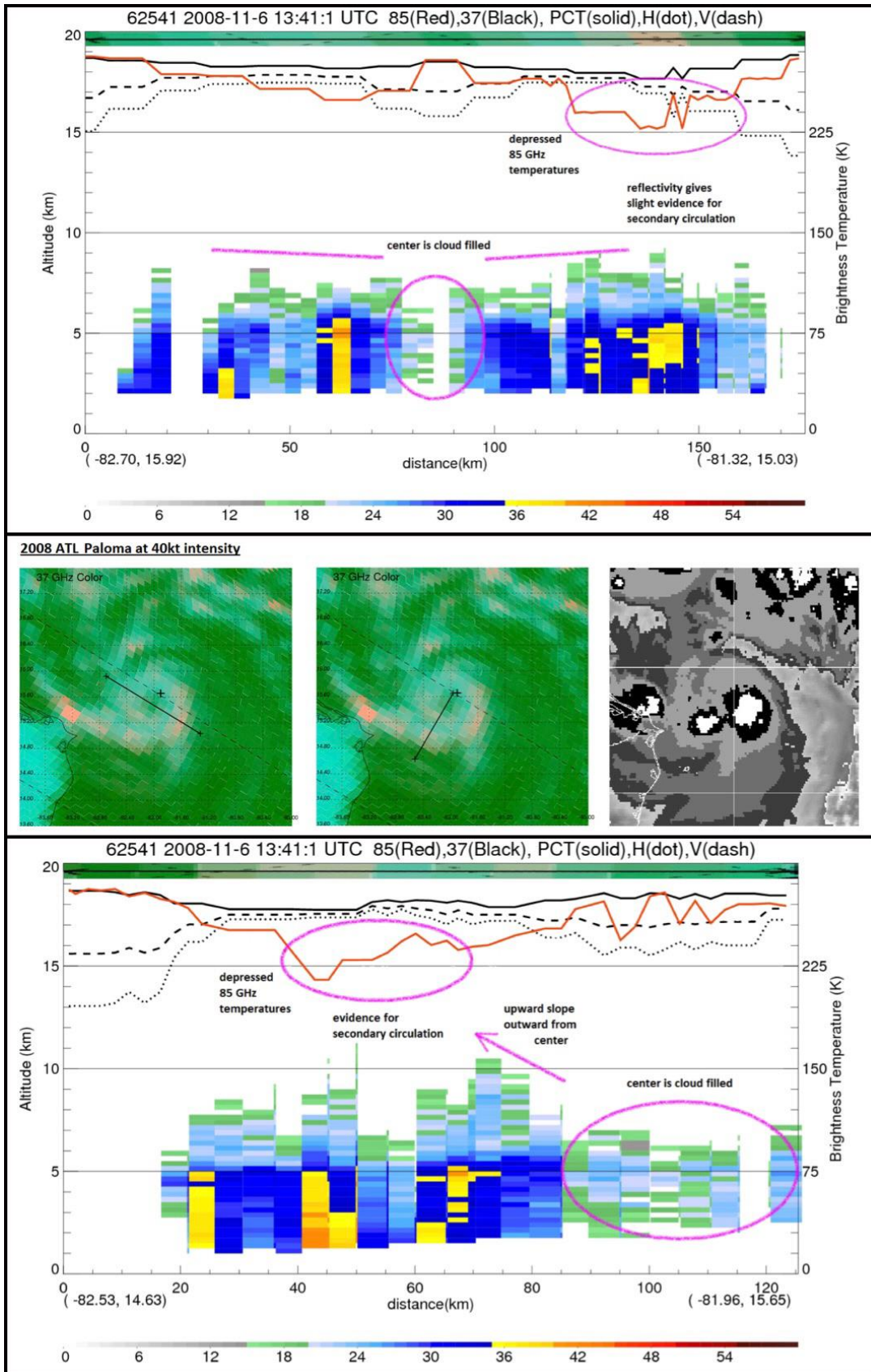
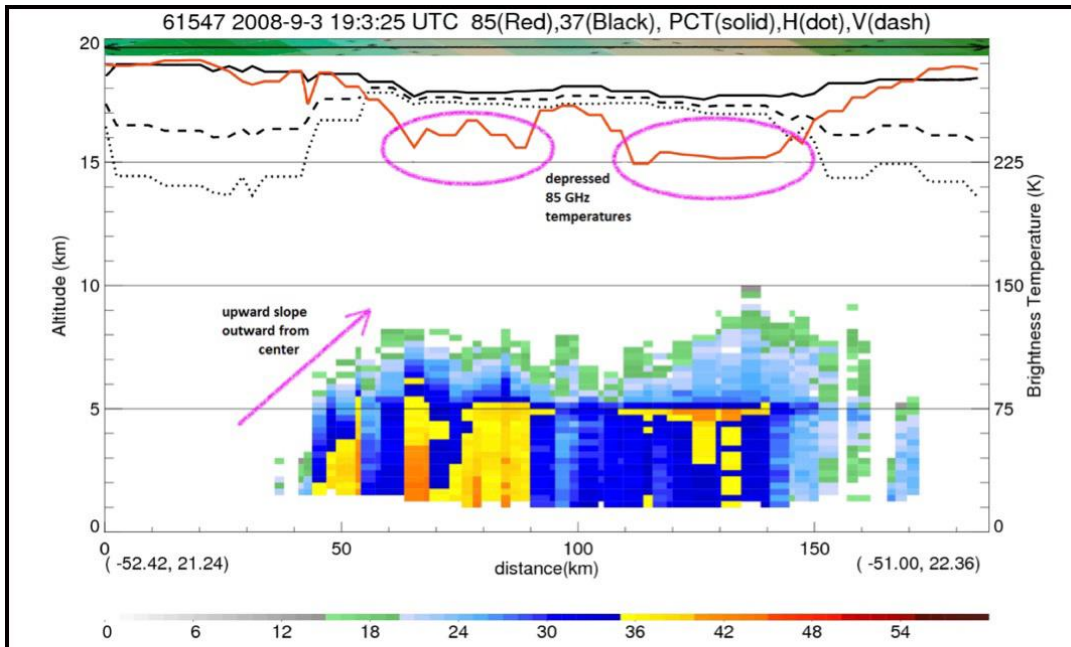


Figure 5.7 (previous page) TRMM PR cross section of 2008 Tropical Storm Paloma. Seen on 1341Z 6 November. The first cross section from NW to SE shows an area with three main SAM areas on the left that is cyan on the 37color, a cloud-filled nascent eye, faded cyan on the 37color, and an area of SAM next to the eye, cyan on the 37color, with a convective updraft at the far right corresponding to a bright pink ice signature, strong enough to correspond to depressed 85 GHz H Tb (seen along the top of the image), ending with an area of light rain seen as faded cyan on the 37color. The SAM is almost all glaciated between heights of 6 to 9 km and there is a developing secondary circulation suggested by a very slight slope outward from the center. On this cross section and on all the following cross sections the cyan areas are seen to correspond to similar H and V temperatures, and the green ocean surface areas, even if containing some faded cyan, correspond to differences in the V and H temperatures.

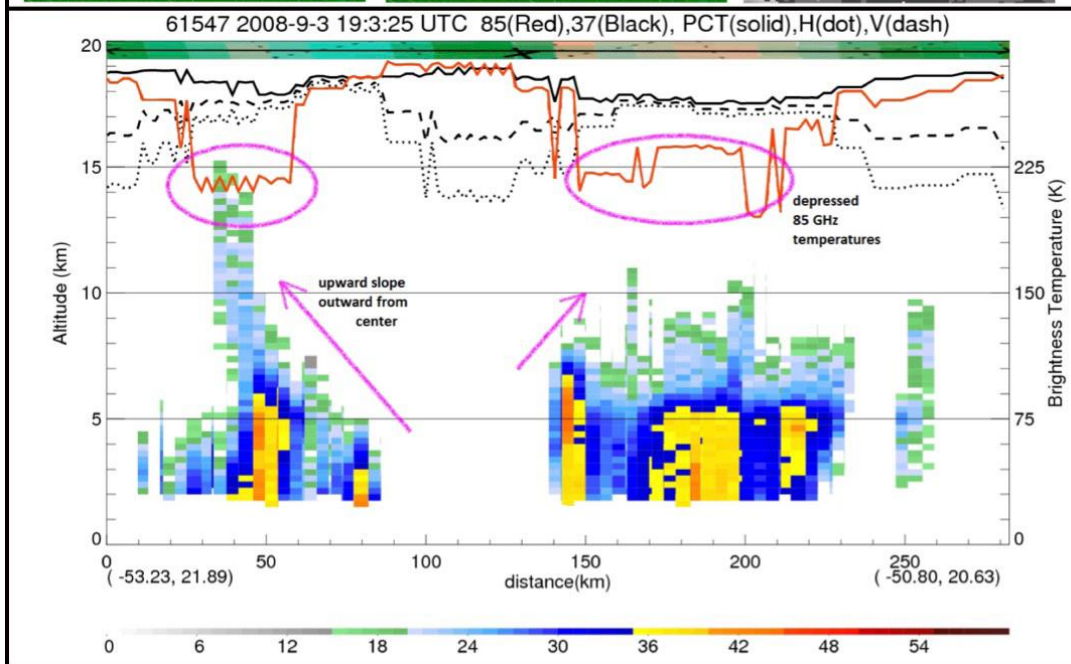
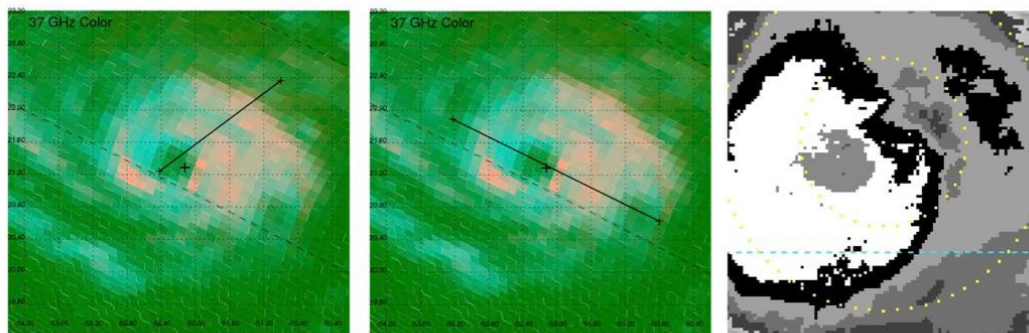
The second cross section is from the SW to the NE to the edge of the PR swath. There is no rain at the beginning corresponding to dark green on the 37color. A mixed area of bright cyan and faded pink on the 37color is interpreted on the radar as primarily SAM with possibly some stratiform rain which corresponds to the weak pink / weak cyan areas. The center is cloud-filled. A clearer indication of the developing secondary circulation is seen. The SAM is glaciated between 6 and 10 km.

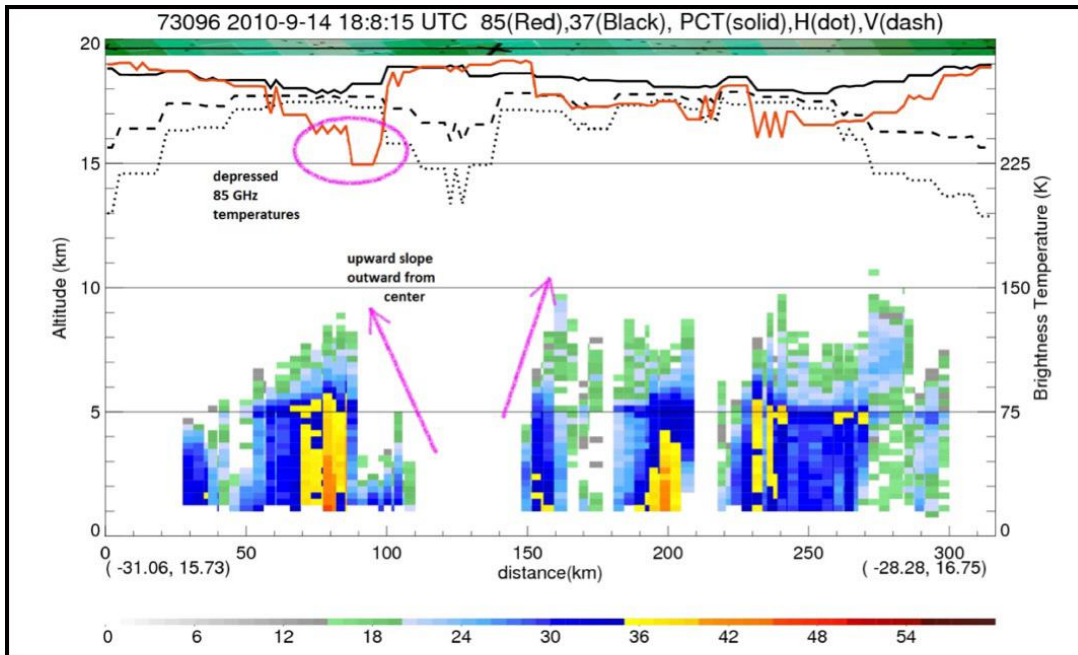
Figure 5.8 (next page) TRMM PR cross section of 2008 Hurricane Ike. Seen on 1903Z 3 September. Again this is a TC that is about to undergo RI and has a maturing eyewall structure. The first pass from SW to NE begins in the clear eye, into an area of SAM transitioning into deep convection, which corresponds to a small area of cyan and then weak pink over bright cyan on the NE side of the eye. This is followed by another developing deep convective area with heavy stratiform rain falling just outside, a weak pink over bright cyan area. Further out, there is heavier stratiform rain (probably from adjacent deep convection near these pixels), lighter stratiform rain, and then light rain.

The second cross section runs from NW to SE and shows an area of SAM with the center cell becoming a deep convective cell. This is just beginning to produce a pink signature on the 37color and is associated with an area of bright cyan. On both sides of the eye a secondary circulation appears established. On the other side of the eye a deep convective cell is in the eyewall with stratiform rain falling outside of the cell and no clear BB signature. Next an area of deep convection outside of that, corresponding to a bright pink area on the 37color with heavy stratiform rain falling outside of that (weak pink over bright cyan). A non-raining area corresponds to green on the 37color, ending with a small area of ice and light rain corresponding to faded cyan and faded pink on the 37color.



2008 ATL Ike at 75kt intensity





2010 ATL Julia at 80kt intensity

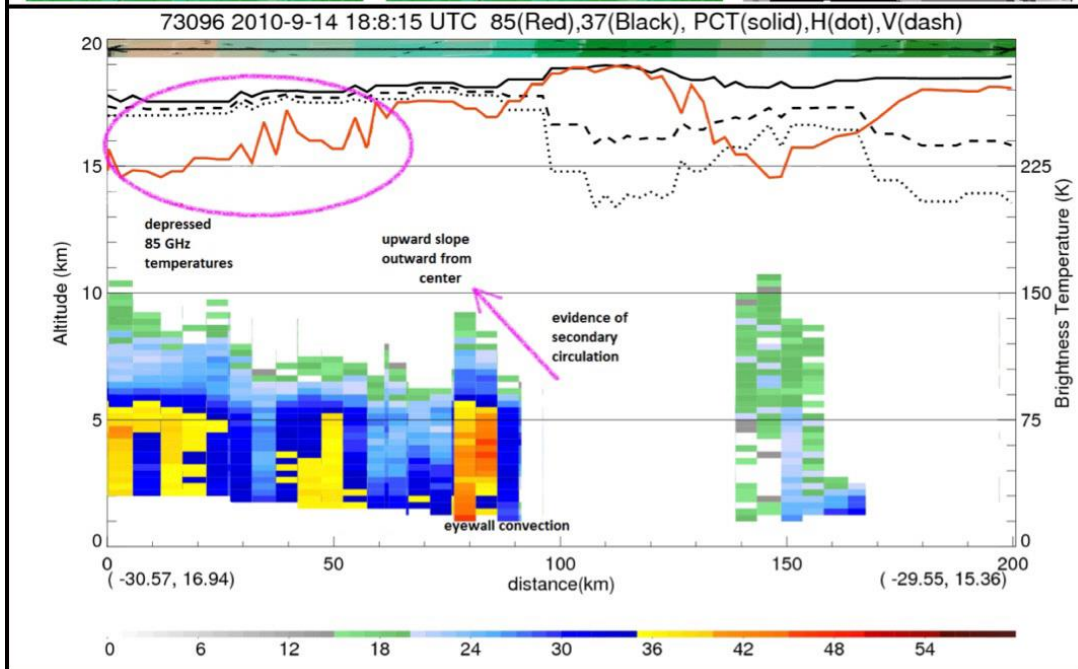
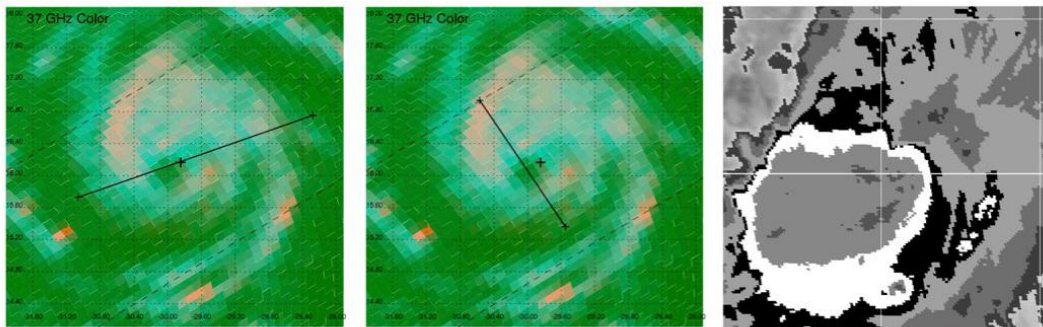
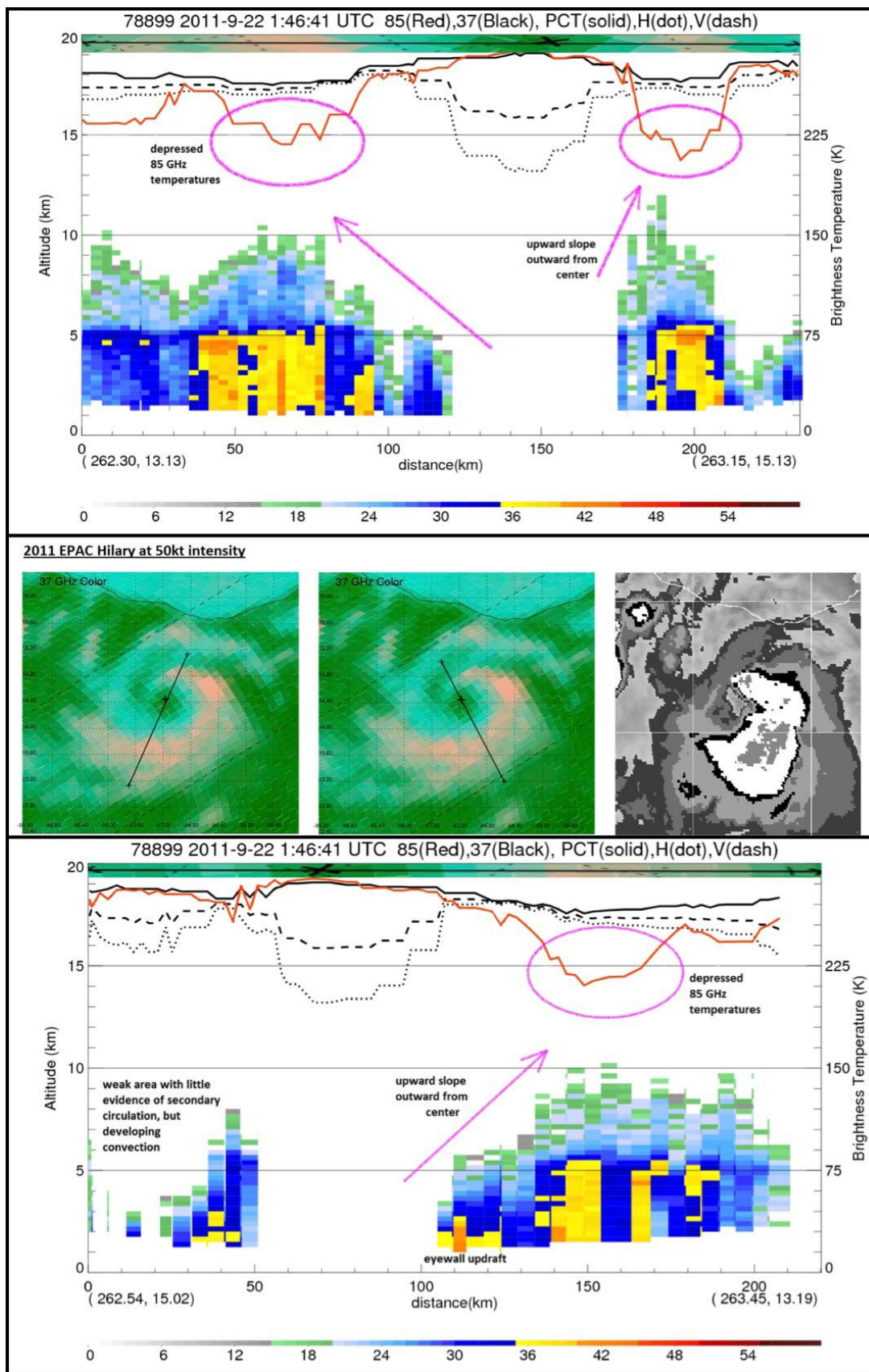


Figure 5.9 (previous page) TRMM PR cross section of 2010 Hurricane Julia. Seen on 1808Z 14 September. The first pass from WSW to ENE goes through the eye and eyewalls, beginning at the edge of the precipitation showing a SAM cell corresponding to cyan on the 37color, then eyewall deep convection with a suggestion of BB at the outer edge, corresponding to bright pink. The eye appears to be cloud filled on the left. Three bands of convection correspond to cyan bands on the 37color, followed by a BB signature of heavy stratiform rain, weak pink over bright cyan, followed by light stratiform rain corresponding to faded pink and faded cyan over green.

The second cross section from NNW to SSE begins in an area of deep convection corresponding to bright pink on the 37color. SAM and an eyewall deep convective cell correspond to cyan on the 37color, followed by a clear eye. On the other side of the eye an ice signature with some rain corresponds to an area of faded pink and faded cyan suggesting the eyewall is open here and light stratiform rain is falling. A clear area that is dark green on the 37color wrapping into the circulation around the west and south corresponding to drier air may have undercut convection here leaving an orphan anvil.

Figure 5.10 (next page) TRMM PR cross section of 2011 EPAC Tropical Storm Hillary. Seen on 0146Z 22 September. The first cross section from SSW to NNE traverses the eye and surrounding circulation and shows a highly organized TC with well-established secondary circulation and developing eyewall appearing stronger than the 50 kt intensity. A bright band (BB) area corresponds to an area of faded pink and faded cyan on the 37color and stratiform rain is indicated, followed by an area of heavy stratiform rain outside deep convection. Subsequently a large area of tilted deep convection extends into the clear eye. This could also be interpreted as SAM adjacent to the eye with the deep convection adjacent further out, which is possible given this is a developing tropical storm and is about to undergo RI. This corresponds to an area of bright cyan edged on the outside with bright pink, and is a typical 37color signature of an eyewall. We see something similar on the other side of the eye where this cross section captures the heavy stratiform rain but not the nearby convective pixels.

In the second cross section a small area of SAM corresponds to cyan and on the other side of the clear eye we see SAM and deep convective cells and suggestion of a secondary circulation, the bright cyan / bright pink area on the 37color, and, again, just outside the deep convection, BB, corresponding to an area of faded pink and faded cyan on the 37color. Again the deep convective area is associated with depressed 85 GHz H Tb. Heavy stratiform rain (weak pink / bright cyan) is falling just outside the eyewall convection.



Bright band generally corresponded with faded pink / faded cyan over green areas on the color37 suggesting light stratiform rain, and stronger BB reflectivities seen in weak pink / bright cyan indicating heavier stratiform rain. Reflectivities in these areas underneath the freezing level were significantly less than in the SAM/cyan areas, consistent with the slow descent of the ice particles, demonstrating that even where there is a bright band in areas of SAM, the convective contribution is probably more significant and these areas should not be considered as characterizing only stratiform rain.

As expected the 37V (dashed black line) and 37H (dotted black line) values differed the most when scattering occurred ocean and were closest together when scattering occurred over cloud ice, but when over warm precipitation the V and H values were a little further apart.

5.3 WSR-88D Radar Cross Section Case Studies Compared with 37color Imagery

Because ground-based radar has a greater sensitivity and smaller pixel footprint closer to the radar and also closer to the ground, cases where a cyan color area on the 37color overpass of a TC were just offshore of ground-based radar were examined. The NWS network of WSR-88D radars was utilized, including Melbourne, FL, Mobile, AL, Charleston, SC, and Morehead City, NC. Near-surface reflectivity was displayed in the plan view using the lowest tilt angle of the radar and the cross sections display the volume scan. The range of colors in the reflectivity are purple for 10-20 dBZ, blue for 20-30 dBZ, green for 30-40 dBZ, yellow for 40-50 dBZ, red for 50-60 dBZ, magenta for 60-70 dBZ, and white/gray for 70-80 dBZ.

In the case of 2019 Sally making landfall over Mobile Bay and surrounding areas, a partial eyewall cross section showed shallow convection (Figure 5.11). A very thin layer of anvil ice existed above the shallow convection that was probably advected around the primary circulation and that was likely too light to be seen by the TRMM PR, which has a threshold of about 17-18 dBZ. In the plan view an adjacent portion of the eyewall that was upwind had deep convection.

Tropical Storm Fay (Figure 5.12) had just emerged over water after more than 24 hours over land and had no inner core although the remaining ring of precipitation had some qualities similar to an eyewall. At this time Fay was a 50 kt tropical storm. The radar cross section passed through a cyan area edged with a light pink over cyan on the outer edge. The radar revealed the ring consisted of a thin convective band. In the cross section, two shallow cells were at the heart of the band. Adjacent to the convective cells on the inner and outer edges of the band, bright bands at about 15,000 ft (about 5 km) with an ice signature above indicate areas of stratiform rain. A secondary circulation is evident from a tilted area of lighter reflectivity outward from the center and extending up to 50,000 ft. The shallow convective area corresponds to the cyan area on the 37color, and the outer stratiform rain area corresponds to the weak pink over cyan. The inner area of stratiform rain has a minimal ice signature above the bright band. Closer to the center some very small shallow cells are seen. The cyan area encompasses these small shallow cells and the two convective cells with the higher reflectivities. On the right is the corresponding TRMM PR 2A23 product showing convective pixels as red and stratiform pixels as blue. This product does not identify the shallow convective cells seen in the

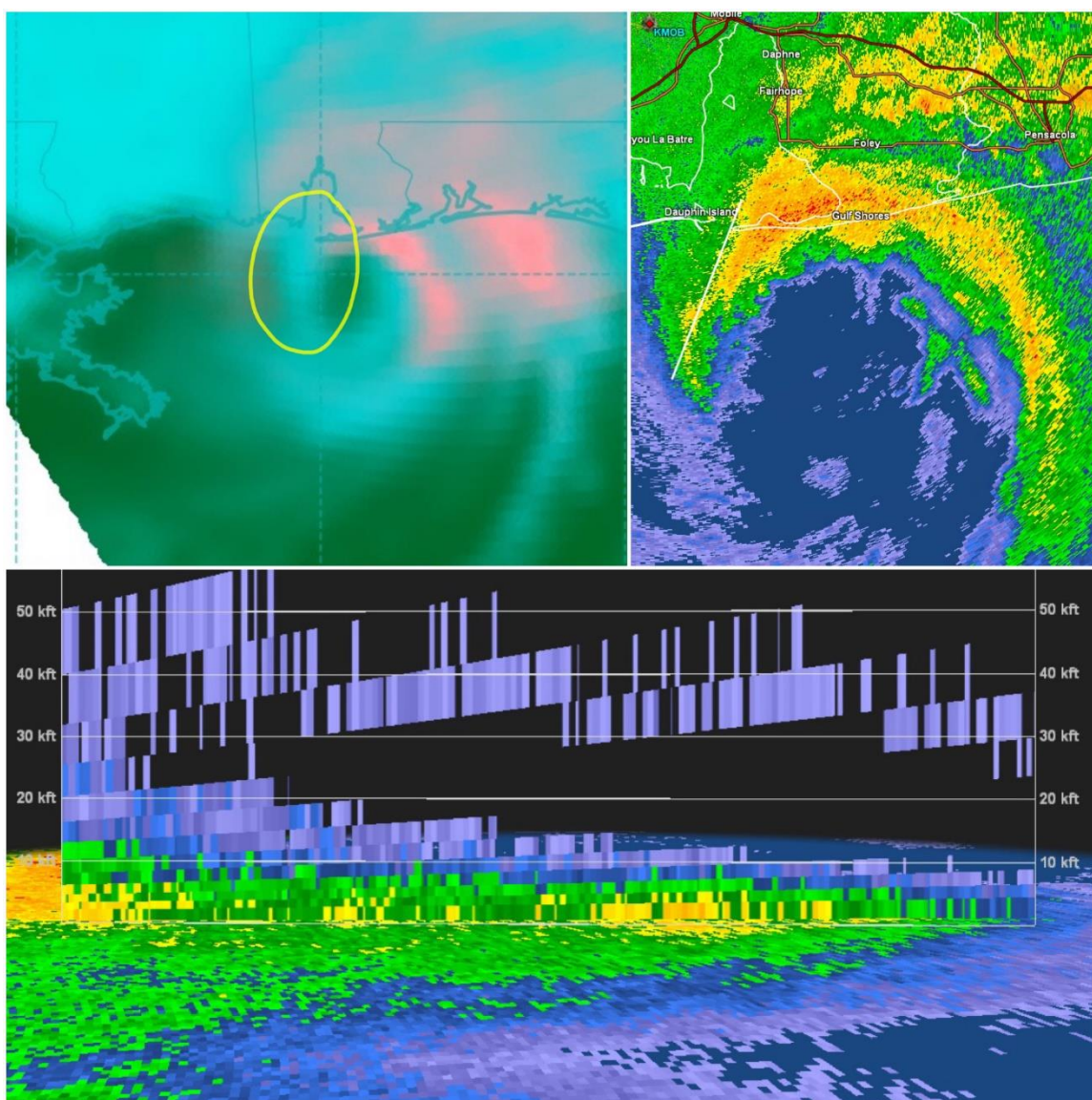


Figure 5.11 WSR-88D radar cross section of 2019 Hurricane Sally.

band in the cross section. It identifies a preponderance of the rain as stratiform in nature, which is unlikely for this convective band surrounding the center.

For Hurricane Dorian (Figure 5.13), a band of cells moving ahead of the main circulation in the forward right quadrant was examined. These cells were cyan on the 37color image. At this time Dorian had moved away from the Bahamas and was off the east coast of Florida in the West Atlantic. The cells were observed by the Melbourne, FL

radar. They were shallow intense small cells that are referred to as miniature supercells (Eastin and Link, 2004). One cell (Figure 5.14) had a near-surface reflectivity of 58 dBZ and an area of tilted enhanced reflectivity similar to a bounded weak echo region (BWER).

In all the cases examined, the cyan area from the 37color corresponded to numerous shallow convective cells below the freezing level.

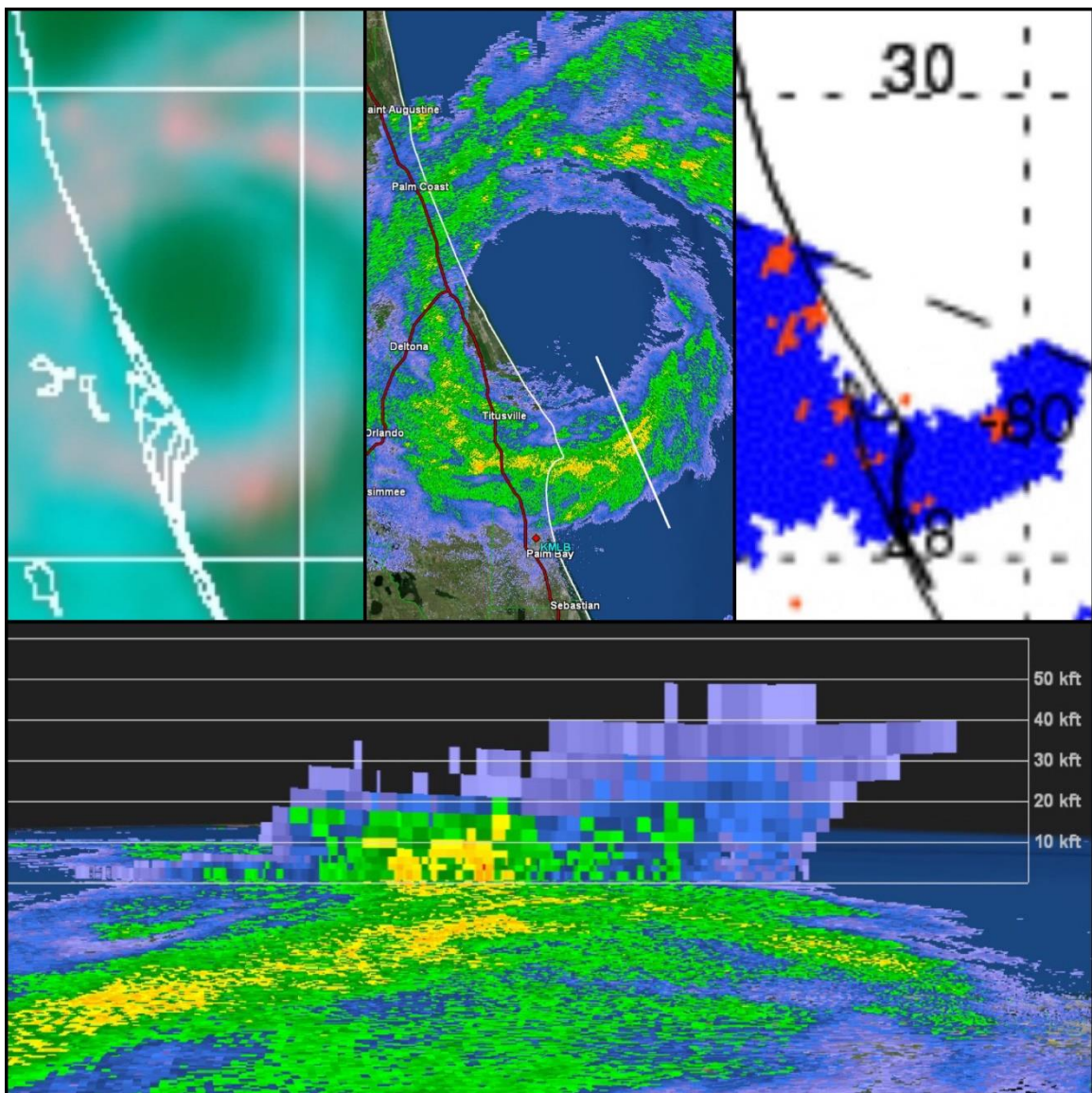


Figure 5.12 WSR-88D radar cross section of 2008 Tropical Storm Fay.

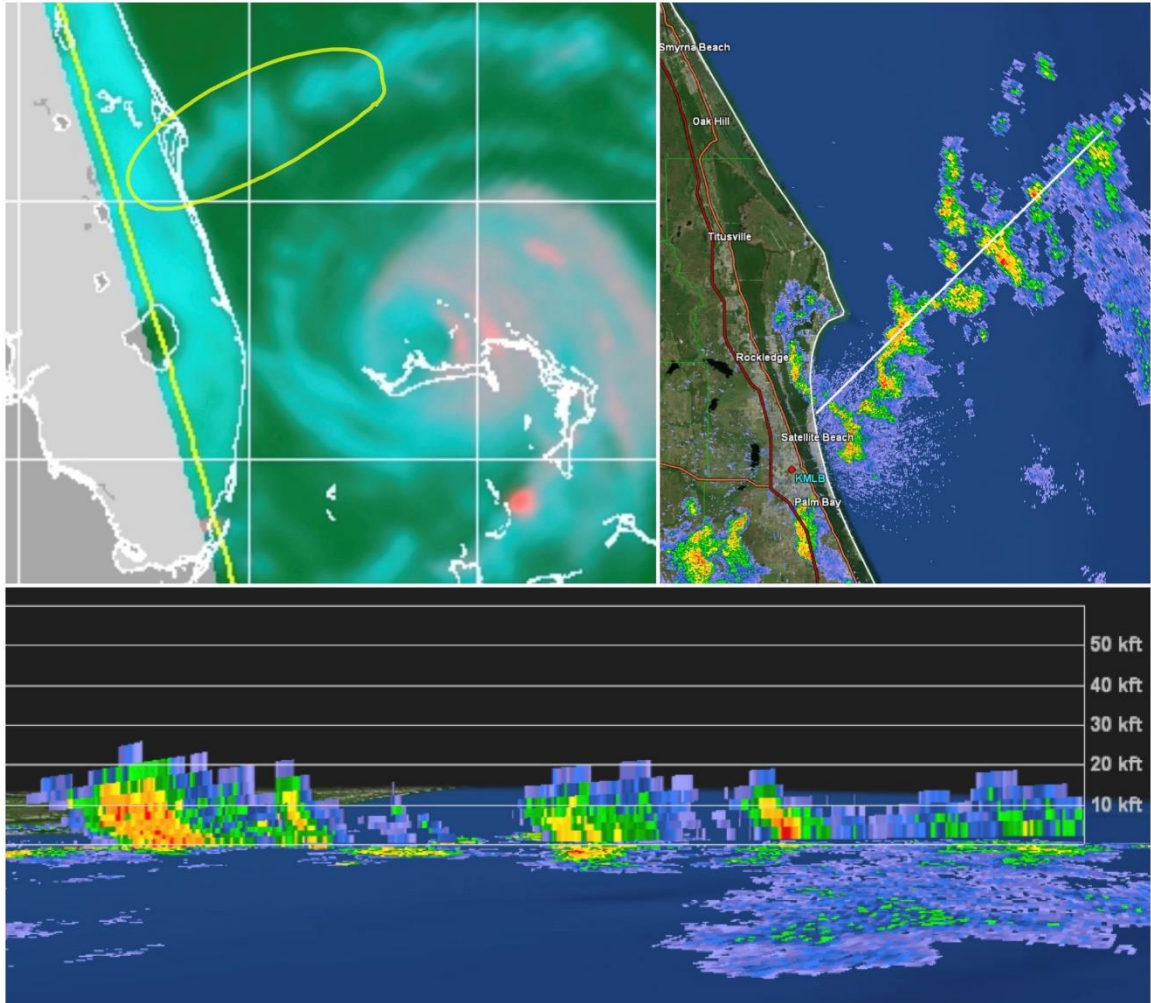


Figure 5.13 WSR-88D radar cross section of 2019 Hurricane Dorian.

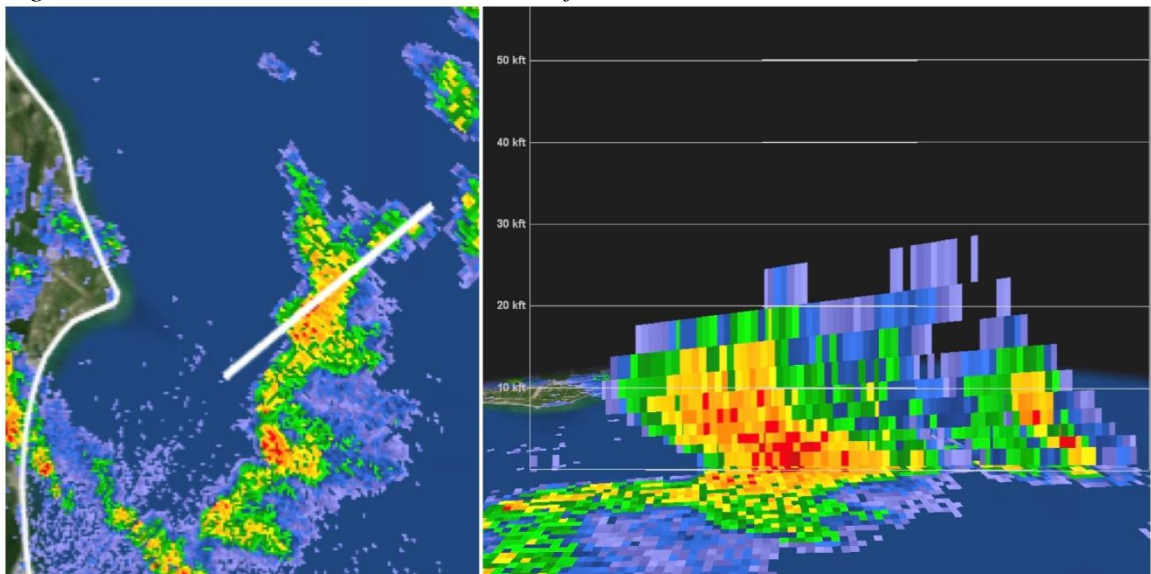


Figure 5.14 WSR-88D radar cross section of miniature supercell 2019 Hurricane Dorian

5.4 Highlighting Differences in Stratiform Precipitation and SAM on the TRMM Radar Cross Sections

A contrast exists among weak cyan/weak pink areas showing a bright band and light stratiform rain, weak pink/bright cyan areas showing heavy stratiform rain, and bright cyan areas with SAM, highlighting the distinct differences in the radar cross sections.

Areas identified as light and moderate stratiform rain with BB signature areas from the above examples are shown side-by-side (Figure 5.15). They are characterized by an ice signature between 5 and 10 km (the two vertical bars), a bright band at around 5 km, with light rain underneath the freezing level, no higher near-surface reflectivity, and stronger reflectivity decreasing between the BB and near the surface. These areas corresponded to a weak pink in combination with a weak cyan color over green on the 37color images. This is the reflectivity signature of a small amount of ice close to the BB and light rain. Examples with the most rain also exhibit more ice above the freezing layer.

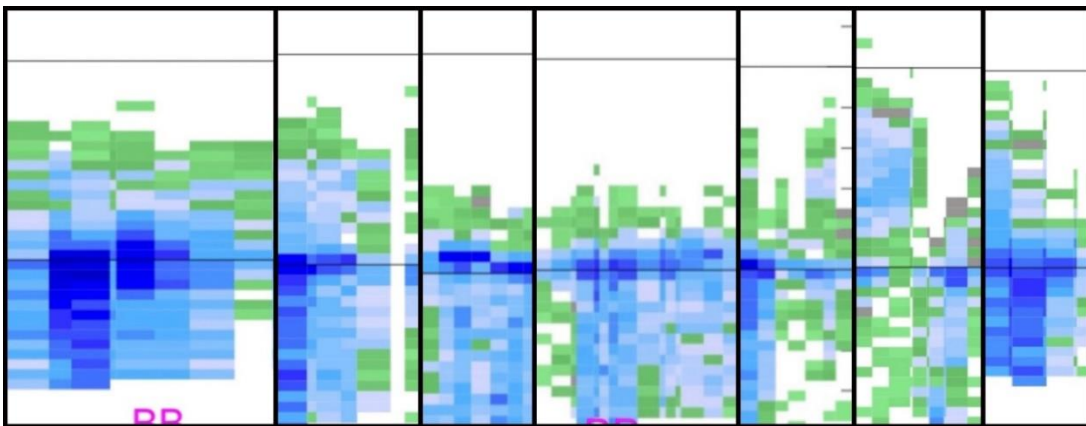


Figure 5.15 Stratiform rain areas from previous cross-sections. TRMM PR examples, corresponding to weak pink and weak cyan over green color on the 37color imagery.

In contrast, two images of SAM with different levels of surface reflectivity corresponding to bright cyan areas, and areas of heavy stratiform rain with a BB of higher reflectivity, corresponding to weak pink/bright cyan, are quite different (Figure 5.16). These SAM areas have both shallow convection, indicated by little or no ice above, and moderate convection where some ice has been lofted above the freezing level. The 37color cyan color does not differentiate between SAM with higher and lower near-surface reflectivity. Areas of heavy stratiform rain are found just outside deep eyewall convection or deep

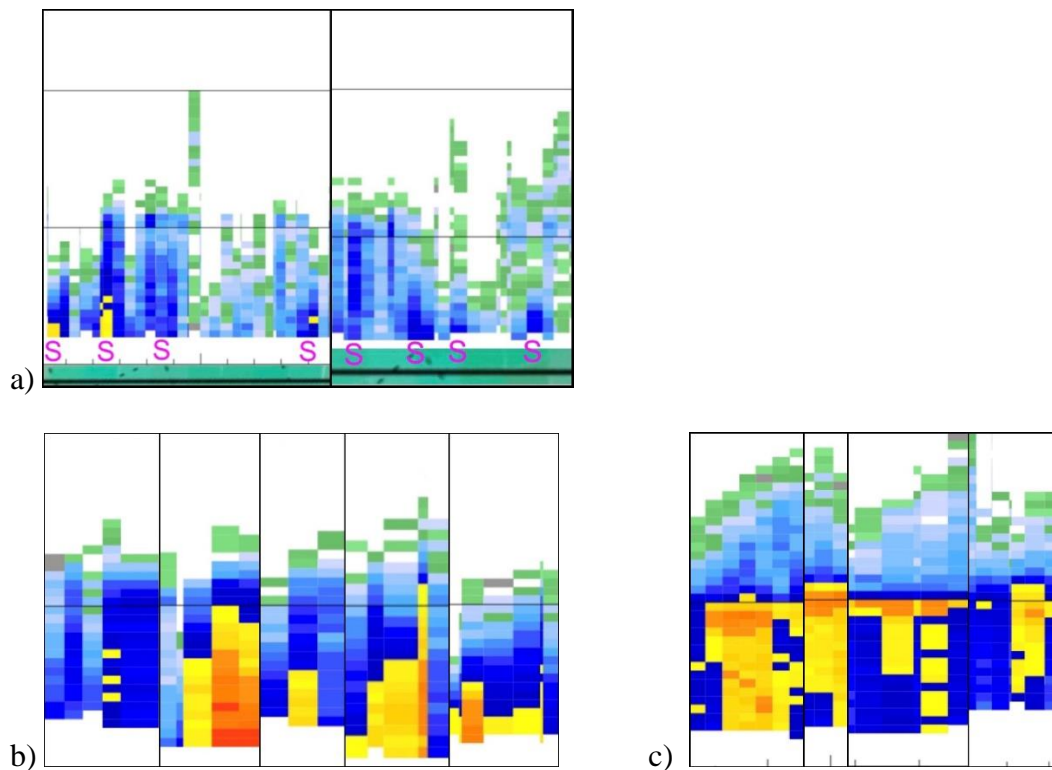


Figure 5.16 Two examples of bright cyan SAM rain with different radar reflectivities, and an examples of heavy stratiform rain. Shown a) lower radar reflectivities and b) higher reflectivities, and c) an example of heavy stratiform rain seen outside convective bands, corresponding to weak pink over bright cyan areas on the 37color imagery.

convective bands. A very strong reflectivity signal is seen, with the higher reflectivities in general closer to the BB. In general, these areas of heavy stratiform rain are in close

proximity to the eyewall/convective band and these areas have a relatively small horizontal extent. In the SAM areas, many convective cells are indicated by higher surface reflectivities, but not much ice above the freezing layer, and no appreciable BB signal. The ice signature is not "top heavy" and the vertical reflectivities are bottom-heavy suggesting collision coalescence.

5.5 Distribution of 37color Tb and Associated 2A23 Convective Rain Estimates

Figure 5.17 graphs all possible 37V/37H values in the 37color images, displayed in the color that was represented in the 37color images by using the RGB formulas for the 37color pixel color. The data was taken from a global set of tropical cyclone overpasses including the center of the TC by the TRMM PR from 1998 through 2011 in a radius of 150 km from the center and over water (<http://tcpf.fiu.edu>).

Three areas corresponding to the 37color product description consistent with the original image interpretation of Lee et al (2002) are: the green area is characterized as ocean, the pink as deep convection, and the cyan as warm precipitation. The transitions between these, identified and interpreted in Table 1.1, are important and each carries a different interpretation stemming empirically from the fundamentals of the 37color image.

Because each of the transition areas encompass a spectrum of precipitation combinations, a broad understanding of what they represent is sufficient for understanding the imagery.

The reflectivities of the 37V and 37H channels over the core areas of TCs have a limited Tb range and a bifurcated distribution. The green/cyan regions lie along a consistent almost-linear plane, tapering upward at either end, but generally indicating that the

differences between the Tb of the 37V and 37H against the ocean surface are consistent over a range of Tb. The difference shifts a little bit at the lower Tb favoring a slightly higher 37V Tb in relation to the 37H. At the other end of the distribution in the right top area, we see that in the cyan area, the ratio of the 37V and 37H Tb not as far apart. In the middle area where the cyan begins to overlap the green, identified as "faded cyan," (Table 1.1) the difference in the Tb due to the ocean surface becomes more prominent with lower Tb. This can be seen in the previous cross section examples of the "faded cyan" areas where the Tb of the 37V and 37H shown above the reflectivity cross section diverge even though there are some light precipitation echoes, for example in the second cross section of Julia. The cross sections show that as the reflectivity below the freezing level increases, the 37V and 37H values are closer together. Thus the slope of these green and green/cyan transition areas up to the bright cyan but not including the bright cyan can be well approximated by the PCT formula as the scattering of the 37V and 37H against the ocean surface are dominant or influencing the areas with lighter rain, but the relationship of the 37V and 37H is closer together in the cyan area where there is warm precipitation and the slope changes in the bright cyan area. Even though it appears that the bright cyan area might be approximated by a slope of a PCT value, observing just the bright cyan area alone shows this is not the best approximation and that the relationship between 37V and 37H is different in this specific area.

The bright pink area where the 37V and 37H values are very close is approximated as expected by a slope close to one. The transition from bright cyan to bright pink is consistent with convective growth from Cu to TCu to Cb and the addition of ice as the height of convection increases above the freezing level.

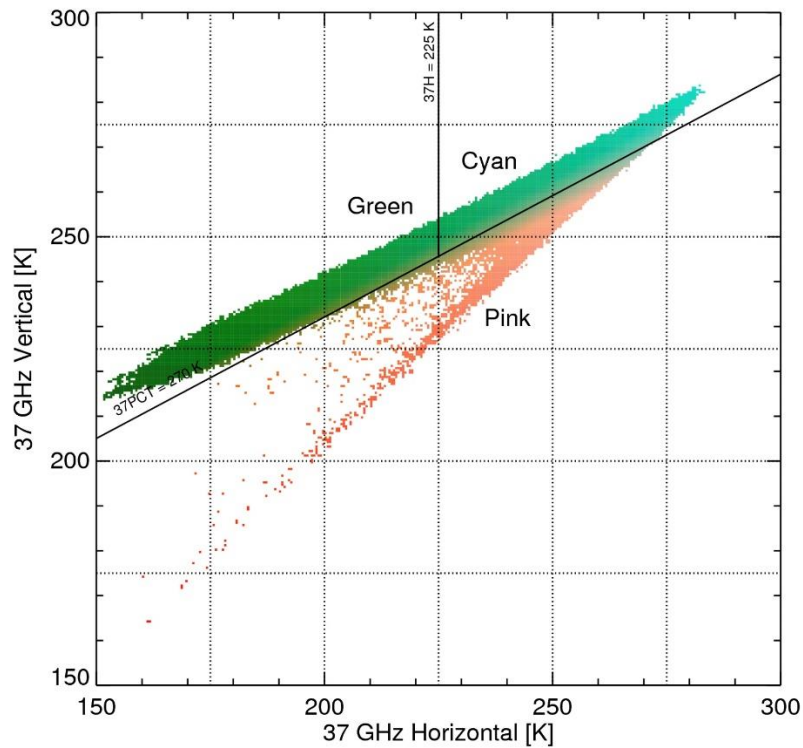


Figure 5.17 Pixels of the 37color imagery graphed by their respective 37V and 37H brightness temperatures. These use the RGB formula for the colors used in the 37color imagery, and an approximate division of the values consistent with the original image interpretation of Lee et al (2002) where the green area is characterized as ocean, the pink as deep convection, and the cyan as warm precipitation. As summarized in Table 1.1 the transitions between these areas are important since each carries a different interpretation that was arrived at empirically from the fundamentals of the 37color image. Because each of the transition areas encompass a spectrum of precipitation species a broad understanding of what they represent is sufficient.

In summary Figure 5.17 is primarily useful for confirming the differences in the 37V and 37H Tb scattering from the radiometrically cold ocean surface as opposed to cloud ice, and in relating the colors in the 37color images to areas of rain and ice in the tropical cyclone. But when compared to the TRMM PR 2A32 product identification of convection, a large disconnect is seen and this is the primary reason for presenting these images.

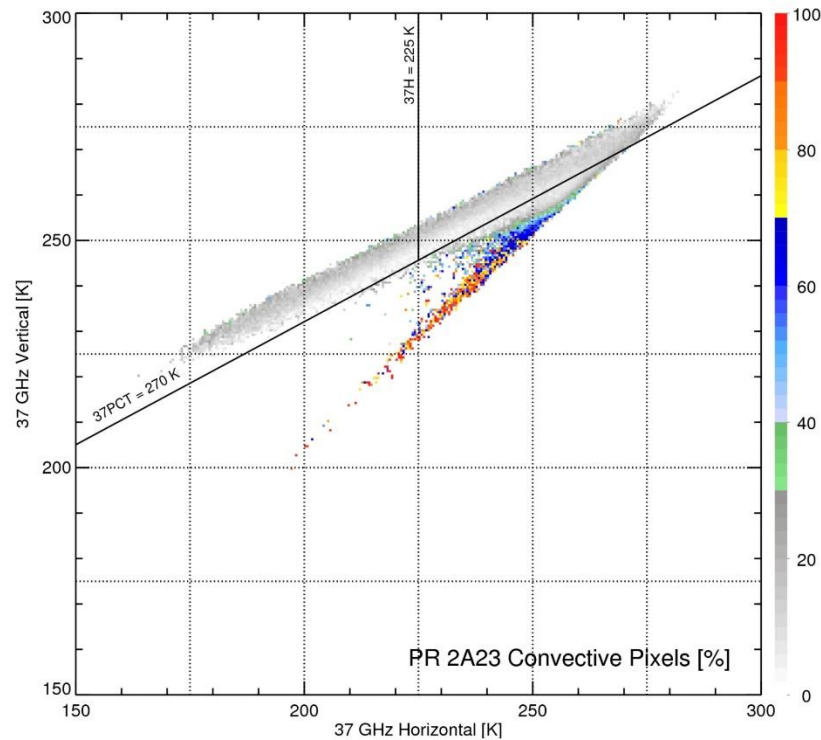


Figure 5.18 Distribution of the pixels that the TRMM PR 2A23 algorithm recognizes as convective. Casual inspection of this distribution shows that only deep convection is primarily identified as convective, and that areas of ocean surface appear to have a higher percentage of convective pixels than the bright cyan area, and, also, that as the ice increases, the less likely the algorithm is to identify a pixel as being convective until enough ice is present to indicate deep convection.

Several corrections have been made to the 2A23 algorithm to include additional pixels that were originally classified as stratiform shallow isolated rain as convective (Schumacher and Houze 2003) and higher-altitude rain over mountainous terrain and shallow non-isolated rain over tropical oceans (Funk et al 2013). These two changes reduced the percentage of identified stratiform rain in the tropics. The changes in Funk et al (2013) reduced the percentage from 40% to 38%. If SAM were identified as convective precipitation it would lead to a further reduction in percentage, *possibly a significant one*.

The cyan areas are dominated by SAM as characterized previously by both empirical evaluation and review of the radar cross sections. The TRMM PR 2A23 algorithm would be expected to recognize convective precipitation in the bright cyan area. But if we look at the second graph (Figure 5.18) we see that this algorithm only recognizes some deep convective areas (pink) as convective precipitation. The cyan area not only has few pixels identified as convective, but as soon as any ice signature appears in the transition areas, the already-small number of convective pixels is reduced, such there are virtually no convective pixels identified in areas of cyan/pink overlap.

5.6 Stratiform Signal Masks the Convective Signal in the 2A23 Product

It is established that the TRMM PR 2A23 algorithm does an extremely poor job of recognizing SAM in tropical cyclones. The tropical cyclone environment is convectively-driven and it is surprising that no studies have recognized this shortcoming of the 2A23 algorithm, although it is noted in the Hense and Houze (2011) study of TC eyewalls,

The TRMM PR convective/stratiform algorithm (TRMM product 2A23) classifies the more intense echoes in the eyewall as "convective" and the rest of the eyewall reflectivities as "stratiform." This algorithm (Awaka et al. 1997) was not designed with hurricane convection in mind, so its usefulness in the hurricane context may be limited.

However the study does go on to heavily utilize the 2A23 stratiform/convective classification, even though it acknowledges that the stratiform pixel count was 57% with the convective pixel count 41% (some pixels are classified by the algorithm as "other"), but does not question the validity of this conclusion.

Two TRMM PR cross sections of Hurricane Katrina are compared with the 2A23 classification, with blue indicating stratiform precipitation and red indicating convective precipitation (Figure 5.19). The eyewall portions of the cross sections are shown for the two passes. The first cross section shows a precipitation profile of deep convection and the second, moderate convection. But the corresponding area of the 2A23 stratiform/precipitation product shows the area associated with both these as stratiform (blue) and not convective (red). This shows that the 2A23 algorithm in this case missed not only SAM but also missed identifying deep convection.

This PR pass of Katrina occurred at 0324Z 28 August. At 0000Z 28 August the best track intensity was 100 kt and Katrina was moving 6 kt to the WNW, with NWly shear of 7 kt, and at 06000Z 28 August the best track intensity was 125 kt and Katrina was moving 7 kt to the WNW with NWly shear of 11 kt. Both these estimated shear values and the satellite imagery at this time show Katrina to be in a low-shear environment, with wind shear and storm motion nearly equal and opposite. Katrina was also over a very high SST environment and intensifying to Category 4. The PR cross sections are in the upshear right quadrant.

Hence and Houze (2011) discusses the special cases of the upshear right quadrant of "low-shear, CAT45, and high-SST groupings" as cases where the upshear right quadrant, not being affected by shear, has similar reflectivity profiles as the upshear left and downshear right. In particular, in the upshear right quadrant, "the low-level intensity

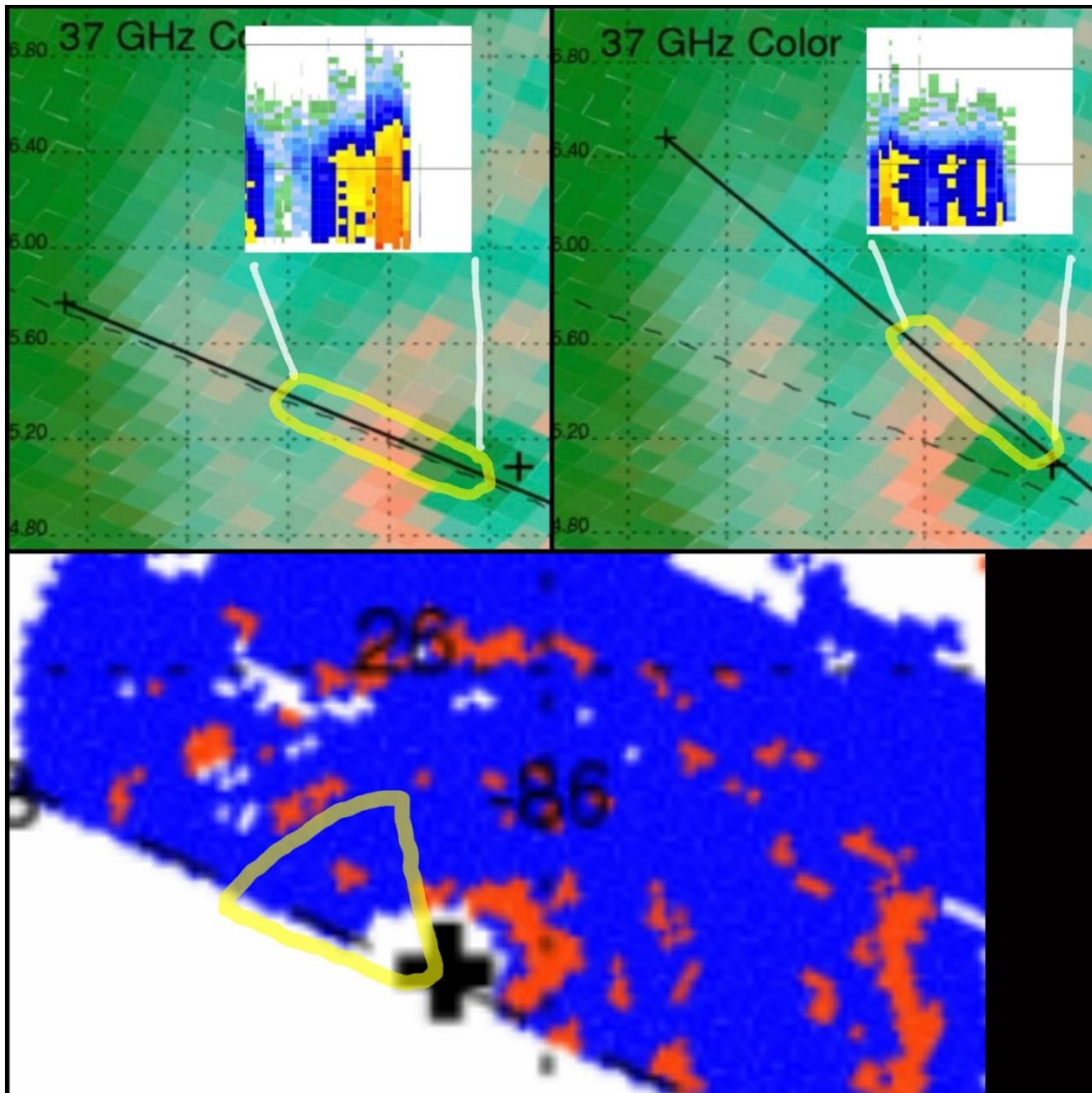


Figure 5.19 2005 Katrina deep convective eyewall labeled as stratiform by the 2A23. Sections of two TRMM PR cross sections for the previous example of Katrina, showing the upshear right quadrant, compared with the stratiform/convective identification of the TRM PR 2A23 product, where blue is stratiform and red is convective. These two cross sections are completely labeled as stratiform. However the first cross section shows deep convection and the second section shows SAM (shallow and moderate convection), with the first showing some stratiform rain outside the convective eyewall and the second showing some stratiform rain has mixed down into the developing convection. Not only does the 2A23 miss SAM, it also misses correctly identifying some deep convection.

increases by about 5 dB relative to the [upshear right of the sheared TC cases]...This

result suggests that there is more new development in this quadrant for these three

categories..." (Hence and Houze 2011). These conclusions also apply to this example.

Both deep convection and developing convection are seen in the two cross-sections in this upshear right quadrant in Katrina (Figure 5.19).

In Figure 5.20 of 2004 Atlantic Danielle's RI ring, pixels identified by the PR 2A23 product as convective rain are shown by the red, pink, and dark bright blue colors - a partial eyewall is indicated. Non-raining anvil is indicated by the pale blue pixels along the edges of the raining areas. Stratiform rain is shown in the green color. The majority

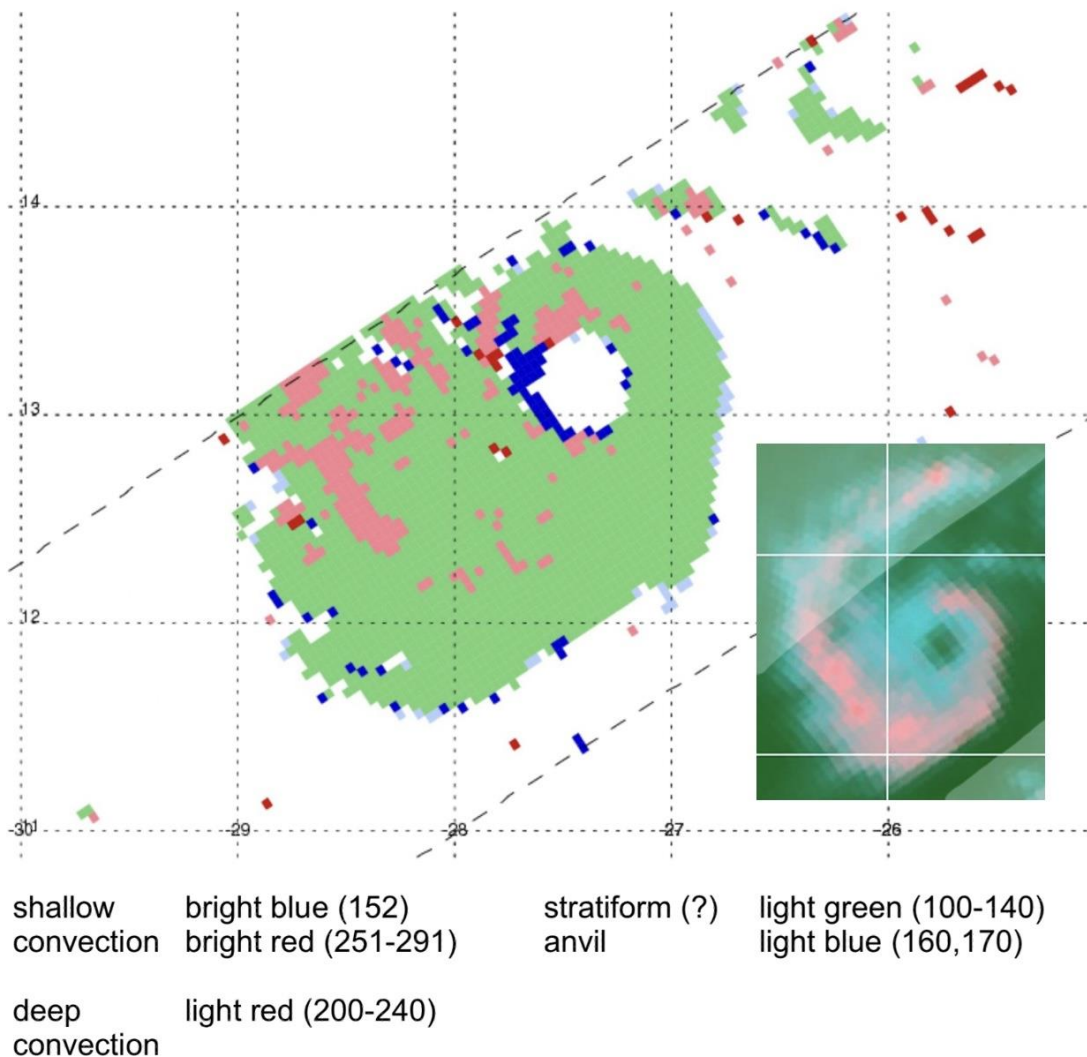
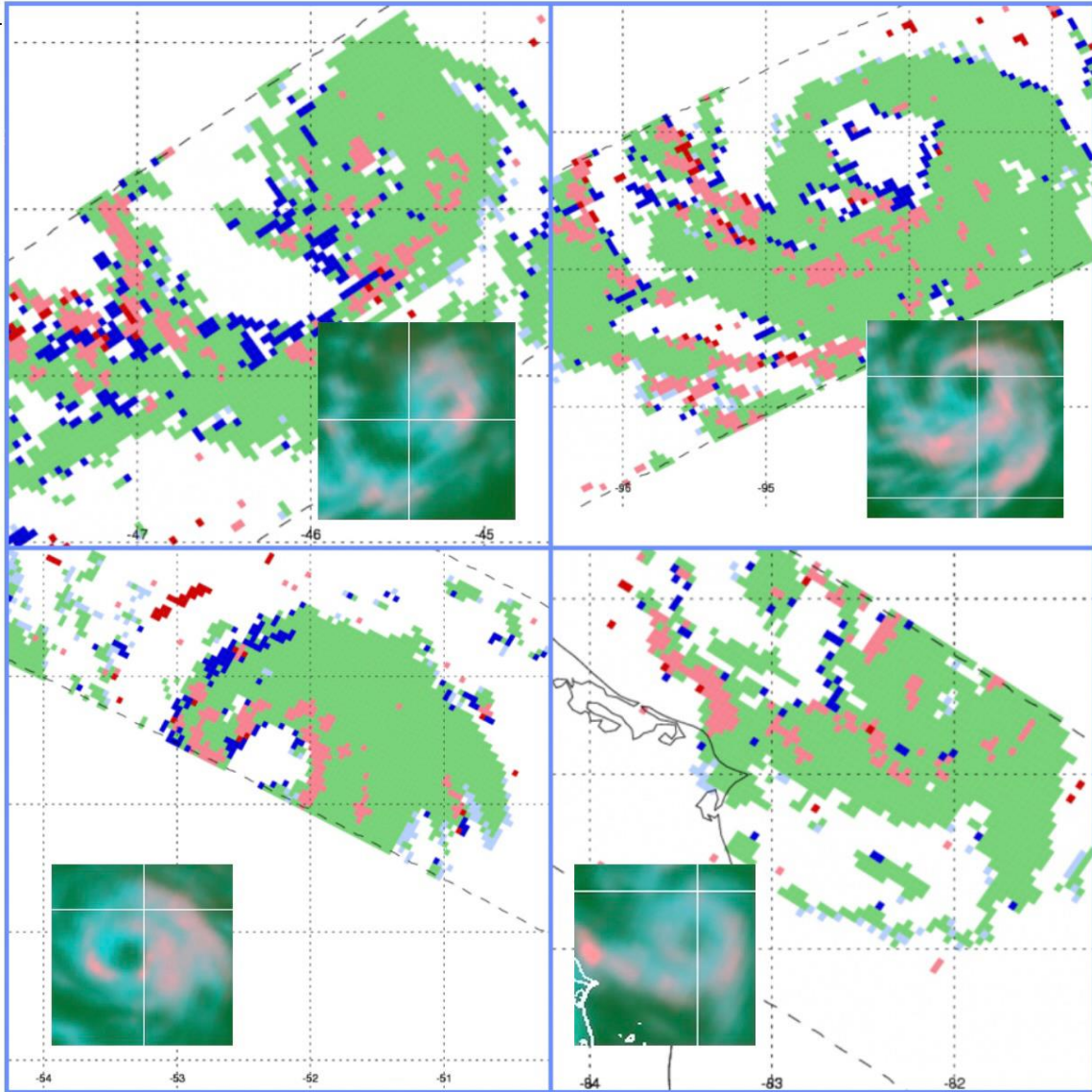


Figure 5.20 2004 Danielle RI ring labeled primarily stratiform by the 2A23. The majority of the precipitation is stratiform even when no ice signature (pink) is present.

of the rain in the developing TC is identified by this algorithm as stratiform.

In Figure 5.21, four more of the RI rings for Atlantic TC are shown (2007 Dean, 2008 Dolly, 2008 Ike, and 2008 Paloma), using the same color conventions as in Figure 5.20. In all these cases the majority of the raining pixels are identified as stratiform rain, even



in cyan areas that have no ice coverage but are purely warm precipitation.

It is pertinent to question why the shallow and moderate convective precipitation is so invisible in the PR 2A23 product. Contoured Frequency by Altitude Diagrams (CFADs, Yuter and Houze, 1995) from Figure 2 of Hense and Houze (2011) provides an intuitive answer. Figure 5.22 produces the three eyewall CFADs from that figure for the total reflectivity pixels in the study, the percentage of those pixels identified as stratiform, and the percentage of those pixels identified as convective. The total CFAD has a strong similarity to the stratiform CFAD, but no similarity to the deep convective CFAD (from Figure 5.18 we know that the majority of pixels identified by the 2A23 algorithm as convective are deep convection as these reside in the "pink" area, so we refer to these convective pixels as deep convective). Yet almost half of the pixels are convective. This shows that *on the CFADs the stratiform profile is dominant and can mask deep convective profiles even when they compose almost half of the population. In the same vein the stratiform CFAD could mask shallow and moderate convective profiles.* While Hense and Houze (2011) extensively compares the stratiform and convective CFADs of the eyewall area with the periphery of the TC, it does not make any comparisons between the total CFAD and the other two. Here the total and stratiform CFADs are similar and the total CFAD is unrepresentative of the convective CFAD.

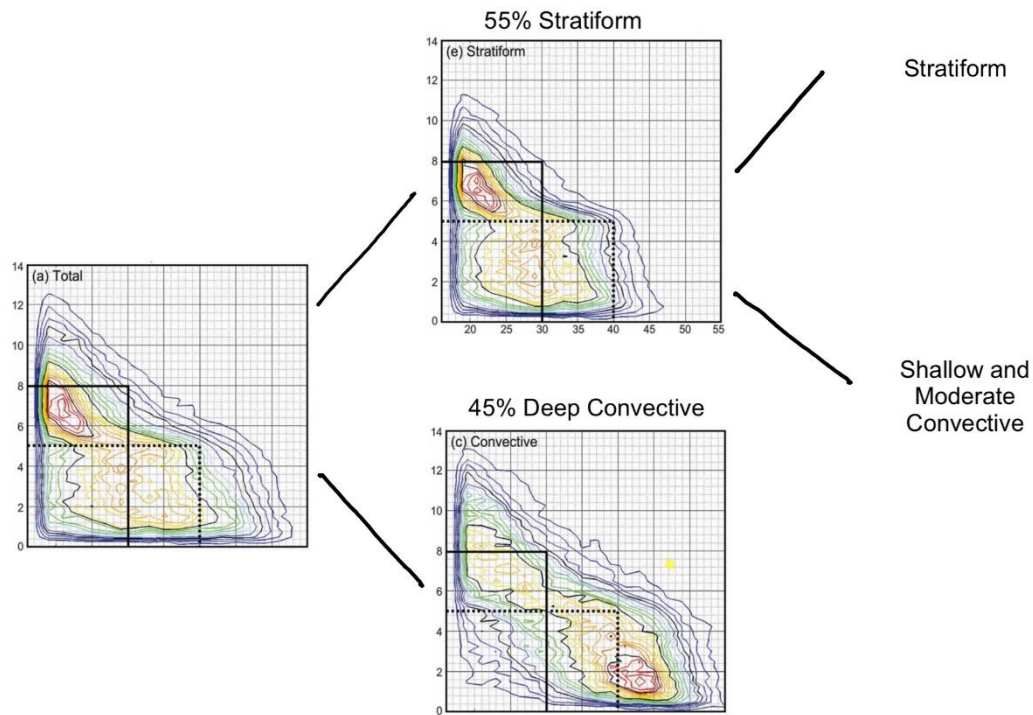


Figure 5.22 Convective and stratiform CFADs from Hence and Houze 2011. Figure 2 CFADs (see Yuter and Houze, 1995) for the eyewall area of all TC in that study, scaled in km in the vertical and dBZ in the horizontal. On the left is the composite CFAD for all reflectivity pixels, and on the right are the CFADs for stratiform and convective pixels. This depiction categorizes primarily deep convective pixels, which is confirmed from Figure 5.18. The total CFAD profile is similar to the stratiform CFAD, and not at all similar to the convective CFAD. Yet almost half of the pixels fall into the latter category indicating that the overall profile of stratiform labeled rain can mask the profile of the convective pixels combined in total. It follows that the stratiform profile masks the profile of SAM convective pixels for strengthening tropical cyclones.

5.7 Conclusions Regarding Shallow and Moderate Convection in TC

Tropical cyclones are driven by diabatic processes as opposed to baroclinic processes; that is, they are driven by convection (Emanuel, 1986). Deep convection results from the convective life cycle, beginning as shallow cumulus. Therefore a population of convective clouds in various stages of maturity must exist in a TC, including shallow,

moderate, and deep convection. Because deep convection is the end result of the convective life cycle, this necessitates the existence of shallow and moderate convection.

The importance of the cyan patterns, uniquely seen on the 37color imagery, led to the understanding that they identified a understudied component of tropical cyclone precipitation, shallow and moderate convection: SAM. These warm precipitative patterns, seen in cyan color on the 37color images, are not visible on any other PMW imagery of TC provided by the NRLMRY TC archive.

SAM is not represented in TC conceptual models or in the most widely-used method of analyzing tropical cyclone intensity, the Dvorak Method. And when the NRLMRY and FNMOC TC web pages began providing PMW imagery, emphasis was placed on the 85H channel which primarily shows the ice signature associated with deep convection, and low cloud bands. The TRMM PR 2A23 product does not recognize SAM but includes it in the category of stratiform rain. It classifies primarily deep convection as convective rain, but does not appear to recognize all deep convection. CFADs of strengthening TCs (Hence and Houze 2011) show that the stratiform signal masks the convective signal, and that the stratiform-only 2A23 pixels are likely masking SAM precipitation. The FIU TCPF 9-panel product that includes images of the stratiform/convective characterization of each TC PR overpass provide a visual that illustrates how this product underestimates the amount of convection present in general. As a result considerations of SAM in tropical cyclone structure and development has not been identified and its contribution to TC processes have been largely overlooked. There has not been a recognition of this category of convection in TC in spite of general

understanding of the convective life cycle as requiring growth from shallow and moderate convection to create deep convection.

The characteristics of the colors of the 37color image precipitative types were empirically determined by considering the different vertical layers represented by the green, cyan, and pink colors and what those combinations mean in the context of TC. Because SAM presents primarily as warm precipitation it corresponds to the bright cyan areas on the 37color, as shown in the examples. This characterization of precipitation types is consistent with case studies of 37color images and TRMM PR and WSR-88D radar cross sections that are shown.

The SAM rings of developing eyes suggest that there is a significant contribution of shallow and moderate convection in developing stages before the TC matures. This could have broader implications beyond eye development. The SAM rings, while not a mature eye, can play a similar role in terms of vortex dynamics. The definition of a TC eye is based on historical understanding of a clear center seen from the ground, and in modern tropical meteorology, able to be observed on geostationary satellite imagery (visible, infrared, and water vapor). Consequently the SAM ring has been referred to as a "microwave eye" and "low-level eye." The role of the SAM rings in eye development might be motivation for modernizing the definition of the eye.

CHAPTER 6. A 37color Precipitative Intensity Estimate (PIE) Utilizing the 37color Imagery

Almost as soon as the NRLMRY TC web page and tcdat archive came online in 1997, there was interest in creating a Dvorak-like technique of current intensity estimation using the PMW imagery. These included Roger Edson (Edson, 2014) using the 85 GHz horizontal imagery and later Jeff Hawkins (Hawkins et al. 2000) using an objective neural net method, also using 85 GHz, and Dan Cecil (Cecil and Zipser, 1999). These methods did not yield a viable forecast aid in the published literature.

The Dvorak technique uses cloud patterns (Figures 6.1 and 6.2) in the visible imagery and was subsequently expanded to include cloud top temperatures in the EIR imagery - a unique "enhanced IR" image that separates IR Tb into a gray scale, also known as a BD-IR image (Dvorak 1984). Dvorak method of estimated maximum sustained winds of TCs has been validated against reconnaissance-based data in the Atlantic basin (Brown and Franklin 2004) and found to be good, with errors under 10 kt seventy percent of the time. Where there is no aircraft reconnaissance Dvorak method is the primary tool for estimating tropical cyclone intensity, so it is an essential forecast tool that is used for every TC forecast.

Even though the Dvorak technique is essentially a subjective technique in that it may be open to the analyst's interpretation, it is a quantitative method that measures cloud features. For this reason it was possible to create an automated version of the Dvorak technique, the ADT (Olander and Velden 2019).

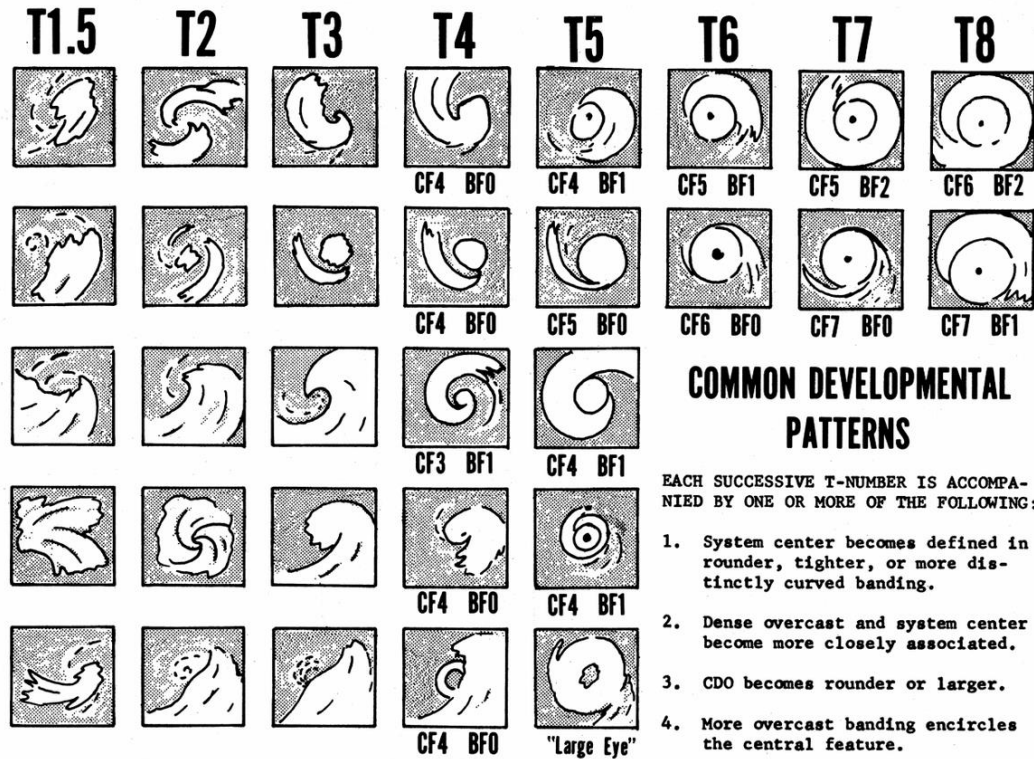


Figure 6.1 The four main Dvorak technique cloud patterns. Curved band, shear pattern, CDO/embedded center, and eye pattern shown. The first steps in the technique are to locate the TC center and then to select a pattern. In some cases more than one pattern may be used.

Knaff et al (2010) found Dvorak technique performed best in a range of 90-125 kt intensities. The use of EIR imagery is well-suited to determine intensities when a mature eye is present in the satellite imagery as small increments in the cloud top and eye temperatures can be related to a current intensity.

A well-known issue with the Dvorak technique is that it tends to lag behind the actual intensities before the eye is apparent (Velden et al 2006) because the CDO obscures the eye development in the early stages.

For this reason a PMW-based analog to Dvorak could provide improved performance for



FIG. 3. Examples of the tropical cyclone patterns illustrated in Fig. 2. The T-numbers shown are the "pattern" T-numbers; these may be adjusted for model considerations.

Figure 6.2 Dvorak intensity estimation technique cloud patterns using satellite imagery.

this phase of development, usually between the onset of tropical storm intensity and prior to intensification to major hurricane (35 kt to 95 kt), although the eye can occasionally become apparent at minimal hurricane intensity. Because the 85 GHz signal primarily identifies deep convection, and the 37color imagery shows warm precipitative patterns of SAM, which have been established here are important in TC, the latter frequencies are better suited for analyzing developing TC. However no previous attempt has been made

to utilize this imagery for intensity estimates. Even the ADT, which has incorporated PMW data into the algorithm, uses the 85 GHz frequencies.

This section will show a methodology for estimating the intensity of TC from 37color imagery that has not been attempted before, for intensities in the range of tropical depression through tropical storm, which is the range at which Dvorak technique falls behind. This method, like Dvorak, is based on patterns, but patterns of precipitation, and is based on Atlantic TC, and as such is called the Precipitative Intensity Estimate (PIE) technique. As currently developed it is not quantitative but could be quantified in future work. Some of the patterns resolve to a range of intensities rather than a single intensity, and the patterns have not been extended to the extent that every 37color image has a pattern match. The PIE patterns are idealized. By comparison patterns seen on the actual 37color images are noisy and also may be elongated.

The PIE precipitative patterns (Figure 6.3) are identified for combinations of the warm precipitative signature and the ice signature characteristic of 37color imagery, with a dark green background for the ocean surface, using the three basic descriptions of ocean surface, rain, and ice from Lee et al (2002). The patterns may need to be rotated depending on the orientation of the TC. Because the sheared characteristic of TCs are readily apparent on this imagery (Chapter 7), and also related to intensity, the patterns are divided into low and moderate shear of 0 to 20 kt, and moderate to strong shear above 20kt. Both sets of patterns show the evolution into a principal band. As the patterns relate to stronger intensities, three of the strongest patterns are also extended to identify

cases with strong moist surface inflow, which provides a more favorable environment, by showing additional thin inflow bands of the cyan SAM inside of the principal band. In contrast to the Dvorak technique, the PIE technique is helpful at differentiating TC intensities in the early stages of development, but once the eye forms it is not helpful, because almost all intensities appear the same on the 37color until the most intense TCs starting at around 115-120 kt of intensity. The strongest TC eyes have a different appearance (Chapter 7). Therefore the PIE technique could be a good complement for the Dvorak technique with further development, and has potential.

Figures 6.4 through 6.14 show examples of 37color images of TC that correspond to the PIE patterns, all from the Atlantic basin.

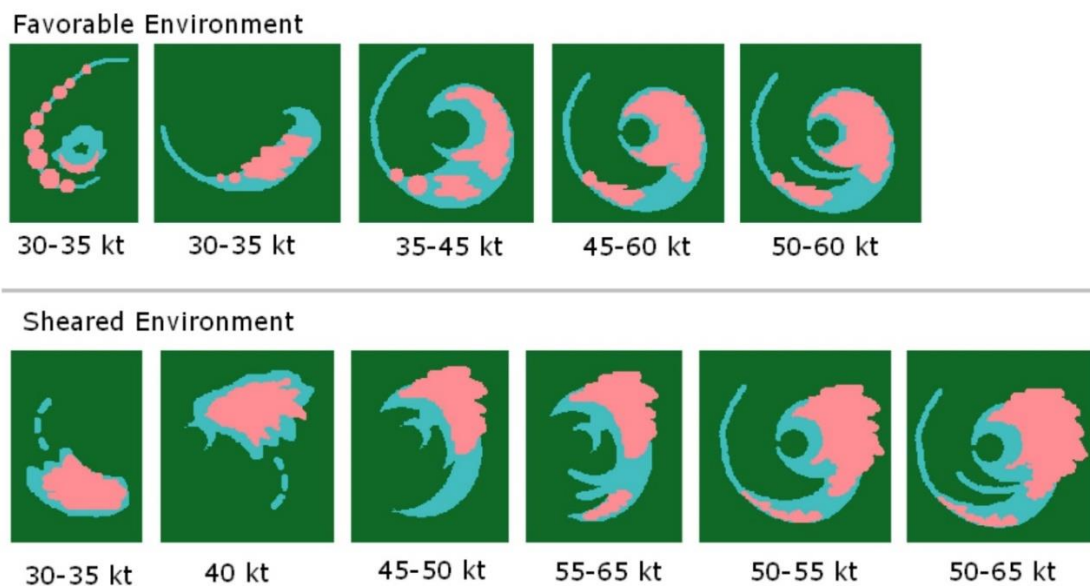


Figure 6.3 PIE intensity estimate patterns for the range of tropical storm intensities. These use the 37color imagery, based on precipitative patterns in the Atlantic basin. A favorable environment includes low-shear (0-5 kt) and moderate shear (5-20 kt) – a sheared environment includes moderate to high shear (above 20 kt), so these categories can be separated into above and below 20 kt of shear.

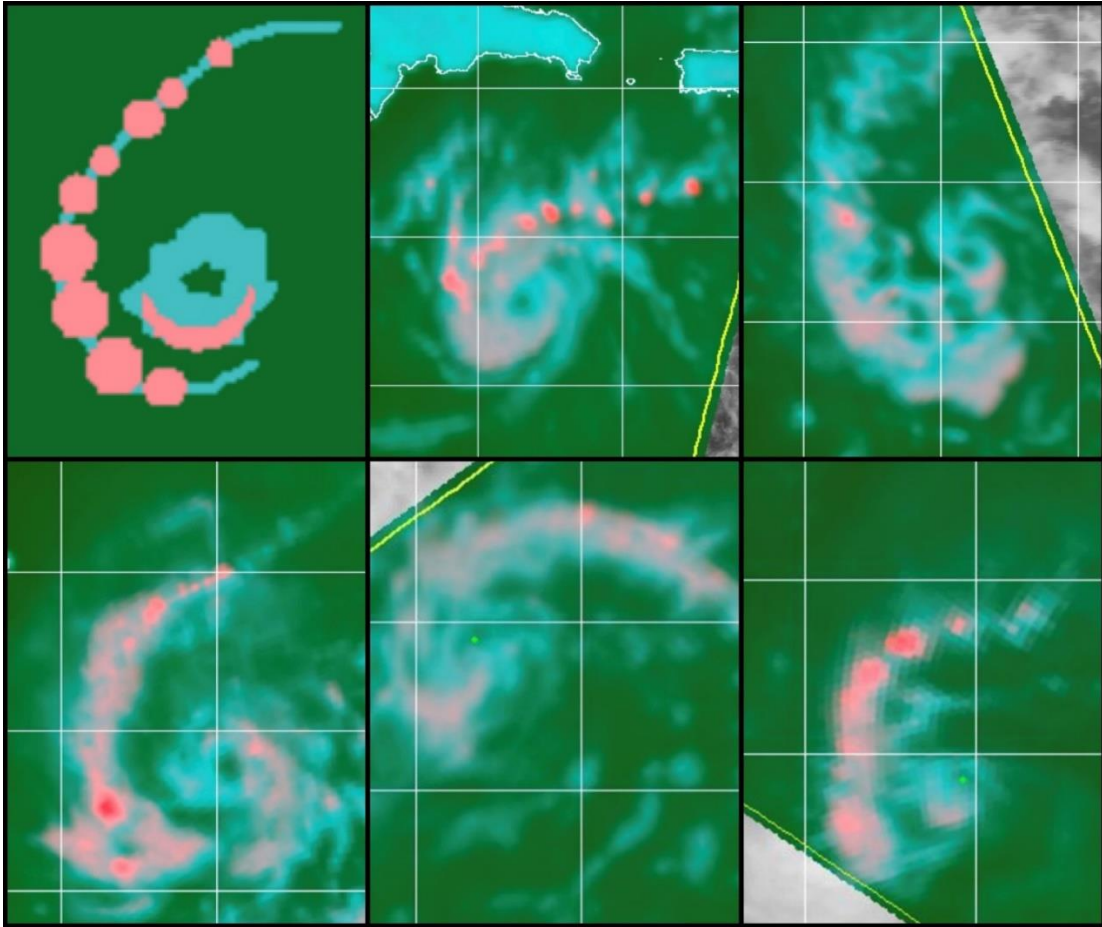


Figure 6.4 PIE pattern for low to moderate shear 30-35 kt intensity. Shown 2008 Gustav, 2016 Gaston, 2015 Fred, 2004 Karl and 2004 Frances.

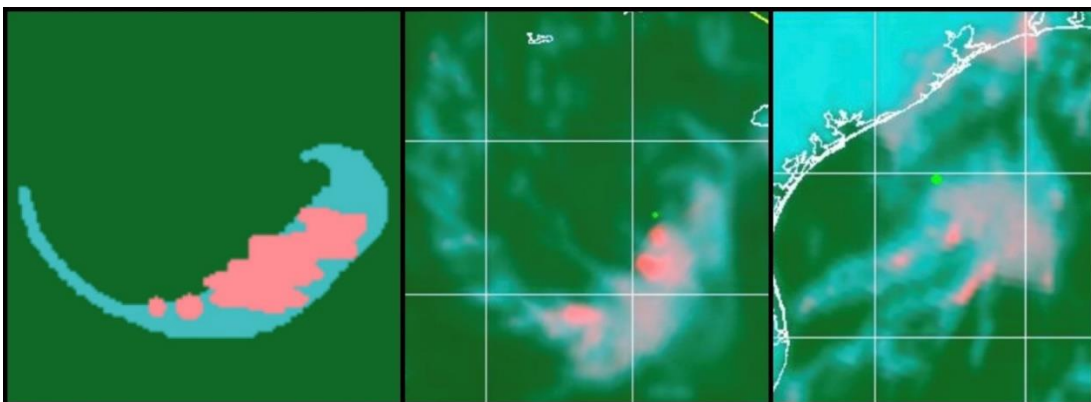


Figure 6.5 PIE pattern for low to moderate shear 30-35 kt intensity. Shown 2005 Wilma and 2007 Humberto.

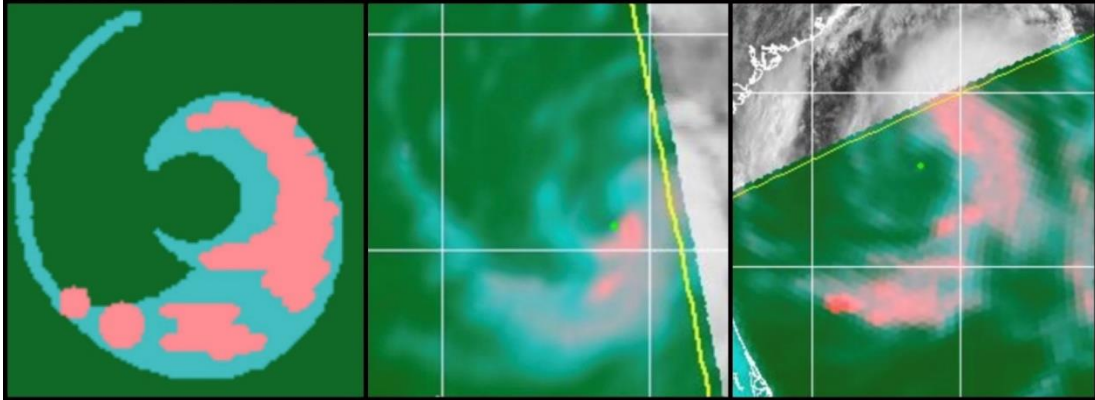


Figure 6.6 PIE pattern for low to moderate shear 35-45 kt intensity. Shown 2005 Dennis and 2004 Gaston.

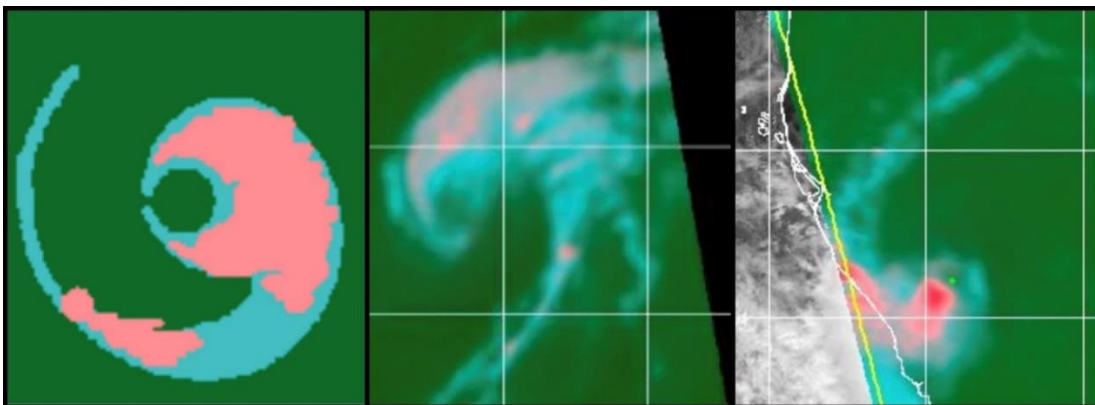


Figure 6.7 PIE pattern for low to moderate shear 45-60 kt intensity. Shown 2012 Tony and 2011 Lorenzo.

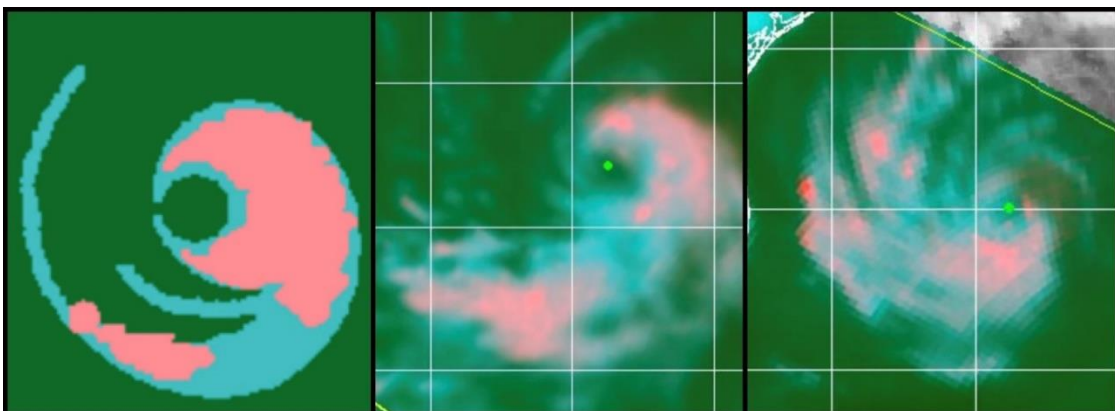


Figure 6.8 PIE pattern for low to moderate shear 50-60 kt intensity. Shown 2004 Ivan and 2003 Erika.

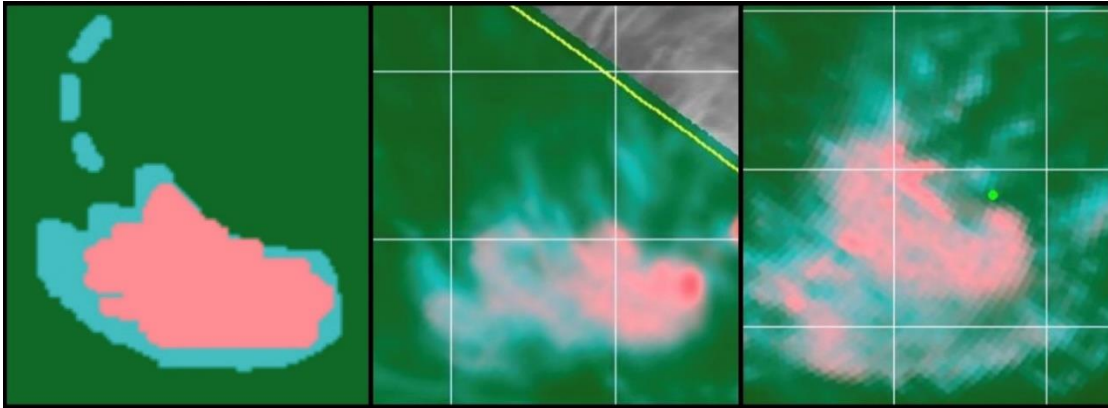


Figure 6.9 PIE pattern for moderate to strong shear 30-35 kt intensity. Shown 2007 Dean and 2003 Isabel.

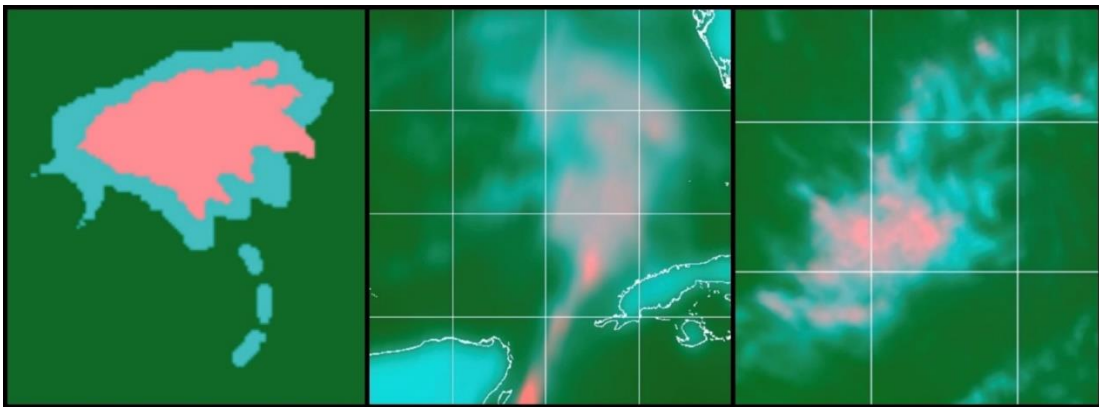


Figure 6.10 PIE pattern for moderate to strong shear 40 kt intensity. Shown 2012 Debbie and 2010 Danielle.

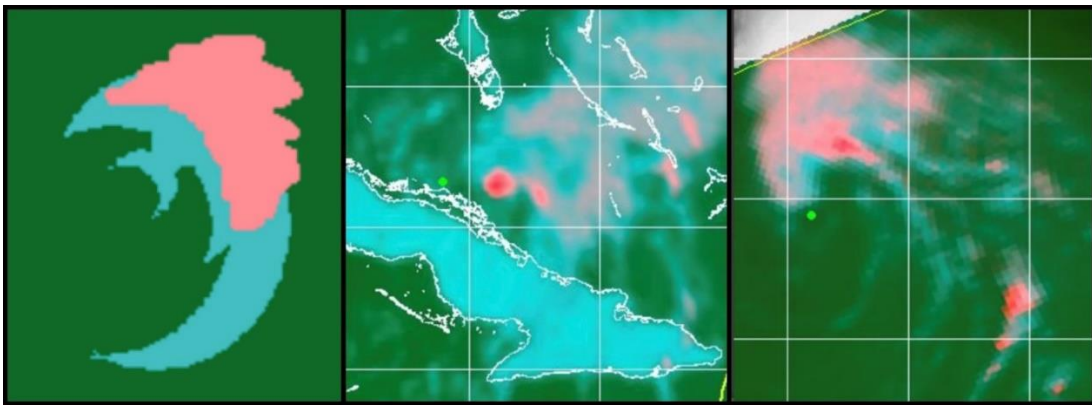


Figure 6.11 PIE pattern for moderate to strong shear 45-50 kt intensity. Shown 2007 Noel and 2003 Juan.

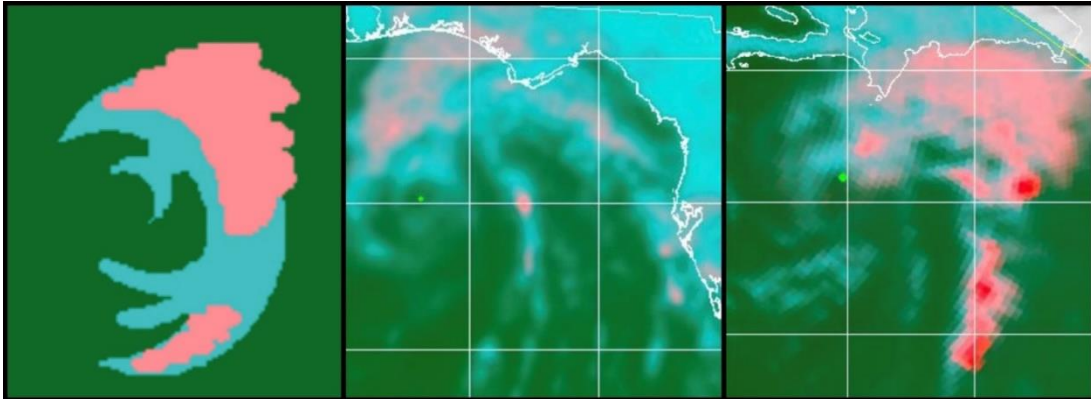


Figure 6.12 PIE pattern for moderate to strong shear 50-65 kt intensity. Shown 2005 Arlene and 2003 Odette.

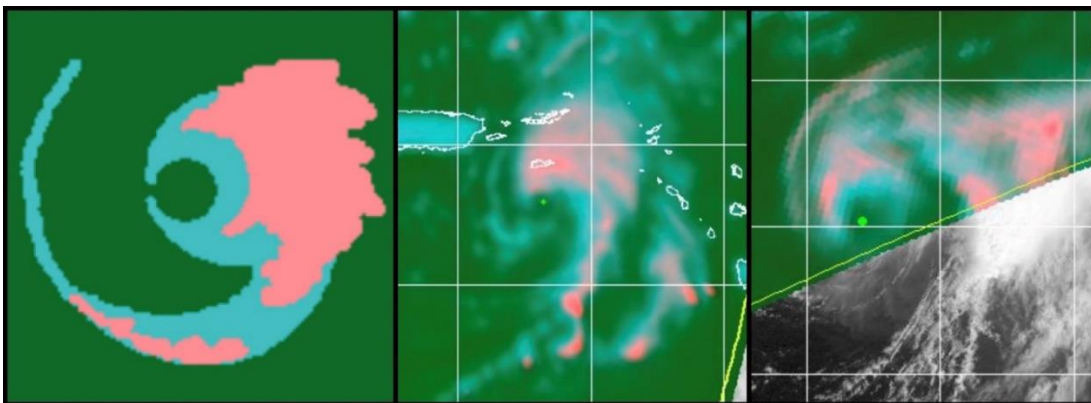


Figure 6.13 PIE pattern for moderate to strong shear 50-55 kt intensity. Shown 2004 Jeanne and 2003 Kate.

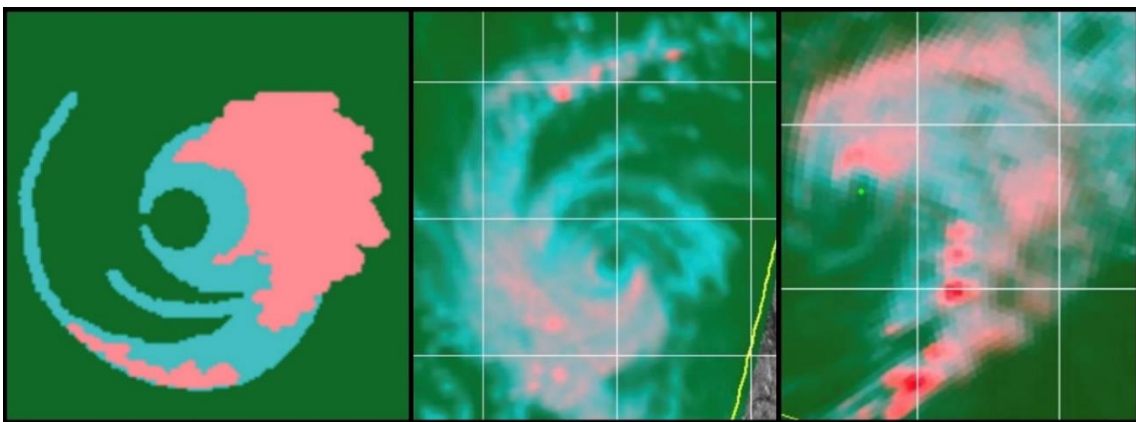


Figure 6.14 PIE pattern for moderate to strong shear 50-65 kt intensity. Shown 2010 Celia and 2003 Kate.

CHAPTER 7. Additional Characteristics of Tropical Cyclones Observed on 37color Imagery: Intense, Sheared, Subtropical, and Monsoon Development

In addition to the SAM ring used for RI forecasting and the identification of Early ERCs, other significant characteristics of TCs are uniquely observed on the 37color imagery.

These include the eyes of intense TC from both NHEM and SHEM basins, low, moderate, and strongly sheared TC, subtropical storms, and TC that develop in a monsoon trough (very common in the West Pacific, not as common in the Atlantic, and somewhat more common in the East Pacific). This is another aspect of the usefulness of the 37color imagery.

7.1 37color Images of Intense Tropical Cyclones

The eyes of intense TC, all but one at the equivalent of Category 4-5 on the Saffir Simpson Wind Scale (SSWS), were observed at intensities ranging from 115 kt to 185 kt (2000 Rosita in the Indian Ocean overpass was at 110 kt). These are not images of the highest intensities that these TC reached in their lifetimes (for instance the PMW pass of 2012 WPAC Haiyan occurred at 150 kt but the maximum intensity reached was 170 kt on the JTWC best track), but they are available 37color passes of intense TC from the NRLMRY tcdat repository, and all TC basins are represented.

On all these overpasses of intense TC there is prominent ice signature indicating deep convection, usually extending completely around the eye, and this is one of the signatures on the 37color that a TC may be at Category 4 intensity or higher. The images have been grouped by diameter of the ice signature at the top of the eye but this does not necessarily correspond to the size of the eye, which is a measure of the eye diameter at the surface.

TC eyes tilt outward with height so the eye diameter is smaller than the ice signature,

although those with the smallest diameter ice signatures do have the smallest eye diameters, of 10 n mi or less (Figure 7.1), those with small diameters range approximately from 10 to 15 n mi (Figure 7.2), and the most of those with the largest diameters are around 20 n mi but some are as small as 5 n mi (Figure 7.3). There is no correspondence between these diameters and intensity, and with the rare exception intense TC observed in recent decades peak around 155-160 kt. Two recent extremely intense TC were 2013 WPAC Super Typhoon Haiyan which peaked at 170 kt, which 2015 EPAC Hurricane Patricia peaked at 185 kt confirmed by aircraft reconnaissance.

There is no correlation between intensity and the diameter of the ice signature of the eyewall on the 37color for these intense TCs, with the range of intensities for the smallest eyes seen in the images ranging from 115 kt to 185 kt, for larger diameters, 110 kt to 160 kt, and for the largest observed diameters, 125 kt to 155 kt (Table 7.1).

Year	Basin	TC name	TC intensity in kt
2006	SHEM	Xavier	115
2020	NATL	Eta	120
2001	EPAC	Juliette	125
2016	NATL	Matthew	130
2016	NATL	Matthew	135
2017	NATL	Maria	140
2004	NATL	Ivan	140
2007	NATL	Felix	140
2005	NATL	Wilma	150
2015	NATL	Patricia	150
2000	WPAC	Damrey	155
2015	NATL	Patricia	185
2000	SHEM	Rosita	110
2006	WPAC	Chebi	115
2007	NATL	Felix	115
2007	IO	Sidr	130
2018	NATL	Michael	135
2004	SHEM	Gafilo	140
2018	WPAC	Yutu	140
2010	WPAC	Megi	145
2019	NATL	Dorian	145
2016	SHEM	Fantala	150
2005	NATL	Rita	155
2006	SHEM	Monica	155
2019	WPAC	Halong	155
2016	WPAC	Meranti	160
2019	NATL	Dorian	160
2019	NATL	Lorenzo	125
2004	NATL	Ivan	130
2016	NATL	Matthew	130
2017	WPAC	Lan	130
2015	SHEM	Pam	135
2006	SHEM	Monica	145
2014	WPAC	Wongfong	145
2013	WPAC	Haiyan	150
2016	SHEM	Winston	150
2017	NATL	Maria	150
2016	SHEM	Winston	155
2017	NATL	Irma	155

Table 7.1 Intense TCs by basin and intensity at the time of the associated 37color overpass. Shown in Figures 3.49-3.51, grouped by eye size.

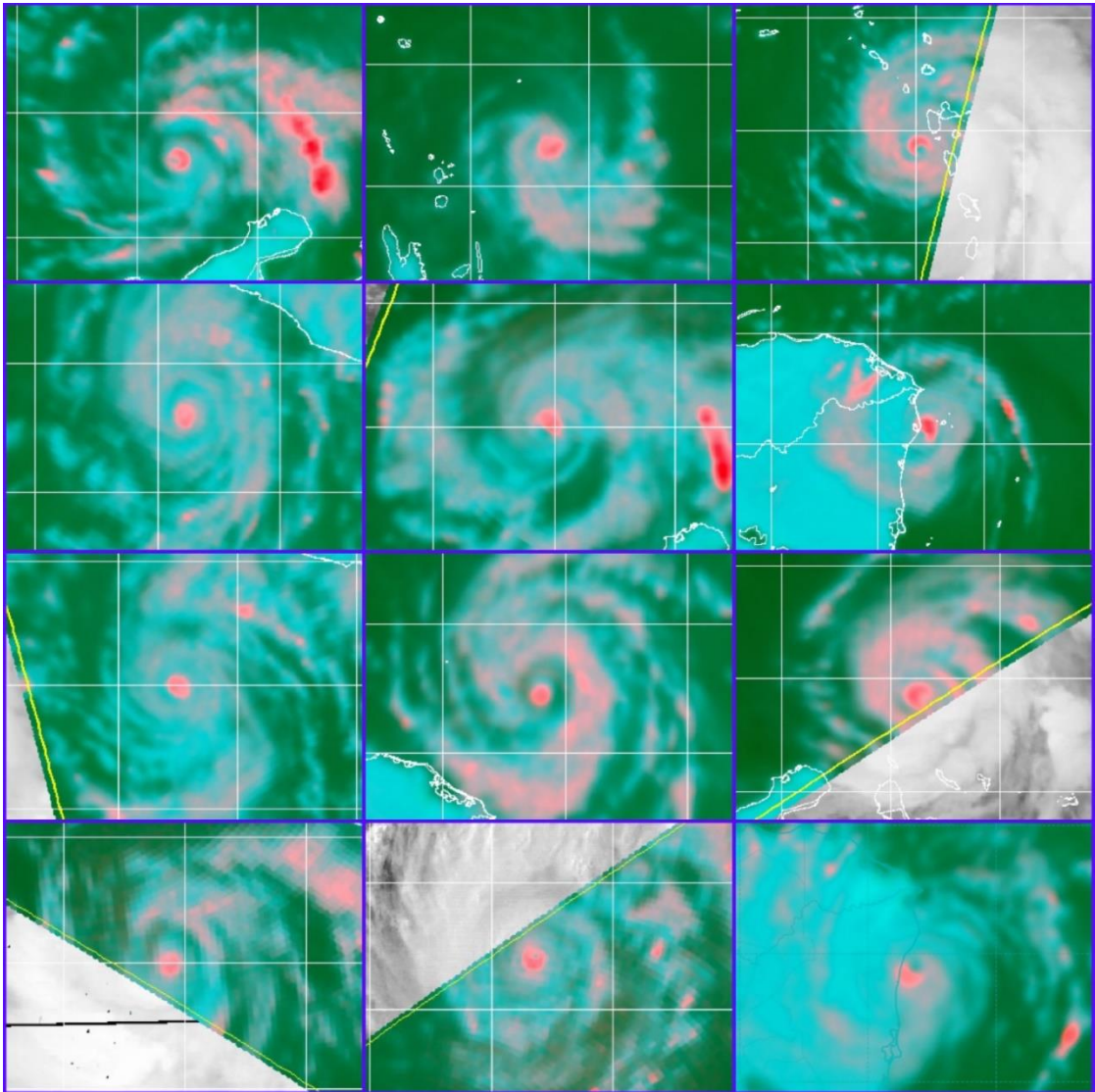


Figure 7.1 37color images of intense TC with very small eyes. Listed in Table 3.3.1.

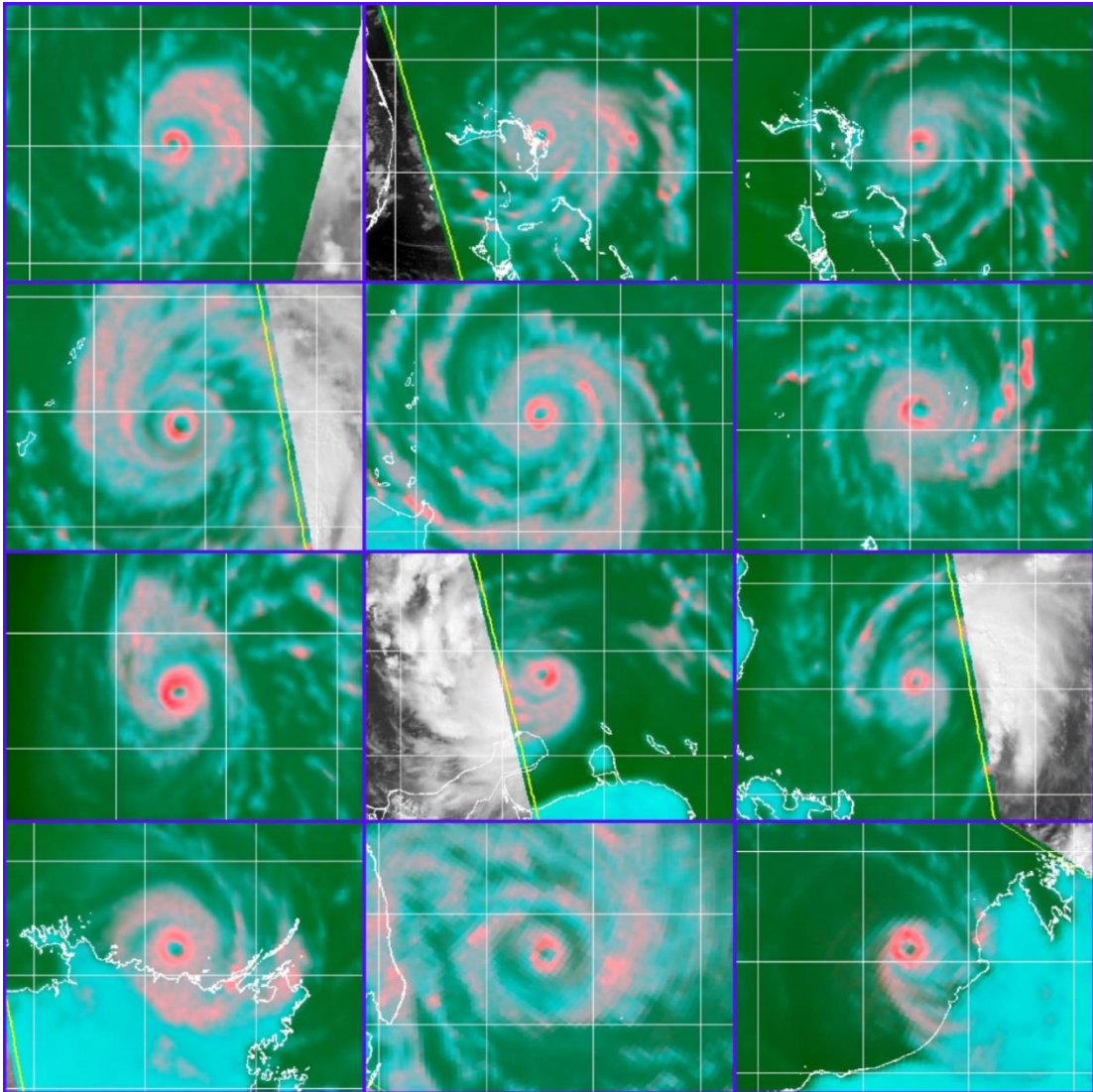


Figure 7.2 37color images of intense TC with small eyes. Listed in Table 3.3.1.

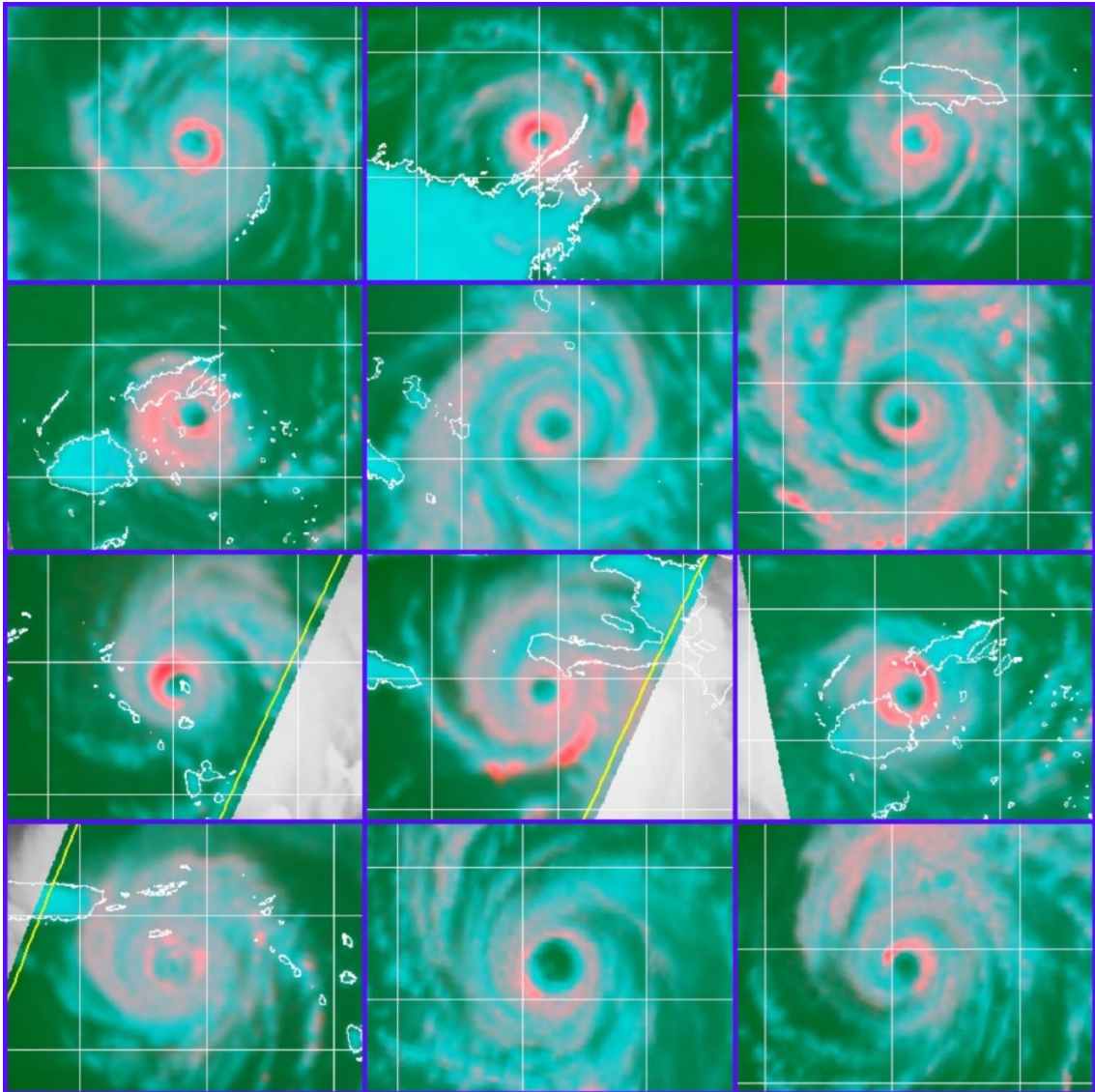


Figure 7.3 37color images of intense TC with eye diameters of about 20 n mi. Listed in Table 3.3.1.

7.2 Sheared Tropical Cyclones Observed on the 37color Imagery

Climatologically the Atlantic basin has a significant amount of vertical wind shear. This is apparent on 37color imagery with increased coverage and large area of the pink/ice signature indicative of sheared convection extending down shear from the center. Strong shear (Figures 7.4 and 7.5) can be differentiated by intense and saturated ice signatures

that are not seen on moderate shear (Figures 7.6 through 7.8). Shear values for the times of the PMW passes were obtained from SHIPS and when SHIPS was not available from the Tropical Cyclone Report (TCR), which mentioned the shear (Table 7.2).

2005 Dennis	moderate shear	10 kt	SHIPS
2005 Wilma	moderate shear	10 kt	SHIPS
2014 Odile	moderate shear	15 kt	SHIPS
2019 Humberto	moderate shear	15 kt	SHIPS
2005 Katrina	moderate shear	15-20 kt	SHIPS
2014 Rafael	moderate shear	15-20 kt	SHIPS
2006 Alberto	strong shear	-	TCR
2006 Ernesto	strong shear	-	TCR
2008 Omar	strong shear	20 kt	SHIPS
2008 Omar	strong shear	25 kt	SHIPS

Table 7.2 Shear values for the Atlantic basin TC in the accompanying imagery.

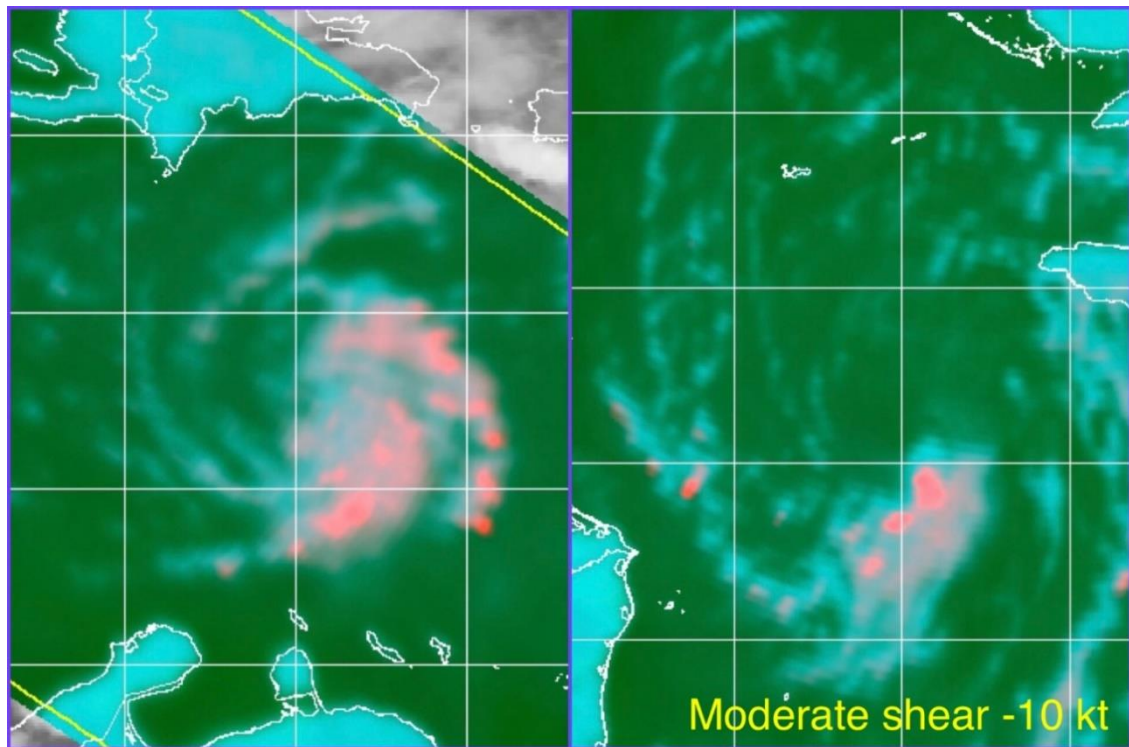


Figure 7.4 2005 Dennis and 2005 Wilma under moderate shear of 10 kt.

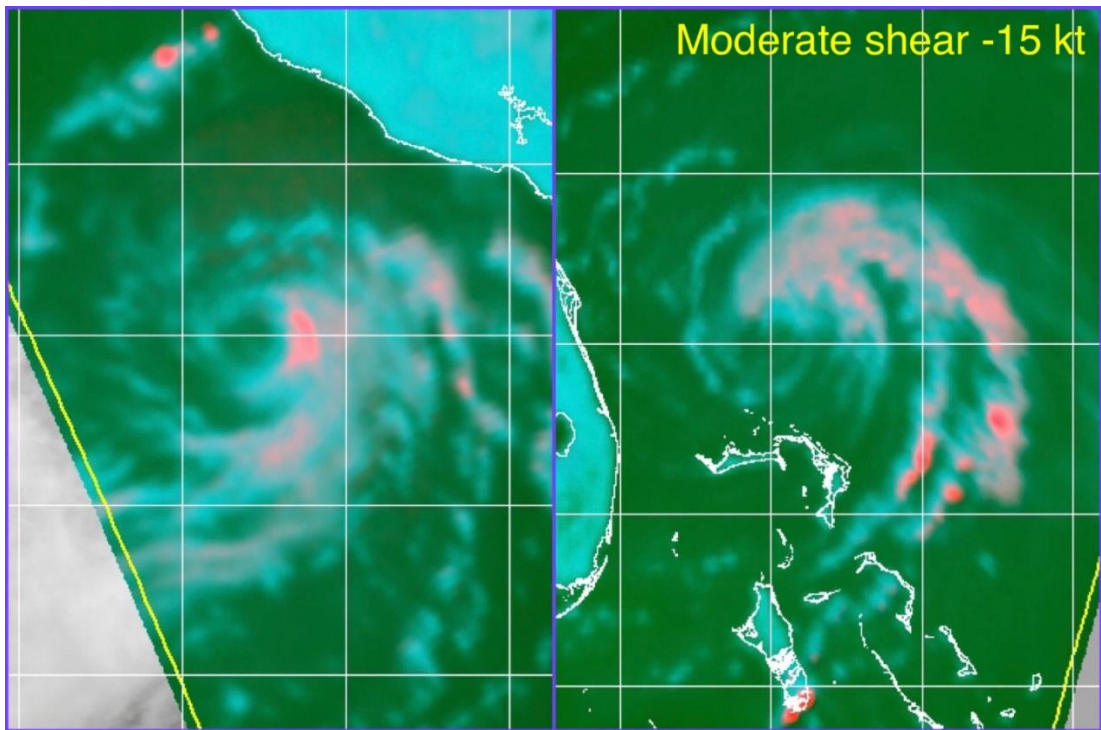


Figure 7.5 2014 Odile and 2019 Humberto under moderate shear of 15 kt.

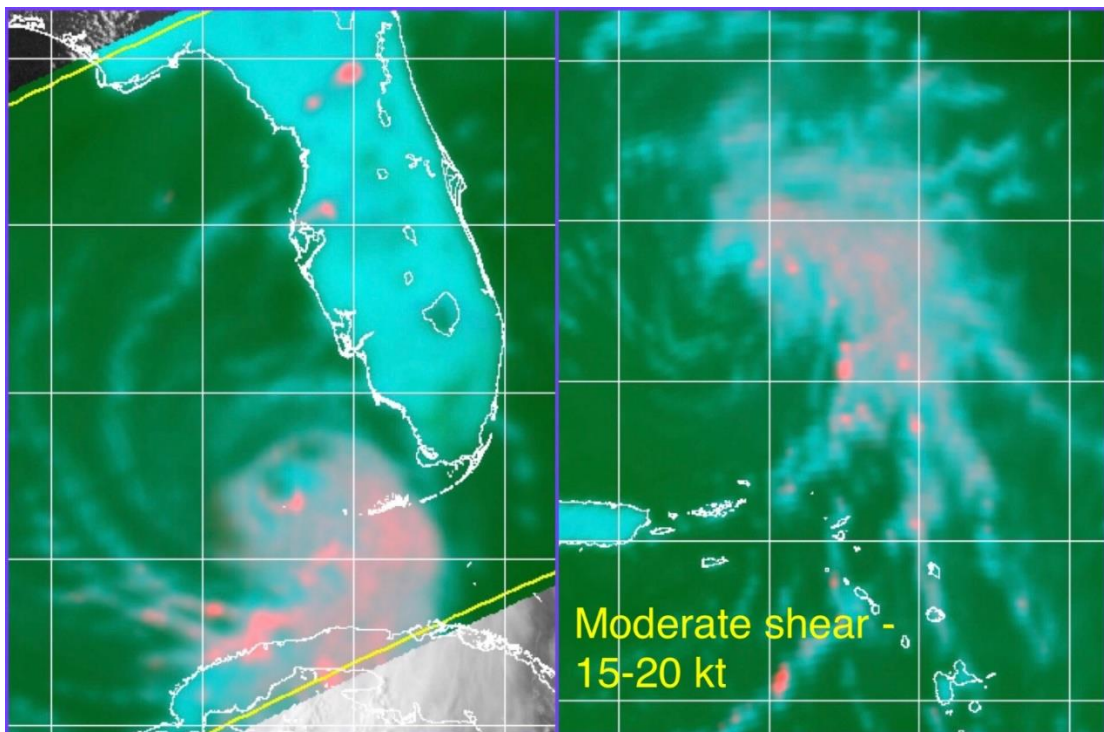


Figure 7.6 2005 Katrina and 2014 Rafael under moderate shear of 15-20 kt.

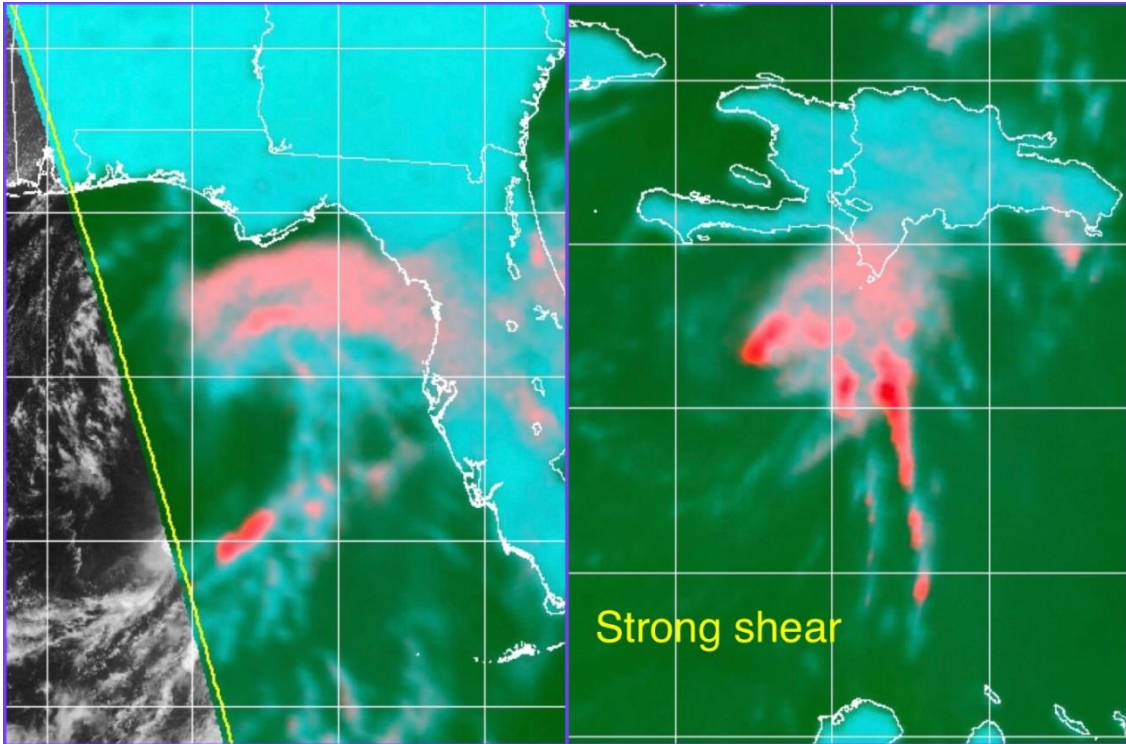


Figure 7.7 2006 Alberto and 2006 Ernesto under strong shear.

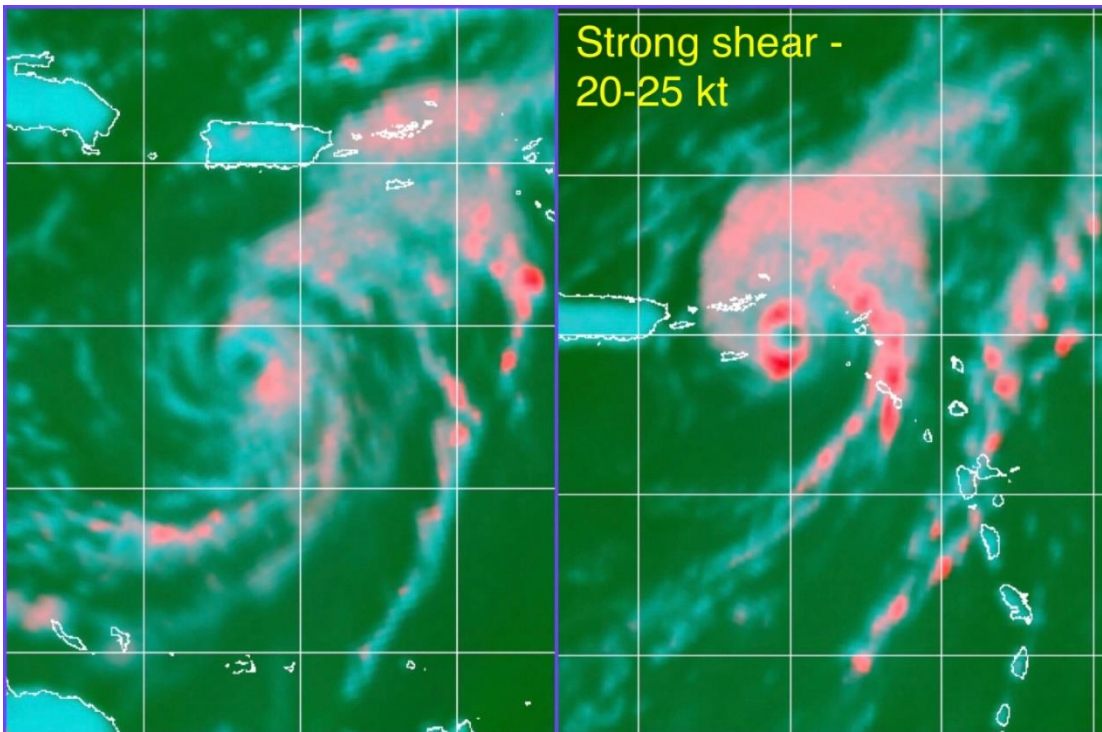


Figure 7.8 Two images of 2008 Omar under strong shear of, respectively, 20 kt and 25 kt.

7.3 Subtropical Cyclones Observed on the 37color Imagery

Subtropical cyclones (STC) have a distinctive appearance on the 37color imagery.

Because of the circumstances of their genesis, they often contain cold dry air aloft, and if under an upper low or suppressed tropopause, have lower convective cloud top heights.

The moisture content of the air masses when subtropical cyclones form is often lower than for tropical cyclones, resulting in less widespread convection and thinner convective bands.

Consequently the 37color images of STC show sparse thin discontinuous bands of SAM with very few deep convective cells, and often show dry air wrapping into the circulation. They often have a large cyclonic envelope so that the overall circulation seen on the 37color is large, with the sparse convective banding distributed throughout the envelope, and not converging into a principal band as is seen on tropical cyclones.

Six instances of STC from 2018 are shown in Figure 7.9 and 2019 Melissa in Figure 7.10. The corresponding CIMSS Advanced Microwave Sounding Unit (AMSU) vertical cross section brightness temperature anomaly for each of the 2018 STC shown in Figure 7.11 indicate the upper tropospheric warm core associated with STC, due to the descent of warmer lower stratospheric air into the upper troposphere.

Notes on the origins and evolutions of these STC and the relevant 37color overpasses are in Table 7.3.

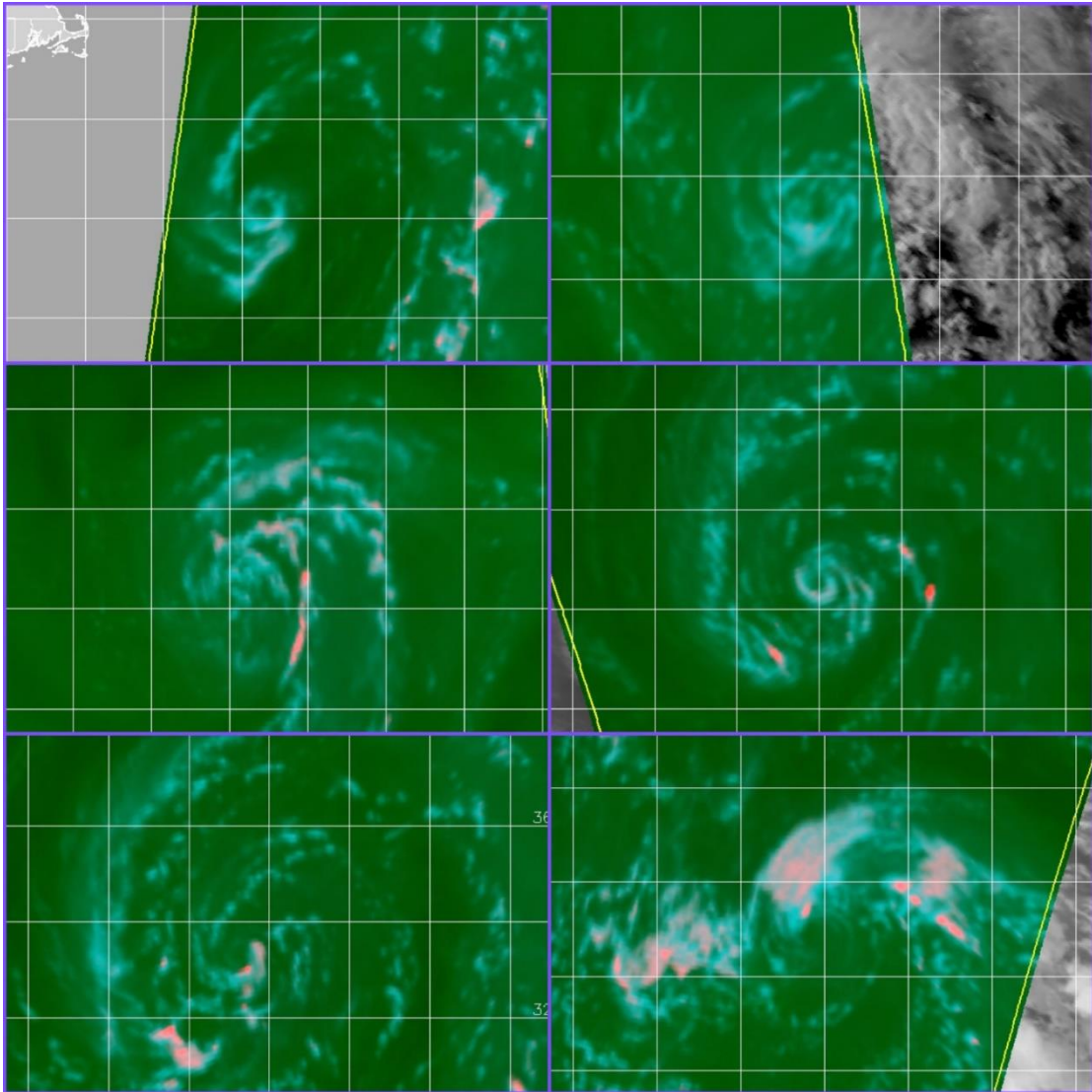


Figure 7.9 Six STC from 2018 Atlantic basin. Seen are Beryl, Debby, Ernesto, Joyce, Leslie, and Oscar, shown left to right top to bottom.

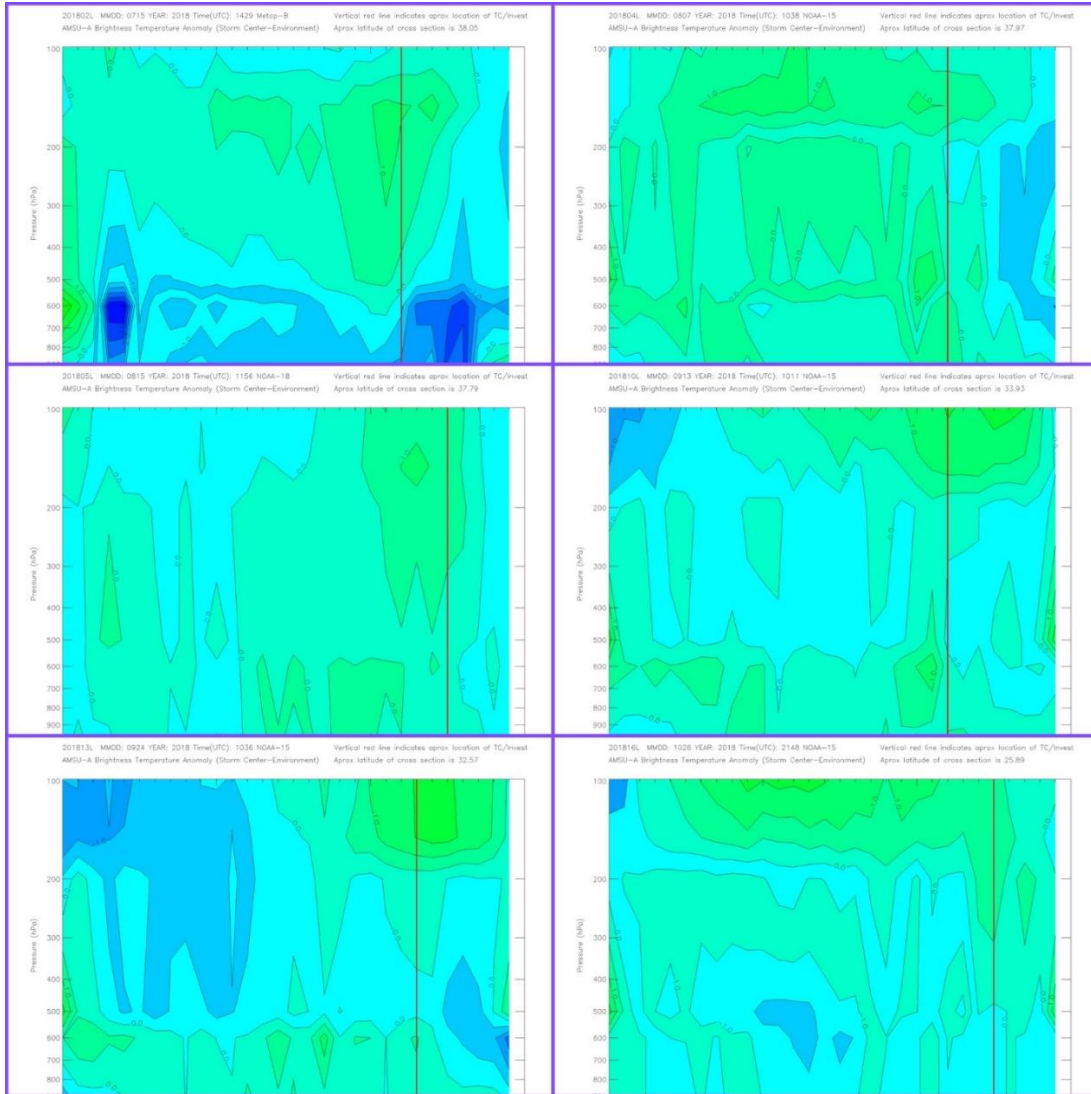


Figure 7.10 Corresponding AMSU vertical cross section temperature anomalies for the six STC in Figure 3.57.

Year	Basin	Storm	Name	Sensor	Date	Time (Z)	Notes
2018	ATL	02	Beryl	AMSR2 GMI AMSR2 AMSR2	2018/07/14 2018/07/14 2018/07/15 2018/07/15	1623 2116 0541 1529	Regenerated as sub trop storm 07/14 1200Z and degenerated into post-trop storm 07/16 0000Z Maintained 35 kt this entire period
2018	ATL	04	Debby	GMI WindSat	2018/08/07 2018/08/07	1256 2125	Non-tropical origin, became sub trop storm 08/07 0600Z for 18 hr until became tropical 08/08 0000Z Maintained 35 kt this entire period
2018	ATL	05	Ernesto	AMSR2 WindSat	2018/08/15 2018/08/15	1447 2039	Non-tropical origin Sub trop TD became sub trop storm for 24 hr, then TS from 15/1200Z to 16/1200Z Maintained 35 kt this entire period
2018	ATL	10	Joyce	WindSat AMSR2 AMSR2	2018/09/12 2018/09/13 2018/09/13	2028 0437 1538	Non-tropical origin Extratrop to sub trop storm, then to TS 12/1200Z to 13/1800Z 40 kt to 35 kt
2018	ATL	13	Leslie	AMSR2	2018/09/23	1615	Extratropical origin Subtropical storm from 23/12Z through 24/18Z Maintained 35k intensity this period then sub trop TD and EX
2018	ATL	13	Leslie	GMI	2018/09/24	1301	Extratropical origin Subtropical storm from 28/12Z through 29/12Z 45/40 kt through this period then TS, HU, TS, HR, EX, dissipated
2018	ATL	16	Oscar	AMSR2	2018/10/27	0503	Formed as subtropical Subtropical storm from 10/26 18Z to 10/27 12Z increased in intensity from 35 to 50 kt

Table 7.3 37color overpasses for subtropical cyclones for 2018 in the Atlantic basin and notes on their origins and evolution.

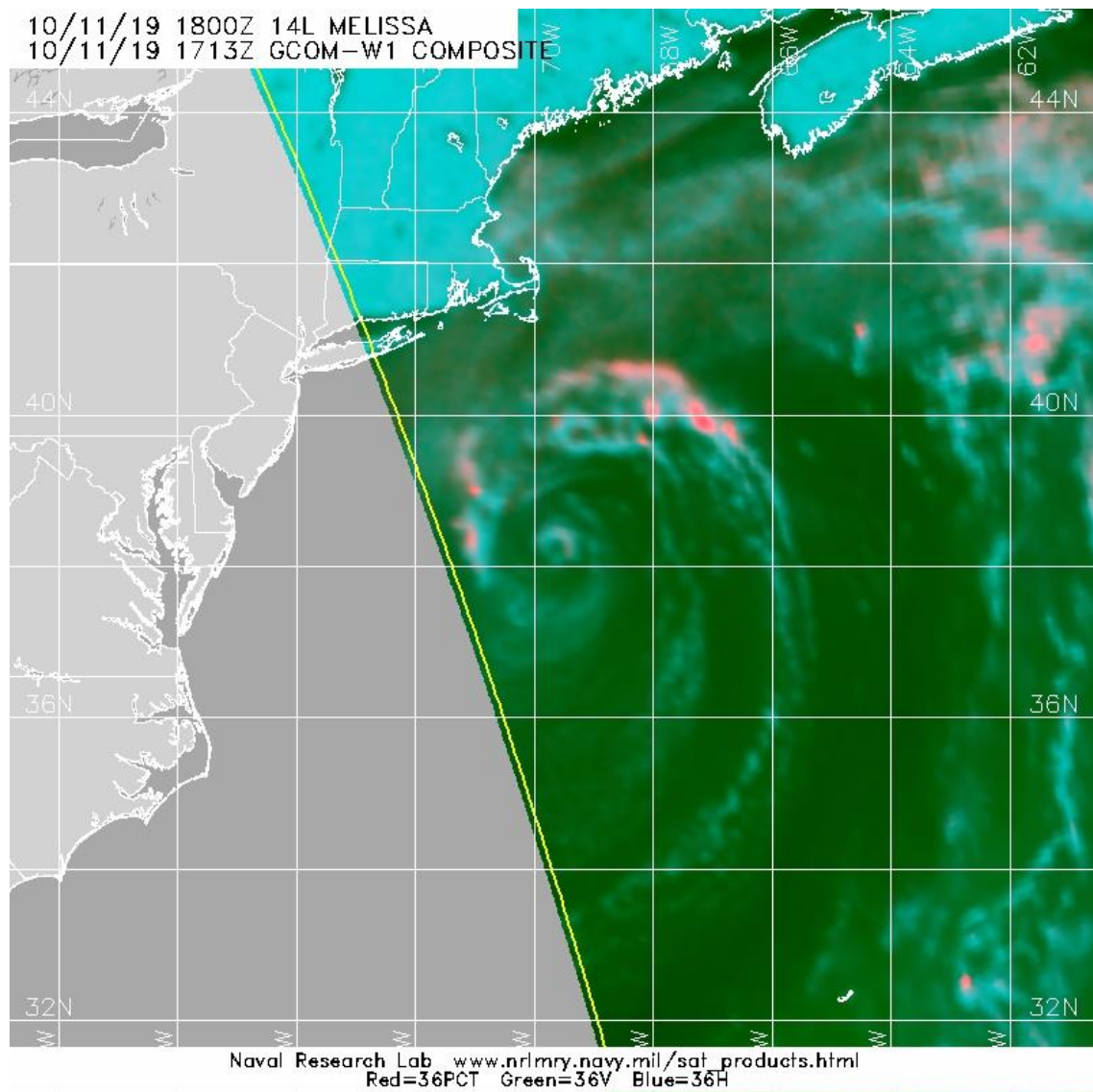


Figure 7.11 Subtropical cyclone ATL 2019 Melissa.

7.4 Monsoon Trough Development Observed on the 37color Imagery

The monsoon trough is a high-moisture vorticity-rich environment, with widespread convection. TC developing in this environment show many thin convective bands in the envelope of the trough, many of which consolidate into a principal band. In two examples shown here, 2015 WPAC Typhoon Goni (Figure 7.12) and 2005 ATL

Hurricane Wilma (Figure 7.13), development is shown from low-end tropical storm to just above minimal hurricane strength. Both these became powerful TC.

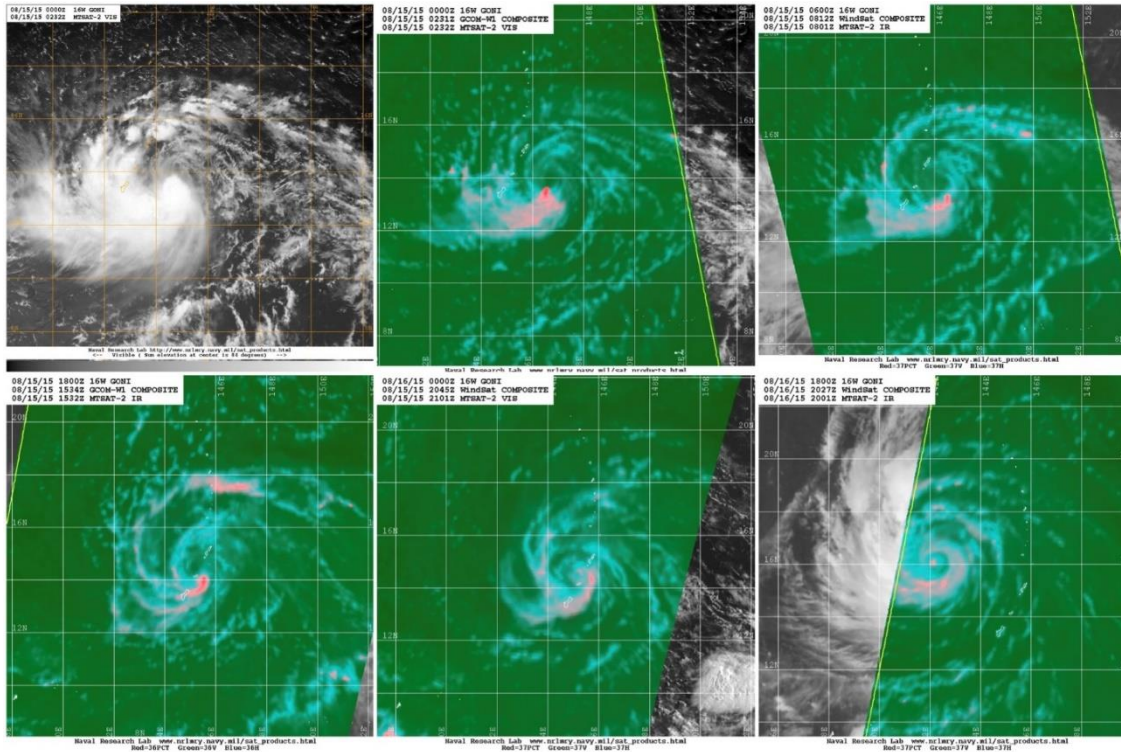


Figure 7.12 Monsoon development of 2015 WPAC Typhoon Goni from TD to 80 kt. At the same time a second TC developed to the east of Goni in the monsoon trough and became Typhoon Atsanti. As the imagery shows, Goni passed over the Marianas while a developing tropical storm.

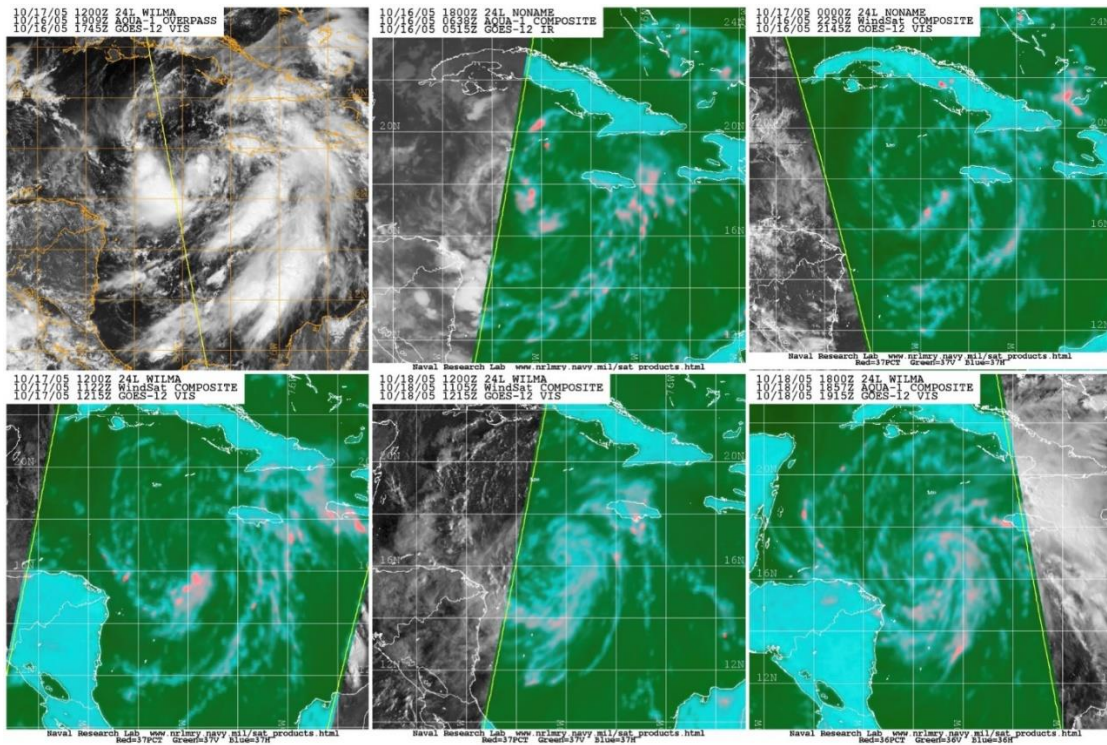


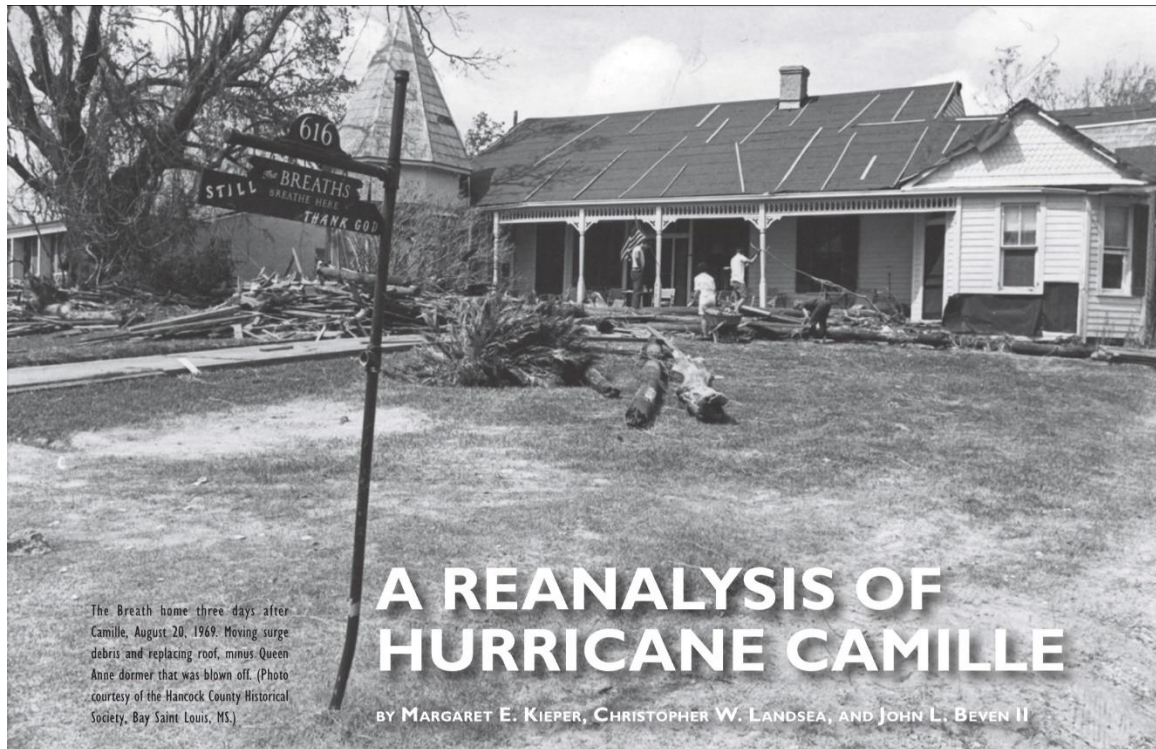
Figure 7.13 Monsoon development of 2005 ATL Wilma from TD to 70 kt.

CHAPTER 8. The 1969 Hurricane Camille Reanalysis

Please read [A Reanalysis of Hurricane Camille](#) (Kieper et al 2015) using the hyperlink or the images provided (Figures 8.1 to 8.18). This section also is intended to provide additional detail and background to the published paper and to provide a more detailed discussion of the satellite imagery used in the reanalysis.

The 1969 Camille reanalysis (Kieper et al. 2015) finished the reanalysis of known Category 5 landfalls in the United States. Camille's landfall intensity had long been uncertain due to lack of accurate wind measurements in the core. Whether Camille was a Category 5 at landfall was in question. Camille was a likely candidate for an eyewall replacement given its intensity while over the Gulf of Mexico. The reanalysis of Camille employed knowledge of TCs that was not known in 1969 (e.g. ERCs). Techniques of interpreting modern satellite images were applied to images of Camille to determine that an ERC occurred.

In 2015 I was asked by Dr. Chris Landsea to head the Hurricane Camille reanalysis of the "best track" data maintained by the National Hurricane Center (NHC) on every tropical cyclone in their historical record, which was documented in the AMS BAMS journal (Kieper et al. 2016). The best track consists of location and intensity information at "synoptic" (forecast) times and also at landfall. The reanalysis is a long-term large-scale effort to review and update the best track information of all the hurricanes in the record, using available materials. Since Camille was the last of the Category 5 U.S. landfalls that had not been reviewed, the reanalysis was a high priority, even though analysis of the



The Breath home three days after Camille, August 20, 1969. Moving surge debris and replacing roof, minus Queen Anne dormer that was blown off. (Photo courtesy of the Hancock County Historical Society, Bay Saint Louis, MS.)

A REANALYSIS OF HURRICANE CAMILLE

BY MARGARET E. KIEPER, CHRISTOPHER W. LANDSEA, AND JOHN L. BEVEN II

A modern look at one of the United States' most destructive hurricanes indicates that it was deeper than, but not quite as intense as, originally estimated.

The pressure gradient must have been tremendously steep. Because of this...I think of Camille as a giant, well-organized tornado rather than as a small, very intense hurricane.

—Dr. Luis R. Rivas in a letter to Leonard G. Pardue of the National Hurricane Center

With the passage of almost 50 years and the recent memory of a number of major hurricane landfalls along the northern Gulf Coast of Louisiana, Mississippi, Alabama, and the Florida Panhandle, including Dennis and Ivan in 2004, and Katrina and Rita in 2005, and, further back, Andrew in 1992, Elena in 1985, and Frederick in 1979, Hurricane Camille in 1969 may not come readily to mind, except for those who lived through it. But for tropical meteorologists, Hurricane Camille holds a continuing fascination as one of the most intense U.S.-landfalling hurricanes on record and for a number of mysteries associated with its meteorological statistics and best-track record.

The African easterly wave that spawned Hurricane Camille traveled across the Atlantic main development region with very little associated convection or organization. However, after entering the Caribbean, the wave amplified and split into two areas of disturbed weather, one in the Bahamas and another near the Cayman Islands. The National Hurricane Center (NHC) sent weather reconnaissance flights to both areas on 14 August 1969, expecting the northern area would be the one to develop but finding that the area in the Caribbean had already developed into a tropical storm. Camille continued to develop rapidly before making landfall at 2200 UTC 15 August over the extreme western edge of Cuba at just under major hurricane strength. A few hours later, Camille moved into the Gulf of Mexico at the onset of the diurnal convective maximum and began rapidly intensifying, achieving category 5 status at 150 knots (kt ; $1\text{ kt} = 0.51\text{ m s}^{-1}$) and a pressure reading of 908 mb ($1\text{ mb} = 1\text{ hPa}$) by 1800 UTC 16 August. Six hours later, the pressure had dropped to 905 mb. At this time, early Saturday evening local

AMERICAN METEOROLOGICAL SOCIETY

MARCH 2016 BAMS | 367

Figure 8.1 Page 1 of *A Reanalysis of Hurricane Camille*

time, Camille was about 290 n mi (1 n mi = 1.852 km) south-southwest of the mouth of the Mississippi River. The hurricane began to significantly affect the Mississippi Gulf Coast on Sunday evening, with the eye making landfall near midnight Sunday local time (0400 UTC 18 August). The bathymetry of the coastline enabled the hurricane to generate a tremendous storm surge that devastated the coastal communities on and near the western Mississippi coast and that would not be approached or eclipsed until Hurricane Katrina in 2005. Camille then moved northward through the Tennessee Valley and eastward through the mid-Atlantic states, where it produced record rainfall over the Appalachians. It subsequently redeveloped into a tropical storm in the Atlantic, after which it underwent extratropical transition and dissipated.

A reanalysis of the NHC's second-generation North Atlantic hurricane database (HURDAT2; Landsea and Franklin 2013) now covers the period from 1851 to the mid-twentieth century (e.g., Hagen et al. 2012). The reassessment of the existing database is necessary to correct random and systematic errors; to incorporate current understanding of tropical cyclones (TCs) upon previously collected raw observations; to include explicit analyses of the time, position, and intensity at landfall; and to add previously unrecognized TCs. Because previous reanalysis results had already addressed the three other category 5 hurricanes on the Saffir–Simpson hurricane wind scale to have impacted the United States during the twentieth century, NHC management requested an expedited reanalysis of Camille because of the need to answer a simple question: which is the strongest hurricane to have struck the United States?

In the context of modern understanding of TC intensity, tropical meteorologists have long held

some skepticism about Camille's landfall intensity, for several reasons. An extraordinary wind speed of 180 kt was reported by the last reconnaissance flight into Camille near 1800 UTC 17 August based on visual estimation of surface wind speeds observed from the surface sea state and an observed dropsonde 901-mb surface pressure. This resulted in a forecast intensity and accepted landfall intensity (10 h later) of 1-min winds of 165 kt, which is near the upper bound for globally known TC intensity in the combined NHC and Joint Typhoon Warning Center best-track data. The 901-mb mean sea level pressure (MSLP) that was noted in real time and in earlier reports (e.g., NHC *Preliminary Report, Climatological Data* monthly summary) disappeared from later reports (e.g., *Monthly Weather Review's* Atlantic hurricane season summary, *Climatological Data* yearly summary), and the earlier 905-mb pressure was identified as the lowest measured pressure (Simpson et al. 1970). In addition, Camille's MSLP and intensity at landfall were at odds with the two other category 5 mainland-U.S.-landfalling hurricanes—the 1935 Labor Day hurricane and Andrew in 1992. Particularly when compared to the Labor Day hurricane, Camille's landfall intensity appeared too high in relation to the MSLP (interestingly, MSLP readings in all three of these category 5 landfalls were taken by private individuals and the barometers were confirmed for accuracy). In addition, the original best track shows Camille gradually strengthening as a category 5 hurricane for more than 24 h before landfall—that contrasts with many other major hurricanes that have made landfall along the northern Gulf Coast, which weakened prior to landfall. All 11 hurricanes—most notably Hurricane Katrina in 2005—during the period from 1985 to 2005 having a central pressure less than 973 mb 12 h before landfall in the northern Gulf of Mexico weakened during these last 12 h (Rappaport et al. 2010).

After almost 50 years, can we answer these questions: During the Gulf of Mexico transit, did any weakening occur? How strong was Camille at landfall in Mississippi? A reanalysis of Hurricane Camille has enabled us to answer these questions to the extent the data will allow.

The official revisions for Hurricane Camille, which have been approved by the Best-Track Change Committee, are summarized below:

Generally, very small (0.3° latitude–longitude or less) changes were introduced to the center positions of Camille throughout its lifetime based upon a combination of ship, station, aircraft penetration, aircraft radar, land-based radar, and satellite observations

AFFILIATIONS: KIEPER—Florida International University, Miami, Florida; LANDSEA and BEVEN—NOAA/NWS/NCEP/National Hurricane Center, Miami, Florida

CORRESPONDING AUTHOR: Christopher W. Landsea, NOAA/NWS/NCEP/National Hurricane Center, 11691 SW 17th Street, Miami, FL 33165
E-mail: chris.landsea@noaa.gov

The abstract for this article can be found in this issue, following the table of contents.

DOI:10.1175/BAMS-D-14-00137.1

A supplement to this article is available online (10.1175/BAMS-D-14-00137.2)

In final form 30 March 2015
©2016 American Meteorological Society

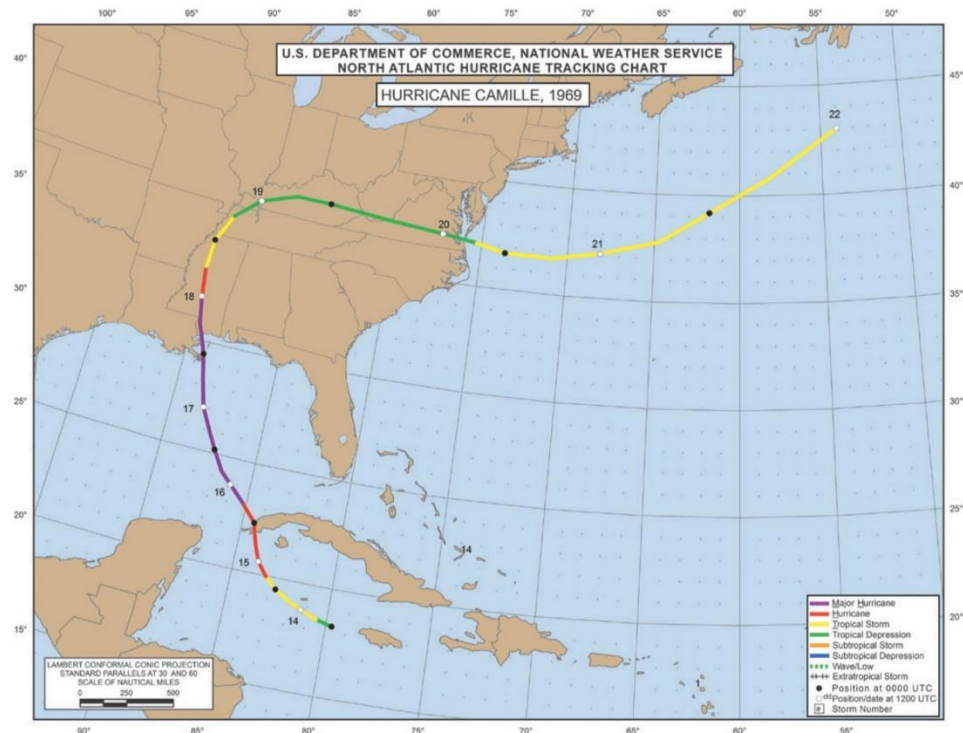


FIG. 1. Track map of Hurricane Camille, 14–22 Aug 1969.

(Fig. 1). Such relatively minor changes in the track are typical of systems in this era, as aircraft reconnaissance allowed for fairly accurate determination of the location of the center. The largest alteration to the positions was early on 20 August by about 50 n mi to the east-southeast when Camille was inland as a tropical depression over Kentucky. This adjustment was made to smooth out changes in forward speed as Camille accelerated eastward.

Minor intensity changes were analyzed for the periods around the Cuban landfall and at the end of the life cycle while the cyclone was moving over the mid-Atlantic states into the Atlantic Ocean. Major changes were made to the period Camille transited the northern portion of the Gulf of Mexico from the completion of the period of rapid intensification through an eyewall replacement to the Mississippi landfall, which resulted in modifications to the peak intensity and the timing of the peak intensity. These more substantial changes will be described in detail.

DATASETS AND METHODOLOGY.

Observational capabilities of Atlantic basin TCs in 1969 continued to evolve from those available earlier in the twentieth century. Through the early 1940s, the only measurements available of these primarily oceanic mesoscale cyclones were from unfortunately placed ships at sea and from coastal weather stations (Landsea et al. 2004b, 2008, 2012). These surface observations continued to play a crucial role in the reanalysis of Camille, from measurements obtained via the Comprehensive Ocean–Atmosphere Data Set (Woodruff et al. 1987), original U.S. station observations obtained from the National Climatic Data Center’s EV2 website (www.ncdc.noaa.gov/EdadsV2/), original Cuban station observations provided by the Cuban Meteorological Service, summaries of observations in *Monthly Weather Review* and other articles, microfilmed hand-drawn synoptic maps by the NHC analysts and forecasters in 1969, and the “storm wallet” of observations/analyses made available in real time and postanalysis to the NHC forecasters.



Fig. 2. Aircraft reconnaissance available in Hurricane Camille. (left) Image from ESSA (1969) provides the individual center fixes (small circles and triangles) and the original 6-hourly best-track positions (large circles). (right) Types of aircraft used to provide aircraft reconnaissance into Hurricane Camille.

For this particular reanalysis of Hurricane Camille, special observations and eyewitness accounts were also used, including Hamilton and Steere (1969, oil platform measurements), Breath (2007, personal communication, interviews of survivors), Mississippi Test Facility (1969, MTF observations), and N. C. Roberts Jr. (1969, unpublished manuscript, collection of unofficial observations).

Beginning in the mid-1940s, rudimentary aircraft reconnaissance missions were conducted for TCs (Hagen et al. 2012). These platforms were quite adept at providing center fixes, either by directly penetrating the eye of the storm, by locating the center from the plane's nose radar, or by circumnavigating the cyclone. The aircraft, however, were not able to accurately measure flight-level winds in hurricane conditions, though they were able to provide visual estimates of the surface winds. If the aircraft did obtain a penetration center fix, then they could also provide a central pressure, either via extrapolating the

flight-level pressure to the surface or by dropping a sonde into the eye. These capabilities and limitations continued into the 1969 hurricane season, with a mix of aircraft: the Navy's WC-121s, the Air Force's C-130s, and the Environmental Science Services Administration's [ESSA; the predecessor to the National Oceanic and Atmospheric Administration (NOAA)] DC-6s (Fig. 2).

In addition, the coastal array of Weather Surveillance Radar-57 (WSR-57) radars had been fully deployed during the 1960s and was available to monitor the position of Camille as it made landfall in the United States (Fig. 3). These radars provided a plethora of center fixes from a few locations every 30 min within a couple hundred miles from the coast.

Finally, an emerging capability available operationally at NHC in the 1960s was satellite imagery (Fig. 4). These were visible images from the polar-orbiting ESSA-8, ESSA-9, and Nimbus-3 satellites, which each provided a snapshot of Camille about once per day.

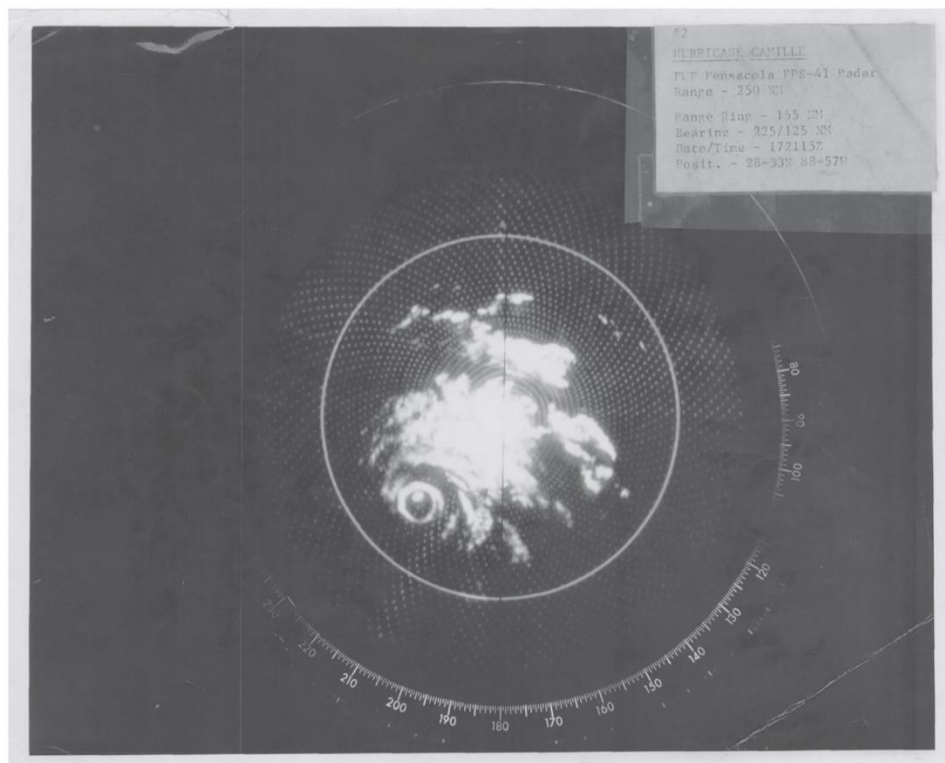


FIG. 3. WSR-57 image of Hurricane Camille at 2115 UTC 17 Aug 1969 from the Fleet Weather Facility Pensacola FPS-41 radar (NHC 1969).

The *Nimbus-3* satellite also had an infrared sensor, which while not available operationally, did show poststorm potential for providing imagery day or night (Allison et al. 1971). The National Aeronautics and Space Administration (NASA) also had an experimental geostationary satellite, the Applications Technology Satellite (ATS), which also provided after-the-fact visible imagery of Camille (Parmenter 1969). These images allowed for some qualitative assessment of Camille, but because of poor navigation, coarse resolution, and spotty temporal coverage, the satellite imagery of 1969 is only marginally of use for knowing Camille's exact position and intensity. For example, the aforementioned issues make it difficult at best to use the Dvorak (1984) technique for estimating TC intensity from satellite imagery. Almost a decade after Camille, *Nimbus* infrared and water vapor imagery and ATS visible imagery were analyzed (Shenk and Rogers 1978).

The methodology for the reanalysis of Camille follows similar steps established in earlier reanalysis efforts: 1) obtain all available raw observational data into a single database, 2) conduct synoptic analysis four times daily, 3) determine genesis changes, 4) determine track changes, 5) determine intensity (maximum sustained surface wind) changes, 6) determine status/dissipation changes, and 7) document all revisions in a metadata file. The track revisions primarily relied on aircraft and radar fixes. The intensity revisions primarily relied on aircraft and coastal central pressure measurements converted to maximum winds via the Brown et al. (2006) and Landsea et al. (2004b) pressure–wind relationships. These intensity values could then be adjusted based on the observed radius of maximum wind (RMW; a measure of inner-core size), radius of the outermost closed isobar (ROCI; a measure of TC size), pressure of the outermost closed isobar (POCI; a measure of

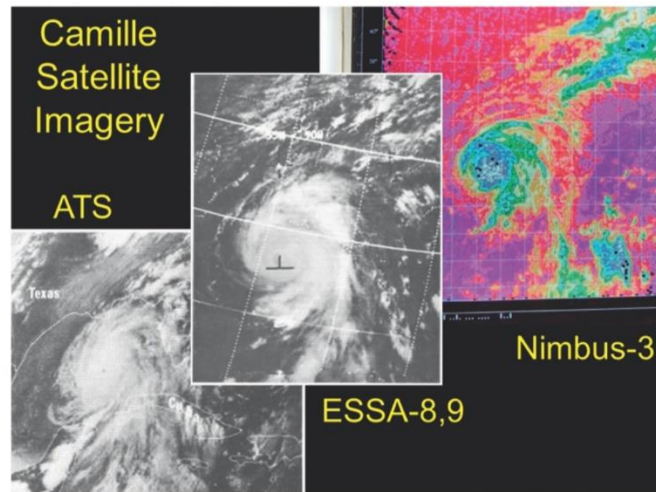


Fig. 4. Satellite imagery of Hurricane Camille. (bottom left) Visible image is from the experimental NASA ATS geostationary satellite at 2340 UTC 16 Aug 1969 (Parmenter 1969). (middle) Visible image is from the ESSA-8 polar-orbiting satellite at 1957 UTC 16 Aug 1969 (ESSA 1969). (top right) Infrared image is from the Nimbus-3 polar-orbiting satellite at 0500 UTC 16 Aug 1969 (Allison et al. 1971).

the environmental pressure), and TC forward motion varied from the climatology of Vickery et al. (2000).

The reanalysis methods documented in Landsea et al. (2004a) have been established in an attempt to provide consistency in the reanalyzed data. Since there is an inherent uncertainty in the wind–pressure

relationships used in the reanalysis, this translates into uncertainties in the reanalyzed best track intensities. Even using today’s data, the NHC considers their best-track intensities accurate to within about $\pm 10\%$ (Landsea and Franklin 2013). The uncertainty would be higher for storms of the Camille era.

More details on the reanalysis of Hurricane Camille, including data, files, and imagery, are available online. The full metadata, consisting of highlights of daily observations and descriptions about the changes to genesis, track, intensity, landfall, and dissipation, is available on the Atlantic Hurricane Database Reanalysis Project website (www.aoml.noaa.gov/hrd/data_sub/re_anal.html). This also includes the most recent HURDAT2

file, a database of all relevant raw observations, all of the NHC microfilm imagery, and comments from and responses to the Best-Track Change Committee. Additionally, comprehensive “storm wallet” archives maintained at NHC from the late 1950s onward (www.nhc.noaa.gov/archive/storm_wallets/cdmp/) also provide a large source of observations, which have been thoroughly mined for the reanalysis of Camille and other TCs.

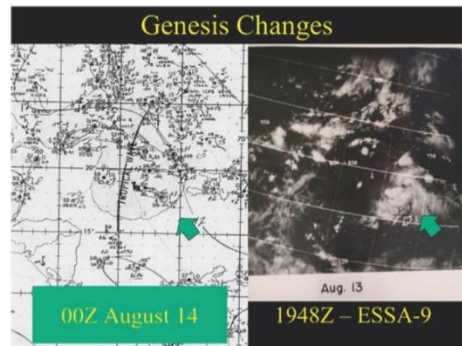


Fig. 5. Observations (0000 UTC 14 Aug 1969; microfilm archives at the NHC library) and satellite imagery (1948 UTC 13 Aug 1969; Weather Bureau 1969) providing evidence for an earlier genesis of Camille than originally indicated.

GENESIS OF CAMILLE. Camille began as a tropical wave that emerged from the coast of West Africa on 5 August, which did not develop until it reached the western Caribbean Sea. Surface observations in the vicinity of the wave during genesis (Fig. 5) are somewhat sparse and are ambiguous as to when the system had a closed circulation. HURDAT2 originally indicated an “instant” 50-kt TC beginning at 1800 UTC 14 August. A closed circulation was not observed at 1200 UTC 13 August when the system passed over Jamaica; however, a closed circulation of tropical storm strength had developed by 1500 UTC 14 August. Satellite imagery late on 13 August (Fig. 5) indicated the deep convection associated with the wave had organized banding. Given the improved structure seen in the satellite imagery at that time, the

ambiguous surface observations, and the subsequent observations of the system being a moderate tropical storm around midday on 14 August, the best estimate of when genesis occurred is now 0000 UTC 14 August. While this is 18 h earlier than originally indicated, the exact time of genesis is uncertain to ± 6 h.

PEAK INTENSITY IN THE GULF OF MEXICO. Near the end of 3 days of rapid intensification, resulting in an intensity increase of 120 kt from its inception as a tropical depression, Camille reached its initial peak intensity of 150 kt from 1800 UTC 16 August to 0000 UTC 17 August. At 1835 UTC 16 August, an Air Force reconnaissance aircraft measured 908-mb central pressures from two separate dropwindsondes inside a circular eye of 10 n mi diameter. This eye size yields an approximate 8 n mi RMW using Kimball and Mulekar (2004). This pressure suggests maximum winds of 151 kt based on the Brown et al. (2006) pressure–wind relationship for intensifying storms south of 25°N latitude. Given a near-average environmental pressure from the 1010-mb outer closed isobar, a slow forward speed of 9 kt, and a tiny RMW of 8 n mi versus the 12 n mi climatology for this latitude and central pressure (Vickery et al. 2000), the intensity is analyzed at 150 kt. This is a 20-kt major increase from the previous best track value for 1800 UTC 16 August.

A similar methodology is used at the subsequent 0000 UTC 17 August best-track time. The same aircraft sortie observed a 905-mb central pressure at 0016 UTC 17 August with no change in eye size. As the cyclone was now straddling the 25°N latitude line, the 905-mb pressure suggests an intensity of 151 and 154 kt based on the Brown et al. (2006)

pressure–wind relationships for intensifying storms both north and south of 25°N latitude, respectively. An intensity of 150 kt at 0000 UTC 17 August is analyzed from these values, an increase of 10 kt from the previous best-track value.

INTERNAL STORM STRUCTURE OF CAMILLE IN THE GULF OF MEXICO. When environmental conditions are very favorable for TC development (low shear, warm SSTs, and deep warm water of the northwestern Caribbean and the Gulf of Mexico Loop Current) and the intensity has reached major hurricane status, hurricanes are likely to begin an eyewall replacement cycle (ERC),

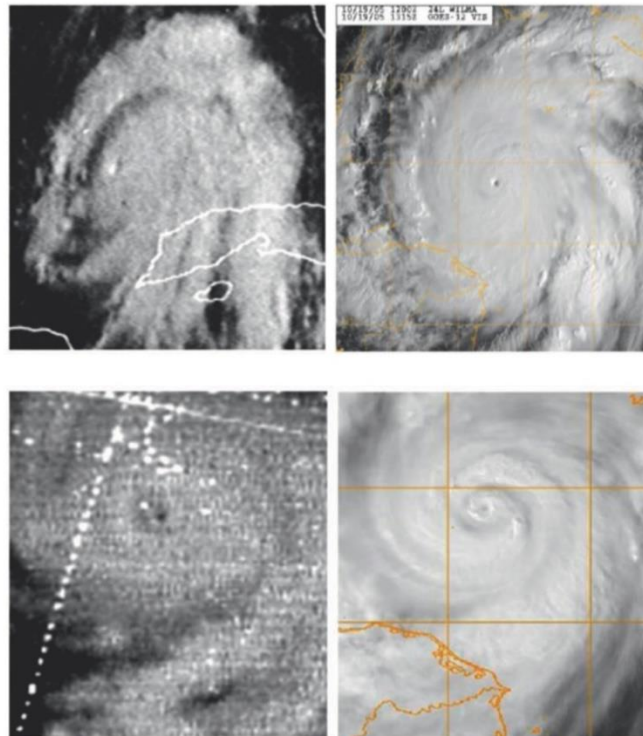


FIG. 6. (top left) Visible satellite image of Hurricane Camille at 1311 UTC 16 Aug 1969 near initial peak intensity and 5 h before 1800 UTC 908-mb pressure and 150-kt intensity. (top right) Visible satellite image of Hurricane Wilma at 1315 UTC 19 Oct 2005 near peak intensity of 882 mb and 160 kt. (bottom left) Visible satellite image of Hurricane Camille suggestive of a double eyewall at 1953 UTC 17 Aug 1969 at 919-mb pressure and 135-kt intensity. (bottom right) Visible satellite image of Hurricane Wilma showing the double eyewall confirmed by aircraft data at 1915 UTC 19 Oct 2005 at 892-mb pressure and 140-kt intensity.

CAMILLE'S 901-MB DROPSONDE

During the penetration of the eye of Camille near 1815 UTC 17 August, an Air Force dropsonde in the eye recorded a 901-mb pressure. For a short time, this was documented in the operational advisories, the *Preliminary Report* (Weather Bureau 1969), the *Climatological Data* (DeAngelis and Nelson 1969), and the *Mariners Weather Log* (DeAngelis 1970) to be Camille's deepest sea level pressure as well as the lowest pressure of record ever recorded by aircraft reconnaissance. Some months later in the *Monthly Weather Review* article on the 1969 hurricane season (Simpson et al. 1970), the 905-mb figure from an earlier drop was identified as the lowest sea level pressure for Camille. A footnote in Simpson et al. (1970, p. 295) said only, "Preliminary reports and other publications indicated a lowest pressure of 901 mb. Recently, a check of the raw data indicates this should be corrected to the 905-mb value given here." This footnote was ambiguous and could have meant two things: either that the earlier drop yielding a 905-mb pressure became the lowest pressure when the 901-mb reading was thrown out, or that the 901-mb reading was recalibrated to achieve a 905-mb reading. It appears that the decision was the former one, to use the 905-mb pressure from the aircraft reconnaissance flight 20 h earlier. There is no documentation on why the 901-mb sea

level pressure was rejected, nor was the decision clarified after contacting the surviving NHC hurricane forecasters from the 1969 hurricane season.

A review of the sonde data (Fig. SBI) indicates that the 850-mb geopotential height was 692 m. This is inconsistent with a 901-mb surface pressure based on comparison to other aircraft data and dropsondes. For example, an aircraft in the eye of 2005's Hurricane Wilma extrapolated a sea level pressure of 901 mb from an 850-mb height of 516 m—176 m lower than the height on the Camille sonde. Two other eye sondes from Camille reported 905- and 908-mb central pressures along with 850-mb heights of 551 and 586 m, respectively. The 850-mb heights from the Camille 905- and 908-mb sondes and the Wilma 901-mb extrapolation are all consistent, while the 850-mb height on the Camille "901-mb" sonde is an outlier.

Several methods were tried to better estimate the central pressure at the time of the 1815 UTC 17 Aug fix. These methods are summarized here.

Method 1.

A rule of thumb used at the NHC is that a 10-m change in the aircraft-reported 850-mb height roughly corresponds to a 1-mb change in the surface pressure. The 692-m height

of the "901-mb" dropsonde is 141 m higher than that of the 905-mb sonde and 106 m higher than that of the 908-mb sonde. This suggests a pressure of 918–919 mb as a first rough estimate.

Method 2.

Inside the eye, the aircraft reported a 700-mb geopotential height of 2390 m and a temperature of 16.6°C. Using standardized tables previously employed at NHC (OFCM 1997) for extrapolating the sea level pressure from these data using the standard environmental lapse rate yield an estimated minimum sea level pressure of 920 mb. It is notable that at the time of the 905-mb sonde, the aircraft reported a 700-mb height of 2240 m and a temperature of 22°C. Using the tables, these numbers yield an extrapolated pressure near 902 mb.

Method 3.

The sonde data (decoded in Table SBI, along with the calculated water vapor mixing ratio and equivalent temperature) were also used to determine sea level pressure using the hydrostatic equation. The mean equivalent temperature of the layer was taken from a skew T analysis to be about 27.0°C, or 300.2 K. The data were entered into the hydrostatic equation below:

$$\begin{aligned} \text{Pressure (sea level)} &= \text{Pressure} \times \exp[(\text{Gravity} \times \text{Geopotential height})/(\text{Gas constant for dry air} \times \text{Mean equivalent temperature})] \\ &= 700 \times \exp[(9.81 \text{ m s}^{-2} \times 2390 \text{ m})/(287 \text{ K}^{-1} \text{ kg}^{-1} \times 300.2 \text{ K})] \\ &= 919 \text{ mb} \end{aligned}$$

TABLE SBI. Decoded Camille eye dropsonde data at 2125 UTC 17 Aug 1969.

Pressure (mb)	Temp (°C)	Dewpoint (°C)	Geopotential height (m)	Water vapor mixing ratio (g kg ⁻¹)	Equivalent temp (°C)
700	16.6	16.6	2390	14.3	19.0
732	19.4	18.4	—	17.5	22.3
850	28.0	26.7	692	27.0	32.5
874	29.4	27.8	—	27.0	33.9
901	30.8	28.3	—	28.0	35.9

Based upon the three methods, a central pressure of about 919 mb is estimated for 1800 UTC 17 August for Camille, with a derived intensity of 135 kt.

There are two questions about the "901-mb" sonde that are likely

unanswerable. First, E. Uhlhorn (2015, personal communication) indicates that a combination of a surface pressure of 919 mb, and surface temperature of 30.8°C, and a 28.0 g kg⁻¹ surface mixing ratio yields a surface θ_s of 382 K, which is 8 K warmer than other such

values in recent dropsondes. Was there an instrumentation error, or were these data representative of extreme conditions in Camille's eye? Second, did the sonde actually reach the surface?

```

NNNN+MEMUUV
URX KCHS 172125Z
GULL THREE CAMILLE THREE
97779 71717 TT 1742/ 99282 70188 08188 99901 30825 00///
///// 85692 28013 70390 166// 88999 77999
VV 1742/ 99282 70188 08188 00901 30825 11874 29413 22732
19410 33700 16600 51515 10168 07370

URXX KCHS 172140ZPOST FLIGHT SUMMARY
CAPT ZUBER AND CAPT WADAGNOLO
FIXED EYE 1815Z AT CORDINATES 28 DEGREES 12 MIN N 88 DEGREES 46 MIN W
WELL DEFINED EYE CLOSED WITH FEEDER BAND IN ALL QUADRANTS MAX SFC WINDS
OBSERVED IN SE QUADRANT OF 180 KTS PLUS MAX FL WND OBS SE QUAD AT
95 KTS MISSION ABORT 0000Z FIX DUE TO SHUTDOWN NO. FOUR ENGINE

```

FIG. SB1. (top) Dropsonde coded message at 2125 UTC 17 Aug 1969 for the sonde released into the eye of Camille near 1815 UTC that day. (bottom) Postflight summary from the Air Force aircraft reconnaissance mission that launched this dropsonde. Images were obtained from the microfilm archives at the NHC library.

where a new eyewall forms outside the original small eyewall. This new eyewall then contracts as the old inner eyewall dissipates. Satellite imagery near the time of peak intensity on 16 August showed a remarkably distinct pinhole eye, which is often seen in an intense hurricane. However, Camille was still 28 h from landfall on the northern Gulf Coast and climatologically, if the environment remained favorable, an eyewall replacement would likely have occurred during that time. The existence of double/concentric eyewalls was known in 1969, as there is one documented radar fix report of a double eyewall for Camille, in reviewing all hourly radar fixes. However, the importance of the ERC—the cycle of temporary weakening followed by reintensification as the ERC completes and the new outer eyewall contracts—would not be fully understood until Willoughby et al. (1982).

The next and last reconnaissance flight into Camille occurred 18 h after 905 mb was measured. It is unknown if Camille intensified further during that time, which would have included the overnight diurnal convective maximum. It is also unknown when an ERC may have started. But 18 h later, there

was evidence of an ongoing ERC from four different sources: radar, reconnaissance, satellite imagery, and ground observations. In a serendipitous coincidence, on 17 August there are radar images from both Naval Air Station (NAS) Pensacola (2115 UTC) and NWS New Orleans (1732 UTC); a visible satellite image from 1953 UTC; and an aircraft penetration near 1815 UTC. Both radar images show a well-formed symmetric double eyewall (Figs. 3 and SB2a). In the description from the aircraft, “Just as we were near the [eye] wall cloud we suddenly broke into a clear area and could see the sea surface below,” the copilot, Robert Lee Clark, wrote in 1982” (Sheets and Williams 2001, p. 152). The clear area was possibly a moat that separated the inner and outer eyewalls. In addition, although faint, the visible satellite image shows what appears to be a moat (Fig. 6, bottom). Finally, observations from Freeport Sulphur Company at Garden Island Bay, Louisiana (near the mouth of the Mississippi River), at 2255 UTC 17 August noted, “the western eye would have been some ten miles distant [to the east]. However a brief lull was observed, with wind velocities dropping to 30–35 mph” (N. C. Roberts Jr. 1969, unpublished manuscript).

CAMILLE LANDFALL PRESSURES

A key parameter in analyzing tropical cyclones is the central pressure. Unfortunately, for Hurricane Camille, no aircraft reconnaissance flights were in the storm during the last several hours before it made landfall. Several pressure measurements obtained along the Mississippi coast were examined to determine which, if any, could provide a central pressure value for Camille.

Two pressures were measured at or near the time of eye passage in Bay St. Louis, 909 and 904 mb (26.85 and 26.70 in. Hg, respectively), and a pressure in the eyewall was measured in Pass Christian, Mississippi, 919 mb (27.15 in. Hg). The estimated distance between the 909- and 904-mb readings and the center of the eye is 3–4 n mi; that is to say, it was on the eastern edge of the small eye (which had a 10 n mi diameter, suggesting a radius of maximum wind of 6–8 n mi). The estimated distance between the Pass Christian eyewall pressure reading and the center of the eye is 7 n mi.

From NHC (1969) a letter detailing the 919-mb eyewall pressure reading in Pass Christian:

Mr. James Cagle, one of my co-workers here, took barometric readings at his home in Pass Christian during the passage of Camille. His lowest reading was 27.05 at 2330, August 17. I checked his aneroid barometer and found it to have a +0.10 error. Therefore the corrected reading should be 27.15. He also reports that there was no "lull" in his area... my own lowest reading of 29.28, [was]...30 miles east of the eye....

The two documented pressure readings in the eye were taken by Charles Breath, a boat dealer and mariner, who had a marine barometer in his home as well as a wall barometer. He logged pressure readings starting a couple days prior to the arrival of Camille and increased the frequency of the readings to hourly and then to half hourly as the hurricane approached landfall. The first low reading, the 909 mb, was taken just as the roof had partially come off and the family was

awaiting the arrival of the eye in order to evacuate to one of their other (rental) homes on their property farther back from the river bluff. He took the marine barometer with him, and once they had walked back to the rental property, took another reading, which was lower—the 904 mb. He provided the 904-mb reading to the MTF (today it is Stennis Space Center) meteorologists and to Nash and Ep Roberts.

Nash Roberts, a local New Orleans meteorologist, put out a request on-air for weather data, and there was a record that he was contacted by phone by Mr. Breath regarding the 904-mb reading (Loyola University 2001). The barometer and possibly the log were provided to Ep Roberts, Nash's brother, a meteorologist as well, who had a store that sold meteorological instruments. The barometer was checked and found to be accurate. It is not known how NHC came to obtain the 909-mb measurement and why they did not use the 904 mb, but it could be that they went by the log, which had the 909 mb as the last entry.

A week after the storm, two MTF employees, meteorologists at the weather station there, talked to Mr. Breath while driving around the area observing damage and trying to determine the extent of the eye passage. At that time, he told them of the 904-mb reading and they documented it in their report (Mississippi Test Facility 1969):

Mr. Breath...always religiously kept up with the weather. His home was over 100 years old, but sturdily built of wood. Although most of the roof was blown off, the studs of the roof still stood...During the brief time they had in the "eye," not more than 10 minutes, they evacuated to a home on higher ground.

He first observed his Aneroid type wall decorative barometer, scaled to 28 inches pressure when the pressure began plunging. He stated the needle just fell off rapidly beyond the 28 inch limit. In the turmoil, he remembered his Marine type barometer and went into another

room and observed it. During some time period when he knew he was in the "eye," he read 26 point something, and later recalled that it was probably 26.7 inches pressure. He stated that this was a reading in the "eye" but possibly was not the lowest he observed.

An interview was conducted with Mr. Breath in 1979 (Pyle 1984) as part of the University of Southern Mississippi oral history program.

Mr. Pyle: As Hurricane Camille started to come up in the gulf that Sunday afternoon, your wife here has got a panoramic view of the gulf right out in front of you, what did you see? What did it look like, the atmosphere?

Mr. Breath: I have had through the years a habit of watching the barometer. I go more by the barometer than anything else. And I started taking hourly checks on it. And then when the barometer really started to fall, regardless of what we saw out in the gulf or whatever, we started really getting ready to leave. We knew something bad was coming up.

...

Mr. Pyle: How aware were you of the time you were in the house before you left?

Mr. Breath: Oh, I was watching closely because I was keeping this log, see. I was watching it close. I had a log in the beginning at every hour. And then as it would start falling more, I'd have it every half hour and make a recording of it.

...

Mr. Pyle: When you saw the barometer, when you could actually see it dropping, what were your thoughts? It might be hard to recall. I was just wondering if you were thinking about your family, your house—

Figure 8.10 Page 10 of *A Reanalysis of Hurricane Camille*

Mr. Breath: Well, I just couldn't believe what I was seeing. Actually, I just [couldn't believe it].

Mr. Pyle: Did you ever question if your barometer was right?

Mr. Breath: Nash Roberts, who is a weather report man, had one of his men come over and interview me. He asked permission to take the barometer to have it checked in New Orleans to see if they were actually accurate, or whether I had made a mistake, or what. And I certainly agreed to it. They brought it back in a couple of weeks, and said that it was within a tenth of a point of being right, and that could be the difference between the sea level here and the sea level in New Orleans.

...

Mr. Pyle: And then, you took your last reading and left about what time?

Mr. Breath: Oh, probably about eleven-fifteen.

Mr. Pyle: And the reading then, for the record, was how low?

Mr. Breath: 26.85!

Mr. Pyle: Inches of mercury, that's terrifically [low]! [laughter]

Mr. Breath: And I feel sure that it dropped a little bit more than that, but that's what I actually have a record of.

In the University of Southern Mississippi interview, Mr. Breath states again that he obtained a lower reading but that he was not able to document it (probably not having brought the log back with him to the other property). It sounds like he meant the 26.70 in. Hg reading, as he says he "felt sure" the barometer fell lower than 26.85 in. Hg.

These 904-, 909-, and 919-mb pressure measurements are crucial for the assessment of a 900-mb central pressure analysis for Camille's landfall as described in the main text. They do highlight the importance of unofficial meteorological observations, even for a hurricane like Camille in a relatively recent era.

An ERC was in progress, but what could this mean for Camille's intensity at this time? Because the plane had radar and their observations focused on the inner eye, this suggests that radar reflectivity of the outer eye was weaker compared to the inner eye and that the inner eye was still the prominent feature. This suggests that the ERC was not complete.

A comparison of Camille to 2005's Hurricane Wilma (Pasch et al. 2006) is instructive, as it appears that the central pressures and inner-core structures may be quite similar. Figure 6 (top) shows Camille's and Wilma's satellite appearance when both storms were near peak intensity. The similarities between the satellite images of the two hurricanes include a very well-defined pinhole eye, smooth central dense overcast (CDO) with subsidence around the CDO, and similar CDO size. Figure 6 (bottom) shows both Camille and Wilma undergoing an eyewall replacement, likely at a similar stage of an eyewall replacement cycle. Both images show a moat between an outer eyewall and the still-well-defined inner eyewall. Wilma's pressure between the peak and the ongoing ERC had increased 10 mb from 882 to 892 mb. Therefore, it is logical for Camille's pressure at this time to have risen about 10 mb from the minimum of 905 mb. An analysis of the "901"-mb dropsonde suggests a central pressure of about 919 mb (see the sidebar "Camille's 901-mb dropsonde"). This is a rise in pressure of about 14 mb and is close

to the expected 10-mb rise in the comparison with Wilma.

Wilma's intensity decreased modestly from 160 to 140 kt at this stage of the ERC. Thus, it is logical for Camille's intensity to also have weakened slightly from its estimated 150-kt peak intensity. The reanalyzed central pressure of 919 mb, which is newly added into the 1800 UTC 17 August best-track time, suggests an intensity of 133 kt. Because of the intensity decrease from the ERC followed by reintensification, both the normal and weakening subsets of the Brown et al. (2006) pressure-wind relationships for north of 25°N latitude were used, with values of 133 and 127 kt, respectively. With the concentric eyewall structure, a low environmental pressure of 1008 mb for the outer closed isobar, a somewhat faster forward speed of 12 kt, and a continued tiny inner RMW, the best-track intensities for Camille are reduced to 135 kt at 1800 UTC 17 August and 140 kt at 0000 UTC 18 August. These are major changes downward from the original 165 kt. Unfortunately, no further aircraft reconnaissance fixes were available before landfall in the United States.

LANDFALL OF CAMILLE IN MISSISSIPPI.

Camille made landfall near Waveland, Mississippi, at 30.3°N, 89.4°W at 0400 UTC 18 August, based on radar fixes and pressure measurements at the coast (Fig. 1). The hurricane displayed a concentric eyewall

Figure 8.11 Page 11 of A Reanalysis of Hurricane Camille

CAMILLE RADAR ANIMATION

For the first time, a radar loop of Hurricane Camille was constructed from archived radar imagery.

In the 1960s, U.S. Weather Bureau radar imagery could only be viewed in real time by the on-site radar operators. A radar coded message containing a center fix and a rough description of precipitative features was transmitted hourly to the NHC. This meant that with the exception of hurricanes within range of the collocated local Miami, Florida, radar, no real-time radar imagery of hurricanes was available to the hurricane specialists. Also, there was no real-time animation of radar data available, even to the radar operators. This is much different from modern-day radar data availability.

The WSR-57 radar had an archive capability with a camera automatically recording the radar image once per minute onto 16-mm film, independent of operator-controlled gain and other radar controls, and not including the transparency overlay of the surface map that the radar operator would change when changing the range of the radar. In August 1969, Camille was at different times within the range of a number of radars at Key West, Florida; Pensacola, Florida; Mobile, Alabama; Jackson, Mississippi; New Orleans, Louisiana; Baton Rouge, Louisiana; and Lake Charles, Louisiana. The best available archive images were from New Orleans, which fortunately was in a position to record imagery of the approach to the coast and the Mississippi landfall. These images were obtained from the National Climate Data Center (NCDC). Sets of two consecutive images, every 10 min, were photocopied from the plan position indicator (PPI) scope image, from 1630 UTC 17 August 1969 through 0730 UTC 18 August (Fig. SB2, top).

To utilize the radar images, the 1969 radar location needed to be determined, and a surface map was created based on the 50 n mi range rings available in the radar data. This map was then precisely overlaid on each radar image (Fig. SB2, bottom), which were subsequently incorporated into a GIF animation.

The entire loop can be viewed in the provided supplemental material.

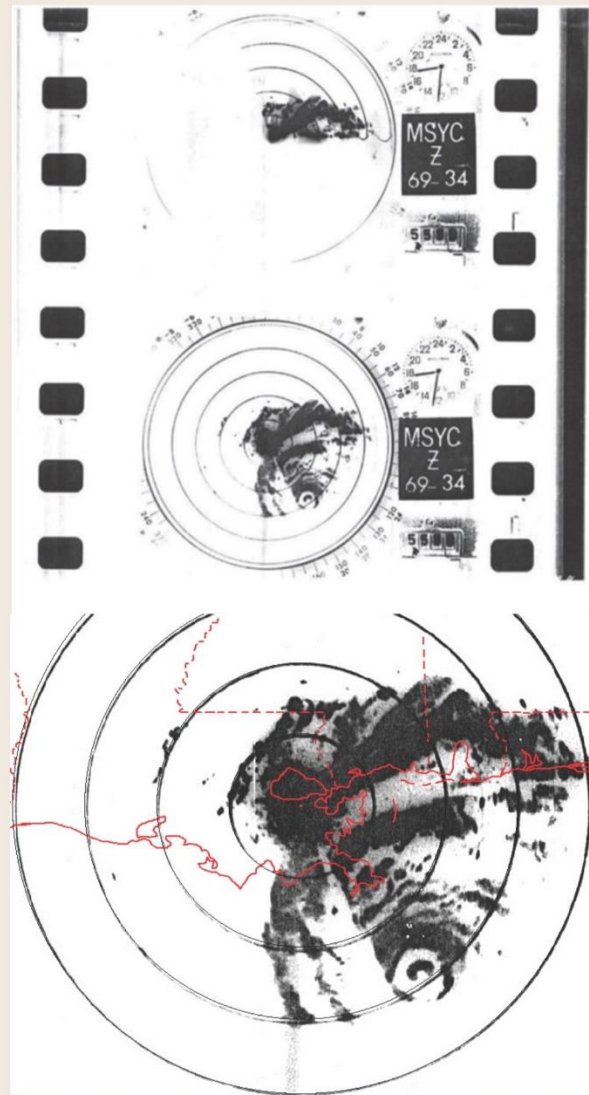


FIG. SB2. (top) Sample of the photocopy of the PPI scope WSR-57 radar from New Orleans of Hurricane Camille at 1732 UTC 17 Aug 1969. (bottom) Subsequent radar image with the map overlay and scaling.

structure with circular eyes with diameters of 10 and 30 n mi with some additional prominent banding at larger radii. The inner eye near the time of landfall could be considered elliptical with a major axis of 12 n mi oriented northwest–southeast and a minor axis of 8 n mi (N. C. Roberts Jr. 1969, unpublished manuscript). The POCI at landfall was a very low 1004 mb, but the hurricane was also quite tiny with an ROCI of 150 n mi. Camille's forward speed had increased to about 15 kt at the time of landfall.

The discovery of additional landfall pressures and radar imagery from the New Orleans Weather Bureau Office aided analysis of the Mississippi landfall. There were three pressure values of interest near the point of landfall. A pressure of 909 mb was measured by Mr. Charles Breath at the onset of the eye in his home just west of the bridge in Bay St. Louis, Mississippi, which was about 3–4 n mi east of the landfall point. This marine aneroid barometer was subsequently tested and determined to be accurately calibrated. The 909-mb value had been the accepted central pressure value at landfall originally as shown in HURDAT2 and discussed in Simpson et al. (1970). However, Mr. Breath also measured a 904-mb pressure at a later point in the eye passage a short distance west of the first measurement (see the sidebar “Camille landfall pressures” for additional discussion about this 904-mb measurement), in one of his rental properties behind his damaged house, as reported by N. C. Roberts Jr. (1969, unpublished manuscript) and confirmed in interviews of the Breath family (Breath 2007). In addition, N. C. Roberts Jr. (1969, unpublished manuscript) documents an even lower value of 897-mb pressure reading, also in Bay St. Louis, with additional details on its location and time from the Loyola University archives of Roberts's records. However, there is no documentation on the accuracy of the instrument and this barometer could not be located today. Moreover, the value provided in inches of mercury—26.50 in.—appears to be rounded to the nearest 0.5 in. Thus, this value cannot be assumed to be completely accurate. Given that the 904-mb pressure reading was taken near the eastern edge of the eye, a 900-mb central pressure is analyzed at landfall. It is of interest that this corresponds closely to the 901 mb that N. C. Roberts Jr. (1969, unpublished manuscript) analyzed as the central pressure, taking a mix of the Waveland–Lakeshore–Bay St. Louis observations.

This central pressure of 900 mb—a roughly 20-mb decrease in the 10 h since the last aircraft data—shows Camille was strengthening at landfall, possibly because of the end of the ERC. Brown et al. (2006) suggest maximum sustained winds at landfall

of 148 kt using the standard relationship or 155 kt using the intensifying subset north of 25°N. Given the competing factors of a tiny RMW of approximately 6–8 n mi and a moderate forward speed of 15 kt, but a very low pressure of the outer closed isobar of 1004 mb, an intensity of 150 kt is reanalyzed for the time of landfall (a graph of the previous and reanalyzed best-track intensities is provided in Fig. 7). The 150 kt at landfall show Camille as a category 5 hurricane at landfall in Mississippi. This intensity assessment confirms the original indication of Camille as a category 5 striking the United States (Hebert and Taylor 1978).

The intensity changes of Camille on 16 and 17 August appear similar to those of 1992's Hurricane Andrew on 23 and 24 August. Andrew reached an initial peak intensity of 150 kt with a 922-mb central pressure near 1800 UTC 23 August (Landsea et al. 2004a). After this, an ERC commenced with the winds decreasing to 125 kt and the pressure rising to 941 mb early on 24 August.¹ As the ERC completed, Andrew rapidly reintensified to an intensity of 145 kt and a central pressure of 922 mb as it made landfall in southern Florida near 0900 UTC 24 August.

Additional indirect support for the landfall intensity comes from inland observations and use of

¹ Aircraft data documenting the ERC available online (http://verif.rap.ucar.edu/jntweb/tcdata/vortex/sources/raw_VDMs_v1.000/1992/vortex_AL041992_ANDREW.txt).

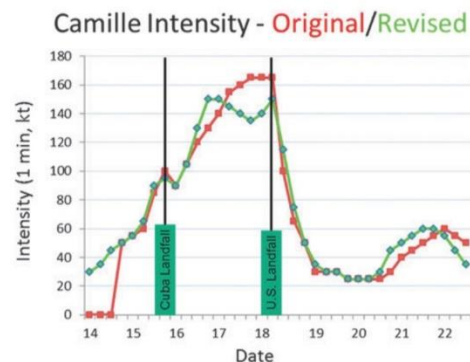


FIG. 7. Original (red) and revised (light green) intensity of Camille. Intensity is the analyzed maximum 1-min surface wind associated with the circulation of the TC. Camille's landfalls in Cuba and in the United States are indicated with the black vertical lines.

TABLE 1. The official revisions for Hurricane Camille in the 6-hourly HURDAT2, 14–22 Aug 1969, which have been approved by the Best-Track Change Committee. Changes are listed in boldface with the original best-track value, if existing, in parentheses. Three new best-track entries were added at the beginning, and two new nonsynoptic-time landfall entries were added for the Cuba and Mississippi landfalls. There were no significant position changes.

Time and date	Lat (°N)	Lon (°W)	Max wind speed (kt)	Central pressure (mb)	Storm status
0000 UTC 14 Aug	18.3	79.7	30	—	Tropical depression
0600 UTC 14 Aug	18.5	80.5	35	—	Tropical storm
1200 UTC 14 Aug	18.8	81.3	45	—	Tropical storm
1800 UTC 14 Aug	19.1 (19.4)	82.0	50	991	Tropical storm
0000 UTC 15 Aug	19.5 (19.7)	82.7	55	991	Tropical storm
0600 UTC 15 Aug	20.0 (20.1)	83.3	65 (60)	—	Hurricane
1200 UTC 15 Aug	20.6 (20.7)	83.8	90 (85)	969 (970)	Hurricane
1800 UTC 15 Aug	21.3 (21.2)	84.1	95 (100)	966 (964)	Hurricane
2200 UTC 15 Aug	21.9	84.3	95	—	Landfall over western Cuba
0000 UTC 16 Aug	22.3	84.4	90	—	Hurricane
0600 UTC 16 Aug	23.1	85.2	105	—	Hurricane
1200 UTC 16 Aug	23.8 (23.7)	86.0 (85.9)	130 (120)	—	Hurricane
1800 UTC 16 Aug	24.3 (24.2)	86.6 (86.5)	150 (130)	908	Hurricane
0000 UTC 17 Aug	25.2	87.2	150 (140)	905	Hurricane
0600 UTC 17 Aug	26.0	87.7	145 (155)	—	Hurricane
1200 UTC 17 Aug	27.0	88.3 (88.2)	140 (160)	—	Hurricane
1800 UTC 17 Aug	28.2 (28.3)	88.7	135 (165)	919	Hurricane
0000 UTC 18 Aug	29.4	89.0 (89.1)	140 (165)	909	Hurricane
0400 UTC 18 Aug	30.3	89.4	150	900	Landfall near Waveland, MS
0600 UTC 18 Aug	30.7	89.6	115 (100)	—	Hurricane
1200 UTC 18 Aug	32.0 (32.2)	89.9 (90.0)	75 (65)	—	Hurricane
1800 UTC 18 Aug	33.4	90.1	50	—	Tropical storm
0000 UTC 19 Aug	34.7	90.0	35 (30)	—	Tropical storm
0600 UTC 19 Aug	36.0	89.3	30	—	Tropical depression
1200 UTC 19 Aug	37.0	88.0	30	—	Tropical depression
1800 UTC 19 Aug	37.6 (37.7)	86.0	25	—	Tropical depression
0000 UTC 20 Aug	37.6 (38.0)	84.0 (84.8)	25	—	Tropical depression

TABLE 1. Continued.					
Time and date	Lat (°N)	Lon (°W)	Max wind speed (kt)	Central pressure (mb)	Storm status
0600 UTC 20 Aug	37.4	80.6 (80.2)	25	—	Tropical depression
1200 UTC 20 Aug	37.2 (37.3)	77.3 (77.0)	30 (25)	—	Tropical depression
1800 UTC 20 Aug	37.0	75.3 (75.1)	45 (30)	1000	Tropical storm
0000 UTC 21 Aug	36.7 (36.6)	73.6 (73.4)	50 (40)	—	Tropical storm
0600 UTC 21 Aug	36.7	70.9	55 (45)	—	Tropical storm
1200 UTC 21 Aug	37.1 (37.3)	68.1 (68.4)	60 (50)	—	Tropical storm
1800 UTC 21 Aug	37.8 (38.0)	64.7 (64.9)	60 (55)	—	Tropical storm
0000 UTC 22 Aug	39.2	61.8 (61.4)	55 (60)	—	Tropical storm
0600 UTC 22 Aug	40.8	58.2	45 (55)	—	Tropical storm
1200 UTC 22 Aug	43.0	54.0	35 (50)	—	Extratropical storm

the Kaplan and DeMaria (1995) inland decay model for TCs. Columbia, Mississippi, reported a “fastest mile” sustained wind of 104 kt about 4 h after landfall in or near the RMW. This value adjusts to 99 kt in converting to a peak 1-min wind (Powell et al. 1996). Application of the Kaplan–DeMaria model with a landfall intensity of 150 kt yields a value of 101 kt, which is close to the Columbia observation.

Other than the observation in Columbia, no anemometer measurement recorded extreme winds near the RMW, mainly because of the lack of anemometers in the landfall area. The highest observed sustained (roughly 10 min) winds in Camille were 113 kt, at which point the anemometer failed, at the Transworld drilling rig block 92 about halfway between the mouth of the Mississippi River and the Mississippi coast, at some point during the eye passage to the east. This measurement was almost certainly higher than 10 m above the ocean, but its exact altitude is unknown.

With the movement of Camille across the marshlands of northeastern St. Bernard Parish, Louisiana, category 5 winds are assessed to have occurred in Louisiana as well as Mississippi. Runs of the Schwerdt et al. (1979) parametric hurricane wind model suggest maximum sustained winds of 75–80 kt in far southwestern Alabama. Category 1 winds for Alabama would be consistent with the impacts observed just west of there in Pascagoula, Mississippi.

The original best track showed a brief landfall in southeastern Louisiana near the mouth of the Mississippi River just before 0000 UTC 18 August (Table 1). However, the numerous radar fixes available indicated that the center of the hurricane remained just offshore, which is consistent with the radar-based track shown in the *Preliminary Report* (Weather Bureau 1969). Camille passed over the marshy regions of northeastern St. Bernard Parish around 0230–0330 UTC 18 August, but no landfall point is indicated here because of the lack of dry land in the vicinity.

It should be noted that the original HURDAT format did not allow for nonsynoptic best-track points. The new HURDAT2 format allows for this, so that position and intensity at landfall can be accurately documented.

EXTRATROPICAL TRANSITION AND DISSIPATION OF CAMILLE. The original best track did not indicate an extratropical stage occurred in Camille; however, Simpson et al. (1970) stated that extratropical transition (ET) did occur. Data examined during the reanalysis show that Camille became embedded within a frontal boundary by 1200 UTC 22 August and ET occurred at that time. The best track has been updated to clarify this by indicating ET at 1200 UTC 22 August. No change was introduced to the timing of Camille’s dissipation, which occurred just after extratropical transition.

COMPARISONS OF CAMILLE WITH OTHER U.S. CATEGORY 5 HURRICANES.

Three other category 5 Atlantic basin hurricanes are known to have struck the United States: the 1928 “San Felipe” hurricane in Puerto Rico, the 1935 “Labor Day” hurricane in the Florida Keys, and 1992’s Hurricane Andrew in southeast Florida. This record of U.S. category 5 hurricanes is likely complete since 1900. However, before that time, coastal U.S. populations were quite sparse—especially in parts of Florida, Louisiana, and Texas—and a category 5 could have struck the coast but not been recognized as such, or may have even been missed completely as one goes farther back in time. In comparing the MSLP and landfall intensity of these category 5 hurricanes, Camille, at 900 mb and 150 kt, ranks in intensity for U.S. hurricanes just below the 1935 Labor Day hurricane, at 892 mb and 160 kt (Landsea et al. 2014); however, it is slightly stronger than Andrew in 1992, at 922 mb and 145 kt (Landsea et al. 2004a), and the 1928 San Felipe hurricane in Puerto Rico, at 931 mb and 140 kt (Landsea et al. 2012), for strongest hurricanes at landfall.

SUMMARY. A reassessment of Hurricane Camille has introduced a number of significant changes into the best-track database:

Genesis time changed to 18 h earlier than originally indicated, at 0000 UTC 14 August.

Major intensity changes of least 20 kt from the original best-track values were introduced for Camille’s intensity at these time periods:

- an increase from 130 to 150 kt at 1800 UTC 16 August;
- a decrease from 160 to 140 kt at 1200 UTC 17 August;
- a decrease from 165 to 135 kt at 1800 UTC 17 August; and
- a decrease from 165 to 140 kt at 0000 UTC 18 August.

Additional intensity changes include reductions in the peak intensity of Camille from 165 to 150 kt and the timing of the peak intensity:

- previous peak intensity of 165 kt was just prior to the Mississippi landfall, at best-track points 1800 UTC 17 August and 0000 UTC 18 August;
- new peak intensity of 150 kt in the Gulf of Mexico at the time of the 908- and 905-mb readings, at 1800 UTC 16 August and 0000 UTC 17 August; and

- the peak intensity of 150 kt was reached again at the time of the Mississippi landfall at 0400 UTC 18 August.

At U.S. landfall at Waveland, Mississippi, at 0400 UTC 18 August, Camille is assessed to have struck with a central pressure of around 900 mb and an intensity of 150 kt. This is deeper but slightly weaker than the original 909-mb and 165-kt landfall intensity implied by the last entry in HURDAT2 before landfall at 0000 UTC 18 August.

A brief extratropical cyclone stage was formally documented at the last point in Camille’s life cycle at 1200 UTC 22 August, but no change to the dissipation timing was indicated.

No major changes were introduced for the track of Camille.

The reanalysis of Camille reconfirms that the devastating hurricane came ashore as a category 5 on the Saffir–Simpson hurricane wind scale, but it is now considered to be the second-most-intense hurricane in the United States’ record. After Camille’s revision, it is not anticipated that any other single storm will be reassessed out of sequence, as this completes analysis of all category 5 U.S.-landfalling hurricanes. The Atlantic Hurricane Database Reanalysis Project will continue to revise the HURDAT2 database through the end of the twentieth century and provide official updates to the database’s roughly 10 hurricane seasons every calendar year.

ACKNOWLEDGMENTS. This work has been sponsored by a grant from the NOAA Climate Program Office on “Atlantic basin tropical cyclone database reanalysis and impact of incomplete sampling.” The authors wish to thank the remainder of the NHC Best-Track Change Committee (Eric Blake, Todd Kimberlain, Richard Pasch, Gladys Rubio, and Eric Uhlhorn) for their comments and detailed suggestions leading to the final revisions to Camille’s best track (the third author on this paper is the chair of the committee). Sandy Delgado provided the revised track map for Camille. Special thanks to Scott Stephens and Gregory Hammer of National Climate Data Center for providing copies of the original archived WSR-57 radar imagery for Camille. Special thanks also Trish Nugent, C. A., special collections and archives coordinator, Monroe Library, Loyola University, New Orleans, for providing access to the Nash Roberts Camille archive papers. Thanks to Hugh Willoughby for assisting with the 901-mb sonde analysis. Many thanks to Louis M. Kyriakoudes, Ph.D., director of the Center for Oral History and Cultural Heritage at the University of Southern

Mississippi, for directly providing scans of the 1984 Camille interviews. Many thanks to William E. (Eddie) Coleman of the Hancock County Historical Society for providing the post-Camille photo of the Breath home. Thanks also are provided to Gloria Aversano, the NHC librarian, for tirelessly tracking down additional sources in support of this reanalysis. Alex Fierro, Dan Lindsey, Bobbi Schwarz-Biederman, Kevin Tyle, and Ryan Wade all provided a scanned version of Camille's infrared image that was on the front cover of the September 1971 *Bulletin of the American Meteorological Society*. Maritza Ballester graciously provided Cuban archive information from Camille, including scanned hand-drawn synoptic maps. Finally, Eric Blake, Sandy Delgado, and Eric Uhlhorn provided helpful reviews of an earlier version of this paper. The first author would also like to acknowledge her advisor, Prof. Haiyan Jiang.

REFERENCES

- Allison, L. J., G. T. Cherrix, and H. Ausfresser, 1971: Color analysis of Hurricane Camille, 1969, using Nimbus infrared radiation data. *Bull. Amer. Meteor. Soc.*, **52**, 862 and cover page.
- Brown, D. P., J. L. Franklin, and C. W. Landsea, 2006: A fresh look at tropical cyclone pressure–wind relationships using recent reconnaissance-based “best track” data (1998–2005). *27th Conf. on Hurricanes and Tropical Meteorology*, Monterey, CA, Amer. Meteor. Soc., 3B.5. [Available online at https://ams.confex.com/ams/27Hurricanes/techprogram/paper_107190.htm.]
- DeAngelis, R. M., 1970: North Atlantic tropical cyclones, 1969. *Mariners Wea. Log*, **14**, 1–11.
- , and E. R. Nelson, 1969: Hurricane Camille, August 5–22, 1969. *Climatological Data National Summary*, No. 8, U.S. Department of Commerce/NOAA/Environmental Data Service, Asheville, NC, 451–475.
- Dvorak, V. F., 1984: Tropical cyclone intensity analysis using satellite data. NOAA Tech. Rep. NESDIS 11, 47 pp.
- ESSA, 1969: Hurricane Camille—A report to the administrator. Department of Commerce Rep. ESSA/PI 690034, 30 pp.
- Hagen, A. B., D. Strahan-Sakoskie, and C. Luckett, 2012: A reanalysis of the 1944–53 Atlantic hurricane seasons—The first decade of aircraft reconnaissance. *J. Climate*, **25**, 4441–4460, doi:10.1175/JCLI-D-11-00419.1.
- Hamilton, R. C., and D. B. Steere, 1969: Covering Hurricane Camille, 17 August 1969. Ocean Data Gathering Program Rep. 2, Baylor Company, 136 pp.
- Hebert, P. J., and G. Taylor, 1978: The deadliest, costliest, and most intense United States hurricanes of this century (and other frequently requested hurricane facts). NOAA Tech. Memo. NWS NHC 7, 24 pp. [Available online at www.nhc.noaa.gov/pdf/NWS-NHC-1978-7.pdf.]
- Kaplan, J., and M. DeMaria, 1995: A simple empirical model for predicting the decay of tropical cyclone winds after landfall. *J. Appl. Meteor.*, **34**, 2499–2512, doi:10.1175/1520-0450(1995)034<2499:ASEMFP>2.0.CO;2.
- Kimball, S. K., and M. S. Mulekar, 2004: A 15-year climatology of North Atlantic tropical cyclones. Part I: Size parameters. *J. Climate*, **17**, 3555–3575, doi:10.1175/1520-0442(2004)017<3555:AYCONA>2.0.CO;2.
- Landsea, C. W., and J. L. Franklin, 2013: Atlantic hurricane database uncertainty and presentation of a new database format. *Mon. Wea. Rev.*, **141**, 3576–3592, doi:10.1175/MWR-D-12-00254.1.
- , and Coauthors, 2004a: A reanalysis of Hurricane Andrew's intensity. *Bull. Amer. Meteor. Soc.*, **85**, 1699–1712, doi:10.1175/BAMS-85-11-1699.
- , and Coauthors, 2004b: The Atlantic Hurricane Database Re-Analysis Project: Documentation for the 1851–1910 alterations and additions to the HURDAT database. *Hurricanes and Typhoons: Past, Present, and Future*, R. J. Murnane and K.-B. Liu, Eds., Columbia University Press, 177–221.
- , and Coauthors, 2008: A reanalysis of the 1911–20 Atlantic hurricane database. *J. Climate*, **21**, 2138–2168, doi:10.1175/2007JCLI1119.1.
- , S. Feuer, A. Hagen, D. A. Glenn, J. Sims, R. Perez, M. Chenoweth, and N. Anderson, 2012: A reanalysis of the 1921–30 Atlantic hurricane database. *J. Climate*, **25**, 865–885, doi:10.1175/JCLI-D-11-00026.1.
- , A. Hagen, W. Bredemeyer, C. Carrasco, D. A. Glenn, A. Santiago, D. Strahan-Sakoskie, M. Dickinson, 2014: A reanalysis of the 1931–43 Atlantic hurricane database. *J. Climate*, **27**, 6093–6118, doi:10.1175/JCLI-D-13-00503.1.
- Loyola University, 2001: Nash Roberts hurricane papers, 1948–2000. 57 Boxes, 7 Portfolios. [Available Monroe Library, Loyola University, 6368 St. Charles Avenue, Suite 198, New Orleans, LA 70118.]
- Mississippi Test Facility, 1969: Hurricane Camille enters Mississippi—August 17, 1969. [Available online at www.nhc.noaa.gov/archive/storm_wallets/cdmp/.]
- NHC, 1969: Tropical Cyclone Storm Wallet Electronic Archive: Camille. [Available online at www.nhc.noaa.gov/archive/storm_wallets/cdmp/.]
- OFCM, 1997: National hurricane operations plan. U.S. Department of Commerce/NOAA Rep. FCM-P12-1997, 150 pp.
- Parmenter, F. C., 1969: Picture of the month—Hurricane Camille. *Mon. Wea. Rev.*, **97**, 828–829, doi:10.1175/1520-0493(1969)097<0828:HC>2.3.CO;2.

- Pasch, R. J., E. S. Blake, H. D. Cobb III, and D. P. Roberts, 2006: Hurricane Wilma, 15–25 October 2005. National Hurricane Center Tropical Cyclone Rep., 27 pp. [Available online at www.nhc.noaa.gov/data/tcr/AL252005_Wilma.pdf.]
- Powell, M. D., S. H. Houston, and T. A. Reinhold, 1996: Hurricane Andrew's landfall in south Florida. Part I: Standardizing measurements for documentation of surface wind fields. *Wea. Forecasting*, **11**, 304–328, doi:10.1175/1520-0434(1996)011<0304:HALISF>2.0.CO;2.
- Pyle, R. W., 1984: An oral history with Charles and Mary Breath, Hurricane Camille survivors. Vol. 228. [Available from the Mississippi Oral History Project, Center for Oral History and Cultural Heritage, University of Southern Mississippi, 118 College Drive, Hattiesburg, MS 39406-0001.]
- Rappaport, E. N., J. L. Franklin, A. B. Schumacher, M. DeMaria, L. K. Shay, and E. J. Gibney, 2010: Tropical cyclone intensity change before U.S. Gulf Coast landfall. *Wea. Forecasting*, **25**, 1380–1396, doi:10.1175/2010WAF2222369.1.
- Schwerdt, R. W., F. P. Ho, and R. R. Watkins, 1979: Meteorological criteria for standard project hurricane and probable maximum hurricane wind fields, Gulf and East Coasts of the United States. NOAA Tech. Rep. NWS 23, 317 pp.
- Sheets, B., and J. Williams, 2001: *Hurricane Watch: Forecasting the Deadliest Storms on Earth*. Vintage Books, 331 pp.
- Shenk, W. E., and E. B. Rodgers, 1978: Nimbus 3/ATS 3 observations of the evolution of Hurricane Camille. *J. Appl. Meteor.*, **17**, 458–476, doi:10.1175/1520-0450(1978)017<0458:NOOTEO>2.0.CO;2.
- Simpson, R. H., and Coauthors, 1970: The Atlantic hurricane season of 1969. *Mon. Wea. Rev.*, **98**, 293–306, doi:10.1175/1520-0493-98.4.293.
- Vickery, P. J., P. F. Skerlj, and L. A. Twisdale, 2000: Simulation of hurricane risk in the U.S. using empirical track model. *J. Struct. Eng.*, **126**, 1222–1237, doi:10.1061/(ASCE)0733-9445(2000)126:10(1222).
- Weather Bureau, 1969: Hurricane Camille—August 14–22, 1969. Preliminary Rep., U.S. Department of Commerce, Environmental Science Services Administration, 58 pp.
- Willoughby, H. E., J. A. Clos, and M. B. Shoreibah, 1982: Concentric eyewalls, secondary wind maxima, and the development of the hurricane vortex. *J. Atmos. Sci.*, **39**, 395–411, doi:10.1175/1520-0469(1982)039<0395:CEWSWM>2.0.CO;2.
- Woodruff, S. D., R. J. Slutz, R. L. Jenne, and P. M. Steurer, 1987: A comprehensive ocean–atmosphere data set. *Bull. Amer. Meteor. Soc.*, **68**, 1239–1250, doi:10.1175/1520-0477(1987)068<1239:ACOADS>2.0.CO;2.

Figure 8.18 Page 18 of A Reanalysis of Hurricane Camille

1960s was not complete. Camille was done earlier and will be the last hurricane to be analyzed out of sequence.

There was a general feeling among many in the tropical cyclone community that this hurricane was probably not a Category 5 at landfall for several reasons that will be explained in the following sections (numerous personal communications). For myself this was a particularly exciting although daunting task. I had done extensive online research and pursued contacts to obtain material that was not available online. Whether Camille was weakening or intensifying at landfall did not matter, but I felt a strong curiosity to come to as close an understanding as was possible almost fifty years later to find out what it was at the Mississippi landfall. The modern methods developed by Dr. Landsea for the reanalysis would result in determination of meteorological values of mean sea level pressure (MSLP) and wind intensity through the life cycle of the hurricane, including landfall times (a new addition to the modern best track). Those were the specific goals of the reanalysis. Those numbers would also be associated with a feel and understanding for what the landfall was like. I was a teenager in 1969, lived on the Mississippi coast when this hurricane made landfall, and had personally seen some of the damage that occurred. Was it the "real deal" in this age when so many media reports are hyped, and incorrect wind data is rampant in the public understanding. This effect is complicated because a hurricane does not have to be strong in order to produce significant damage from wind, surge in onshore areas, or rain. At the conclusion of the reanalysis we could confirm that Camille was a very intense small hurricane at landfall, and confirmed that it was a Category 5 hurricane at that time. In the historical record

there was evidence of wind damage associated with intense hurricanes (wind streaks) as well as the well-known surge damage.

Some background information first must be provided to understand how important it was to find satellite imagery for 1969's Hurricane Camille. In modern day tropical meteorology, the original landfall intensity for Camille, 165 kt, prior to the adjustment to 150 kt in the 2016 reanalysis (Kieper et al. 2016), was viewed with extreme skepticism for three reasons: it's ostensible landfall intensity, the trend of hurricanes weakening as they approached the northern Gulf Coast, and the likelihood that an eyewall replacement cycle (ERC) had occurred prior to landfall and not completed, resulting in a weakening storm at landfall, which will first be discussed next some detail.

In summary it was likely that an ERC occurred, since this would tally with today's understanding of the typical evolution of strong tropical cyclones in favorable conditions. It was essential in the reanalysis that we find evidence if it did occur, and assess whether it caused weakening or whether it was completing successfully resulting in Camille maintaining intensity or even strengthening at landfall. Satellite (or radar) imagery would be the primary way to identify an ERC.

The scrutiny accorded Camille's intensity estimates are not just numbers. There is a responsibility to understand the tropical cyclones that approach the upper bounds on intensity, and also to accurately gauge intensity of significant tropical cyclones at landfall. A meteorologist communicated to the NHC second in command upon understanding the pressure gradient in Camille, "I think of Camille as a giant, well-organized tornado rather than as a very small, intense hurricane" (Sullivan, 1986). The

estimated wind speed of 180 kt (205 mi/hr) from the last Camille reconnaissance flight before landfall, leading to a 165 kt current intensity by NHC in their advisory (a 25 kt increase in only 18 hr and a 35 kt increase in 24 hr), was a main point of contention by modern-day tropical meteorologists.

8.1 Background on the Observed Intensity by Reconnaissance and Related Forecast Landfall Intensity

A 165 kt intensity is close to the upper bound for tropical cyclones and extremely rare. Generally 165 - 170 kt is a typical calculated upper bound for tropical cyclone intensity and this is supported today by MPI (maximum potential intensity) calculations based on differences between sea surface temperature and upper tropospheric temperature (Emanuel 1986). Our understanding of possible maximum intensity has changed with the extraordinary 185 kt of 2015 Hurricane Patricia (Kimberlain et al. 2016, Rogers et al. 2017). Patricia's highest operational MPIs were in the 170-174 kt range throughout its rapid intensification.

This original 165 kt landfall intensity of Camille was not supported by hard data, and was based on a visually estimated intensity of 180 kt from the appearance of the ocean surface observed from a reconnaissance aircraft when it was at an altitude of about 10,000 ft, in an area *outside* of the eyewall, at a time significantly 10 hours before landfall. Hurricane intensity can change significantly in 10 hours before landfall because drier air over land can be entrained into the circulation.

In 1969 there were no instruments on reconnaissance aircraft that accurately measured flight level wind speed, so visually estimating surface wind speeds from the ocean state

was standard practice. Today, flight level winds can be accurately measured, and in addition the SFMR instrument aboard hurricane reconnaissance aircraft, a passive microwave instrument, can provide surface wind speed measurements over water, and, when hurricanes are not within aircraft range, an active satellite instrument, ASCAT, can provide information on surface wind speeds over water up to about 80 kt. However the core of a TC is often smaller than the 25 km footprint of the ASCAT and in those cases it cannot resolve the strongest winds. Today visual estimation of surface wind speeds on the sea surface is not considered a reliable method. This skepticism was compounded by the actual estimated surface wind speed of Camille as being 180 kt (more on this later).

In a detailed report filed after Camille by two meteorologists from the Mississippi Test Facility, who experienced the western eyewall and who subsequently drove around the area to determine the location of the eye and eyewall passage and extent of damage, one estimated the winds to have been 140 kt, and "Perhaps somewhat higher" (USWB/MTF, 1969). This estimate was proved to be fairly accurate, but even though this report was submitted to NHC, it was not factored into determining the landfall intensity. The original forecast of 165 kt made ten hours prior to landfall, based on the estimate of 180 kt surface winds ten hours earlier, became the landfall intensity maintained in the official record until the reanalysis.

Minimum sea level pressure (MSLP) was more commonly used as an intensity gauge for tropical cyclones intensity at that time. Thus it is likely that knowledge of wind pressure relationships used in that era was a factor in the selection of 165 kt as the intensity.

Concurrent with the wind estimate, a 901 mb measured by a dropsonde (later determined

to be in error but considered valid in real time), and the 165 kt intensity may have been calculated based on that pressure reading.

8.2 The Historical Record of Hurricanes Making Landfall on the Northern Gulf Coast

In the recent historical record, a significant number of strong hurricanes – almost a dozen - had made landfall along the northern Gulf Coast and all had weakened in the last twelve hours before landfall, with no exceptions (Rappaport et al. 2010). Ironically, this was a trend that subsequently reversed recently with 2018 Hurricane Michael, a threshold Category 5, 140 kt at landfall in Florida panhandle (Beven et al. 2019); 2020 Hurricane Laura, a high-end Category 4, 130 kt at landfall in southwest Louisiana (Pasch et al. 2021); and 2021 Hurricane Ida, a high-end Category 4, 130 kt at landfall in southeast Louisiana (Beven et al. 2022, in preparation; NHC Hurricane Ida Special Advisory Number 13, Brown and Brennan). But in 2015 the general feeling was that because of the recent record of hurricanes weakening at landfall along the Northern Gulf Coast, and the ten hour gap between the last penetration of the eye by reconnaissance aircraft and landfall, weakening was likely to have occurred. For Camille to maintain a high intensity this entire time would have been anomalous. Had the Camille analysis begun this year rather than in 2015, the conventional wisdom would have been that it was possible Camille made landfall as a high-end Category 4 or Category 5 hurricane.

8.3 Significance of an Eyewall Replacement Cycle for Camille

In continuing favorable environmental conditions, the dynamics of intense mature hurricanes lead naturally to eyewall replacement cycles, abbreviated as ERCs (Willoughby et al. 1982 and Willoughby 1988). In 1969, while "double eyewalls" were

known as 1966, their significance was not understood, until the landmark 1982 treatise on eyewall dynamics. When a hurricane is close to landfall, land interaction can interfere with ERCs completing successfully due to both dry air entrainment and partial removal of the energy source of the warm ocean, resulting in the outer eye not able to completely close or to maintain a closed eyewall. Hurricanes also normally weaken somewhat during the transition to the outer eyewall as part of the ERC, so if the ERC does not complete, this results in a reduced intensity and loss of storm structure prior to landfall. Since Camille was in a favorable environment, as evidenced by its rapid intensification in the Gulf of Mexico and distinct small eye, conditions favored an ERC. It seemed likely that one had subsequently occurred before landfall. In the meteorological record for Camille, only one radar fix observation out of many from a number of different radar locations (over half a dozen) did identify a double eyewall using the phrase, "APRNT DOUBLE WALLED" (Figure 8.19, NHC Camille Storm Wallet), but at this time, 1969, its significance was not understood.

NPA
PENSAOOR

171245Z	27.3	88.4	
171350Z	27.26	88.33	SPRL OVR LAY (15 degree)
171455Z	27.33N	88.41W	15 deg SPRL OVR LAY
171550	27.48	88.42	15 deg SPRL OVR LAY
171650	27.57N	88.37W	15 deg SPRL OVR LAY
171730Z	27.57N	88.37W	15 deg SPRL - APRNT DOUBLE WALLED
—	—	—	EYE OUTER DIAM. 32 MILES. ONLY
—	—	—	NORTHERN PORTION INNER EYE APRNT.
171930	28.25N	88.55W	15 deg OVR LAY
172140	28.53N	88.58W	
172230Z	29.08N	88.58W	WELL DEFINED EYE

Figure 8.19 Camille radar fix indicating a double eyewall.

8.4 Available Satellite and Radar Imagery for Camille

Remarkably few satellite images exist today for Camille after almost 50 years – not more than a dozen images (Figure 8.20) – but surprisingly they included a satellite image (available on the internet) that showed Camille near peak intensity and a second image that clearly showed a moat around a small eye suggesting a double eyewall. In general in 1969 there were few satellite images per day, which had to be printed out to view them, and since the Dvorak technique had not yet been invented no intensity estimates were made. Then satellite images could be used to track the center of the storm, observe its general structure, and to observe visually the synoptic setup in the environment. But with today's understanding we can learn more from these images. In addition, the first six smaller images were useful in determining that Camille's genesis occurred earlier than

stated in the original best track, which had started Camille as a 50 kt tropical storm with no previous evolution.

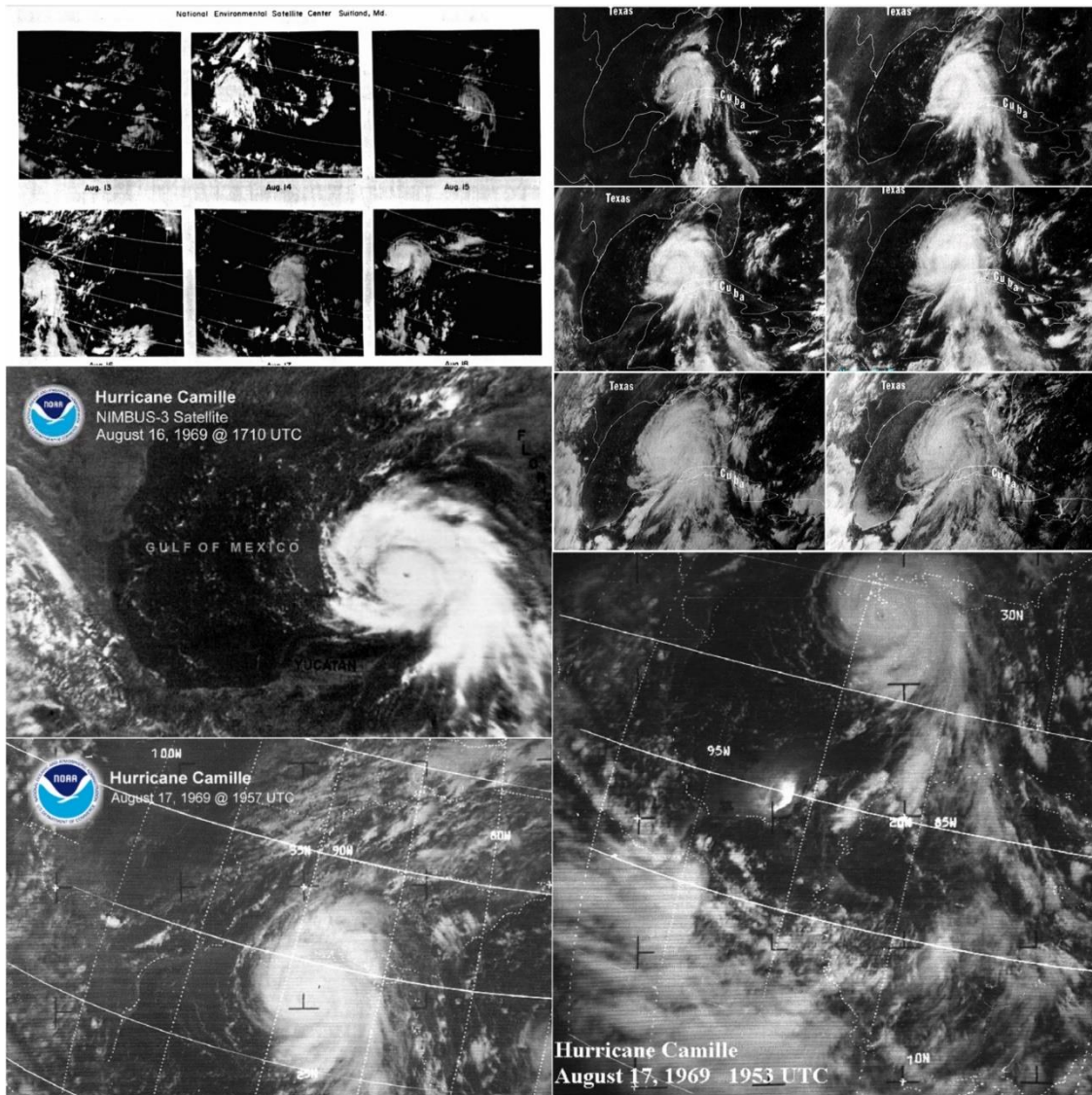


Figure 8.20. All of the available visible satellite imagery remaining today for 1969 Hurricane Camille.

8.4.1 Comparison of Camille and Wilma Eyewall Replacement Cycle

Fortunately, two of the available satellite images were found to be particularly significant. One image showed a distinct small eye, near the time of the lowest MSLP

obtained by aircraft reconnaissance. This is remarkable given the poor resolution of satellite imagery in 1969. The second, a critically important image, suggested an ERC after the first image. These images were compared with two similar images of Wilma for more understanding of the intensity changes during the ERC (Figure 8.21, and Kieper et al. 2016).

As noted earlier, under the ideal conditions for development that existed for Camille in the Gulf of Mexico, and our modern understanding of ERCs, it seemed almost a certainty that an ERC must have occurred before landfall, and often these ERC cannot complete and thus result in weakening at landfall. However evidence in Camille's case, including surface pressure observations, showed that Camille's ERC had progressed to the point that the hurricane was re-intensifying at landfall.

This contention was supported by observations at landfall. Another example of a hurricane structure that was similar was 2005 Hurricane Wilma, which was observed to have a 2-4 mile wide eye during aircraft reconnaissance at its greatest intensity of 160 kt (Pasch et al. 2006). Wilma's structural evolution and subsequent ERC were used as a proxy to understand Camille's evolution before landfall, by comparing Camille's 1969 satellite images with those of 2005 Wilma, which set new records for lowest MSLP in the Atlantic basin, 882 mb, while intensifying at a record pace in 24 hours from a 60 kt tropical storm to a 160 kt Category 5 hurricane.

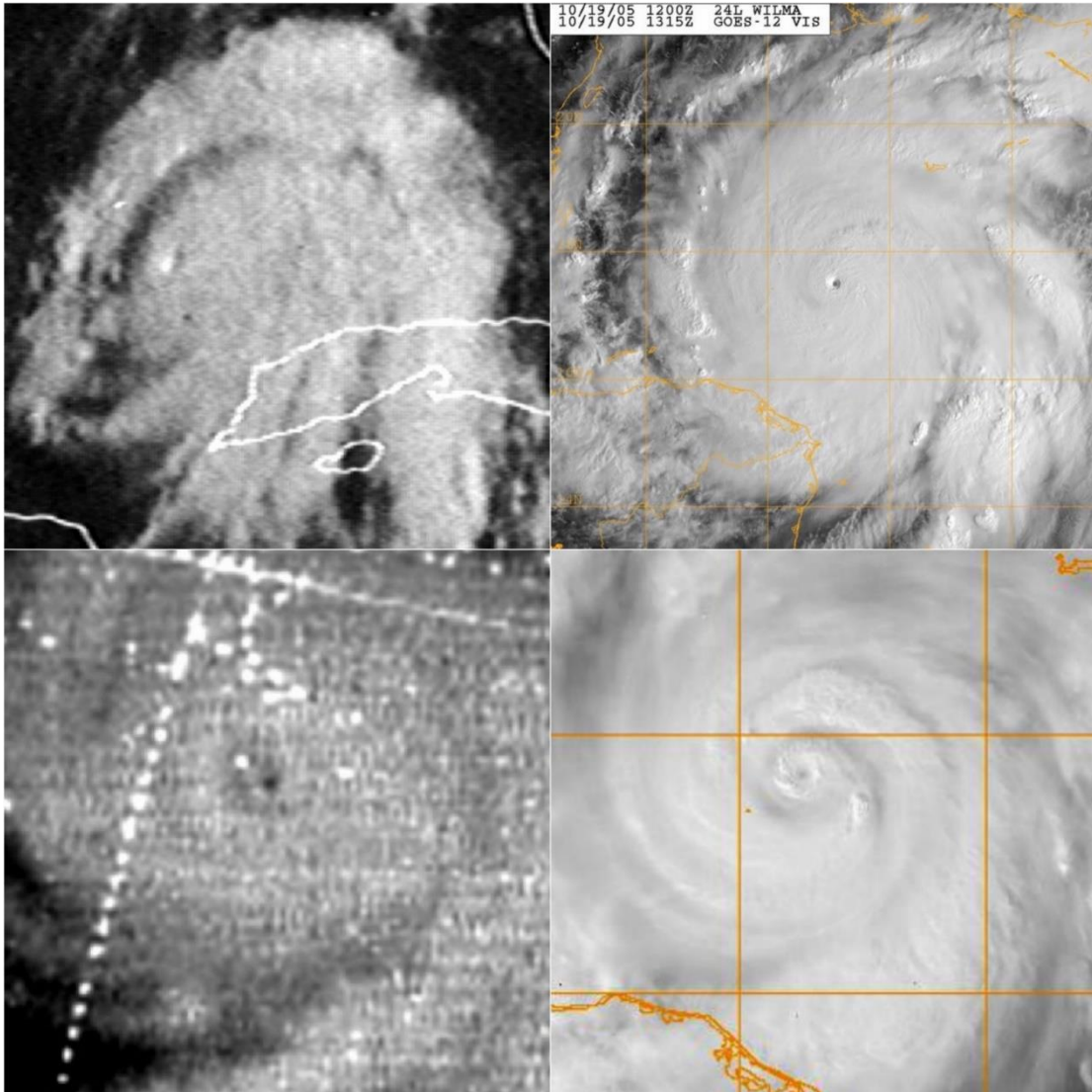


Figure 8.21. Comparison of satellite imagery from hurricanes 1969 Camille (left) and 2005 Wilma (right) at two similar key stages in development. At (top left) Visible satellite image of Hurricane Camille at 1311 UTC 16 Aug 1969 near initial peak intensity and 5 h before 1800 UTC 908-mb pressure and 150-kt intensity. (top right) Visible satellite image of Hurricane Wilma at 1315 UTC 19 Oct 2005 near peak intensity of 882 mb and 160 kt. (bottom left) Visible satellite image of Hurricane Camille suggestive of a double eyewall at 1953 UTC 17 Aug 1969 at 919-mb pressure and 135-kt intensity. (bottom right) Visible satellite image of Hurricane Wilma showing the double eyewall confirmed by aircraft data at 1915 UTC 19 Oct 2005 at 892-mb pressure and 140-kt intensity. (Kieper et al. 2015)

In satellite imagery, Camille and Wilma were remarkably similar when compared side by side at similar points in their development and at the same scale. This image (Figure

8.21) is provided at a higher resolution than what was published in the reanalysis (Kieper et al. 2016). When put into one image to view side by side, these images were sized so that they are viewed to the same scale.

In the earlier images the very small clear eyewall is remarkably distinct for Camille and compares very favorably with the corresponding image of Wilma at a similar point in the life cycle. Both happened to be observed at a similar time of day so that the sun glint on the side of the eyewall is clearly seen. Both central dense overcasts (CDOs) surrounding the eye are round and surrounded by an area of subsidence, with outer banding outside of that. With Camille there is also evidence of remarkably strong moist surface inflow from the south evidenced by strands of cloud bands feeding into the central core. All of these signs in the satellite imagery support evidence of a mature intense hurricane. Even though Camille developed from a tropical wave and Wilma from a slowly-developing monsoon trough, at this intense stage the size of their CDOs are approximately the same.

In the lower images of both hurricanes a moat is clearly seen outside of the small eye and its accompanying eyewall. The CDO is no longer solid but shows spiraling bands of clouds encircling the moat. The mean sea level pressure for the times of all four of these images (or near time) were known. Wilma's intensities at each of these times were known. It was then possible to use this quantitative information to assess Camille's intensity change associated with the ERC.

Finding the ERC was the logical and believable evolution of Camille in the Gulf of Mexico transit, and comparing these satellite images visually, and the corresponding

maximum intensities and low pressures was an important and effective way to show Camille's ERC.

This perspective underscores the importance that viewing satellite imagery still has today both for real-time forecasting and for historical purposes, and the importance of case studies in tropical cyclone research as opposed to the trend in tropical cyclone research to evaluate large data sets of satellite data without relating back to the spatial and visual context of the data. Among the tropical forecasters skill in evaluating satellite imagery is essential and the forecasters are extremely knowledgeable in interpreting satellite imagery. Dvorak analysis is the primary method of determining tropical cyclone intensity throughout the world and is completely based on evaluation of satellite imagery.

The final determination that Camille was intensifying at landfall as the ERC was completing was indicated by the radar loop (online Supplemental, Kieper et al. 2016), more importantly by a number of verified barometer readings, and by the Kaplan and DeMaria inland decay model (Kaplan and DeMaria, 1995) in conjunction with an anemometer reading in Columbia, MS four hours after landfall, which corresponded with the 150 kt landfall intensity.

5.4.2 Cloud Motion Analysis of Camille

A later analysis of Hurricane Camille's intensification utilizing cloud motions and infrared temperatures (Shenk and Rogers 1978) showed inflow of warm moist air from the northwestern Caribbean and outflow channels, all significant in terms of coverage and magnitude.

These two images from that analysis of Camille from 16 August 1969 are reproduced here, and overlay low cloud vectors over an analysis of IR temperatures, and high cloud vectors over an analysis of water vapor temperatures (Figures 8.22 and 8.23). The cloud height is with respect to the depth of the troposphere. These cloud motion vectors were computed for the paper by Ted Fujita, as noted in the acknowledgements. These images hallmark features of a very favorable environment for significant intensification.

The low cloud vectors in Figure 8.22 identify inflow of moist warm air from the Western Caribbean, from the Eastern Caribbean and also crossing Central America from the East Pacific. The rate of inflow into the hurricane is high, ranging from 15-20 kt to a maximum of two 37 kt vectors. Significant inflow from the Western Atlantic is also observed with speeds from 19 to 25 kt. These rates of inflow and the broad coverage of the inflow are not normally seen except in the strongest hurricanes, and certainly provided a rich energy source for the hurricane.

The high and mid-level cloud vectors in Figure 8.22 demonstrate significant outflow. Outflow occurs at the convective top level of the hurricane usually near the tropopause or in the upper troposphere. Providing more outflow to a mature hurricane ventilates the convection, increasing its intensity, and contributing to the intensification process that increases the maximum wind speed. Outflow concentrates in what are termed "outflow channels." The first such channel seen in the image is to the north of the hurricane, with many vectors above 40 kt and one vector of 50 kt. This is a significant outflow speed for a hurricane. The second outflow channel is seen flowing to the SE and wrapping around

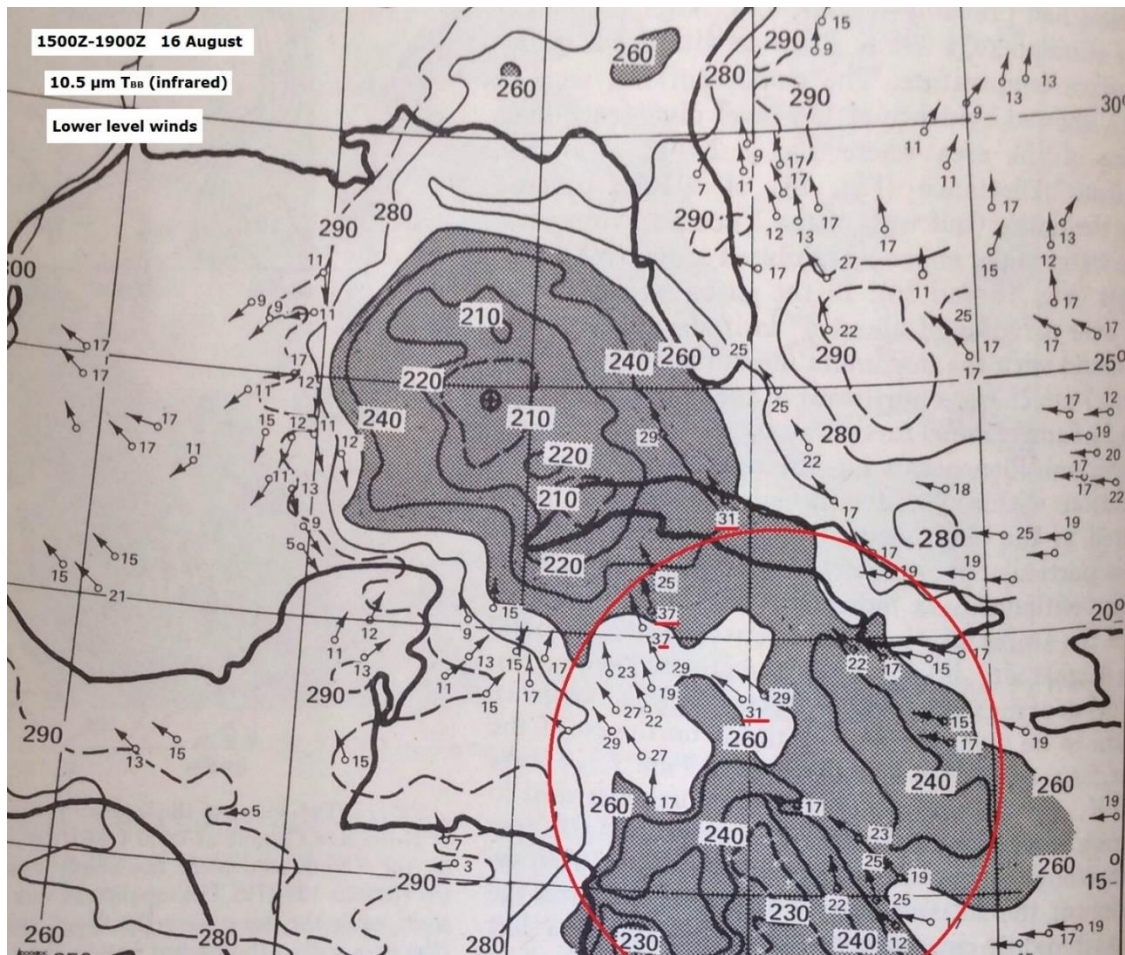


Figure 8.22 Analysis of low level winds for Hurricane Camille showing significant inflow velocities over 25 kt. (Shenk and Rogers 1978).

an upper low to the SE of the hurricane, possibly a TUTT low. These speeds are also significant, with many vectors in the high 40 kt range and two 52 kt vectors, and 30 to 40 kt quite some distance away from the hurricane in the Southern Caribbean. Camille could be seen to have two strong outflow channels in the upper air synoptic pattern at this time.

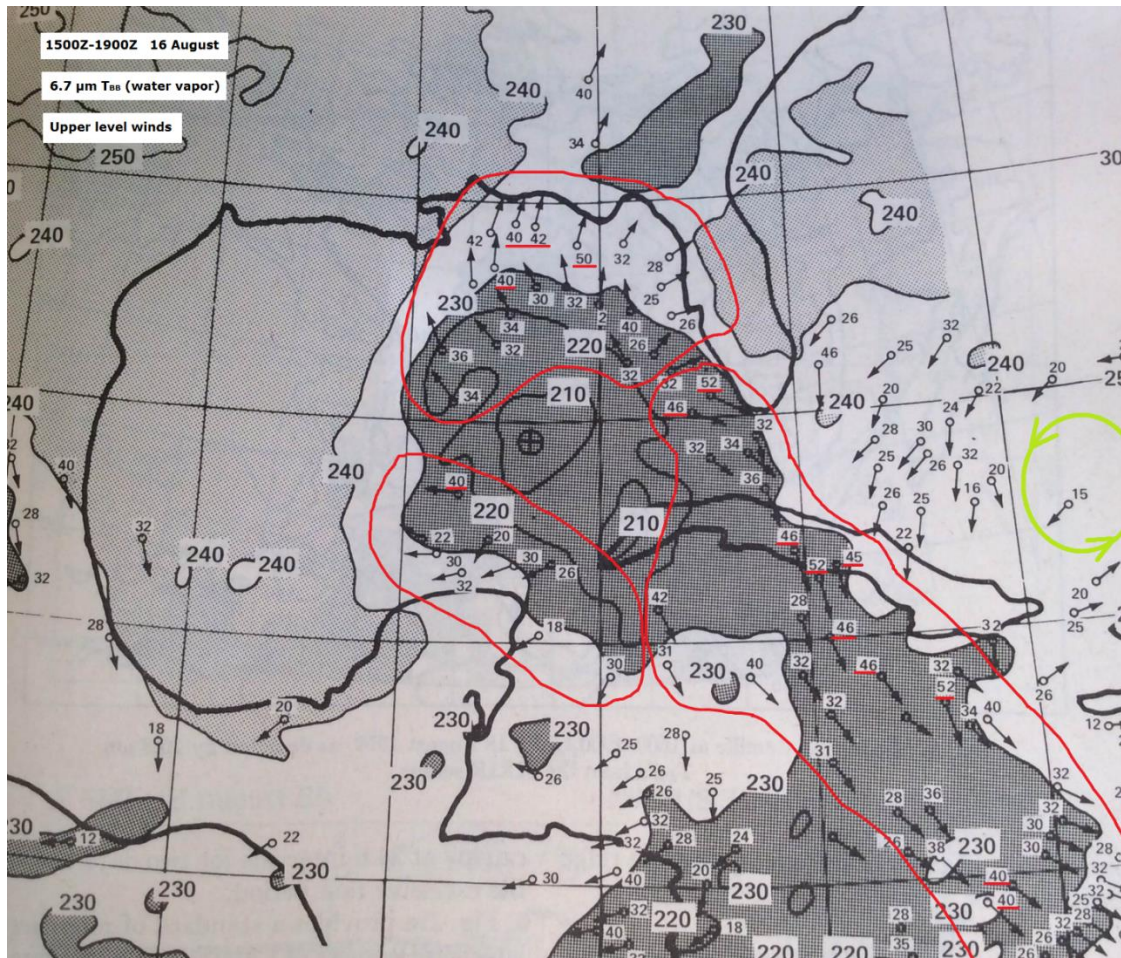


Figure 8.23 Analysis of upper level winds for Hurricane Camille showing a number of very significant outflow velocities in the 40-50kt range, with two main outflow channels. One to the north, and one to the southeast into an upper low (Shenk and Rogers 1978).

Strong outflow in the upper atmosphere and strong inflow of tropical air near the surface, increase the ability of the hurricane to strengthen rapidly. Today it is not necessary to do this analysis by hand as cloud motion products for tropical cyclones are generated and available to the public on the CIMSS TC website. An example for the upper level winds of Hurricane Wilma near peak intensity is provided (Figure 8.24).

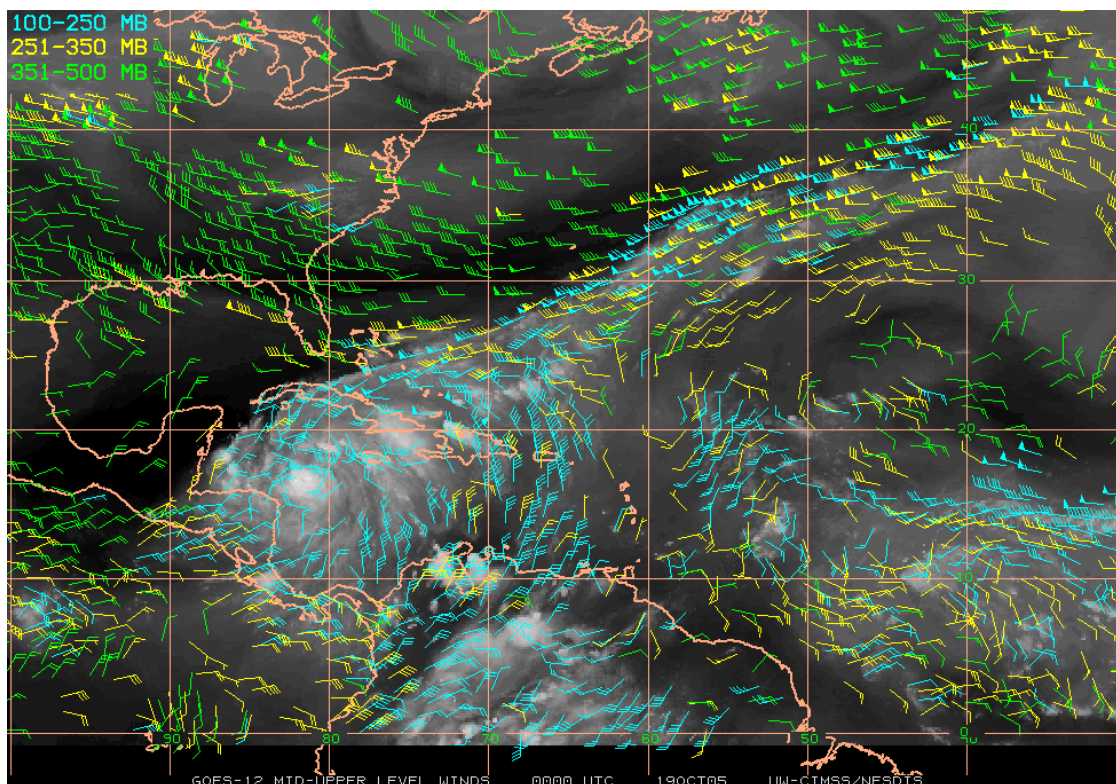


Figure 8.24 Upper level wind analysis for Hurricane Wilma showing a significant outflow channel to the northeast aided by strong westerlies. From October 19 0000Z (CIMSS Tropical Cyclone website archive).

8.4.3 Comparison of Camille Radar Imagery and Wilma 37color Imagery

As noted in Chapter 2, the 37 Color Composite satellite imagery (37color) indicates warm precipitation (cyan color) and ice (pink color). A 37color image of Wilma during the ERC shows a very similar precipitative structure to a radar image of Camille prior to landfall (Figure 8.25). This suggests that the radar imagery available for Camille could be considered in a sense a proxy for today's 37color imagery.

Provided are other comparisons of precipitative structure seen on 37color and radar close in time, all showing how well these comparisons identify similar precipitative structure: 2005 Vince off the coast of the Iberian peninsula (Figure 8.26), 2003 Claudette off the

Texas coast (Figure 8.27), and 2005 Katrina over the South Florida peninsula (Figure 8.28). Vince and Katrina radar images were obtained in real time and the Claudette image was obtained from an online search for a radar loop of Claudette at landfall.

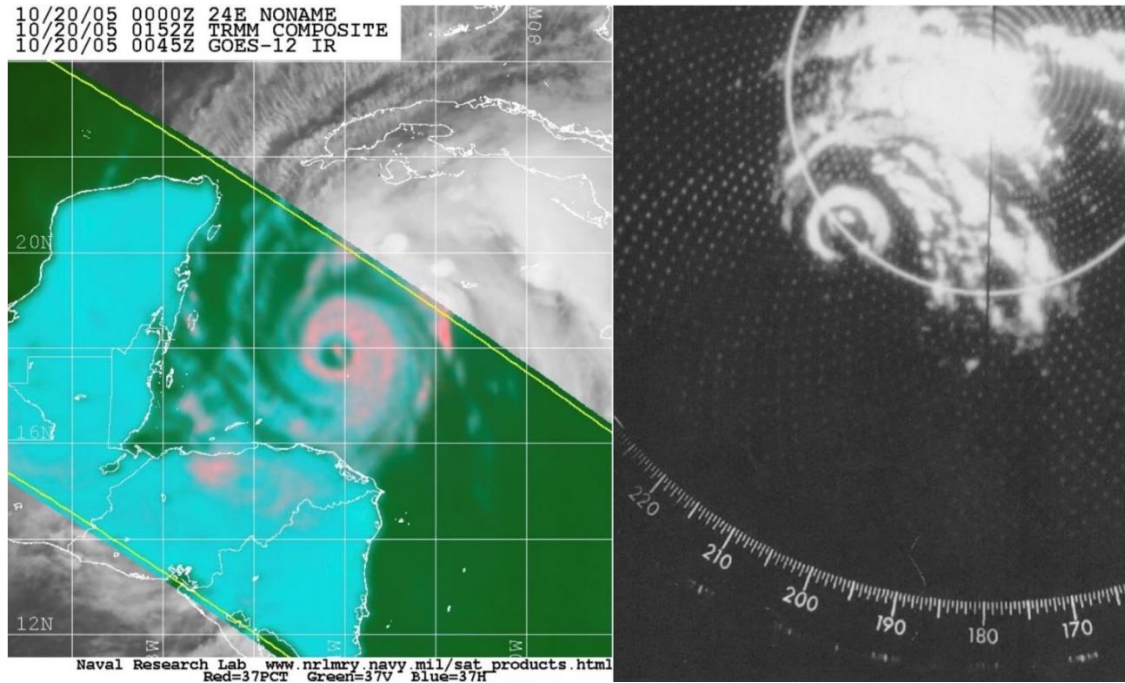


Figure 8.25 Comparison of 37 Color Composite imagery of Wilma with radar image of Camille. These are during a similar time period in the ERC.

Even though the 37color imagery is at a relatively low resolution, and is not a radar as on the TRMM and GPM satellites, these comparisons show us that the cyan (precipitation) on 37color imagery corresponds well to precipitation seen by ground-based radar, and that the pink (ice) signature corresponds to areas of higher reflectivity which indicate higher cloud tops. That the pink is bright indicates that it is part of a cumulonimbus (Cb) structure with precipitation underneath, not an orphan anvil that would be associated with drizzle and light rain (see Chapter 5).

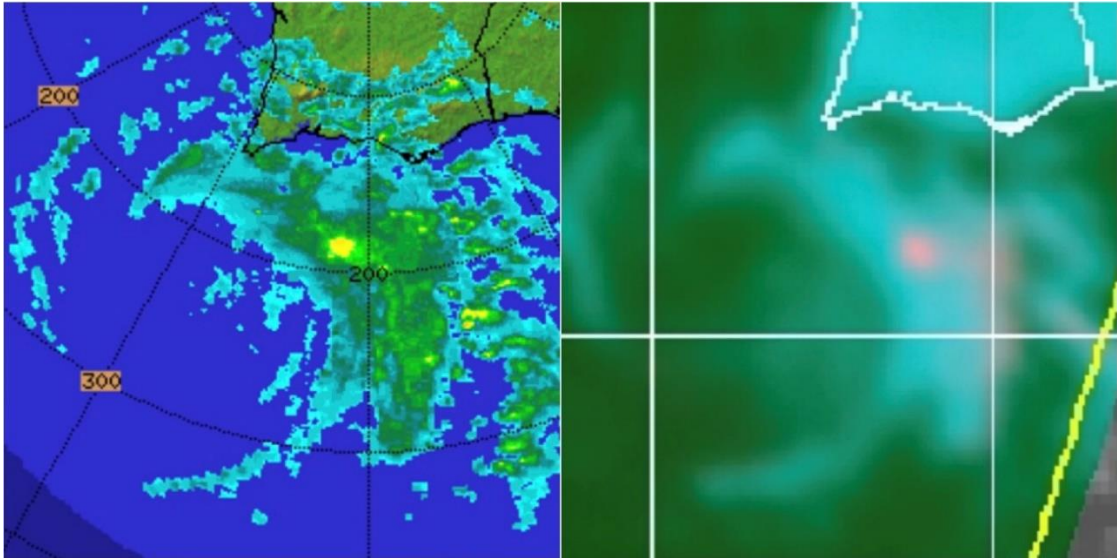


Figure 8.26 Comparison of 37 Color Composite imagery of 2005 Vince with corresponding radar image.

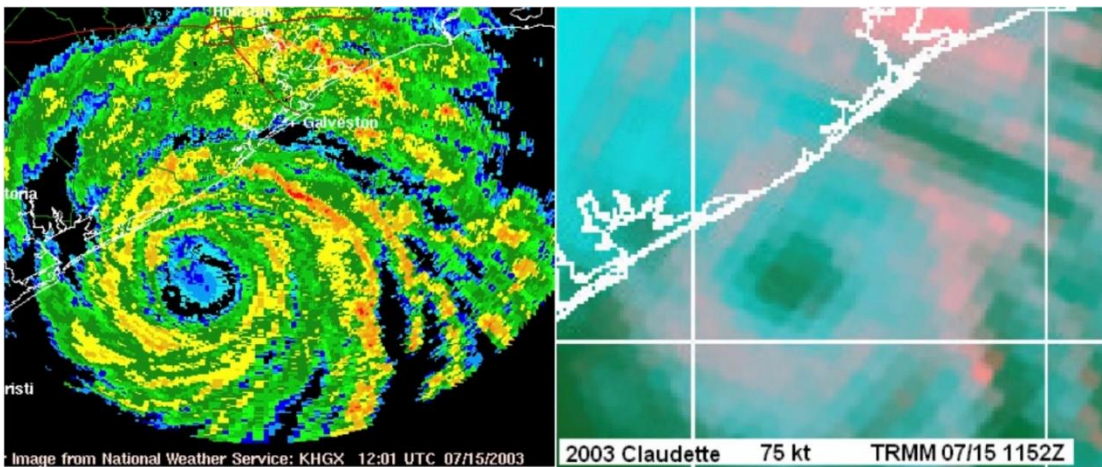


Figure 5.27 Comparison of 37 Color Composite imagery of 2003 Claudette with corresponding radar image.

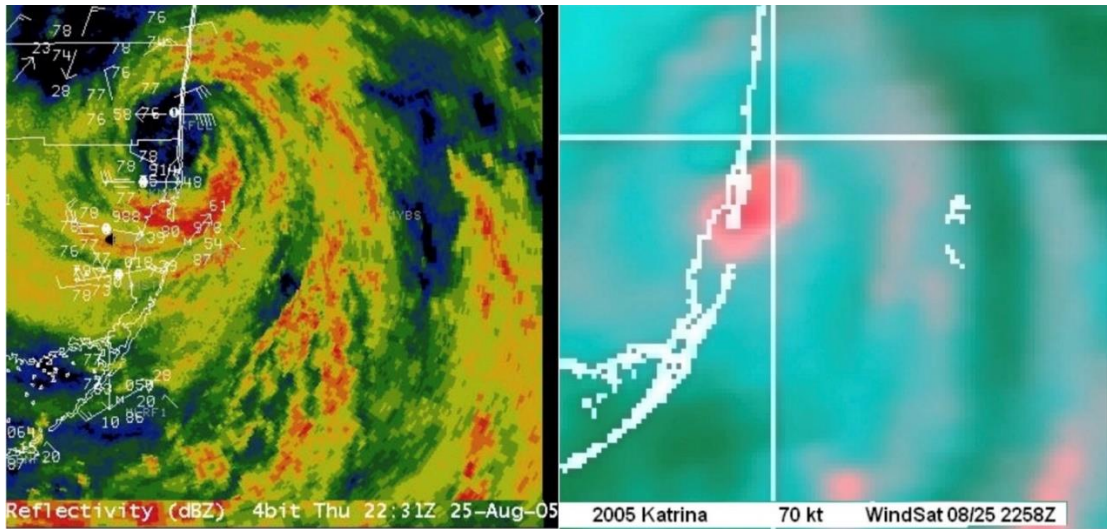


Figure 5.28 Comparison of 37 Color Composite imagery of 2005 Katrina with corresponding radar image.

8.4.4 Radar Imagery for Hurricane Camille

In addition individual two radar images showing a double eyewall were also found on the internet (see Kieper et al 2016 and Figure 8.29) and the one existing radar fix that identified a double eyewall (Figure 8.19). Possibly no one in the tropical meteorological community had searched for these before so the question of whether Camille went through an ERC prior to landfall was still unanswered, but these available images confirmed that an ERC did begin prior to landfall. Subsequently a search for radar imagery uncovered historical imagery of the New Orleans radar maintained by NCEI (National Centers for Environmental Information and formerly NCDC National Climate Data Center), that covered the period prior to landfall and provided an understanding of the storm structure – in summary the ERC was completing at landfall.

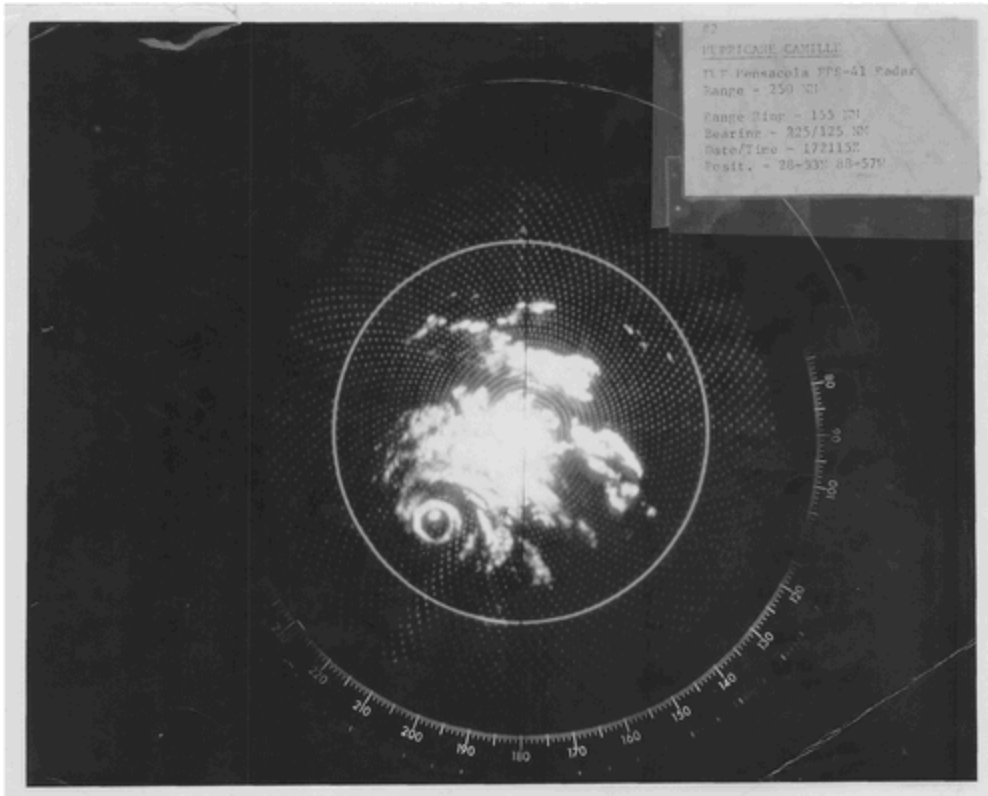


Figure 8.29 Radar image of Hurricane Camille from NAS Fleet Weather Facility showing a double eyewall. The military designation for the WSR-57 radars was AN/FPS-41. (Kieper et al. 2015)

At that time, the WSR-57 radars had a capability to take a roll of film and automatically photograph the radar scope image once every minute, which could then be processed later. In 1969 the radar imagery was only seen by the radar operator, and only a coded message describing rain band locations and eye information was sent by the radar operator to the National Hurricane Center. Forecasters did not have the capability to observe the radar imagery themselves. The radar operators could only observe the current image and there was no radar loop capability as we have today on the NWS WSR-88D.

To create a radar loop of Hurricane Camille from the individual photographs of the scope, when one had never existed before because the capability did not exist in 1969, was an exciting opportunity and a unique way to create a window to see into the past. It would provide a way to view the actual landfall.

The archived imagery was printed and sent to NHC and then scanned into digital images, but the scope had only the radar rings, as the map was overlaid onto the surface of the scope by the operator (Figure 8.30). Ninety-one sets of radar images were received for the requested time frame, selecting only one image per every five minutes, to reduce the total number of images received. The images were not all legible so a set of two images was printed for every five minutes. Figure 8.30 shows an example where only one image in a pair was usable, Figure 8.31 shows the final template overlay, and Figure 8.32 how the same radar image looked with the overlay.

The final images for incorporation into a GIF were created using the following steps:

- Identify the distance between each range ring (50 miles).
- Identify the location of the radar in 1969 (note this was originally placed at the airport but subsequent documentation showed the radar location to be in the city, so the imagery actually had to be rebuilt a second time. This was important to accurately place the landfall location on the map.
- Create a map outline with a scale that would cover the area around the radar (250 miles out from the center in all directions).
- Mark a scale for the location of the range rings.

- Create a set of range rings in the same scale and overlay onto the map. Later, in order to add the copyright at the bottom, the overlay had to be redone and the imagery had to be rebuilt a third time (Figure 5.11)
- For each image, select the best choice of the two images, and save.
- For each image, add the overlay, adjusting the range rings of the image to the range rings of the map adjusting for the best overall correspondence (Figure 5.12)
- Incorporate all the images into a GIF, in order, creating GIFs that would run at different speeds.

The final loop is available online as supplemental material to the AMS BAMS article but has been modified to a download rather than being viewable online. Therefore the MP4 movie will be attached to the dissertation.

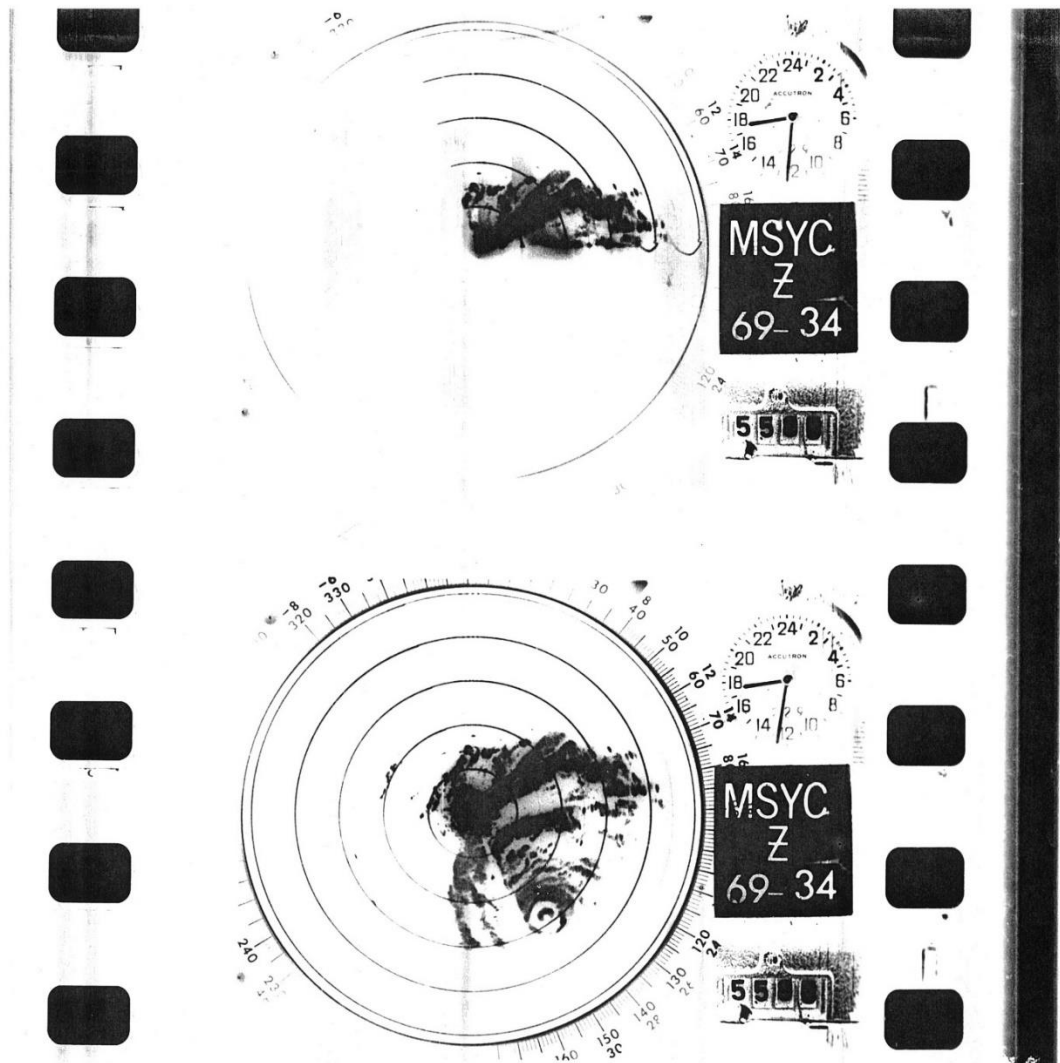
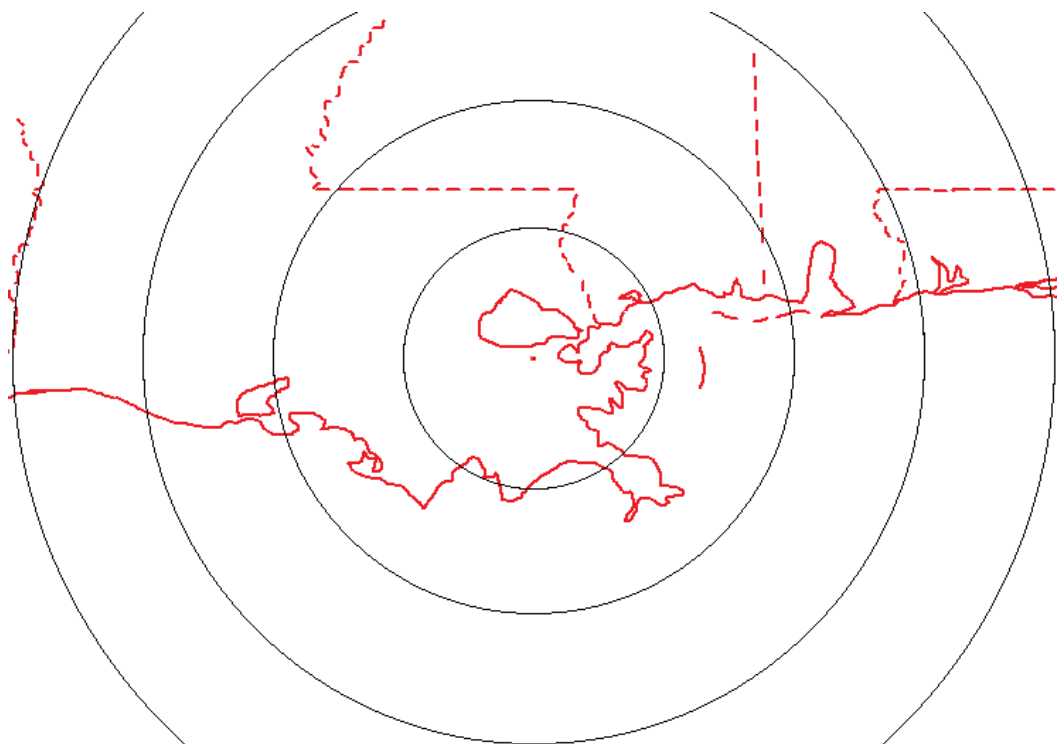


Figure 8.30 One of the radar images retrieved from the NCEI archive. These Hurricane Camille images were printed and subsequently each image was individually digitized at NHC. (SB2 of Kieper et al. 2015)



From 'A Reanalysis of Hurricane Camille' by M. E. Kieper et al.
(DOI:10.1175/BAMS-D-14-00137.1); ©2016 American Meteorological Society

Figure 8.31 The template overlay for the radar images with scaled map and radar rings.

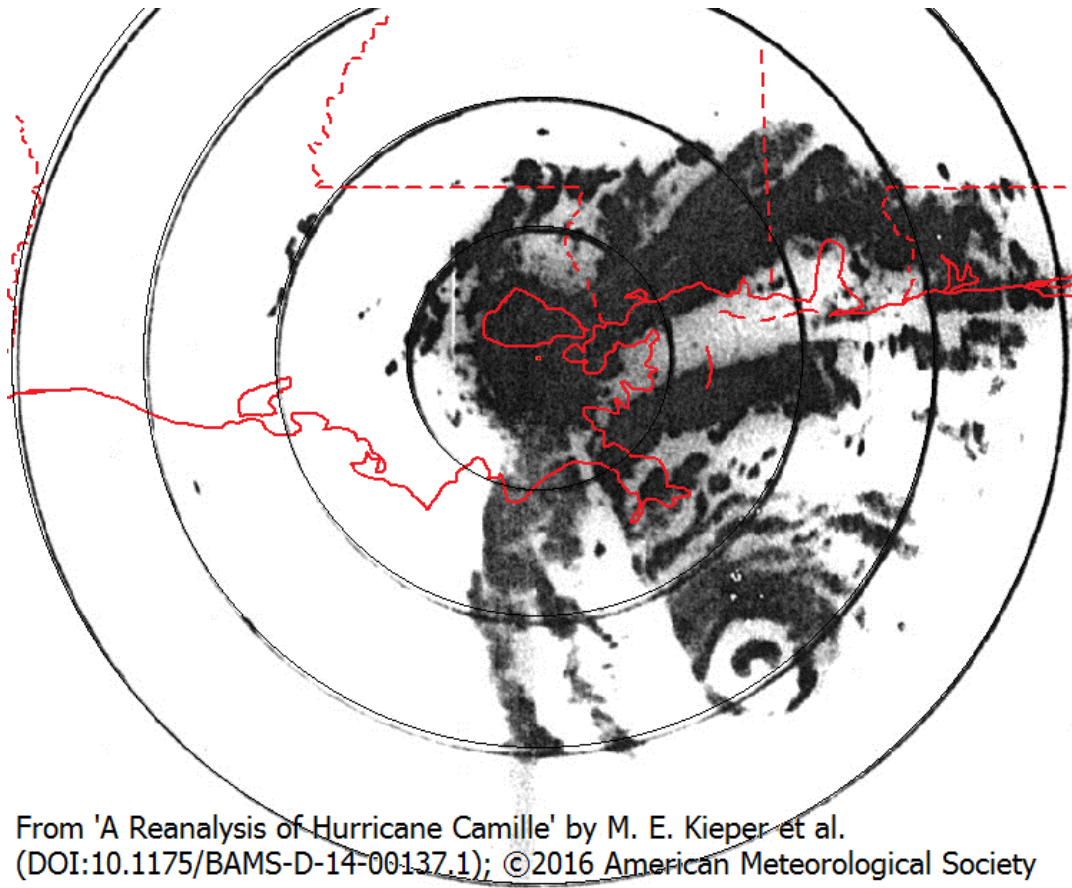


Figure 8.32 The radar image from 5.29 with the overlay. The overlay with the scaled map and range rings provides the location and distance of the archived radar image.

8.5 The Last Reconnaissance Flight into Camille

The basis for the extraordinary 165 kt forecast intensity for Camille based on an estimated 180 kt intensity (which was maintained in the 1969 storm post analysis and subsequent best track record, which stood until the 2016 reanalysis) is the last recon flight into Camille prior to landfall.

On Saturday afternoon 16 August the NHC 4pm forecast maintained Camille's 100 kt intensity, but the next forecast issued at 8pm increased the current intensity to 130 kt (NHC Camille Preliminary Report, 1969). This was due to a recon flight that afternoon

that measured separate MSLP of 908 and 905 mb. Camille could have had a lower MSLP as there were no readings during the overnight diurnal max following the last aircraft fix on the 16th.

At the midnight advisory the intensity was increased further, to 140 kt, but it is not known what led to that additional increase. In 1969 there was no documented forecast discussion component associated with the very brief public information statements. On 18 August Sunday afternoon was the last reconnaissance flight into Camille. On this flight, an MSLP of 901 mb was measured, and on the form where the data was recorded at the National Hurricane Center (NHC), was boldly written to the side, "New Record Low *for aircraft* in Atlantic Hur. 901 = 26.61" Aug 17 1815Z" (Figure 8.33 – italics mine, as an 892 mb land observation existed for the 1935 Labor Day storm). At a much later time the 901 was crossed out with a different pen and "ERROR!" was written. In the Camille reanalysis it was noted that this occurred much later, as the 901 mb continued to be documented as a valid reading in a number of publications in the remaining months of 1969 and it was not until the season review in 1970 that an ambiguous footnote discounted the 901 mb reading; the reanalysis determined that the MSLP was likely 919 mb (Kieper et al. 2016). So in real time and for some time afterwards, the 901 mb was thought to be an accurate reading. At the time this presumed record low MSLP would have been considered very significant regards the forecast and historically – such a reading would have been significant even today.

RECONNAISSANCE DATA MESSAGE				ADDRESS:
VEHICLE NUMBER:	DATE:	SCHEDULE FIX TIME:		
AIRCRAFT COORDINATES:	AIRCRAFT NUMBER:	WEATHER OBSERVER:		
UNIDENTIFIED FIX WITH OTHER AIRCRAFT: Q YES Q NO	TRANSMISSION TIME:	GROUND STATION RECEIPT TIME:		PRIORITY: 1 2 3 4 5 6 7 8 9 10
MESSAGE DURING:				
1	2	3	4	5
EYE OR CENTER FIELD BY: (Note 1)				
LATITUDE CENTER FIX. (DEG./MIN.)				
LONGITUDE CENTER FIX. (DEG./MIN.)				
DATE AND TIME OF FIX.				
CENTER DETERMINATION: 1. POSITIVE, 2. FAIR, 3. POOR. (Note 2)				
NAVIGATION FIX ACCURACY IN NAUTICAL MILES. (Note 3)				
MINIMUM COMPUTED SEA LEVEL PRESSURE OR COMPUTED DEPRESSION. (MILLIBARS)				
CONTINUATION OF FIX. POSITION (DEG./MIN.) DATE, TIME				
ESTIMATE OF MAXIMUM SURFACE WIND OBSERVED. (KNOTS)				
BEARING AND RANGE FROM CENTER OF MAXIMUM SURFACE WINDS. (DEG. AND NM)				
THE SHAPE AND ORIENTATION (CIRCULAR, OVAL, CONCENTRIC), ORIENTATION OF MAJOR AND MINOR AXIS (TENS OF DEGREES/ NM). (Note 3)				
MINIMUM HEIGHT AT STANDARD LEVEL. (MIS./METERS)				
FLIGHT LEVEL/ MAXIMUM TEMPERATURE INSIDE THE EYE. (DEGREES)				
FLIGHT LEVEL/ MAXIMUM TEMPERATURE OUTSIDE THE EYE. (DEGREES)				
ABSOLUTE ALTITUDE OF AIRCRAFT (METERS)				
MAXIMUM FLIGHT LEVEL WINDS BEAR CENTER (DEG. AND KNOTS)				
BEARING AND RANGE OF MAXIMUM OBSERVED FLIGHT LEVEL WINDS FROM CENTER. (DEG. AND NM)				
PRIMARY MEANS OF NAVIGATION: (Note 4)				
EYE CHARACTER: CLOSED EYE, POORLY DEFINED, OPEN SK. ETC.				
COM OR CENTER CENTER: OBSERVE POSITIVE, FAIR, OR POOR WITH WIND TEMPERATURE PRESSURE. (Note 5)				
AIRCRAFT POSITION IF RADAR FIX. (DEG./MIN.)				
REMARKS: RAIN FRONTS, CLOUDS IN EYE, ETC. (Fill After Item 3 and Section 1)				

Note 1. Transmit Number in accordance with the following code:

1. Wind
2. Pressure
3. Radar
4. Penetration
5. Temperature
6. Cloud
7. Spiral Overlay
8. Triangulation
9. Radar Hole in Sea Return

Note 2. Center Determination:

1. Positive (0-9 NM)
2. Fair (10-19 NM)
3. Poor (20 NM or greater)

The aircraft may send this information in code figures 1, may indicate the accuracy of the center fix in nautical miles. Example: Figure 1 would indicate Positive Center Determination accuracy of 0 to 9 nautical miles. Figure 5 would indicate determination within 5 nautical miles.

Note 3. Eye Shape will be transmitted: C = Circular, CO = Concentric, E = Elliptical. Orientation of Major Axis in tens of deg: 01-010 to 190; 17-170 to 350; etc. Diameter in NM.

EXAMPLES: C8 = Circular eye 8 miles in diameter. E09/15/5 = Elliptical eye, major axis 090-270, major axis 15 NM, length of minor axis 5 nm. CO8/14 = Concentric eye, diameter inner eye 8; outer eye 14 NM.

Note 4. Transmit Number in accordance with the following code:

1. LORAN
2. Radar
3. Doppler
4. Celestial
5. Dead Reckoning
6. TACAN

Note 5. Transmit in code as follows: W=Wind, T=Temperature, P=Pressure, R=Radar, 1=Positive, 2=Fair, 3=Poor. Example: WZPT1 = 1 Pressure Positive, Temperature Positive.

Items W-Z will be as determined by the specific agency with Storm Responsibility, i. e., JTWC in Western Pacific, NHC in Atlantic, Hq. Francisco in Eastern North Pacific, and HNO Honolulu in Central No.

New Record Low for Aircraft in ATLANTIC Hqn.

901 = 26.64" (error)

Aug 17 1815Z

NCS

Figure 8.33 Camille 901 mb drop later found to be in error.

There were not one but two extraordinary observations from that recon flight. In addition to MSLP of 901 mb, an unheard-of wind speed was estimated by the flight crew.

The equipment used to measure flight-level winds in 1969 on reconnaissance aircraft was less capable than that available today. There was a visual guideline for how to estimate wind speeds by observing the ocean surface from the aircraft. This was the method used to determine Camille's intensity on the recon flights. These photographs of the sea state at different wind velocities are still available at NHC today - in a folder, an aged and dog-eared series of photographs of actual sea states at different velocities (Figure 8.34). In 1969 this packet of photographs was an essential component of determining wind speeds in hurricanes by observations of the sea surface and one was on every recon flight (personal communication, Jeff Masters and Pete Black). Whether these photographs accurately depict sea surface states equivalent to the state velocity in knots is a little

questionable, but what the series of photos does show clearly is that as the wind speed increases, the sea surface becomes more and more covered with white foam, so that at higher wind speeds the sea surface would appear as a field of white.

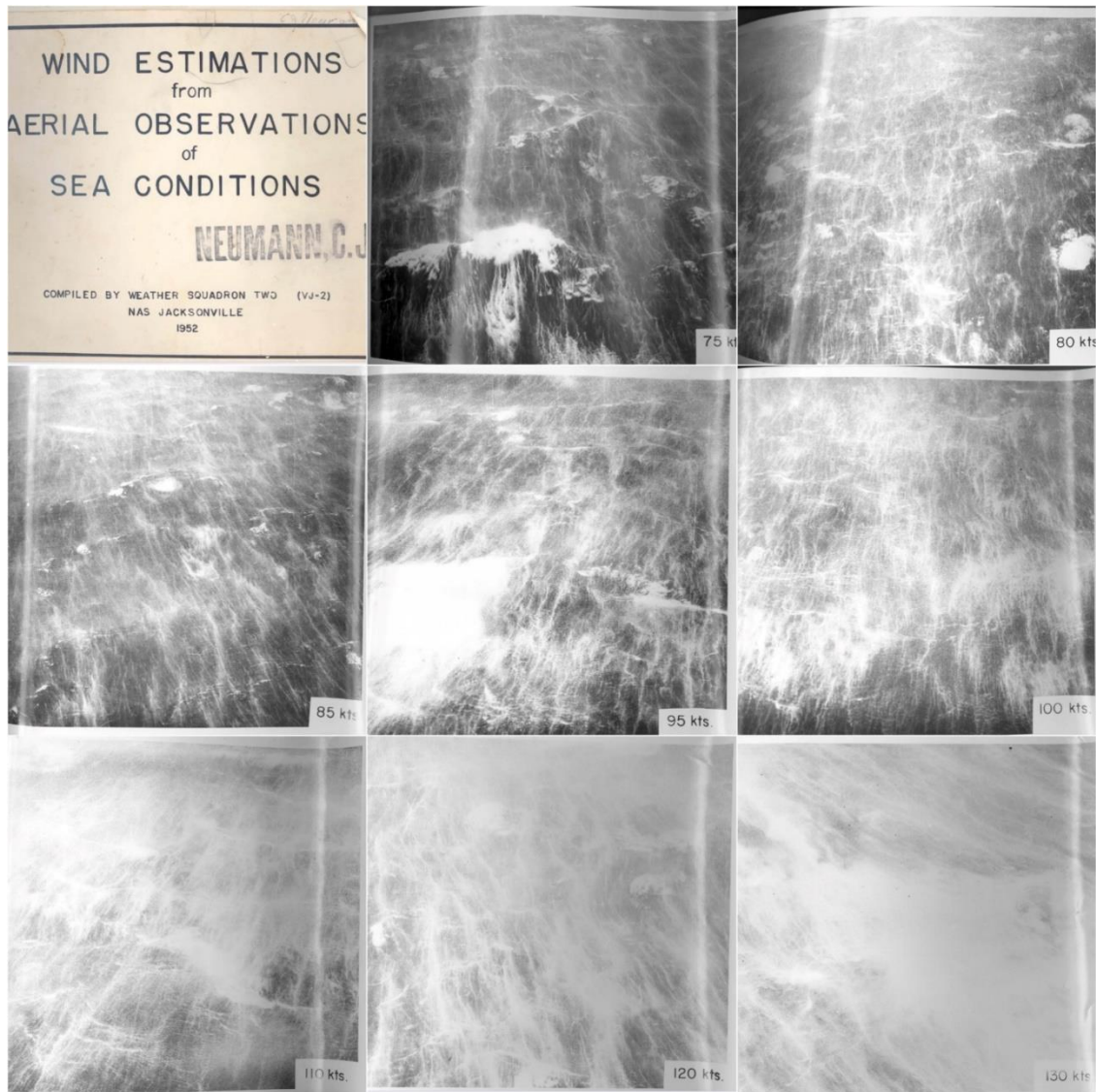


Figure 8.34 Photographs used for estimating surface wind speeds. These were referenced in visual observations seen in hurricane reconnaissance flights.

The wind estimate was based on an unusual visual observation of the sea state seen below the reconnaissance plane, flying at 700 mb (10,000 ft). To understand the proper context

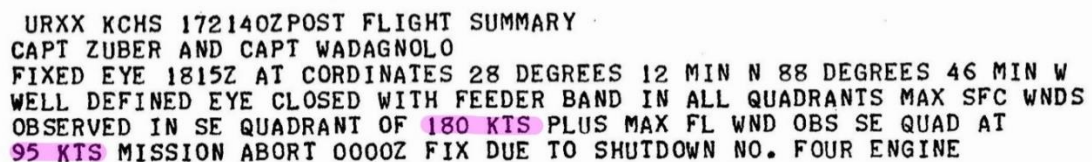
for the extreme wind estimate it is important to look at the complete quote from the co-pilot Robert Lee Clark (Clark, 1982) and partially referenced in Hurricane Watch (Sheets and Williams, 2001):

“Just as we were nearing the [eye] wall cloud *we suddenly broke into a clear area and could see the sea surface below*. What a sight! Although everyone on the crew was experienced except me, no one had seen the sea whip the winds like that before...Instead of the green and white splotches normally found in a storm, *the sea surface was in deep furrows running in the wind direction*. Variations of green and white mixed together, and the whole thing reminded me of looking down on a cotton field...The velocity was beyond the descriptions used in our training (up to about 150 mph) and far beyond anything we had ever seen. The best we could do was describe the scene to NHC via HF radio and offer a guess of winds over 200 mph on the surface. At our altitude of 10,000 ft, winds were recorded at 190 mph. Because no one at the NHC had ever seen a similar sea condition, they finally accepted our 190 mph as an accurate wind...By this time we were set for the eye wall penetration. We lurched our way in and again found the eye was full of clouds and very disturbed.” (Italics mine)

Note that the clear area likely referred to a moat associated with an ERC and as discussed in the reanalysis there was ample evidence for such an ERC. This was key information used to identify an ongoing ERC in the reanalysis (Kieper et al. 2016). However the reanalysis did not go into detail regards the sea state description used to provide the wind estimate. The "furrows" might not have been the best choice of word but what is clearly

understood is that parallel streaks of white foam and dark ocean surface alternated along the curved direction of the wind just outside the eyewall.

Also note the statement from Mr. Clark that 190 mph winds were seen at flight level is incorrect. Referencing the post flight summary (Figure 8.35), “WELL DEFINED EYE CLOSED ... MAX SFC WNDS OBSERVED IN SE QUADRANT OF 180 KTS PLUS MAX FL WNDS OBS SE QUAD AT 95 KTS,” the surface winds of 180 kt, equivalent to 205 mph, corresponds to the “guess of winds over 200 mph” in the quote by Clark. The lower flight level winds of 95 kt were due to the anemometers in the AF planes of the time which were problematic in eye wall conditions. NHC did not use the 180 kt surface winds estimated by the crew based on the sea surface state. It is unknown why 165 kt was selected when 180 kt surface winds were estimated by the reconnaissance crew, and this information is simply not recoverable.



URXX KCHS 172140ZPOST FLIGHT SUMMARY
CAPT ZUBER AND CAPT WADAGNOLO
FIXED EYE 1815Z AT CORDINATES 28 DEGREES 12 MIN N 88 DEGREES 46 MIN W
WELL DEFINED EYE CLOSED WITH FEEDER BAND IN ALL QUADRANTS MAX SFC WNDS
OBSERVED IN SE QUADRANT OF 180 KTS PLUS MAX FL WND OBS SE QUAD AT
95 KTS MISSION ABORT 0000Z FIX DUE TO SHUTDOWN NO. FOUR ENGINE

Figure 8.35 Flight summary from last reconnaissance flight into Camille.

So in summary the forecast 165 kt for Camille was based on two unusual observations: a presumed MSLP of 901 mb, later found to be in error, observed shortly after two other low MSLPs the previous day, 908 mb and 905 mb, and on an observed visual estimate of surface winds of 180 kt.

8.6 The Mystery of the Sea State Described in Camille's Extreme Wind Speeds

No camera was on board and so there exist no images of the previously unobserved sea state identified in Hurricane Camille from this recon flight. Over fifty years later, this description of a sea state near the eyewall of an intense hurricane that was labeled visually as being 180 kt is a forgotten mystery, and there is nothing in the literature about this unknown sea state and no photographs. However new evidence of this unknown sea state is now available and presented for the first time here.

This author observed what she believed to be this same phenomenon reviewing a video of the reconnaissance flight into EPAC 2015 Hurricane Patricia. At the time Patricia had a maximum intensity of 185 kt, making it the strongest hurricane on record in the combined EPAC and ATL basins (Kimberlain et al. 2016). There were several images in the video where parallel lines of foam on the water at the surface was visible under the eyewall and to some distance from the eyewall (Figure 8.37). These lines curved with the curve of the eyewall and so were parallel to the direction of the wind. And so a meteorological mystery can finally be set to rest: the crew did indeed see a sea state that had not been documented before.

Research found two more cases with a similar sea state. The first is a photograph by Peter Black on a NOAA reconnaissance flight into 1989 Hurricane Hugo when the plane was circling at a low altitude in the small eye (Figure 8.38, published with permission). The second photograph was taken inside the eyewall of 1988 Hurricane Gilbert by Jeff Masters (Figure 8.39, published with permission). At the time of the images, Hugo and Gilbert were intense Category 5 hurricanes as well.

One can go on the assumption that such parallel lines caused by the eyewall winds are visible from both just inside and just outside the eyewall, since they were seen in the moat in Camille just *outside* the eyewall. The photographic images in these three cases happened to be three Category 5 hurricanes, but no conclusions about the actual wind speeds associated with this sea state are currently possible.



Figure 8.36 Sea state under eyewall of 2015 EPAC Hurricane Patricia (NOAA Hurricane Hunter Facebook video 2015).



Figure 8.37 Sea state under eyewall of ATL 1989 Hurricane Hugo (published with permission of Peter Black, retired NOAA AOML).



Figure 8.38 Sea state under eyewall of ATL 1988 Hurricane Gilbert (published with permission of Jeff Masters).

8.7 Research Materials on Hurricane Camille

A tremendous amount of effort went into obtaining sources for both imagery and data for Hurricane Camille's reanalysis. A large variety of sources were examined. Not all material was relevant to the specific task of determining changes to the best track, which consists of location, MSLP, and intensity in kt for synoptic times and landfall times. Some material was useful in that it supported the validity of data (the two Breath interviews). Some provided indirect support for the landfall intensity (the Mississippi Test Facility report, NHC Camille Storm Wallet). The AMS 2014 Hurricanes and Tropical Meteorology presentation of the reanalysis provided additional material that is also included here. The Nash Roberts archived material were obtained during trip to New Orleans where the Monroe Library Special Collections Librarian graciously allowed me to photograph everything in their archives on Hurricane Camille, a process that took two full days. The oral histories were not scanned and online but USM quickly added them online so that I could download them.

Some of the sources of information for the reanalysis included:

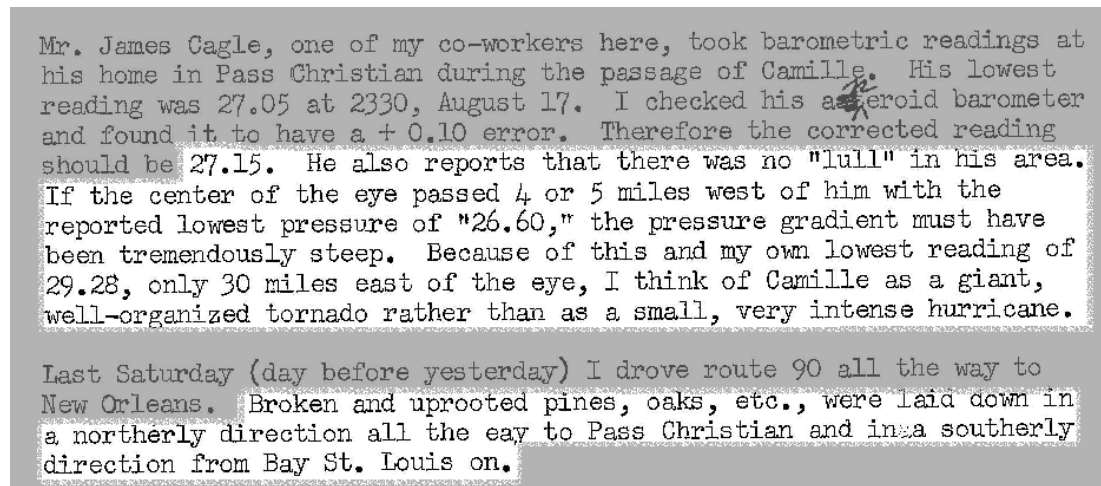
- The existing best track for Hurricane Camille and associated archived synoptic maps.
- The NHC storm wallet materials.
- Satellite and radar imagery obtained from the internet.
- Original archived radar imagery of Camille from the New Orleans WSR-57 radar provided by NCEI.

- Nash Roberts archive material on Hurricane Camille from the special collections of Monroe Library, Loyola University.
- All of the Camille related interviews from the University of Southern Mississippi Center for Oral History and Cultural Heritage, and an interview with Charles Breath's son and daughter.
- The Hancock Historical Society provided key photographs of the Breath house including the photograph of the damage three days after, replacing a very poor high contrast photocopy that had been my only previous source of the image.
- Cuba provided archive information on Camille including hand-drawn synoptic maps.
- A number of other items obtained from internet searches, including the Journal of Forestry report on Camille and the Aerospace Historian article on the flight into Camille.

8.8 Key Data Relevant to Landfall Parameters

The previous official low pressure reading of 909 mb for Camille's Mississippi landfall was made by Charles Breath (Kieper et al 2016). It is known that a log of readings leading up to landfall were taken by Mr. Breath ending with the 909 mb reading, but it is not known how that reading came to NHC in the 1969 time frame, and came to be the accepted low pressure documented in the best track. If the log was obtained by NHC it was lost as it was not among the storm wallet materials.

Review of the Camille storm wallet material uncovered two additional low pressures – a 917 mb taken in the eyewall in Pass Christian (east of the eye), documented in a letter to the NHC Deputy Director, and a second reading by Mr. Breath taken some minutes after the first reading, 904 mb, documented in the MTF (Mississippi Test Facility – now known as the Stennis Space Center – a rocket test facility) report. We don't know why the 904 reading was not in the best track, since the MTF report was submitted to NHC and was in the Camille Storm Wallet. These two additional pressure readings at landfall were important in analyzing the landfall intensity. It is notable that in both the letter to NHC regarding the 917 mb pressure, and in a hand-written note made by Nash Roberts and discovered in the papers that were donated to Loyola University, it was calculated that Camille had an extremely steep pressure gradient (Figures 8.40 and 8.41), indicative of a stronger storm.



Mr. James Cagle, one of my co-workers here, took barometric readings at his home in Pass Christian during the passage of Camille. His lowest reading was 27.05 at 2330, August 17. I checked his ~~aneroid~~^p aneroid barometer and found it to have a + 0.10 error. Therefore the corrected reading should be 27.15. He also reports that there was no "lull" in his area. If the center of the eye passed 4 or 5 miles west of him with the reported lowest pressure of "26.60," the pressure gradient must have been tremendously steep. Because of this and my own lowest reading of 29.28, only 30 miles east of the eye, I think of Camille as a giant, well-organized tornado rather than as a small, very intense hurricane.

Last Saturday (day before yesterday) I drove route 90 all the way to New Orleans. Broken and uprooted pines, oaks, etc., were laid down in a northerly direction all the way to Pass Christian and in a southerly direction from Bay St. Louis on.

Figure 8.39 Letter to NHC Deputy Director regards Camille's steep pressure gradient (NHC Camille Storm Wallet).

BILDAI 11:30-11:50 PM
28.94"
WAVEZAND - LAKE SHORE
BAY ST. LOUIS
26.61" 11:30 PM

- 2.33" IN 25 MILES
5.4 mb / km
or
3 mb / n mi
25 / 2.33 =
1/10" PER MILE

EXTREMELY STEEP
PRESSURE GRADIENT

Figure 8.40 Nash Roberts notes on Camille's steep pressure gradient. (special collections, Monroe Library, Loyola University, New Orleans, Nash Roberts archive papers)

In the 1960s it was common to have weather instruments in the home and common to maintain them for accuracy. But it is important to calibrate barometers to ensure the readings were accurate. The barometers that took the 917 mb and 909/904 mb readings were both calibrated (Kieper et al 2016). Additional confidence is provided by the two interviews with Charles Breath, the MTF interview that happened days later, and the Mississippi Oral History project interview taken ten years later (these included witness accounts of Camille survivors that were transcribed from taped interviews, a project of the Center for Oral History and Cultural Heritage at the University of Southern Mississippi), as well as an interview I did with Charles Breath's son and daughter for Weather Underground, which all showed that the approach to monitoring severe weather taken by Charles Breath was very similar to a meteorologist's approach. In the MTF interview he states in effect that the 904 mb was not the lowest reading he took but the lowest one he was able to recall quantitatively. He doesn't try to speculate on what the lower reading(s) might have been. And in the oral history interview conducted with Mr. Pyle, his reaction to the remarkable drop in pressure was not that of a layman, but that of someone who was familiar with marine barometer readings, having experience at sea, and similar to the reactions of a meteorologist:

Mr. Pyle: As Hurricane Camille started to come up in the gulf that Sunday afternoon, your wife here has got a panoramic view of the gulf right out in front of you, what did you see? What did it look like, the atmosphere?

Mr. Breath: I have had through the years a habit of watching the barometer. I go more by the barometer than anything else. And I started taking hourly checks on it. And then when the barometer really started to fall, regardless of what we saw out in the gulf or whatever, we started really getting ready to leave. We knew something bad was coming up.

...

Mr. Pyle: How aware were you of the time you were in the house before you left?

Mr. Breath: Oh, I was watching closely because I was keeping this log, see. I was watching it close. I had a log in the beginning at every hour. And then as it would start falling more, I'd have it every half hour and make a recording of it.

...

Mr. Pyle: When you saw the barometer, when you could actually see it dropping, what were your thoughts? It might be hard to recall. I was just wondering if you were thinking about your family, your house—

Mr. Breath: Well, I just couldn't believe what I was seeing. Actually, I just [couldn't believe it].

And in the interview with Charles Breath's children (personal communication) we learn more about the barometer readings. This interview is a little lengthy but included here in full to provide some historical perspective on the context of their experience during the eye passage, which ripped off much of their roof. Photographs of the home prior to and after Camille are shown in Figures 8.42 and 8.43. The post-Camille image was taken three days later and show temporary repairs to the roof and the height of the surge, which washed up debris around the home. The home was completely washed away by Katrina's surge in 2005 and an open expanse of lawn and hint of the path to the front door are all that remain, but the house sign is still there and the Breaths resided in a home further back on the property after Hurricane Katrina.

The Breath home, prior to Katrina, was the third-oldest home in Bay St. Louis. It had been built in 1820, on what is known as North Beach, and had been owned by the Breath family for 110 years. Underneath the home was a brick cellar (very unusual in the coastal South) that the historical society believed was all that remained of what was originally a fort, on that location. In front of the home was a camellia tree over twenty feet tall, that had been planted around 1880. The home faces the bay on the bluff just south of the modern bridge that connects Hwy 90 to Pass Christian, along with several other homes owned by the Breath family, which were to the west of the bay front home, along Breath Lane. Charles A. Breath Jr and III were born there, and five generations of Breaths had lived in that home. Hurricane Katrina totally destroyed the home along with five others along the Breath property, including the historic barometer (and also possibly the log).

The 909 mbar reading had been taken by Charles A. Breath, Jr. I recently spoke to Charles A. Breath III, and he recalled to me, "Daddy was in the boat business all his life. He was an old salt! He had a sailboat that he named Romac, which was a ketch built by Jacky Jack Covacevich. Weather meant a lot to him. Nash Roberts was his hero in predicting the weather."

Jacky Jack owned a well-known boatyard in Biloxi Back Bay and built many of the ships used in the seafood industry centered on Biloxi Point Cadet at that time in history.

Nash Roberts was a well-known NOLA meteorologist who had a penchant for correctly predicting landfall locations of hurricanes. He had a brother, Ep Roberts, who owned a store that sold scientific instruments. Ep was also a meteorologist, and would sometimes fill in for Nash if he had to miss a broadcast.

Charles Breath told me his recollection from what his father had said, was that the eye passed over Bay St. Louis, the bay, and Pass Christian. He had been in the service at that time, but his sister, Sue, rode out the storm with their parents.

As Camille was approaching the Louisiana and Mississippi Gulf Coasts, Sue Breath McGuire, who was in her mid-twenties and living in NOLA with a roommate, was told by her father to return home to BSL, and bring her roommate, because NOLA was like a saucer and was not safe in the event of a strong hurricane; BSL would be much safer. Sue recalled that Nash Roberts had said this storm was going to be a bad one.

So she and the roommate packed up and got in the car and drove east, one of the few cars to do so, as most everyone was driving west to leave the MS coast. She said her dad always had his hurricane precautions, and boarded up the windows with removable shutters. The breakfast area of the home had a magnetic hurricane tracking map, where the magnets would be moved to the new location every time they would get the current coordinates of the storm. Her father had several barometers, but one very good one that he was always careful to keep calibrated, and no one was allowed to touch it. For days before the storm, the barometric pressure would start dropping, and he would keep a log starting at that time, always noting the time and pressure.

When Camille came in 1969, Charles Breath Jr. was 65. Sue said of her father, "Daddy, being the sailor that he was, on the coast all the time, was always so conscious of the weather." He had been logging the weather for several days prior to Camille's landfall, and that evening he logged pressure readings every 15 minutes or so, tapping the glass to make sure the needle was giving the correct reading. Sue said she could tell her father was getting nervous as the pressure dropped, sometimes rubbing his head after noting a reading.

Sue recalled that it was awful being in such a storm at night. She said that the cotton caulking around the doors would whistle when the wind picked up. At one point during the evening the attic stairway blew down, and when they went to see

what had happened, they were hit in the face with salt water, because the wind had blown off the front gable of the roof. When the eye came, they left the house to move to one further back from the bluff. Water had never come more than halfway up the walkway from the bay, yet when they went out the back door, they walked into knee deep water. She recalled that her father carried the precious barometer, wrapped in a cloth, and her mother, their dachshund, as she, her roommate, and her roommate's sister, walked with them to the adjacent house on their property. She said the low reading that was the official low pressure was taken just before the eye, before they left the main house.

Afterwards, she didn't recall how, Nash Roberts came to know of the reading, and the barometer was carefully packaged up and sent to his brother Ep Roberts store, and found to be accurate. After this, Charles Breath recalled, a group from Nash Roberts came to Bay St. Louis and sat down and talked with his father about the readings.

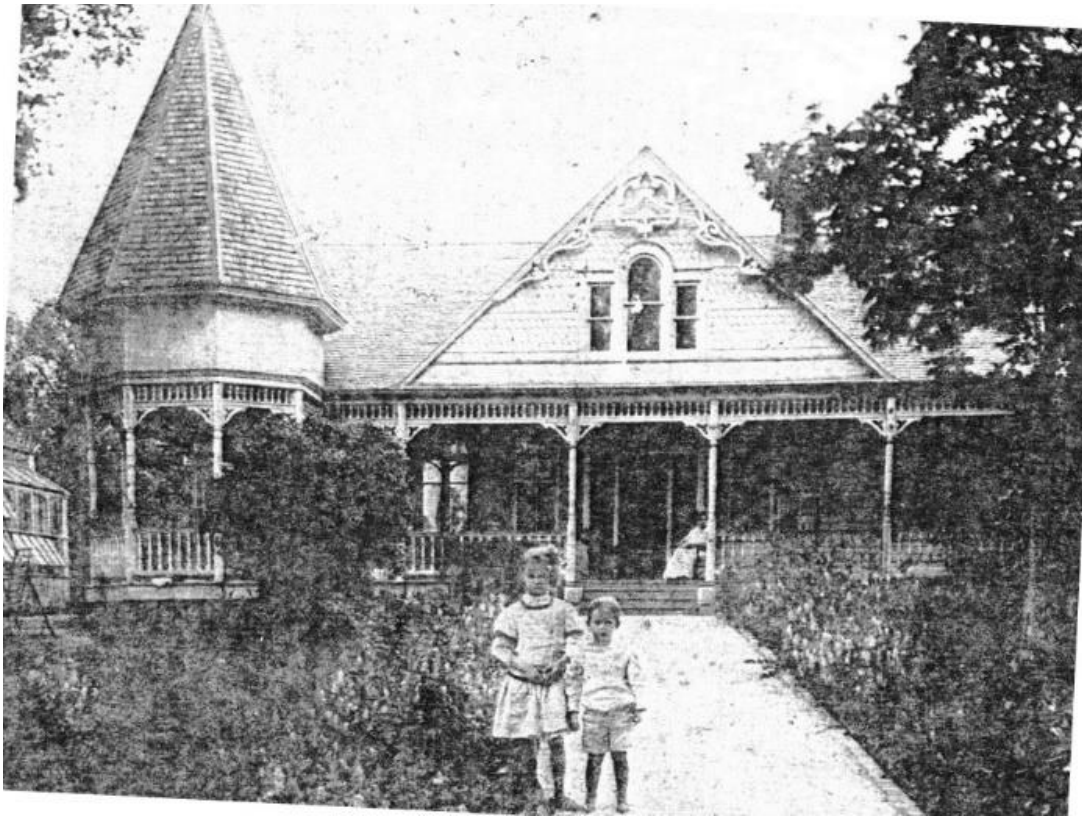


Figure 8.41 Photo of the Breath home early 1900s. The central portion of the home was built in 1818 for Judge Monet, and the turreted porch and front central gable were added in 1909. (Hancock County Historical Society, Bay St. Louis, MS).



Figure 8.42 Photo of the Breath home three days after the landfall of Hurricane Camille (Hancock County Historical Society, Bay St. Louis, MS).

We can imagine the difficulty Charles Breath had taking additional readings in a house further back from their home with no electricity, probably having to use a flashlight or light a match to see the readings on the barometer. This is probably why he recalled taking the 904 mb reading but adding that "was possibly not the lowest he observed," wanting to be accurate. Perhaps there was a lower reading that he was not able to see well enough to be absolutely confident in the number, before the barometer began rising, but we do know that he did get at least the one reading, the 904 mb, in the eye, after evacuating to another house on his property, and it is likely the pressure may have fallen a few millibars lower than that. The reanalysis determined an MSLP of 900 mb in the eye at landfall so a reading slightly lower than 904 mb would have been possible. But the

known 904 mb reading was very important in helping to determine the landfall pressure using the reanalysis techniques.

The MTF report noted detailed barometric pressure readings. The MTF was located to the northwest of the eye at landfall and the eye did not pass over the facility. The lowest reading at the weather station building was 28.06 in. Hg. (950 mb) at 11:15pm CDT and 28.00 in. Hg. (948 mb) at 11:55pm CDT at the S-II Test Stand one mile southeast of the weather station.

The report also documents the anemometer readings at these locations. The observations in the MTF report note that the weather station anemometer, which was at a height of 47 feet, was blown off the pole at 8:58pm CDT with a peak gust prior to failure of 49 kt. At the S-II Test Stand, the anemometer, at a height of 204 ft, recorded 100 mph gusts starting at 10:42pm, and subsequently higher gusts, with the wind gauge breaking at 11:35pm, with the lowest pressure reading occurring 20 minutes later.

No anemometers recorded Camille's maximum wind speeds but there were telling pieces of information in the MTF report from the NHC Camille Storm Wallet to support significant wind speeds at the surface from Camille. This is not always the case as in some tropical cyclones the highest winds don't make it down to the surface or only do so intermittently as gusts. The MTF report contains personal observations from the one of the two meteorologists who wrote the report, John Rhyne:

From personal observations of the effects of previous hurricanes, the letup from occasional strong hurricane gusts was not evidenced in Camille. During the approach of the height of the storm, the wind was of a steady nature with no momentary letups. It must be noted that I was in an acoustically blast proof building.

...

In February 1957 this writer observed hurricane damage at Swan Island, West Indies occasioned by Hurricane Janet in 1955. I observed the 6,000 coconut trees that were all snapped off at a height of 12 to 15 feet. At the time I observed them only the trunks were left standing. In my opinion there are forest areas in and around the MTF Weather Station that suffered similar damage.

...

In the Westchester Heights and Pondorosa Subdivisions [in Picayune, MS] some substantial \$20,000 to \$30,000 homes were completely destroyed (not tree damage) and other homes next to them undamaged.

Mr. Rhyne attributed the home damage to tornadoes associated with Camille's core winds. We know today that is not possible but that this type of damage, seen in 1992 Hurricane Andrew south of Miami (as a Category 5) and in 1989 Hurricane Hugo over St. Croix (as a Category 4), can be attributed to wind streaks, which occur in strong tropical cyclones, and are produced by boundary layer rolls (Wurman and Winslow, 1998).

A report from the Journal of Forestry (Touliatos and Roth 1971) mapped the extensive forest damage from Camille. This is overlaid with the track of the center of the eye and the track that the reanalysis determined for the radius of maximum winds (RMW) at landfall based on eye diameter, showing that the most damage was along the path of the strongest winds (Figure 8.44).

Observations from Kenneth Seal, the meteorologist in charge, included:

During 2 the prior hurricanes [experienced, Audrey and Abby] definite lulls or decrease in wind velocity was noted. Not the case in Hurricane Camille. From approximately 10:30 pm CDT Sunday until 2:00am CDT Monday a continuous velocity with a definite absence of lulls was noted. If there were any lulls they were indiscernible due to high jet like noise of the wind. Indications of extremely high wind velocities were noted everywhere. Trees were cleanly snapped from within heights of 10 to 75 feet. The diameters of the snapped trees ranged upward

to 3 feet. The possibility of tornadoes snapping all of the trees is low. Entire groves ranging in size from 1 to 20 acres had felled trees amounting to as much as 70%...awnings were broken loose and took the shape of the object upon which they were blown, and buildings of a reinforced nature even sustained wind damage (not caused by falling trees or flying objects). All indices either observational or impressional leads this author to believe that the highest winds were 140 knots at the Weather Station. Perhaps somewhat higher.

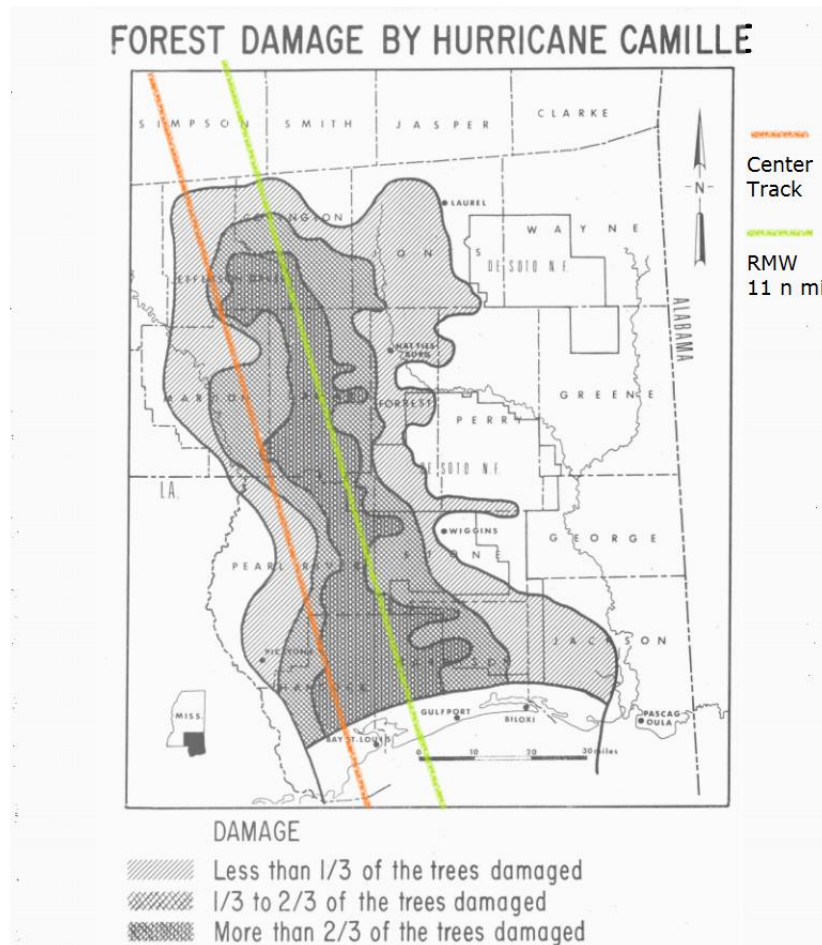


Figure 8.43 Forest damage from Camille overlaid with the track and RMW. This was determined from the reanalysis, indicating the most significant damage was along the swath of highest winds.

The reanalysis determined winds of 150 kt at landfall. In addition, excerpts from notes from personnel at NHC and taken from phone conversations and typed ("JRG" with

CHAPTER 9. Conclusions

This research expanded the understanding of the 37color imagery of tropical cyclones, by improved identification of precipitation types derived from a conceptual model. Patterns of warm precipitation reveal processes including rapid intensification and eyewall replacement cycles only observed on the 37color and not on other PMW imagery from the NRLMRY PMW archive. These are identified by early eye development of a symmetric shallow convective ring observed as cyan on the 37color.

A conceptual model of the 37color imagery noted that the colors corresponded to separate vertical layers of the atmosphere and that color combinations on the image related to different combinations of rain and ice. This model also distinguished between stratiform and convective rain, and *identified the cyan color as being shallow and moderate convection: "SAM."* This was validated by evaluating radar cross-sections of tropical cyclones from both the TRMM PR and by NWS WSR-88D ground-based radar. *This is important because in general the role of SAM in TC development has been under-examined, and SAM may play an important role in understanding TC dynamics.*

Complicating understanding of the nature of convection in TC, the TRMM PR 2A23 product that was used in many studies that aggregated data from the PR overpasses of tropical cyclones, identified most shallow precipitation in TC as stratiform, not convective.

A feature in 37color imagery was found that was important in diagnosing the potential for rapid identification (Kieper and Jiang 2012). A symmetric ring of warm precipitation, the cyan color, is observed, indicating a nascent eye, usually with a partial outer arc of an

ice signature corresponding to tilted deep convection and partial development of a secondary circulation. This is likely convective precipitation as the area immediately outside the warm center is an area of surface convergence. Because symmetric heating is important in TC intensification, it is likely this is a factor in the precipitative ring appearing at the onset of a period of RI. Since warm precipitation in the cyan color is shown by the conceptual model and radar cross-sections to be shallow and moderate convection, *this ring can now be identified as the SAM ring.*

In Kieper and Jiang 2012, using 37color TC overpasses from the Atlantic basin between 2003 and 2007, all rings were identified. With SHIPS as a discriminator for a favorable environment, a forecast methodology for RI (30 kt in 24 hr) yielded a POD of 75% and a FAR of 9%. The forecast method uses the first ring occurring during an RI event, and the particular 24-hour period following the appearance of the ring can be the period with the highest rate of intensity increase during the entire RI event.

An additional case study primarily in the Atlantic basin identified TC between 2008 and 2019 where a SAM ring occurred prior to a 24-hour period of RI, documenting 37 instances of RI preceded by a SAM ring. Examples of the SAM ring from the 2003-2019 period in the Atlantic, and examples from the East Pacific, West Pacific, South Pacific, South Indian Ocean, and Southwest Indian Ocean TC basins are shown.

It is suggested that some improvement in NHC intensity forecasts between about 2010-2015 and perhaps later can be attributed to use of the SAM ring in intensity forecasting where there is the potential for RI.

The 37color imagery revealed eyewall replacement cycles (ERCs) occurring in developing TC. ERCs occur in mature TC, so these are termed "early ERCs." They produce the same result, but are different in these key characteristics:

- Early development
- Lower initial intensity
- Small inner eye size
- Stationary Band Complex (SBC)
- SEF generated from the principal band
- Part of a longer RI event
- No intensity decrease during the ERC completion
- Major hurricane strength at ERC completion

This process also begins with a SAM ring development of a small eye in a SBC, and the parallel development of the outer secondary eyewall originating from the head of the principal band suggests that the same processes in the SBC are responsible for both.

Both the RI indicator and early ERC TC processes where the 37color shows SAM rings indicating early eye development identify periods of rapid intensification in favorable environments. Both of these processes can affect intensity forecasts. This suggests shallow and moderate convection is important in TC, especially in the case of symmetric SAM rings indicating developing eyes. Although additional areas of research were pursued, this result is the most significant of the conclusions in this research.

The SAM rings of developing eyes suggest that there is a significant contribution of shallow and moderate convection in developing stages before the TC matures. This could have broader implications beyond eye development. The SAM rings, while not a mature eye, can play a similar role in terms of vortex dynamics. The definition of a TC eye is based on historical understanding of a clear center seen from the ground, and in

modern tropical meteorology, able to be observed on geostationary satellite imagery (visible, infrared, and water vapor). Consequently the SAM ring has been referred to as a "microwave eye" and "low-level eye." The role of the SAM rings in eye development might be motivation for modernizing the definition of the eye.

A Precipitative Intensity Estimate (PIE) based on 37color precipitative patterns of TC is in an early stage of development. It is intended to provide a complement to the Dvorak technique prior to eye formation, by categorizing precipitative structures by intensity in both favorable and sheared environments.

The need for a passive microwave image repository is identified, that allows the end user to peruse the imagery temporally in order to view the progression of the tropical cyclone life cycle. The dwindling availability of 37color imagery, noted by forecasters, is a loss of a unique perspective of TC, considering the importance noted here of the role of SAM in tropical cyclone development.

The 1969 Camille reanalysis (Kieper et al. 2015) finished the reanalysis of known Category 5 landfalls in the United States. Camille's landfall intensity had long been uncertain due to lack of accurate wind measurements in the core. Whether Camille was a Category 5 at landfall was in question. Camille was a likely candidate for an eyewall replacement given its intensity while over the Gulf of Mexico. The reanalysis of Camille employed knowledge of TCs that was not known in 1969 (e.g. ERCs). Techniques of interpreting modern satellite images were applied to images of Camille to determine that an ERC occurred.

The work included extensive research of NHC's Camille Storm Wallet, several days spent at Loyola University Special Collections in New Orleans, LA, reviewing the papers of meteorologist Nash Roberts, interviews, internet searches, participating in the best track reanalysis and lead writer for the publication. This research uncovered new landfall pressure data that aided the revision of the landfall intensity. The Kaplan DeMaria inland decay model validated the new proposed landfall intensity. Techniques of interpreting modern satellite images were applied to visible satellite imagery of Camille to determine that an ERC occurred and to estimate how the intensity was affected. The reanalysis showed that Camille weakened during the ERC but subsequently re-intensified after the ERC completed, until landfall, and was a Category 5 at landfall with maximum winds of 150 kt. Photographs and video from modern reconnaissance flights into three Category 5 hurricanes had near eyewall sea surface characteristics similar to an unusual and previously unseen sea state described by the last reconnaissance flight into Camille, solving a mystery as to what that flight observed.

REFERENCES

- Awaka, J., Iguchi, T., Kumagai, H., & Okamoto, K. I. (1997, August). Rain type classification algorithm for TRMM precipitation radar. In IGARSS'97. 1997 IEEE International Geoscience and Remote Sensing Symposium Proceedings. Remote Sensing-A Scientific Vision for Sustainable Development (Vol. 4, pp. 1633-1635). IEEE.
- Beven, J., 2007: Tropical cyclone report: Hurricane Daniel, 16-26 July 2006. NOAA/NHC, 9 pp. https://www.nhc.noaa.gov/data/tcr/EP052006_Daniel.pdf
- Beven, J. L., II, R. Berg, and A. Hagen, 2019: National Hurricane Center Tropical Cyclone Report, Hurricane Michael (7–11 October 2018). AL142018, National Hurricane Center, 86 pp., https://www.nhc.noaa.gov/data/tcr/AL142018_Michael.pdf
- Blake, E. S., 2018: Tropical cyclone report: Hurricane Lee, 14-30 September 2017. NOAA/NHC, 16 pp. https://www.nhc.noaa.gov/data/tcr/AL142017_Lee.pdf
- Brennan, M. J., 2009: Tropical cyclone report: Hurricane Lee, 7-12 September 2009. NOAA/NHC, 13 pp. https://www.nhc.noaa.gov/data/tcr/AL072009_Fred.pdf
- Brown, D. P., 2016: Tropical cyclone report: Hurricane Gaston, 22 August-2 September 2016. NOAA/NHC, 19 pp. https://www.nhc.noaa.gov/data/tcr/AL072016_Gaston.pdf
- Brown, D. P., 2019: Tropical cyclone report: Hurricane Jerry, 17-24 September 2019. NOAA/NHC, 17 pp. https://www.nhc.noaa.gov/data/tcr/AL102019_Jerry.pdf
- Cecil, D. J., & Zipser, E. J. (1999). Relationships between tropical cyclone intensity and satellite-based indicators of inner core convection: 85-GHz ice-scattering signature and lightning. *Monthly weather review*, 127(1), 103-123.
- Clark, Robert Lee. "Flight into Camille." *Aerospace Historian* 29, no. 2 (Summer/June 1982): 74-80. <https://www.jstor.org/stable/44523713>
- DeMaria M, Franklin JL, Onderlinde MJ, Kaplan J. Operational Forecasting of Tropical Cyclone Rapid Intensification at the National Hurricane Center. *Atmosphere*. 2021; 12(6):683. <https://doi.org/10.3390/atmos12060683>
- Dunion, J. P., & Marron, C. S. (2008). A reexamination of the Jordan mean tropical sounding based on awareness of the Saharan air layer: Results from 2002. *Journal of Climate*, 21(20), 5242-5253.
- Dvorak, V. F., 1984: Tropical cyclone intensity analysis using satellite data. NOAA Tech. Rep. NESDIS 11, 47 pp.
- Eastin, M. D., & Link, M. C. (2009). Miniature supercells in an offshore outer rainband of Hurricane Ivan (2004). *Monthly weather review*, 137(7), 2081-2104.
- Edson, R., 2014: Current methods of tropical cyclone analysis using microwave imagery and data. 31st Conf. on Hurricanes and Tropical Meteorology, San Diego, CA, Amer. Meteor. Soc., 16A.5, <https://ams.confex.com/ams/31Hurr/webprogram/Paper245061.html>.

- Emanuel, K. A. (1986). An air-sea interaction theory for tropical cyclones. Part I: Steady-state maintenance. *Journal of Atmospheric Sciences*, 43(6), 585-605.
- Franklin, J. L., Black, M. L., & Valde, K. (2003). GPS dropwindsonde wind profiles in hurricanes and their operational implications. *Weather and Forecasting*, 18(1), 32-44., https://journals.ametsoc.org/view/journals/wefo/18/1/1520-0434_2003_018_0032_gdwpjh_2_0_co_2.xml
- Funk, A., Schumacher, C., & Awaka, J. (2013). Analysis of rain classifications over the tropics by version 7 of the TRMM PR 2A23 algorithm. *Journal of the Meteorological Society of Japan. Ser. II*, 91(3), 257-272.
- Hawkins, J., 2000: Automated tropical cyclone intensities utilizing objective Dvorak input to passive microwave algorithm. 24th Conf. on Hurricanes and Tropical Meteorology, Fort Lauderdale, FL, Amer. Meteor. Soc., P1.39, https://ams.confex.com/ams/last2000/techprogram/paper_12881.htm
- Hawkins, J. D., Lee, T. F., Turk, J., Sampson, C., Kent, J., & Richardson, K. (2001). Real-time Internet distribution of satellite products for tropical cyclone reconnaissance. *Bulletin of the American Meteorological Society*, 82(4), 567-578.
- Hawkins, J. D., Helveston, M., Lee, T. F., Turk, F. J., Richardson, K., Sampson, C., ... & Wade, R. (2006, April). Tropical cyclone multiple eyewall configurations. In *Preprints, 27th Conf. on Hurricanes and Tropical Meteorology*, Monterey, CA, Amer. Meteor. Soc. B (Vol. 6).
- Hence, D. A., & Houze Jr, R. A. (2011). Vertical structure of hurricane eyewalls as seen by the TRMM Precipitation Radar. *Journal of the Atmospheric Sciences*, 68(8), 1637-1652.
- Houze Jr, R. A. (2010). Clouds in tropical cyclones. *Monthly Weather Review*, 138(2), 293-344.
- Johnson, R. H., Rickenbach, T. M., Rutledge, S. A., Ciesielski, P. E., & Schubert, W. H. (1999). Trimodal characteristics of tropical convection. *Journal of climate*, 12(8), 2397-2418.
- Kaplan, John, and Mark DeMaria. "A simple empirical model for predicting the decay of tropical cyclone winds after landfall." *Journal of Applied Meteorology and Climatology* 34, no. 11 (1995): 2499-2512.
- Kieper, M. E., & Jiang, H. (2012). Predicting tropical cyclone rapid intensification using the 37 GHz ring pattern identified from passive microwave measurements. *Geophysical Research Letters*, 39(13). - <https://agupubs.onlinelibrary.wiley.com/doi/epdf/10.1029/2012GL052115>
- Kieper, M. E., & Jiang, H. (2012, December). Using the 37 Color Composite PMW for Rapid Intensification Forecasts of Tropical Cyclones. In *AGU Fall Meeting Abstracts* (Vol. 2012, pp. A13L-0351).

- Kieper, Margaret E., Christopher W. Landsea, and John L. Beven, II. " A Reanalysis of Hurricane Camille", *Bulletin of the American Meteorological Society* 97, 3 (2016): 367-384, accessed Apr 21, 2021, <https://doi.org/10.1175/BAMS-D-14-00137.1>
- Kimberlain, T. B. and Zelinsky, D. A., 2012: Tropical cyclone report: Hurricane Michael, 3-11 September 2012. NOAA/NHC, 13 pp.
https://www.nhc.noaa.gov/data/tcr/AL132012_Michael.pdf
- Kimberlain, T. B., E. S. Blake, and J. P. Cangialosi, 2015: Hurricane Patricia. National Hurricane Center Tropical Cyclone Rep. EP202015, 32 pp.
https://www.nhc.noaa.gov/data/tcr/EP202015_Patricia.pdf
- Kimberlain, T. B. and Latta, A. S., 2016: Tropical cyclone report: Hurricane Nicole, 4-18 October 2016. NOAA/NHC, 29 pp.
https://www.nhc.noaa.gov/data/tcr/AL152016_Nicole.pdf
- Knaff, J. A., Brown, D. P., Courtney, J., Gallina, G. M., & Beven, J. L. (2010). An evaluation of Dvorak technique-based tropical cyclone intensity estimates. *Weather and Forecasting*, 25(5), 1362-1379.
- Kodama, Y. M., Katsumata, M., Mori, S., Satoh, S., Hirose, Y., & Ueda, H. (2009). Climatology of warm rain and associated latent heating derived from TRMM PR observations. *Journal of climate*, 22(18), 4908-4929.
- Kossin, J. P., & Sitkowski, M. (2009). An objective model for identifying secondary eyewall formation in hurricanes. *Monthly Weather Review*, 137(3), 876-892.
- Lee, T. E., Hawkins, J. D., Turk, F. J., Richardson, K., Sampson, C., & Kent, J. (1999). Tropical cyclone images now can be viewed "live" on the Web. *Eos, Transactions American Geophysical Union*, 80(50), 612-614.
- Lee, T. F., Turk, F. J., Hawkins, J., & Richardson, K. (2002). Interpretation of TRMM TMI images of tropical cyclones. *Earth Interactions*, 6(3), 1-17.
- Mapes, B. E. (1993). Gregarious tropical convection. *Journal of Atmospheric Sciences*, 50(13), 2026-2037.
- Mayfield, M. (1992). Hurricane Bob Preliminary Report. National Hurricane Center, Miami, Fla, 4.
- Murillo, S. T., Lee, W. C., Bell, M. M., Barnes, G. M., Marks, F. D., & Dodge, P. P. (2011). Intercomparison of ground-based velocity track display (GBVTD)-retrieved circulation centers and structures of Hurricane Danny (1997) from two coastal WSR-88Ds. *Monthly Weather Review*, 139(1), 153-174.
- NHC Camille Preliminary Report, NHC Camille Storm Wallet, 1969.
- Olander, T. L., & Velden, C. S. (2019). The Advanced Dvorak Technique (ADT) for estimating tropical cyclone intensity: Update and new capabilities. *Weather and Forecasting*, 34(4), 905-922.

- Pasch, R. J. (1997). Preliminary report: Hurricane Danny 16–26 July 1997. National Hurricane Center. <http://www.nhc.noaa.gov/1996danny.html>.
- Pasch, R. J., Blake E. S., Cobb H. D. III, and Roberts D. P., 2006: Tropical cyclone report: Hurricane Wilma, 15–25 October 2005. NOAA/NHC, 27 pp.
https://www.nhc.noaa.gov/pdf/TCR-AL252005_Wilma.pdf
- Pasch, R. J., 2021: National Hurricane Center Tropical Cyclone Report, Hurricane Laura (in preparation)
- Rappaport, Edward N., James L. Franklin, Andrea B. Schumacher, Mark DeMaria, Lynn K. Shay, and Ethan J. Gibney. "Tropical cyclone intensity change before US Gulf Coast landfall." *Weather and forecasting* 25, no. 5 (2010): 1380-1396.
- Rogers, Robert F., Sim Aberson, Michael M. Bell, Daniel J. Cecil, James D. Doyle, Todd B. Kimberlain, Josh Morgerman, Lynn K. Shay, and Christopher Velden. "Rewriting the Tropical Record Books: The Extraordinary Intensification of Hurricane Patricia (2015)", *Bulletin of the American Meteorological Society* 98, 10 (2017): 2091-2112, accessed Apr 21, 2021, <https://doi.org/10.1175/BAMS-D-16-0039.1>
- Shapiro, L. J., & Willoughby, H. E. (1982). The response of balanced hurricanes to local sources of heat and momentum. *Journal of the Atmospheric Sciences*, 39(2), 378-394.
- Schumacher, C., & Houze, R. A. (2003). The TRMM precipitation radar's view of shallow, isolated rain. *Journal of Applied Meteorology and Climatology*, 42(10), 1519-1524.
- Sheets, B., and J. Williams, 2001: Hurricane Watch: Forecasting the Deadliest Storms on Earth, Vintage Books, pp. 152-153
- Shenk, W. E., and E. B. Rodgers, 1978: Nimbus 3/ATS 3 observations of the evolution of Hurricane Camille. *J. Appl. Meteor.*, 17, 458-476, doi:10.1175/1520-0450(1978)017<0458:NOOTEO>2.0.CO;2.
- Simpson, J., Halverson, J. B., Ferrier, B. S., Petersen, W. A., Simpson, R. H., Blakeslee, R., & Durden, S. L. (1998). On the role of “hot towers” in tropical cyclone formation. *Meteorology and Atmospheric Physics*, 67(1), 15-35.
- Sitkowski, M., Kossin, J. P., & Rozoff, C. M. (2011). Intensity and structure changes during hurricane eyewall replacement cycles. *Monthly Weather Review*, 139(12), 3829-3847.
- Smith, R. K., 1981: The cyclostrophic adjustment of vortices with application to tropical cyclone modification. *Journal of Atmospheric Sciences* 38 (9), 2021-2030
- Smyth, T. J., & Illingworth, A. J. (1998). Radar estimates of rainfall rates at the ground in bright band and non-bright band events. *Quarterly Journal of the Royal Meteorological Society*, 124(551), 2417-2434.

- Spencer, R. W., Goodman, H. M., & Hood, R. E. (1989). Precipitation retrieval over land and ocean with the SSM/I: Identification and characteristics of the scattering signal. *Journal of Atmospheric and Oceanic Technology*, 6(2), 254-273.
- Stewart, S. R., 2016: Tropical cyclone report: Hurricane Danny, 18-24 August 2015. NOAA/NHC, 18 pp. https://www.nhc.noaa.gov/data/tcr/AL042015_Danny.pdf
- Sullivan, C. L., 1986: Hurricanes of the Mississippi Gulf Coast, (Biloxi, Miss.: Gulf Publishing, 1986), call number QC959.G84 S94x 1986 (Cook, McCain, Cox)
- Touliatos, P. & Roth, E. (1971) Hurricanes and Trees: Ten Lessons from Camille, *Journal of Forestry*, Volume 69, Issue 5, May 1971, Pages 285–289, <https://doi.org/10.1093/jof/69.5.285>
- USWB/MTF, Hurricane Camille Enters Mississippi, NHC Camille Storm Wallet, 1969.
- Velden, C., Harper, B., Wells, F., Beven, J. L., Zehr, R., Olander, T., ... & McCrone, P. (2006). The Dvorak tropical cyclone intensity estimation technique: A satellite-based method that has endured for over 30 years. *Bulletin of the American Meteorological Society*, 87(9), 1195-1210.
- Wang, Y. F., & Tan, Z. M. (2020). Outer Rainbands–Driven Secondary Eyewall Formation of Tropical Cyclones. *Journal of the Atmospheric Sciences*, 77(6), 2217-2236.
- Weinkle, J., Landsea, C., Collins, D. et al. Normalized hurricane damage in the continental United States 1900–2017. *Nat Sustain* 1, 808–813 (2018). <https://doi.org/10.1038/s41893-018-0165-2>
- Willoughby, H. E., J. A. Clos, and M. B. Shoreibah, 1982: Concentric eyewalls, secondary wind maxima, and the development of the hurricane vortex. *J. Atmos. Sci.*, 39, 395–411.
- Willoughby, H. E., Marks, F. D., & Feinberg, R. J. (1984). Stationary and moving convective bands in hurricanes. *Journal of the Atmospheric Sciences*, 41(22), 3189-3211.
- Willoughby, H. E., 1988: The dynamics of the tropical cyclone core. *J. Aust Meteor Soc.*, 36, 183–191 (text of an invited review paper at the International Conference on Tropical Meteorology held at the University of Queensland, 4–8 July 1988).
- Wurman, J., & Winslow, J. (1998). Intense sub-kilometer-scale boundary layer rolls observed in Hurricane Fran. *science*, 280(5363), 555-557.
- Zelinsky, D. A. (2019). National Hurricane Center Tropical Cyclone Report: Hurricane Lorenzo (AL132019).
- Zhang, F., Tao, D., Sun, Y. Q., & Kepert, J. D. (2017). Dynamics and predictability of secondary eyewall formation in sheared tropical cyclones. *Journal of Advances in Modeling Earth Systems*, 9(1), 89-112.

VITA

MARGARET ELIZABETH KIEPER

1974-1979	S. B., Art and Architecture Massachusetts Institute of Technology Cambridge, Massachusetts
2012 -2021	Doctoral Candidate Florida International University Miami, Florida

PUBLICATIONS AND PRESENTATIONS

AMS 28th Conference on Hurricanes and Tropical Meteorology, 2008, A Technique for Anticipating Initial Rapid Increases in Intensity in Tropical Cyclones, Using 37 GHz Microwave Imagery, Extended Abstract Appendix I

AMS 29th Conference on Hurricanes and Tropical Meteorology, 2010, Tropical Cyclone Morphology and Phenomenology as Depicted in Passive Microwave Imagery

Kieper, M. E., & Jiang, H. (2012). Predicting tropical cyclone rapid intensification using the 37 GHz ring pattern identified from passive microwave measurements. *Geophysical Research Letters*, 39(13).

AMS 30th Conference on Hurricanes and Tropical Meteorology, 2012, The 37 GHz Cyan Ring and Tropical Cyclone Rapid Intensification, What Does the Cyan Color Truly Represent?

AGU 2012, Using the 37 Color Composite PMW for Rapid Intensification Forecasts of Tropical Cyclones

AMS 31st Conference on Hurricanes and Tropical Meteorology, 2014, The Internal Structure of 1969 Hurricane Camille for the Atlantic Hurricane Database Reanalysis Project and A Reanalysis of 1969's Hurricane Camille (second author), and An Analysis of Rapidly Intensifying Tropical Cyclones Derived from 13 Years of TRMM Data (fourth author).

Kieper, M. E., Landsea, C. W., & Beven, J. L. (2016). A reanalysis of Hurricane Camille. *Bulletin of the American Meteorological Society*, 97(3), 367-384.

AMS 32nd Conference on Hurricanes and Tropical Meteorology, 2016, Tropical Cyclone Passive Microwave Precipitative-Structure-Based Intensity Estimates

AMS 33rd Conference on Hurricanes and Tropical Meteorology, 2018, Questions on Tropical Cyclone Structure as Analyzed from Precipitative Patterns Observed in Passive Microwave Imagery

AMS 34th Conference on Hurricanes and Tropical Meteorology, 2018, A Compilation of Tropical Cyclone Precipitative Characteristics Observed in Passive Microwave 37 GHz Color Composite Imagery

Joint Typhoon Warning Center, Honolulu, Hawaii, 2015, 37color Rapid Intensification Forecast Methodology and Advantages of a PMW Life Cycle Repository